Université du Québec
Institut national de la recherche scientifique
Centre – Eau Terre Environnement

A NON-DESTRUCTIVE CHARACTERIZATION OF MATERIALS IN EARTH AND ENVIRONMENTAL SCIENCES THROUGH A MULTISPECTRAL APPROACH WITH X-RAY TOMOGRAPHY

Par

Margherita Martini

Thèse présentée pour l'obtention du grade de Philosophiae Doctor (Ph.D.)

en sciences de la terre

Jury d'évaluation

Président du jury et Examinateur interne	Mathieu J. Duchesne Centre – Eau Terre Environnement National Institut national de la recherche scientifique
Examinateur interne	Christian J. Dupuis Centre – Eau Terre Environnement Institut national de la recherche scientifique
Examinateur externe	William Arnott Department of Earth and Environmental Sciences University of Ottawa
Examinateur externe	Gregory Robert Brooks Natural Resources Canada Ottawa
Co-directeur de recherche	Philippe Després Département de physique, d'ingénierie physique et d'optique Université Laval
Directeur de recherche	Pierre Francus Centre – Eau Terre Environnement Institut national de la recherche scientifique

To my mother,
who always believed in me.
To my father,
who never did.

REMERCIEMENTS

Ceci n’est pas une thèse

Ceci n’est pas une thèse, en fait, c'est beaucoup plus. C'est l'expérience la plus incroyable que j'aie jamais vécue, c'est la croissance, c'est l'espoir, c'est l'amour, c'est la douleur ; c'est ce que j'étais et ce que je suis devenu. Ces remerciements sont un résumé de moi pendant ces cinq années, car sans vous, je n'y serais jamais arrivée. Ces remerciements seront probablement grammaticalement incorrects et avec mes expressions typiques, un peu random, mais je m'en fiche, car lorsque vous les lirez, j'espère que vous pourrez imaginer ma voix et mes mots s'adressant à votre visage, et non quelque chose qui ne sert qu'à la façade.

Tout d'abord, je dois remercier les fondateurs de ce projet, c’est-à-dire : *Fonds de recherche du Québec–Nature et technologies*, *Natural Sciences and Engineering Research Council of Canada*, *Canada Research Chairs Program* et *Fonation canadienne pour l’innovation*. Je ne veux pas être vénale, mais c’est clair que sans eux, rien n'aurait été possible!

Aussi important que soit l'argent, aucun projet ne peut être mené à bien sans une équipe spéciale; et c'est à vous que je dois mes remerciements les plus sincères, pour chaque moment passé ensemble, pour chaque idée, chaque déception, chaque joie partagée. Merci à mon co-directeur de recherche Philippe, pour tout ce qu'il m'a appris et comment il m'a stimulé à réfléchir et à m'améliorer. Merci à Leonardo, mon ange physicien, qui m'a toujours patiemment aidé à comprendre ces difficiles formules mathématiques. Merci à Arnauld, notre McGyver, lui qui est la colonne vertébrale de notre équipe. Lui, sur qui tout le monde compte et personne n'est jamais déçu. Merci à Philippe, ami plus que collègue, car tu as toujours rendu nos journées au Labo Lourd agréables et drôles. Merci à Milena, pour toutes les conversations que nous avons eues à l'INRS et en dehors. Bien sûr merci à Léo, qui depuis ce fameux été 2020 m'a fait sortir de ma coquille, en révélant la vrai moi; merci aussi pour toutes ces bières passées à parler de science et d'idéaux. En fin, merci à tous les collègues avec lesquels j'ai partagé (même si ce n'est que pour une petite partie) ce doctorat ; merci Mathieu, merci Marie-Eugénie, merci Feng, merci Antoine, merci Obinna, merci Clarance, merci Fred.

Merci à tous les garçons et à toutes les filles que j'ai mentorés, vous m'avez aidé à grandir et j'espère que j'ai fait, sinon un bon au moins un décent travail. Évidemment, merci à mon mentor aussi, Pierpaolo

Ai-je oublié quelqu'un? Allez, tu sais que c'est toi… n’aurais pas pensé de lire des remerciements banals de ma part, n'est-ce pas?! Pierre, le fait est que je ne sais pas par où commencer, je pense que je pourrais écrire une autre thèse tellement sont nombreux les raisons pour te remercier. Tout d'abord, je dois te remercier car tu as été la première personne à croire en moi; je ne sais pas ce que tu as vu dans cette Italienne qui parlait un anglais un peu croche, mais je sais que tu as décidé de parier. Je voudrais te remercier d'avoir toujours été là, de m'avoir fait grandir et de m'avoir soutenue. Tu n'as pas été juste mon directeur de recherche, mais mon maître. Tu n'étais pas seulement là pour m'enseigner et me corriger, tu étais là pour partager, tu étais aussi un ami et, avouons-le, un peu un père. Je ne sais pas si j'ai toujours été une bonne élève, j'ai certainement eu des up et des down, mais une chose est sûre : j'espère ne jamais t’avoir déçu, j'ai poursuivi mon, ton, notre travail avec le cœur sur la main, tous les jours et j'espère te l'avoir fait comprendre.

Ensuite, cette expérience a également impliqué de nombreuses personnes dehors du travail et même ici, vous êtes si nombreux que je ne sais pas vraiment par où commencer. En suivant la ligne du temps, je voudrais remercier avant tous Laura, la première personne que j'ai rencontrée et la première amie…et notre amitié s'est toujours maintenue (et se maintiendra!); puis, merci à notre petit gang, pour tous les bons et moins bons moments passés ensemble: merci à Matthieu, à Dan, à Majo.

Merci à tous les habitants (réels et acquis) du 727 rue D'Aiguillon: quels moments incroyables nous avons vécus ensemble! Combien de fêtes, combien de soirées, combien de nuits qui nous avons partagé! Merci tout d'abord à Ophé, Alice, Simon x 2, Whitney, Désirée, Amine, Sav, Khawla, Antoine, Anissa, Moktar, Marc-Alexandre... mais en réalité vous êtes bien plus nombreux, et merci à chacun d'entre vous pour chaque toast que nous avons porté ensemble. Merci à tous les amis français (surtout Simon, Arnaud, Ced et Ben), dont la plupart sont revenus ou reviendront et avec lesquels je prendrai bientôt un verre en souvenir du bon vieux temps. Et merci à mes amis québécois, il y a quelque chose de spécial en vous: merci Alice, merci Guillaume, merci François, merci Jasen.

Je voudrais ensuite remercier les différentes "familles" dont j'ai fait partie, que je porte et porterai toujours dans mon cœur. Tout d'abord, merci à la famille du Tequila Lounge (en particulier Ari, Caro et Kath). Merci de m'avoir accueillie et soutenue dans tous les moments heureux et moins heureux, comme on sait bien. Merci à toutes les familles d'arts martiaux, c’était un honneur s’entrainer et se battre ensemble: merci avant tous à mon sifu, mes sihing (mais surtout le *sin*!) et tous mes frères et sœurs de Kung Fu, avec un câlin spécial à Véronique, l'une des personnes les plus gentilles que j'ai rencontrées dans ma vie. Merci de m'avoir accueillie dans l’école alors que j'étais perdue et merci de m'avoir aidée à retrouver mon centre. Merci à mes compagnons du Krav Maga et à George, merci pour tous les coups que nous nous sommes donnés en riant et en apprenant ensemble. Merci au Nordik Fight Club et à tous mes coaches et amis de BBJ (même si je suis nulle, on le sait!) et surtout de Muay Thai…spécialement les filles qui fight like a girl_Nordik. Merci pour le sparring, les sueurs, les bleus, la fatigue et les rires. Merci de m'avoir permis de me défouler et d'avoir enfin fait re-sortir la bête.

Mais parmi tous ces amis de combat, il y en a deux qui sont plus spéciaux que les autres: Romain et Léo. Vous deux vous êtes incroyables et si je devais énumérer toutes les choses pour lesquelles je suis heureuse de vous avoir dans ma vie, cela me prendrait des heures. Bien que nous soyons et serons dans deux parties opposées du monde, j'ai la certitude que nous nous reverrons, même si je ne sais pas encore où.

Mais, mais, mais….pour être honnête ce doctorat n'a pas été marqué que par des choses positives et sur mon chemin, il y a eu beaucoup de personnes plus ou moins toxiques qui m'ont attristée, déçue et parfois détruite. Au début, j'ai pensé écrire une de ces choses motivantes comme "vous m'avez rendu plus fort", "vous m'avez jeté entre les loups et j'en suis sorti chef de meute" et bla bla bla....mais ce ne sont que des conneries! Si j'avais eu le choix, j'aurais volontiers évité de partager ma vie avec vous, mais malheureusement je ne peux pas le faire et je dois me rendre à l'évidence, je dois accepter cette horrible expérience et en prendre note dans l'espoir de ne plus jamais trouver des "amis" comme vous. À la fin, j'ai survécu malgré vous. Par ces mots, je suis heureuse de vous dire que j'espère ne jamais vous rencontrer à nouveau et donc, au revoir pour toujours.

Et puis, toi. Toi que je n'ai pas besoin de nommer car il est trop évident de savoir de qui je parle, toi qui n’étais ni excellent ni fatal ou mieux, toi qui as été à la fois excellent et fatal, toi qui as joué un rôle très important dans mes émotions pendant la plus grande partie de ce doctorat. Quoi dire? Merci et pas merci: avec toi dans ma vie, je me suis sentie vivante comme jamais auparavant et puis je me suis sentie morte à l'intérieur comme jamais auparavant. À la fin, comme le phénix, j’ai ressuscité et j'ai même appris à voler. Maintenant, je suis à la page 162.

Now, let’s switch to English... I don’t have to thank only Francophones! Indeed, I had the chance to meet so many people from so many countries, who helped make this journey even more special. Thanks to all the people with whom I shared great evenings and/or quick chats in

Grenoble, in Bariloche, in Ghent, in Granada. Thanks to all the people who have opened my eyes to an unknown and immense world of which I still know too little (and I'm not just talking about academia!).

Thanks to all the professors at Ghent who welcomed, helped and encouraged me (Veerle Cnudde, Marteen Van Daele and Matthieu Boone). Thank you for sharing a part of your world with me. But in Ghent, where there is and there will remain forever a part of my heart, I have to thank Jan, Loïc, Pierre, Florian and especially my dear Laurenz (you are not only a colleague, but you are also a dear friend!).

I would like to thank the organizers of ICTMS, my first conference, which was not only an incredible experience, but allowed me to find my future work team and I can’t wait to move to Lyon.

Thank you very much for the experience I had at the IAP IPA in Argentina, where I was able to get to know wonderful places and people (especially Pablo and Nahuel).

And…last but not least, thank you very much for the Excite meeting in Granada! Again, I met several incredible people and I am very grateful. Anyway, two guys are more incredible than others: I'm really happy to have met Giovanni and Alessandro, with whom I shared three crazy days (eh raga lo so che sembro cretina a menzionarvi in inglese, però cadete nella tematica “conferenze” quindi ve la baccate…anche se forse è meglio così, l’inglese mi censura di più!).

Then, I would like to thank *you*: sorry, but I am not brave enough to write to you in your language. Thank you for giving me three magical months, even if *it’s harder to breathe when you’re gone, I dream of the day you were eating for two*.

Bene, ora passiamo alla madre lingua! Il ringraziamento più grande va senza dubbio a mia mamma e mia sorella. Poi vorrei ringraziare con il cuore la mia famiglia in generale e soprattutto mandare un pensiero a quelle persone (consanguinee e non) che non sono più qui per leggere queste parole.

Vorrei ringraziare quelle che persone che mi sono state accanto all’inizio di questo percorso e che per varie ragioni non fanno più parte della mia vita : nonostante ciò, io non vi dimentico e vi ringrazio per il vostro sostegno. Poi vorrei ringraziare quelle persone che invece sono tornate!

Grazie Linda, sono davvero contenta di poter condividere non solo l’inizio ma anche la fine di questo dottorato.

Vorrei ringraziare tutte quelle persone che ci sono sempre state. Prima di tutto grazie al Branduccello, mia affinità elettiva. Poi grazie a Barbara, presenza costante nella mia vita da eoni. Grazie a tutti quegli amici con cui ho condiviso un caffè, una birretta o una sidreria ogni volta che tornavo (Fede, Sala, Mitsu, Sara, Marzia, Andre, Cossu, Gabri, Yuri).

Grazie alla mia adorata nanetta, mi spiace che non ci si senta troppo (ok che fai il medico, ma menatela di meno!) ma sei speciale Madda maleddeta. Grazie per farmi venire ogni valta male agli addominali dalle risate. Grazie al mio caro Zac, la distanza non ci ha mai divisi e mai ci dividerà!

Grazie al GAM e in particolare ad AUT, nonostante la lontananza abbiamo comunque condiviso momenti bellissimi. Grazie soprattutto a Gianluca.

Grazie a Fra, tu che potresti vincere il premio come il più citato nei miei ringraziamenti di tesi! Ahahaha e infatti sei ancora qui, anche se in veste diversa. Grazie mille per il tuo sostegno e la compagnia che ci siamo fatti per telefono, è sempre bello parlare con te.

Grazie a molti torinesi speciali, nonostante siano passati anni ci si vede e ci si sente ancora! Grazie Elo, grazie Zoll, grazie Manu e soprattutto grazie Ste!

Per terminare, grazie Alessandro Re, il moi relatore di tesi magistrale, grazie perché sono qui per merito tuo, perché tutto è partito da te, che mi hai insegnato ad amare i raggi X. E grazie a Dora, la mia terapeuta, che mi ha presa per i capelli e mi ha tirata fuori dall’abisso, è anche grazie a te se sono qui.

In conclusion (now I write in English just because it is the international language), thanks to all those who have shared a small or large part of this PhD, because it is also thanks to you that I can now say out loud: "I am a scientist".

RÉSUMÉ

Depuis les années 2000, de nombreux projets visant à quantifier les données obtenues à partir de deux tomodensimètres (médical et micro-) ont été réalisés au *Laboratoire multidisciplinaire de tomodensitométrie pour les ressources naturelles et génie civil*, INRS, Québec, Canada, mais l'approche multispectrale n'a jamais été explorée systématiquement. L'objectif de cette thèse est de développer un protocole de mesure pour la tomodensitométrie en biénergie afin d’obtenir des informations qualitatives et quantitatives en 3D et de manière non-destructive.

Plusieurs méthodes existantes sont décrites dans la littérature. Il a d'abord fallu sélectionner la plus appropriée. La méthode de calibration stœchiométrique pour la tomodensitométrie à double énergie, précédemment élaborée à des fins médicales, a été choisie. Des minéraux purs ont été analysés avec le tomodensitomètre médicale pour tester l'applicabilité de la méthodologie sur des échantillons aussi denses que ceux rencontrés en géologie. Les minéraux les plus importants et les plus courants, qui ne sont généralement pas distinguable par tomodensitométrie à simple énergie, ont été identifiés avec succès, démontrant ainsi l'utilité de cette technique en géologie.

Deuxièmement, une étude d’un cas réel a été réalisée : une carotte de sédiments varvés du lac South Sawtooth (Arctique), contenant un enregistrement paléoclimatique de 2,9 ka. L'utilisation de la tomodensitométrie à double énergie a permis de caractériser trois faciès différents (varves clastiques à grain fin, varves clastiques à grain grossier et couches à dépôt rapide de sable et de lamines riches en grains), ce qui n'était pas possible avec la tomodensitométrie à simple énergie. Les bases d'une nouvelle approche qualitative et quantitative de l'analyse des sédiments ont ainsi été jetées.

Troisièmement, trois roches impures ont été analysées avec trois scanneurs différents (médical, micro-CT personnalisé et micro-CT commercial) afin d'examiner les similitudes et les différences des résultats entre les instruments et d'évaluer quels sont les paramètres qui fonctionnent mieux par rapport aux objectifs de la recherche. Cette dernière étude permet de définir quelques lignes directrices importantes pour l'utilisation de la tomographie à double énergie, bien qu'un protocole général applicable à tous les scanneurs et à tous les types d'échantillons se soit avéré irréaliste.

En conclusion, cette thèse jette les bases d'une caractérisation quantitative et qualitative sur une variété d'échantillons analysés en sciences de la terre par tomodensitométrie à double énergie. Cette méthode est facile à utiliser, ne nécessite pas de calculs complexes et est applicable non seulement en géologie, mais aussi dans plusieurs autres domaines.

Mots-clés :

- Tomodensitométrie médicale
- Micro-tomodensitométrie
- Rayons X
- Biénergie
- Protocole
- Géologie
- Caractérisation
- Minéraux
- Sédiments

ABSTRACT

This thesis arises from the scientific needs of the *Laboratoire multidisciplinaire de tomodensitométrie pour les ressources naturelles et génie civil*, *INRS*, Québec, Canada, which is equipped with two CT-scanners, a medical- and a micro-CT. Since the 2000s, numerous projects aimed at quantifying the data obtained from the scanners have been carried out, but the multispectral approach was never systematically explored. Thus, the goal of this thesis is to develop a multispectral measurement protocol for X-ray CT (both medical and micro) to non-destructively retrieve qualitative and quantitative information in 3D.

Several existing methods are described in the literature. The most appropriate one had first to be selected. The stoichiometric calibration method for dual-energy CT, previously used for medical purposes, was chosen. Pure minerals were scanned with a medical CT to test the applicability of the methodology on samples as dense as those encountered in geological studies. The most important and common minerals (i.e., quartz, calcite, dolomite), that are usually not distinguishable using single energy CT, have been successfully identified, demonstrating the suitability of the technique in Earth Science.

Second, an actual case study was investigated: a varved sediment core from South Sawtooth Lake, in the Arctic, containing 2.9 ka long paleoclimate record. Using dual-energy CT scanning, three facies, namely fine-grained clastic varves, coarse-grained clastic varves and grain-supported sand-rich-laminae rapidly deposited layers, were successfully characterized, something that was not possible using single energy CT.

Third, three impure rock specimens were analyzed using three different scanners (a medical CT, a custom-built micro-CT and a commercial micro-CT) in order to investigate the similarities and differences in the outputs among the three instruments and to evaluate which settings and workflow worked best in relation with the research objectives. This last study allows defining some important guidelines for the use of dual-energy CT, although a general protocol applicable to all scanners and types of samples proved to be unrealistic.

In conclusion, this thesis provides the foundation for a successful quantitative and qualitative characterization of a variety of samples analyzed in Earth Science by a dual-energy CT scanning method. This method is easy to use, does not require complex calculation, and is applicable not only in geology but also in many other fields.

Keywords:

- Medical computed tomography
- Micro-CT
- X-ray
- Dual-energy
- Protocol
- Geology
- Characterization
- Minerals
- Sediments

SOMMAIRE RÉCAPITULATIF

Introduction

La tomodensitométrie à rayons X est une technique non destructive qui permet de visualiser la structure interne d'un échantillon; elle a vu le jour dans la seconde moitié du 20e siècle à des fins médicales et ne permettait d'analyser que la tête des patients (Alvarez and Macovski, 1976). Par la suite, au fil des années, l'instrument a connu de nombreuses évolutions, permettant d'analyser l'ensemble du corps de manière de plus en plus précise (on passe des instruments dits de *première génération* à ceux de *quatrième génération*). En général un scanneur médical se compose d'une source de rayons X et d'un détecteur, qui se font face et tournent autour de l'échantillon. Des projections radiographiques bidimensionnelles sont acquises à différents angles de 0° à 360°, puis traitées par un algorithme mathématique (reconstruction d'image) afin d'obtenir une visualisation en 3D de l'objet (Kalender, 2011; Luke *et al.*, 2013).

Bien que son objectif initial ait été lié à l'étude du corps humain, son énorme potentiel a été rapidement perçu et les applications en dehors du domaine médical n'ont pas manqué de paraître (Cnudde & Boone, 2013). En effet, cette technique a apporté d'innombrables bénéfices dans les domaines de la botanique (Barron, 2023), de l'archéologie (Re *et al.*, 2015), de l'ingénierie (Vinegar & Wellington, 1987) et, bien sûr, de la géologie (Van Geet *et al.*, 2000).

Dans les années 80, afin de répondre aux besoins d'applications de plus en plus étendues, un type de scanneur permettant d'atteindre une résolution plus élevée (de l'ordre du micromètre) a été développé : le scanneur micro-CT (également appelé scanneur industriel). Sa conception diffère de celle du scanneur médical, car la source et le détecteur sont fixes, et l'échantillon, situé entre les deux, tourne autour de son propre axe (Elliott & Dover, 1982). Il est évident que cet instrument a connu un succès considérable dans le domaine scientifique, et en particulier en géologie, en permettant d'étudier de nombreux types d’échantillons plus en détail (Akbari A., 2015; Alves *et al.*, 2014a; Van Geet *et al.*, 2001b).

Principes physiques de la tomodensitométrie

Le principe physique sur lequel la tomodensitométrie à rayons X repose est l'atténuation du faisceau incident par un échantillon, qui peut absorber totalement ou partiellement le rayonnement. Cette relation est décrite par la loi de Lambert-Beer (équation 1.2 dans le texte principal). L'absorption des rayons X dépend à la fois de l’épaisseur de la cible, de sa composition chimique et de sa densité et cette absorption différente en fonction du matériau permet de visualiser la structure interne de l'objet étudié (Hendee, 2002).

Les interactions entre les photons et la matière, essentiels pour la tomodensitométrie, sont l'absorption photoélectrique et la diffusion de Compton : la première, liée à la composition chimique du matériau irradié, se produit lorsque le photon incident transfère toute son énergie à un électron interne, qui est émis sous la forme d'un photoélectron. Par la suite, une cascade d'électrons se produit pour combler le vide créé et un rayon X caractéristique de l'élément est émis. La seconde qui est liée à la densité de l'échantillon se produit lorsque le rayonnement incident frappe un électron externe qui est éjecté. Le photon est dévié inélastiquement de sa trajectoire initiale. En fonction de la composition de l'échantillon et de l'énergie incidente, un phénomène prévaudra sur l'autre (Bushberg, 2012).

On en déduit qu'en tomodensitométrie par transmission « classique », ces deux effets se superposent dans le résultat final ce qui a pour effet qu’il est possible d'obtenir des images avec le même niveau de gris alors que les matériaux sont différents par leur composition chimique ou densité. Pour résoudre ce problème, la tomodensitométrie en bi-énergie a été développée dans le 1970.

Tomodensitométrie biénergétique

Dans les années 70, deux scientifiques ont inventé cette technique afin d'améliorer la visualisation et la caractérisation des matériaux par tomodensitométrie; cette technique a été initialement conçue pour l'étude des tissus humains (Alvarez & Macovski, 1976).

Le principe scientifique derrière la biénergie réside dans la possibilité de séparer les informations obtenues par les deux effets (l'absorption photoélectrique et la diffusion Compton) en utilisant le faisceau de rayons X incidents à deux énergies différentes, une basse et une haute. Plus précisément, les propriétés des matériaux étudiés avec la biénergie sont le numéro atomique effectif (Z_{eff}) et la densité électronique (ρ_e). Le premier peut être défini comme l'expression numérique de la composition chimique et n'a pas d'unité de mesure (Alves *et al.*, 2015), tandis que la seconde est le nombre d'électrons par unité de volume et se mesure en électrons par centimètre cube (Azevedo *et al.*, 2016).

Depuis les premiers développements jusqu'à aujourd'hui, il existe de nombreux exemples de méthodologies de tomodensitométrie en bi-énergie dans la littérature et de nombreuses équations ont été développées pour caractériser les matériaux sur la base des propriétés susmentionnées (Bazalova *et al.*, 2008; Torikoshi, 2003; Tsunoo *et al.*, 2004; Watanabe, 1999).

Bien que cette technique ait été conçue à des fins médicales, les applications dans d'autres domaines n'ont pas manqué, surtout dans le domaine géologique. Si d'un côté les différentes méthodologies ont apporté de bons résultats, de l'autre elles nécessitent généralement le calcul du spectre incident, ce qui n'est pas à la portée de tous et nécessite souvent des calculs complexes (Alves *et al.*, 2014b; Paziresh *et al.*, 2016; Remeysen & Swennen, 2008).

Mise en contexte et objectifs de recherche

L'idée de ce travail de recherche est née dans les murs du *Laboratoire multidisciplinaire de tomodensitométrie pour les ressources naturelles et génie civil*, *INRS*, Québec, Canada. Le laboratoire est équipé d'un scanneur médical (Siemens Somatom Definition AS+128) et d'un micro-CT (CoreTOM, TESCAN), qui est une acquisition récente.

Depuis les années 2000, de nombreux projets visant à quantifier les données obtenues à partir des scanneurs ont été menés, mais sans jamais aboutir à une élaboration d'une méthode précise qui puisse être utilisée à la fois au quotidien et comme référence pour tous les autres laboratoires. Les principaux travaux sur ce sujet ont été réalisés par Boespflug *et al.* (1994), Duchesne *et al.* (2009) et Larmagnat *et al.* (2019).

Dans ce contexte, il est important de mettre au point un protocole de mesure adapté à la recherche en sciences de la Terre capable de fournir des informations non seulement qualitatives, mais aussi quantitatives, en trois dimensions et de manière non destructive.

Pour ce faire, les techniques multispectrales sont particulièrement appropriées. Comme expliqué précédemment, les méthodologies sont variées et il faut choisir celle qui est la plus adaptée au domaine géologique et qui peut également être facilement utilisée par tous les laboratoires impliqués dans ce type de recherche; il s'agit de trouver une méthodologie qui ne soit pas trop compliquée au niveau de calculs (comme les techniques qui nécessitent de connaître le spectre des rayons X incidents) de le rendre accessible à tous les laboratoires de géologie, même si le personnel n'a pas un niveau élevé de connaissances en physique et qui fonctionne en même temps sur des matériaux denses tels que ceux étudiés en géologie. Ce second objectif n'est pas trivial, car la plupart des méthodes ont été développées à des fins médicales et les applications de la biénergie au domaine géologique ont toujours été très limitées en termes de gamme d'échantillons.

La meilleure méthodologie possible doit d'abord être évaluée. En se basant sur la facilité d'application et la simplicité des calculs mathématiques à effectuer, notre choix s’est porté sur les méthodes stœchiométriques (voir section suivante). La technique sera appliquée à des matériaux d'intérêt géologique : tout d'abord, des minéraux, courants et ayant une composition simple, seront identifiés pour tester l'adéquation de la méthode. Par la suite, des matériaux plus complexes des sciences de la Terre seront étudiés afin de tester son applicabilité réelle. Pour terminer et rendre la méthodologie encore plus générale, elle sera appliquée à d'autres instruments, par exemple le nouveau micro-CT, afin d'étudier et de comparer la qualité des résultats.

Méthode de calibration stœchiométrique

Comme déjà mentionnées, de nombreuses méthodologies requièrent la connaissance du spectre incident afin d'obtenir de meilleurs résultats, mais certains physiciens médicaux (Landry *et al.*, 2013) ont récemment développé des techniques qui ne requièrent pas cette connaissance, ce qui simplifie grandement l'analyse.

La méthodologie de calibration stœchiométrique (Bourque *et al.*, 2014) est basée sur l'idée, comme toutes les calibrations, de scanner différents échantillons ayant des Z_{eff} et ρ_e connues. Il existe de nombreuses équations dans la littérature pour calculer ces deux propriétés à partir de leur composition chimique, et selon la recherche à effectuer, l'une ou l'autre peut être choisie. Dans le cadre de ce projet de recherche, l'utilisation de formules mathématiques impliquant le numéro atomique Z_i du *i*-ième atome du composé est préférable en raison de leur simplicité d'application (Bonnin *et al.*, 2014).

Ces échantillons de composition connue (étalons) doivent être scannés deux fois, à basse et à haute énergie, puis les coefficients d'atténuation linéaire (μ) respectifs doivent être calculés.

Ensuite, deux courbes de calibration différentes (relatives aux deux propriétés) doivent être tracées : la première est liée à Z_{eff} et la seconde est liée à ρ_e. Pour Z_{eff}, le rapport des deux valeurs d'atténuation linéaire (à basse et haute énergie) et la valeur connue de Z_{eff} des étalons sont tracés dans un diagramme afin de pouvoir ajuster la meilleure courbe et en estimer les coefficients. Ensuite, pour ρ_e, il faut tracer le rapport entre le coefficient d'atténuation linéaire mesuré, soit à basse énergie, soit à haute énergie, et la valeur connue du ρ_e normalisé par la densité électronique de l'eau, et le Z_{eff} déterminé dans l'étape précédente. Donc, un autre ensemble de coefficients sera déterminé. Dans les deux cas de cette thèse, une régression polynomiale du 2^e ordre produit le meilleur ajustement, en donnant un coefficient de corrélation R^2 le plus élevé.

Les articles scientifiques

Afin d'atteindre les objectifs proposés, trois articles scientifiques représentant les étapes nécessaires au développement de ce protocole de mesure seront présentés; tout d'abord le travail commence par les cas les plus simples, puis a été progressivement rendu plus complexe. Pour finir, on a essayé de répondre aux questions scientifiques qui ont émergé de ces expériences.

1. Le premier article de cette thèse vise à tester la méthodologie de calibration stœchiométrique afin d'identifier les minéraux communément trouvés dans les contextes géologiques. Tout d'abord, un étalonnage a été effectué comme décrit. Les matériaux étalons utilisés étaient de différentes natures : minéraux purs, barres métalliques et solutions liquides de différentes concentrations. Les deux séries de coefficients des équations polynomiales du second degré ont donc été obtenues et 23 minéraux "inconnus" ont été identifiés en définissant leur numéro atomique effectif et leur densité électronique. Afin de valider ces résultats, deux routines ont été écrites en langage de programmation *Python* : le premier est un dictionnaire dans lequel 69 minéraux courants sont cartographiés en fonction de leurs deux propriétés, tandis que le second permet la saisie des Z_{eff} et ρ_e calculés par la méthode stœchiométrique et fournit une liste des minéraux du dictionnaire qui ont la plus petite distance euclidienne et sont donc les plus probables. Bien que les 23 minéraux n'aient pas tous été correctement identifiés, les plus courants et les plus importants d'un point de vue géologique (i.e., calcite, dolomite et quartz) ont été parfaitement caractérisés. Cet article a démontré le potentiel de la méthode stœchiométrique dans les sciences de la terre également, en fournissant la base d'un accès nouveau et facile aux informations minéralogiques.

2. Le deuxième article vise à appliquer la méthode de calibration stœchiométrique à une étude de cas réel. Une carotte de l'Arctique canadien, plus précisément du lac South Sawtooth, a été choisie : elle était particulièrement intéressante, car elle avait déjà fait l'objet d'études approfondies dans le cadre de recherches antérieures du laboratoire. Elle est caractérisée par des varves et contient des enregistrements paléoclimatiques de 2,9 ka. Dans le cas de l'étude par biénergie stœchiométrique d'une carotte de sédiments meubles, l'objectif n'est évidemment pas d'identifier un numéro atomique effectif et une valeur de densité spécifique. En effet, ce type d'échantillon est caractérisé par des variations importantes de porosité, de la composition minéralogique des particules qui constituent les varves. Dès lors, l'objectif est plutôt de reconnaître les trois faciès sédimentaires principaux de cette séquence : les varves clastiques à gros grains, les varves clastiques à grains fins et les couches déposées rapidement (RDL). Pour ce faire, de Z_{eff} et ρ_e ont été calculées à l'aide de la méthode stœchiométrique et leurs plages de valeurs ont été identifiées. Les résultats montrent que la biénergie permet de séparer et de caractériser ces différents faciès sédimentaires, qui seraient autrement impossibles à distinguer si l'on n'analysait la carotte avec une seule énergie. En plus, les résultats ont été comparés aux mesures micro-XRF : bien que l'alignement des résultats n'ait pas porté ses fruits, la corrélation entre certains éléments et les faciès était significative.

3. Le troisième article de cette thèse vise à répondre à certaines questions scientifiques qui se sont posées au cours du projet et qui sont en même temps très importantes pour généraliser la méthode afin qu'il puisse être utilisée par un grand nombre de laboratoires. Trois instruments différents ont été comparés : le CT médical, le micro-CT CoreTOM et le micro-CT HECTOR de l'Université de Gand. Avec ces trois scanneurs différents, trois roches dont la composition est connue grâce à des analyses XRD et ICP-OES, ont été étudiées. L'objectif était de voir dans quelle mesure on pouvait se rapprocher des propriétés réelles avec les trois scanneurs; en outre, plusieurs étalonnages ont été effectués afin de vérifier ou d'infirmer la dépendance instrumentale. Cette comparaison a mis en lumière plusieurs facteurs importants : il n'existe pas de calibration universelle pour la caractérisation des matériaux et la dépendance à l'égard de l'instrument (et du spectre de rayons X) utilisé est cruciale. Malgré cela, des lignes directrices ont été fournies pour mener à bien une analyse par biénergie de matériaux géologiques, en prêtant attention aux détails à respecter, comme l'utilisation de la moyenne ou du mode de l'histogramme

des niveaux de gris, la forme de la courbe de calibration du numéro atomique effectif ou le choix des énergies à utiliser.

Discussion

Bien que la tomographie à double énergie remonte aux années 70 et que les applications en sciences de la Terre n'aient pas manqué, cette technique n'est jamais devenue une mesure de routine. Une explication probable réside dans le fait que les matériaux géologiques sont très divers : les minéraux, les roches et les sédiments ont une structure très différente en termes de densité, d'hétérogénéité, de cohésion ou de composition chimique. Pourtant, il n'est pas facile de trouver une analyse générale qui réponde aux besoins de chaque groupe de recherche. En outre, pour être plus performantes, de nombreuses techniques de biénergie nécessitent la connaissance du spectre de rayons X incidents, et cette caractéristique n'est pas toujours facile à calculer.

Après avoir expérimenté d'autres méthodologies, c.à.d., la paramétrisation des rapports d'énergie pour dériver les numéros atomiques effectifs à partir de la technique en biénergie développée par Landry *et al.* (2013), la méthode de calibration stœchiométrique, expliquée précédemment, s'est avérée la plus appropriée au contexte géologique.

Premièrement, des minéraux, qui constituent les matériaux les plus basiques dans le domaine géologique, ont été analysés. L'objectif final de cette étude n'est pas de trouver une alternative à l'identification des minéraux, mais d'ouvrir la voie à des analyses en biénergie réussies, rapides et faciles à appliquer pour tous les laboratoires géologiques. Elle pourrait s’avérer très utile dans le cas où l’assemblage des minéraux composant une roche est connu et qu’il faut identifier l’occurrence d’un minéral bien spécifique dans une roche.

Ces mesures réalisées sur des minéraux ont donné des résultats prometteurs, démontrant que cette méthode de calibration stœchiométrique peut caractériser avec succès même des échantillons avec des plages de valeurs de Z_{eff} et ρ_e plus élevés que les tissus humains, pour lesquels elle a été élaborée initialement.

Deuxièmement, un échantillon géologique plus complexe a été analysé en biénergie afin de tester le potentiel de cette méthodologie sur un cas réel à la démonstration de l'utilité de cette méthodologie pour l'identification des différents faciès.

Grâce à cette étude, les bases d'une nouvelle approche de la caractérisation des enregistrements sédimentaires, accessible à tous, ont ainsi été jetées. En plus, la méthode peut être applicable dans plusieurs recherches, telles que la sédimentologie environnementale, la reconstruction du climat, la paléosismologie et la caractérisation des réservoirs.

Enfin, trois instruments de tomodensitométrie différents (un scanneur médical, un micro-CT sur mesure et un micro-CT commercial) ont été comparés et cette partie du travail représente la clé de voûte de la détermination d'un protocole de mesure pour l'approche multispectrale par tomodensitométrie à rayons X. En effet, concevoir un protocole de mesure signifie non seulement trouver quelque chose qui fonctionne dans un cas particulier, mais aussi le rendre utilisable dans plusieurs cas tout en garantissant sa répétabilité. Il est donc essentiel de fournir des lignes directrices pour les analyses en biénergie avec n’importe quel scanneur afin d'aider les futurs utilisateurs de différents laboratoires géologiques à obtenir les meilleurs résultats possibles.

L'étude a mis en évidence les facteurs clés qui doivent être pris en compte avant de commencer les analyses en bi-énergie. Tout d'abord, il a été observé que les spectres de rayons X sont différents les uns des autres, même si les instruments sont similaires, et qu'ils interagissent différemment avec les échantillons. Cette interaction spécifique entre le faisceau incident et les matériaux analysés affecte également la calibration et le choix des échantillons pour l'effectuer. De plus, la paire d'énergies la plus appropriée n'est pas universelle, mais dépend du scanneur.

Malgré ces considérations et bien que l'on puisse affirmer qu'il peut exister des conditions d'analyse parfaites pour chaque instrument, mais pas parfaites en général, les lignes directrices à suivre sont plus simples. Même sans connaître le spectre des rayons X, il est conseillé de choisir une paire d'énergies suffisamment élevée pour que les rayons X puissent pénétrer les matériaux étudiés, et ainsi réduire le bruit du signal perçu par les détecteurs. Il est suggéré de choisir une large gamme de matériaux étalons et de vérifier de manière pratique quels sont ceux qui donnent les meilleurs résultats, par exemple en effectuant un test avec un échantillon connu. Il est recommandé que ces échantillons étalons aient des Z_{eff} et des ρ_e variés et qu'ils soient aussi semblables que possible aux échantillons à étudier. Pour obtenir de meilleurs résultats, il est important de vérifier que la forme de la courbe d'étalonnage de Z_{eff} doit être concave et, si les matériaux étudiés sont très denses, il est préférable d'utiliser le mode plutôt que la moyenne de l'histogramme des niveaux de gris pour calculer μ afin d'atténuer l'influence du durcissement du faisceau.

Bien qu'il ne soit pas possible de définir un protocole de mesure généralisable à tous les laboratoires, car chaque scanneur est différent, ces lignes directrices permettent de réussir la caractérisation des matériaux géologiques à l'aide de la biénergie.

Conclusions

Bien que les méthodes à double énergie aient été utilisées dans certains travaux de recherche, elles ne sont jamais devenues une technique de routine et leur potentiel dans les sciences de la terre n'a jamais été exploré en profondeur et cette thèse vise à démontrer son grand potentiel.

Après avoir évalué certaines techniques en bi-énergie, la méthode de calibration stœchiométrique a été choisie en raison de sa simplicité d'application, qui la rend facilement utilisable par n'importe quel laboratoire géologique. Tout d'abord, la technique a été appliquée à un scanneur médical afin d'identifier des minéraux courants dans les sciences de la terre : l'étude a été menée à bien, démontrant la pertinence de la méthode dans ce domaine. Elle a ensuite été appliquée à une étude de cas réelle, une carotte du lac South Sawtooth dans l'Arctique, et trois faciès sédimentaires différents ont été bien distingués, jetant les bases d'une méthode applicable dans plusieurs recherches.

Ensuite, trois échantillons de roches impures, dont la composition est connue grâce à des mesures XRD et ICP-OES effectuées précédemment, ont été caractérisés à l'aide de trois scanneurs différents : un scanneur médical, un micro-CT sur mesure et un micro-CT commercial. Différents réglages ont été testés, démontrant que les meilleures conditions d'acquisition sont différentes pour chaque instrument, et qu'il n'est pas réaliste de développer un protocole de mesure valable pour chaque laboratoire. Cependant, des lignes directrices importantes sont définies pour aider les scientifiques dans leur étude de caractérisation.

En conclusion, cette thèse fournit toutes les étapes à suivre pour réaliser une caractérisation robuste des matériaux géologiques par tomodensitométrie, mais celle-ci peut également être applicable à d’autres domaines d’études.

Références

Akbari A. GS (2015) Micro-CT scanning of soil aggregate: the importance of image thresholding. in *2nd International Conference on Tomography of Materials and Structures*Québec, QB, Canada), p 622-626.

Alvarez RE, Macovski A (1976) Energy-selective reconstructions in X-ray computerized tomography. *Physics in Medicine & Biology* 21(5):733-744.

Alves H *et al.* (2014a) Comparison of pore space features by thin sections and X-ray microtomography. *Applied Radiation and Isotopes* 94:182-190.

Alves H *et al.* (2015) Mineralogy evaluation and segmentation using dual-energy microtomography. *X-Ray Spectrometry* 44(3):99-104.

Alves H, Lima I, Lopes RT (2014b) Methodology for attainment of density and effective atomic number through dual energy technique using microtomographic images. *Applied Radiation and Isotopes* 89:6-12.

Azevedo SG *et al.* (2016) System-Independent Characterization of Materials Using Dual-Energy Computed Tomography. *IEEE TRANSACTIONS ON NUCLEAR SCIENCE* 63(1):341-350.

Barron A (2023) Applications of Microct Imaging to Archaeobotanical Research. *Journal of Archaeological Method and Theory* 10.1007/s10816-023-09610-z.

Bazalova M *et al.* (2008) Tissue segmentation in Monte Carlo treatment planning: a simulation study using dual-energy CT images. *Radiotherapy and Oncology* 86(1):93-98.

Boespflug X *et al.* (1994) Tomodensitométrie axiale: relation entre l'intensité tomographique et la densité de la matière. *Canadian Journal of Earth Sciences* 31(2):426-434.

Bonnin A *et al.* (2014) Concept of effective atomic number and effective mass density in dual-energy X-ray computed tomography. *Nuclear Instruments and Methods in Physics Research Section B: Beam Interactions with Materials and Atoms* 318:223-231.

Bourque AE, Carrier JF, Bouchard H (2014) A stoichiometric calibration method for dual energy computed tomography. *Physics in Medicine & Biology* 59(8):2059-2088.

Bushberg JT, Seibert, J.A., Leidholdt, E.M., Boone, J.M. (2012) *The essential physics of medical imaging.* LWW, Third edition

Cnudde V, Boone MN (2013) High-resolution X-ray computed tomography in geosciences: A review of the current technology and applications. *Earth-Science Reviews* 123:1-17.

Duchesne MJ *et al.* (2009) A rapid method for converting medical Computed Tomography scanner topogram attenuation scale to Hounsfield Unit scale and to obtain relative density values. *Engineering Geology* 103(3-4):100-105.

Elliott JC, Dover S (1982) X-ray microtomography. *Journal of microscopy* 126(2):211-213.

Hendee WR, Ritenour, E.R. (2002) *Mediacal Imaging Physics.* A JOHN WILEY & SONS, INC., PUBLICATION, USA, fourth

Kalender W (2011) *Computed tomography : fundamentals, system technology, image quality, applications.* Wiley-VCH, Weinheim, 3rd rev.

Landry G *et al.* (2013) Deriving effective atomic numbers from DECT based on a parameterization of the ratio of high and low linear attenuation coefficients. *Physics in Medicine & Biology* 58(19):6851-6866.

Larmagnat S *et al.* (2019) Continuous porosity characterization: Metric-scale intervals in heterogeneous sedimentary rocks using medical CT-scanner. *Marine and Petroleum Geology* 109:361-380.

Luke AM *et al.* (2013) Comparison of spiral computed tomography and cone-beam computed tomography. *Journal of Indian Academy of Oral Medicine and Radiology* 25(3):173-177.

Paziresh M *et al.* (2016) Tomography of atomic number and density of materials using dual-energy imaging and the Alvarez and Macovski attenuation model. *Journal of Applied Physics* 119(21).

Re A *et al.* (2015) X-ray tomography of a soil block: a useful tool for the restoration of archaeological finds. *Heritage Science* 3(1).

Remeysen K, Swennen R (2008) Application of microfocus computed tomography in carbonate reservoir characterization: Possibilities and limitations. *Marine and Petroleum Geology* 25(6):486-499.

Torikoshi M, Tsunoo T., Sasaki M., Endo M., Noda Y., Ohno Y., Kohno T., Hyodo K., Uesugi K., Yagi N. (2003) Electron density measurement with dual-energy x-ray CT using synchrotron radiation. *Physics in Medicine & Biology* 48:673–685.

Tsunoo T *et al.* (2004) Measurement of electron density and effective atomic number using dual-energy x-ray CT. in *IEEE Symposium Conference Record Nuclear Science 2004.*), p 3764-3768.

Van Geet M, Swennen R, Wevers M (2000) Quantitative analysis of reservoir rocks by microfocus X-ray computerised tomography. *Sedimentary Geology* 132(1-2):25-36.

Van Geet M, Swennen R, Wevers M (2001b) Towards 3-D petrography: application of microfocus computer tomography in geological science. *Computers & Geosciences* 27(9):1091-1099.

Vinegar HJ, Wellington SL (1987) Tomographic imaging of three-phase flow experiments. *Review of Scientific Instruments* 58(1):96-107.

Watanabe Y (1999) Derivation of linear attenuation coefficients from CT numbers for low-energy photons. *Physics in Medicine & Biology* 44(9):2201-2211.

TABLE OF CONTENTS

LIST OF FIGURES

LIST OF TABLES

LIST OF EQUATIONS

LIST OF ABBREVIATIONS

Ai: ATOMIC MASS OF ELEMENT

CHN: CARBON-HYDROGEN-NITROGEN ANALYSIS

CT: COMPUTED TOMOGRAPHY

DECT: DUAL-ENERGY COMPUTED TOMOGRAPHY

e^-: ELECTRON

E: ENERGY

E_0: INCIDENT ENERGY

EM: ELECTROMAGNETIC

f: FRACTION OF MATERIAL MASS

GPU: GRAPHIC PROCESSING UNIT

h: HIGH ENERGY

HU: HOUNSFIELD UNIT

I: TRANSMITTED RADIATION

I_0: INCEDENT RADIATION

ICP-OES: INDUCTIVELY COUPLED PLASMA ATOMIC ÉMISSION SPECTROSOPY

IRLS*:* ITERATIVE REWEIGHTED LEAST SQUARES

$K\alpha$: X-RAY CHARACTERISTIC RADIATION EMITTED WHEN THE ELECTRON IS FROM THE SHELL DIRECTLY ABOVE

$K\beta$: X-RAY CHARACTERISTIC RADIATION EMITTED WHEN THE ELECTRON IS FROM AN UPPER SHELL

k: PARAMETER ESTABLISHING THE ACCURACY LEVEL

l: LOW ENERGY

N_A: AVOGADRO’S NUMBER

r: ELECTRON RADIUS

R^2: CORRELATION COEFFICIENT

RDL: RAPIDLY DEPOSITED LAYERS

ROI: REGION OF INTEREST

s: THICKNESS OF INVESTIGATED SAMPLE

SEM: SCANNING ELECTRON MICROSCOPY

u: REDUCED HOUNSFIELD UNIT

x: ORIGINAL VALUE BEFORE THE NORMALIZATION

x': NORMALIZED VALUE

XRD: X-RAY DIFFRACTION

XRF: X-RAY FLUORESCENCE

Z: ATOMIC NUMBER

Z_i: ATOMIC NUMBER OF THE *I*TH ATOM OF A MIXTURE

Z_{eff}: EFFECTIVE ATOMIC NUMBER

Z_{eff_Calc}: EFFECTIVE ATOMIC NUMBER OF CALIBRATION SAMPLES

Z_{eff_Meas}: EFFECTIVE ATOMIC NUMBER MEASURED USING DECT METHOD

$Z_{eff\_Meas\_sIM}$: EFFECTIVE ATOMIC NUMBER MEASURED USING DECT METHOD AND SIMULATED μ

α: RATIO BETWEEN PHON ENERGY AND ELECTRON REST MASS

β: EXPONENT VARYING BETWEEN 2.94 AND 3.8, FUNCTION OF OPHOTON ENERGY, SAMPLE MATERIALS ANS SYSTEM SPECIFICS

Γ: RATIO OF REDOUCED HOUNSFIELD UNIT AT LOW AND HIGH ENERGY

μ: LINEAR ATTENUATION COEFFICIENT

μ_{LOW}: LINEAR ATTENUATION COEFFICIENT AT LOW ENERGY

μ_{HIGH}: LINEAR ATTENUATION COEFFICIENT AT HIGH ENERGY

μ/ρ: MASS ATTENUATIION COEFFICIENT

ρ: MASS DENSITY

ρ_e: ELECTRON DENSITY

ρ_{e_Calc}: ELECTRON DENSITY OF CALIBRATION SAMPLES

ρ_{e_Meas}: ELECTRON DENSITY MEASURED USING DECT METHOD

$\rho_{e\_Meas\_sIM}$: ELECTRON DENSITY MEASURED USING DECT METHOD AND SIMULATED μ

σ: PROBABILITY OF COMPTON SCATTERING OR KLEIN-NISHINA COMTON CROSS SECTION

τ: PROBABILITY OF PHOTOELECTRIC ABSORPTION

1 INTRODUCTION

1.1 Introduction: history and application of CT scan

The discovery of X-rays dates back to 1895 by the German physicist Wilhelm Conrad Röntgen. This discovery was completely accidental, occurring while the scientist was performing experiments with vacuum tubes. Röntgen observed that these “unknown” rays were able to impress photographic plates and penetrate opaque materials inversely proportional to their density (Rontgen, 1896). The foundations of X-ray imaging were thus laid.

After this discovery, which earned Röntgen the Nobel Prize in 1901, the usefulness and potential of X-rays was immediately clear: the resulting black-and-white images, called radiographs, allowed the visualization of the 2D internal structure of materials and their first applications in both the medical and industrial fields were not long in coming (Coolidge, 1913; Hall-Edwards, 1901).

Radiographies are going to be called projections later: they contain information about the X-rays attenuation through an object starting from the source prior to its impact on the detector.

The evolution of X-ray radiography is X-ray computed tomography (CT). This medical imaging technique allowed visualization of internal 3D structure of objects (Kalender, 2006) and was developed in the seventies. An X-ray source faces the detector, and they rotate together around the sample, acquiring bi-dimensional projections at various angles from 0° to 360°. These radiographies are processed through so-called *image reconstruction* obtaining a set of slices permitting the 3D visualization (Bushberg, 2012; Kalender, 2011).

The first mathematical algorithm to reconstruct CT images was proposed by Radon (1917) but for practical applications it was necessary to wait until computer power was easily available. Allan MacLeod Cormack (Cormack, 1963) was the first to publish the theoretical basis of CT, which was then developed by Godfrey Newbold Hounsfield (Hounsfield, 1972). CT earned both scientists the Nobel Prize in 1979. The CT scanner they developed is called the “first generation”: it is characterized by a source generating a pencil beam and a single detector (Figure 1.1 A). The “second generation” are the first commercial scanners, very similar to the first generation, except for the beam, which turns out to be multiple pencil (Figure 1.1 B). Both types of scanners functioned according to the translation–rotation principle in which source and detector scan the object in a linear translatory motion; this procedure is then successively repeated after a small rotational increment. In “third generation” CT scanners, the beam becomes a fan, and the detector is larger and curved, which improves image acquisitions (Figure 1.1 C). The “fourth generation” uses a stationary ring of detectors; the X-ray source rotates around the object inside the detectors ring (Figure 1.1 D) (Kalender, 2006; Luke *et al.*, 2013).

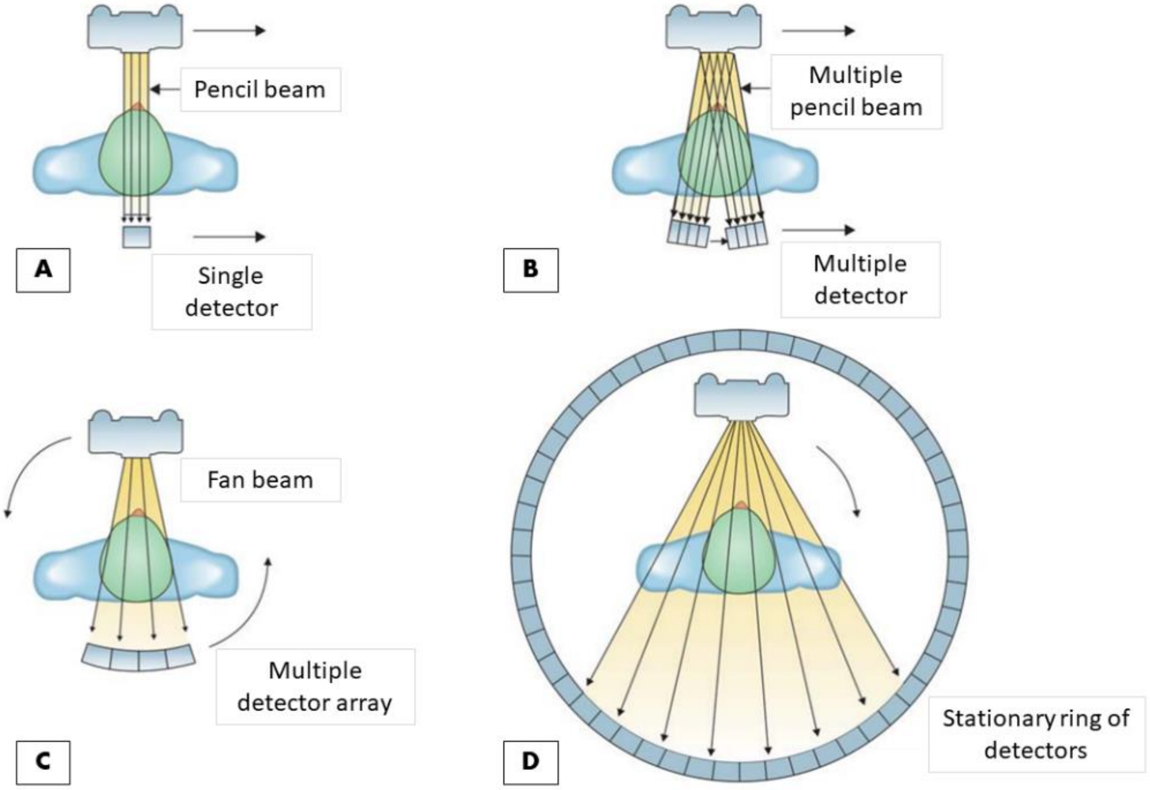

Figure 1.1: Evolution of CT scan system.

A) First generation CT scanner. B) Second generation CT scanner. C) Third generation CT scanner. D) Fourth generation CT scanner. From Luke *et al.* (2013).

Even if this technique was developed for medical purposes, it has been widely used in different research fields, primarily in paleontology to study the cranial morphology of an ancient tetrapod (Fourie, 1974). CT allowed the restoration of archeological finds (Re *et al.*, 2015), investigation of the shape of ancient botanical species (Barron, 2023), or the study of biological soft tissues (Mizutani & Suzuki, 2012). Moreover, this technique was implemented in soil research (Hainsworth & Aylmore, 1983; Helliwell *et al.*, 2013; Petrovic *et al.*, 1982; Pierret *et al.*, 2002), meteorite analysis (Arnold *et al.*, 1983) or fluid flow experiments by petroleum engineers (Vinegar & Wellington, 1987).

In geology and Earth sciences X-ray CT has been widely used and some examples are Fortin *et al.* (2013), who evaluated sediment cores density by comparing CT attenuation with other destructive techniques; Brunelle *et al.* (2016) combined CT and particle imaging techniques to better understand the sediment transport processes; Larmagnat *et al.* (2019) estimated continuous porosity in reservoirs and Gaillot *et al.* (2020) developed a procedure to quantitatively describe CT images.

However, in order to meet the needs of an increasingly wider range of applications, a CT allowing even higher resolution (order of micrometres) was developed by Elliott and Dover (1982): micro-CT scanner (also called industrial CT). Its design differs from medical one because the source and the detector are fixed, and the sample is located between them, rotating on its own axis. Distance object-detector and source-detector can be modified to change the final resolution. Figure 1.2 shows a framework of the instrument.

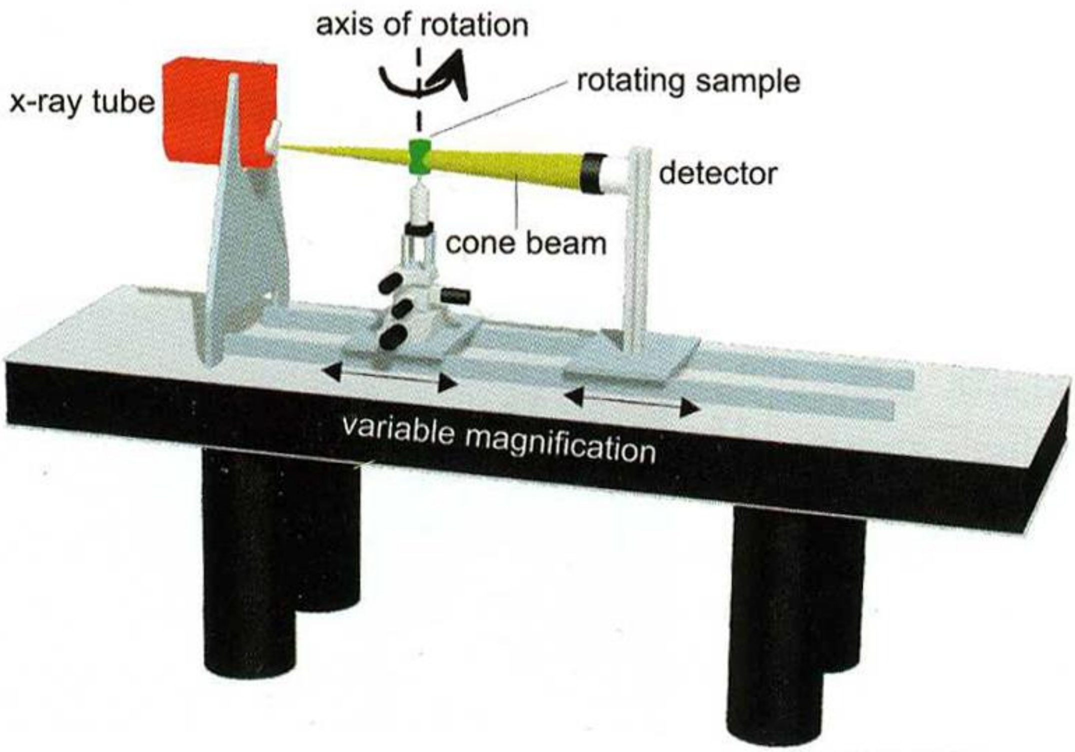

Figure 1.2: Typical design of a micro-CT.
From Kalender (2011).

In the geological field, micro-CT has become more popular than medical-CT because it allows additional features (i.e., higher resolution) to be visualised and therefore studied; e.g. Ketcham and Carlson (2001) and Van Geet *et al.* (2001a) tested many geological applications and compared the results with different techniques, giving an overview of its possibilities; Baker *et al.* (2012) studied igneous rock and Alves *et al.* (2014a)Alves *et al.* (2014a)Alves *et al.* (2014a)Alves *et al.* (2014a)Alves *et al.* (2014a)Alves *et al.* (2014a) compared micro-CT with thin sections to investigate pore space features. Other noteworthy research papers include Cnudde and Boone (2013), Schlüter S. (2014) Bendle *et al.* (2015), Schröer *et al.* (2018) and Lisson *et al.* (2023).

The resolution of the X-ray CT technology can be further improved reaching the order of nanometers using high-flux, monochromatic, highly collimated X-ray beams with high brightness, but nowadays it is done only at synchrotron facilities (Sedigh Rahimabadi *et al.*, 2020; Zhao *et al.*, 2018).

1.2 Basic physics

X-rays are a specific type of electromagnetic (EM) radiation (Figure 1.3) characterized by a wavelength shorter than 0.1 nm and frequency <10^{19} Hz; they are produced when electrons hit a target or reorganize themselves inside an atom (unlike gamma rays, which are emitted by radioactive decay). EM radiation has no mass, it is not affected by either magnetic or electric field, and it travels in straight line, although it can be altered by interaction with matter: X-rays can change their trajectory (scattering), removed from radiation (absorption), or converted into particulates (transformation), although the latter occurs only at very high energy (Bushberg, 2012).

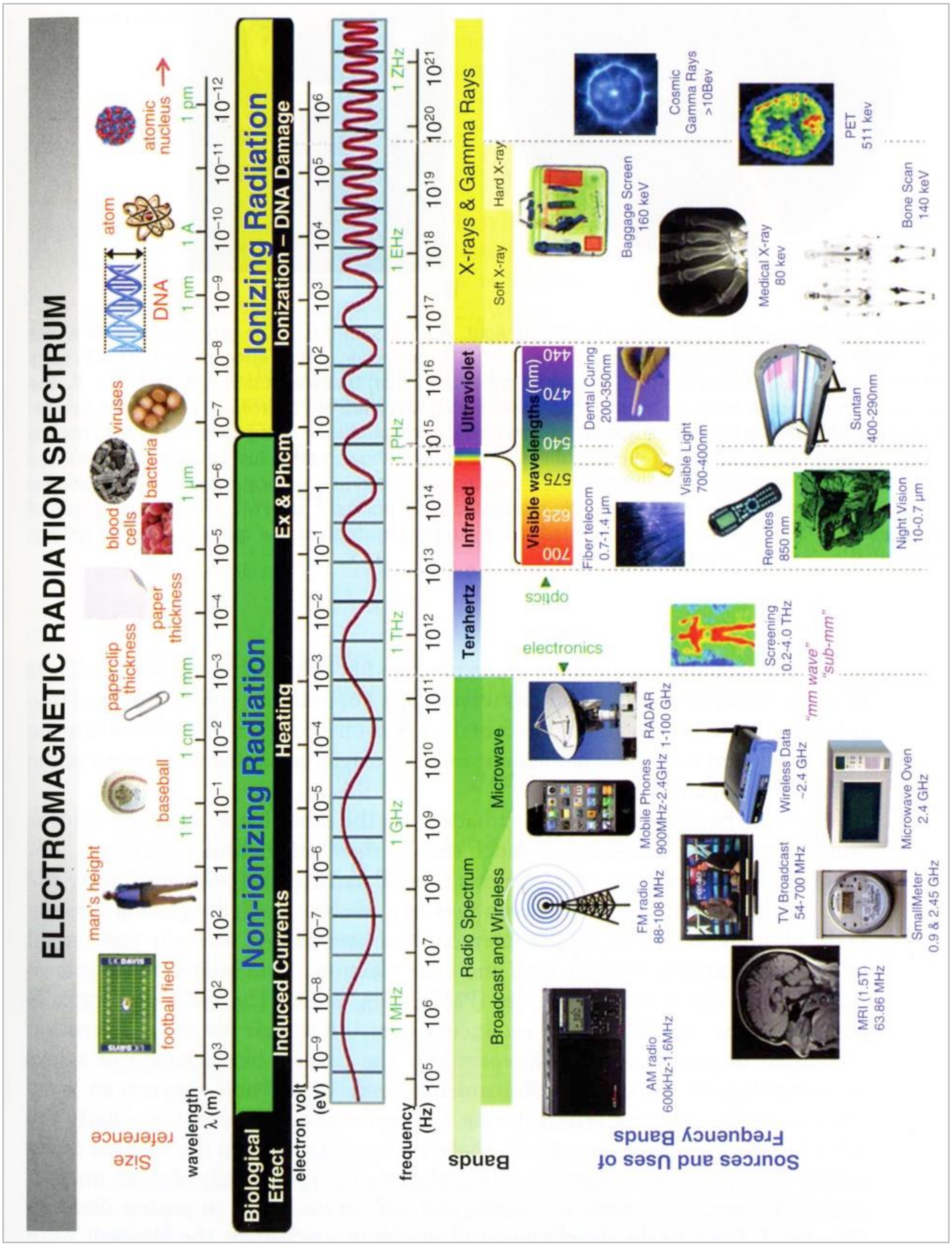

Figure 1.3: Electromagnetic radiation spectrum.

From Bushberg (2012).

1.2.1 X-ray production

The most common mechanism to produce X-rays is using a vacuum glass tube with a cathode and anode inside. The cathode (negative electrode) is a filament, generally made of tungsten, that is heated by a high voltage electric current, producing electrons by thermionic emission. These electrons are accelerated by the electric field towards the anode (positive electrode) that is a metal target. Electrons hitting the target produce X-ray photons. Depending on the CT instrument some parameters can change; the X-ray tube voltage is set to values from 70 to 140 kV for medical CT and from 30 to 240 kV for micro-CT (or more for very large industrial scanners), while the quantity of electrons per second flowing from the cathode to the anode is proportional to X-ray tube current, measured in mA (Bushberg, 2012; Pauwels, 2017).

Another X-ray source is the one produced by synchrotron. Electrons are accelerated up to a 100 MeV or multi-GeV, then they are injected into a vacuum storage ring, containing bending magnets to guarantee the circular orbit of electrons. The consequence of this centripetal acceleration is the emission of so-called “synchrotron light”, which is tuned to the beamline. The X-ray beam is very bright, monochromatic and highly collimated, and consequently the quality of CT images is incomparable (Sedigh Rahimabadi *et al.*, 2020).

In some CT instruments, the radiation is produced by radioactive decay, but in this case the rays are called γ-rays. On one hand, the beam is monochromatic, but on the other the photon flux is low, uniformly emitted in space and unsafe for the users (Pauwels, 2017).

1.2.2 X-ray spectrum

The typical X-ray CT spectrum created by conventional X-ray tubes consists of *Bremsstrahlung* and *characteristic radiation*. When electrons strike the anode, they are deflected because the nucleus of the target is positively charged, causing a loss of kinetic energy. This energy is emitted as X-rays, and the X-ray’ energy is equal to the lost kinetic energy. This radiation emission with electron deceleration is called Bremsstrahlung (or “breaking radiation”), also defined as the probability distribution of X-ray photons as function of photon energy. The Bremsstrahlung emission per atom is proportional to the square of the absorber’s atomic (Z) and inversely proportional to the square of the mass of the incident particle, meaning that a high Z value entails higher Bremsstrahlung (Bushberg, 2012).

Moreover, when incident electrons have enough energy to eject an inner shell electron from the target, a vacancy occurs, which is then immediately filled by a higher-shell electron. The difference of binding energy is emitted as photons having a characteristic energy, i.e., characteristic radiation, and it depends on the elemental composition of the anode. If the higher-shell electron is from a shell directly above, the characteristic radiation is called *Kα*, however, if it is from an upper shell, it is called *Kβ* radiation (Bushberg, 2012; Pauwels, 2017). Figure 1.4 shows an example of typical X-ray spectrum.

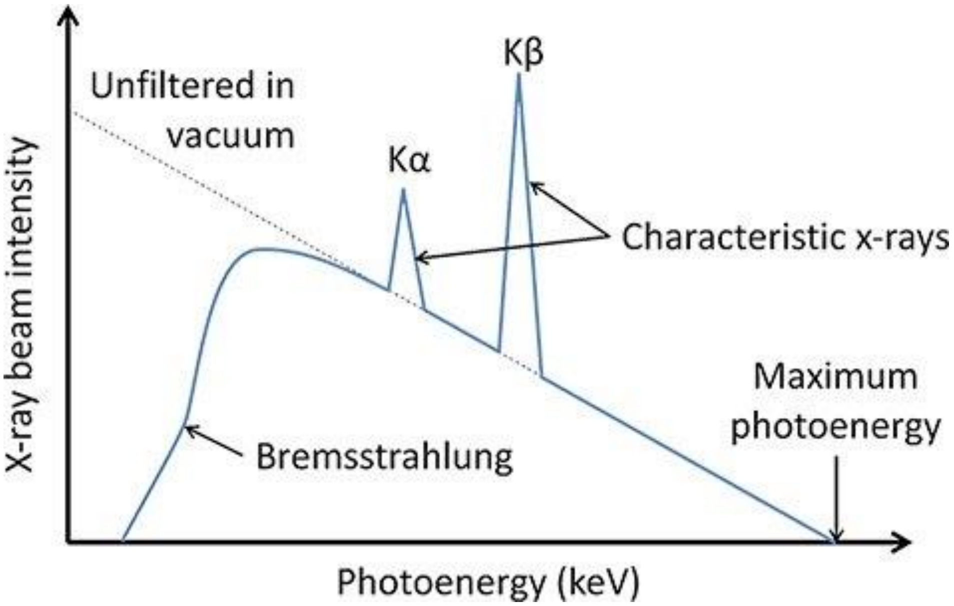

Figure 1.4: example of typical X-ray spectrum.
From https://physicsopenlab.org/.

1.2.3 Photoelectric absorption

This phenomenon is related to the *characteristic radiation* described above and is illustrated in Figure 1.5. Photoelectric absorption occurs when the incident photon transfers all its energy to an electron in an atom's inner shell (*k* or *l* are the most probable), which is emitted as a *photoelectron*. It has a kinetic energy equal to the difference between incident photon energy and binding energy of the orbital electron. The atom is thus ionized, and an electron cascade takes place from the outer to the inner shell, filling the electron vacancy. A characteristic X-ray or Auger electron is emitted (Bushberg, 2012).

The incident photon energy must be greater than or equal to binding energy. The probability of photoelectric absorption (defined as τ) to occur decreases with decreasing target atomic number, property to which it is strongly dependent (Bushberg, 2012). This total probability (the cross section) is proportional to Z^n/E^m, where Z is the atomic number of target atoms and E is the photon energy; $n = 5$ has been considered for *K*-shell (Jussiani & Appoloni, 2015), but it could be lower as well depending on specific experimental set-ups (Pauwels, 2017). However, *m* is a parameter energy-dependent and it is generally equal to 3 (Brabant *et al.*, 2012).

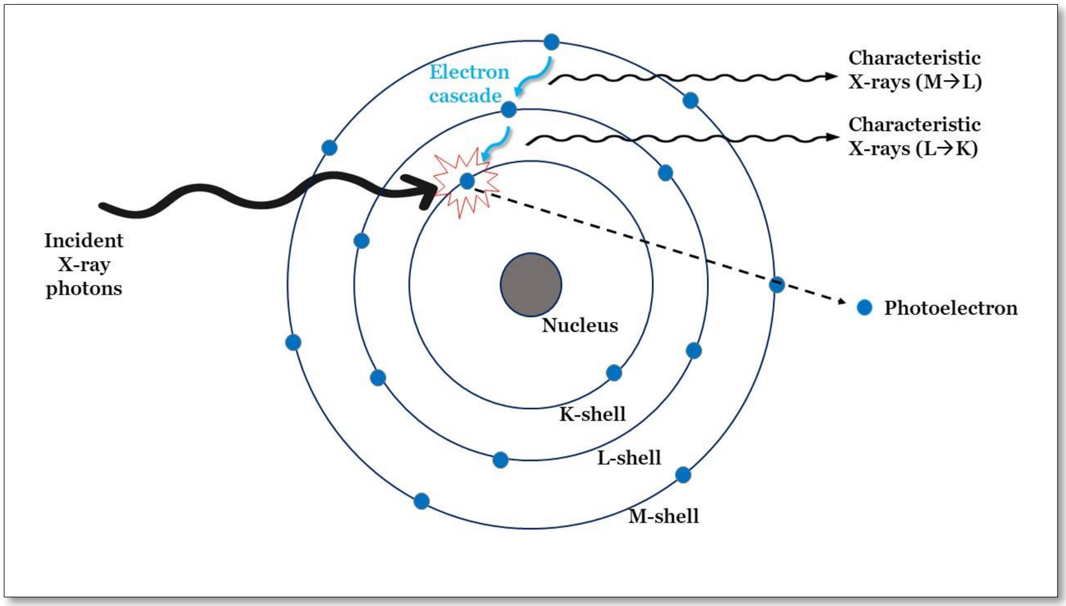

Figure 1.5: Photoelectric absorption.

1.2.4 Compton scattering

Compton scattering (Figure 1.6), also called incoherent or inelastic scattering and, occurs when an incident photon having energy E_0 strikes an outer ("valence")-shell electron: the photon is thus scattered at an angle θ to its original trajectory and the electron (*Compton electron*) is ejected from the atom (Bushberg, 2012).

This phenomenon is predominant at higher incident energies compared to the Photoelectric effect (from a few keV to Mev) and it is strongly related to sample density (Dernaika, 2013).

Finally, the total probability of Compton scattering (σ) occurring is also called Klein-Nishina Compton cross section and it is expressed as follows (Alenezi *et al.*, 2018):

$$\sigma = 2\,\pi r^2 \left[\left(\frac{2(1+\alpha)}{\alpha^2}\right)\left\{\frac{2(1+\alpha)}{1+2\alpha} - \frac{\ln(1+2\alpha)}{\alpha}\right\} + \frac{\ln(1+2\alpha)}{\alpha} - \frac{1+3\alpha}{(1+2\alpha)^2}\right] \tag{1.1}$$

where *r* is the electron radius and *α* is the ratio between the photon energy and the electron rest mass (= 9.11· 10^{-31} kg according to International System) (Alenezi *et al.*, 2018).

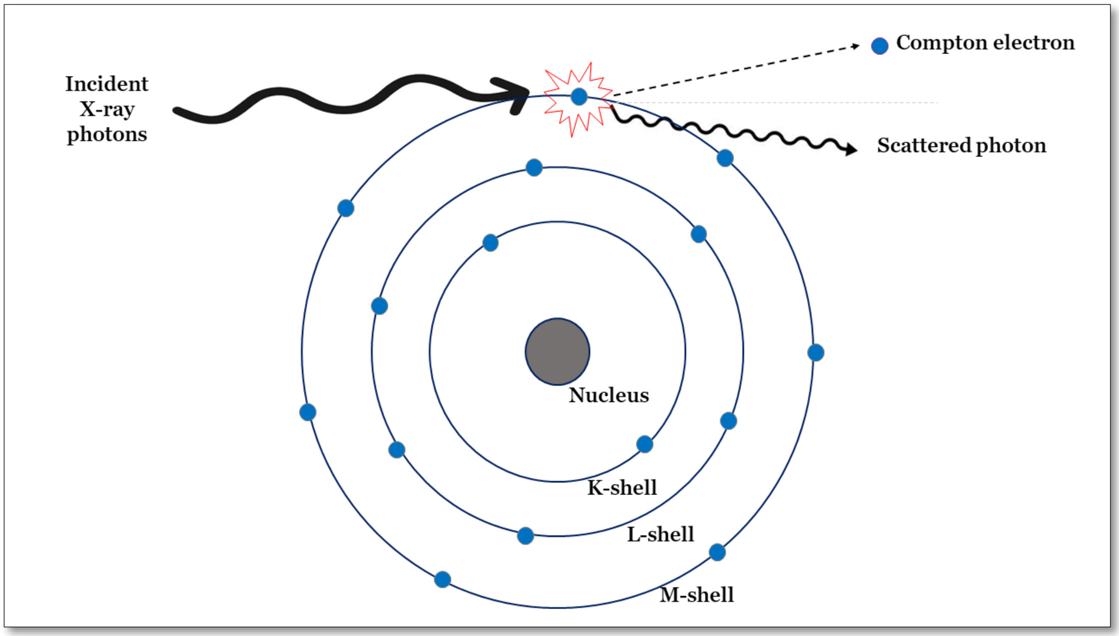

Figure 1.6: Compton scattering.

1.2.5 Other interactions photon-material

Rayleigh scattering and pair production are other possible interactions between photons and materials. The first one (Figure 1.7), also known as coherent scattering, occurs when the collision between incident photon and atom target is elastic: no energy is transferred, thus the atom is not ionized nor excited. The incident photon is only deflected from the original trajectory. The total probability of Rayleigh scattering occurring decreases rapidly with increasing incident energy: above 70 keV only the 5% of X-rays is involved in this phenomenon (Bushberg, 2012).

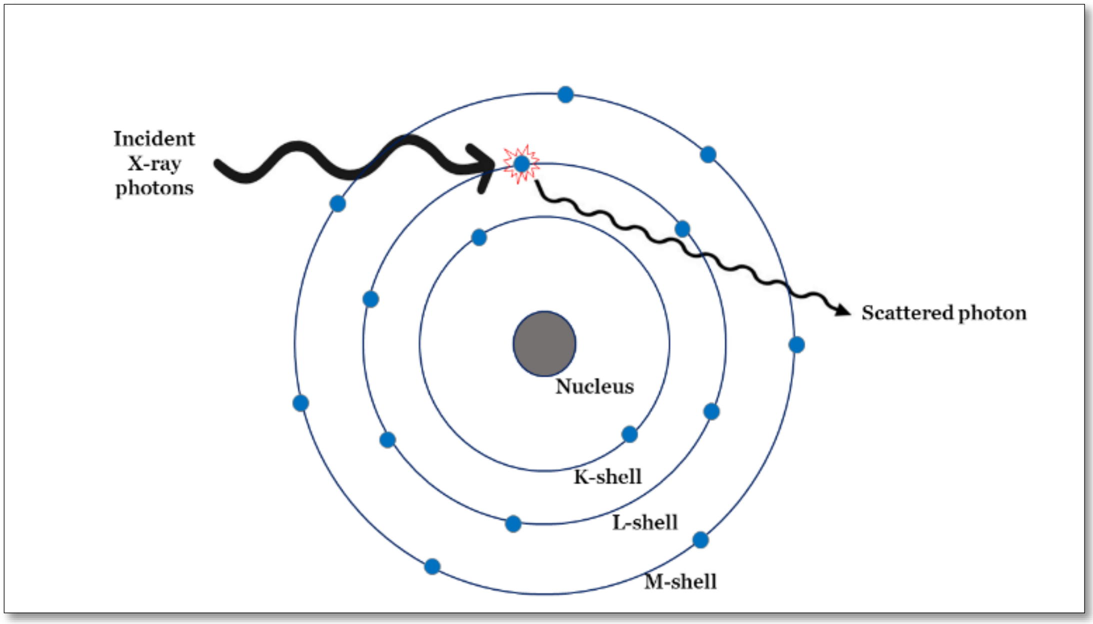

Figure 1.7: Rayleigh scattering.

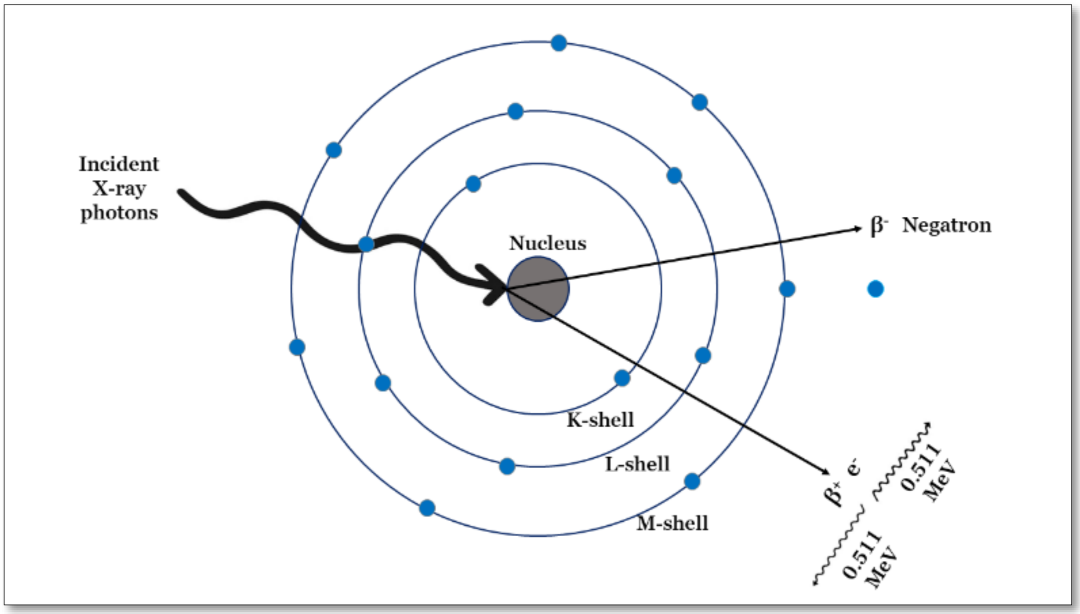

Figure 1.8: Pair production.

Pair production (Figure 1.8), on the contrary, occurs only at high incident energy (above 1.02 MeV). The incident radiation interacts with the electric field of the nucleus atom: the energy of the incident photon is transformed into an electron-positron pair, having an energy of 0.511 MeV each.

For the purpose of this research project Rayleigh scattering and pair production are irrelevant: the first one, predominant at low incident energies, has a negligible effect on CT outcomes and the second is not involved at all at the energy range of CT scanners. Figure 1.9 clearly pinpoints the relative importance of the three principal photon interaction processes depending on target atomic number and energy; due to the maximum energy achievable by the CT in this context (about 0.24 MeV), only Photoelectric absorption and Compton scattering are relevant.

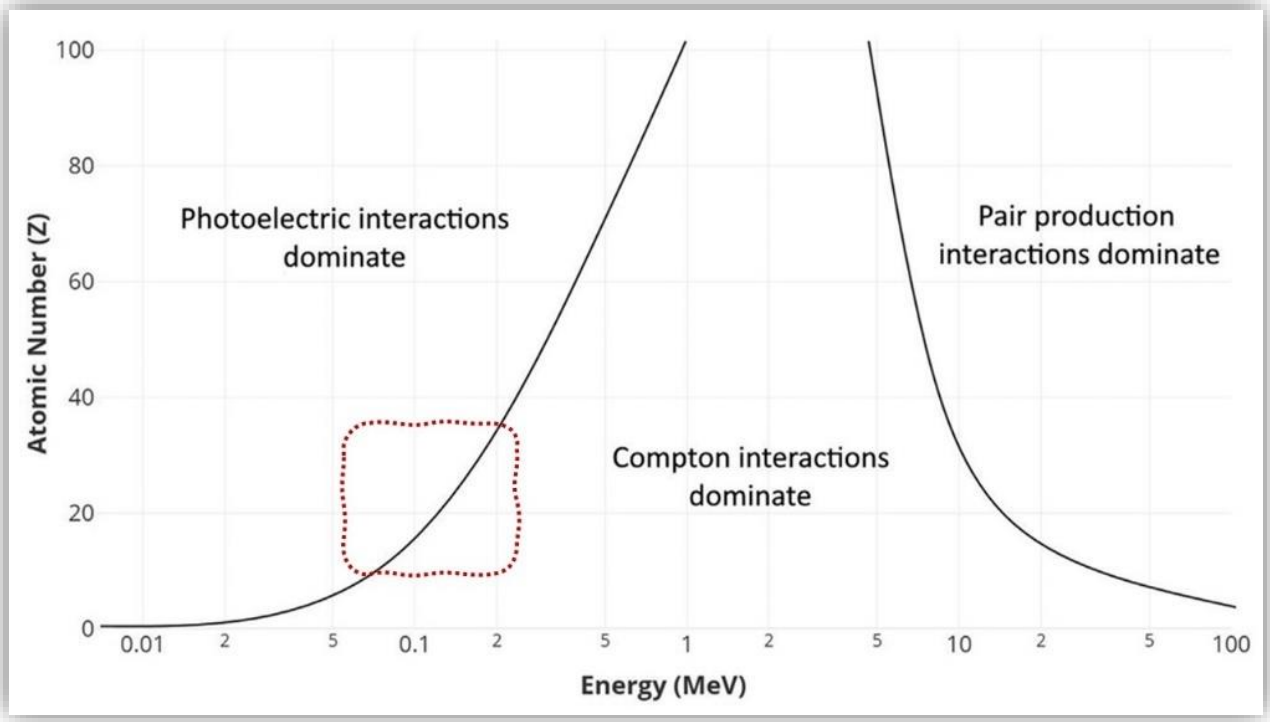

Figure 1.9: Three principal interaction processes between photons and materials.

The picture pinpoints the relative importance of the three principal photon interaction processes depending on target atomic number and energy. The red dashed line indicates the measurement area of interest for this thesis.

1.2.6 X-ray attenuation

Incident beam energy and target materials' characteristics (i.e., chemical composition, density, and thickness) influence the probability of photon-target interaction: X-rays can be completely absorbed (e.g., if the target is made of lead) or just lose a part of their energy (e.g., when human body is subjected to medical analysis). This physical phenomenon follows the Lambert-Beer law, which describes the relation between incident (I_0) and transmitted (I) radiation (Hendee, 2002):

$$I = I_0 e^{-\mu(E)s} \tag{1.2}$$

where s is the material's thickness and μ is the linear attenuation coefficient of the medium as energy (E) function. This equation expresses well the behavior of a monochromatic beam, whichis a characteristic achievable only in specific conditions like synchrotron facilities and γ-ray CT (1.1 and 1.2.1 sections). If the beam is polychromatic, the equation becomes (Pauwels, 2017):

$$I = \int_0^{E_{max}} I_0 (E) e^{-\mu(E)s} dE \tag{1.3}$$

Linear attenuation coefficient, key-parameter of X-ray attenuation, can be defined as the material's ability to absorb radiation. Due to the above-mentioned differences in the interactions between photons and materials, it is also considered as the sum of the individual linear attenuation coefficients (Bushberg, 2012):

$$\mu = \mu_{Rayleigh\ scatter} + \mu_{Photoelectric\ effect} + \mu_{Compton\ scatter} + \mu_{pair\ production} \tag{1.4}$$

Considering the relative importance of each interaction (c.f. section 1.2.5), here μ can be approximated as follows:

$$\mu = \mu_{Photoelectric\ effect} + \mu_{Compton\ scatter} \tag{1.5}$$

Relating the atomic cross section of the interactions (τ in 1.2.3 section and σ in 1.2.4 sections), the linear attenuation coefficient can also be expressed as follows (Pauwels, 2017):

$$\mu = \frac{N_A}{A}\rho(\tau + \sigma) \tag{1.6}$$

where N_A is Avogadro's number, A the atomic weight and ρ the material's mass density. For completeness of information, the linear attenuation coefficient is often normalized for material density and the so-called mass attenuation coefficient μ/ρ is used.

1.2.7 Beam hardening

Beam hardening is an artifact resulting from the broad polychromatic spectrum of the incident X-ray beam. It depends on the energy, the scanned object and projection direction. Indeed, materials preferentially absorb low energy photons and, consequently, the mean effective energy of the incident beam increases as it penetrates deeper into the sample. This increase of effective energy results in a decrease in beam attenuation in the center of the sample, resulting in an erroneous value for μ and altered gray level, as if the material had a lower density or a lighter chemical composition (Kalender, 2011). This artefact is the major drawback in image reconstruction and material characterization, and it causes streaks (darker and lighter) in the images around denser objects and cupping artifacts in attenuation profile as illustrated in Figure 1.10 (Bushberg, 2012).

To minimize this artifact, filters of different composition and thickness (Al, Cu and Sn are the most common) can be used to "harden" the beam, even if the number of photons decreases: the spectrum changes as illustrated in Figure 1.11. Moreover, correction algorithms (either in raw or reconstructed data) can be applied (Remeysen & Swennen, 2006).

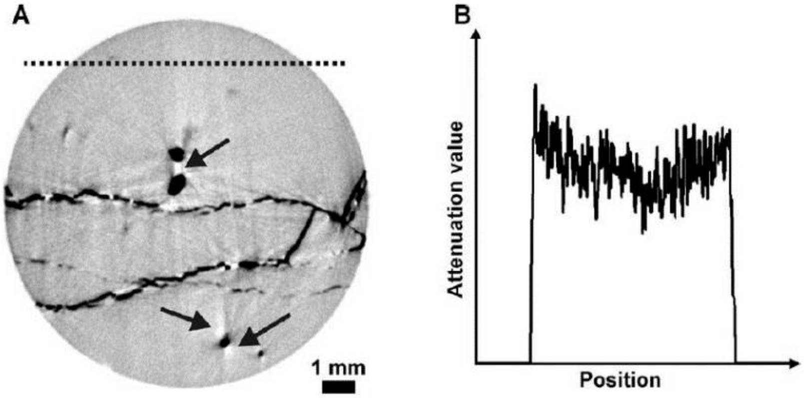

Figure 1.10: Example of beam hardening.

A) CT slice of coal with an inclusion of ankerite; typical beam hardening artifacts are marked with black arrows. B) Attenuation profile along the dotted line in A: the borders have higher attenuation values because of beam hardening, from Remeysen and Swennen (2006).

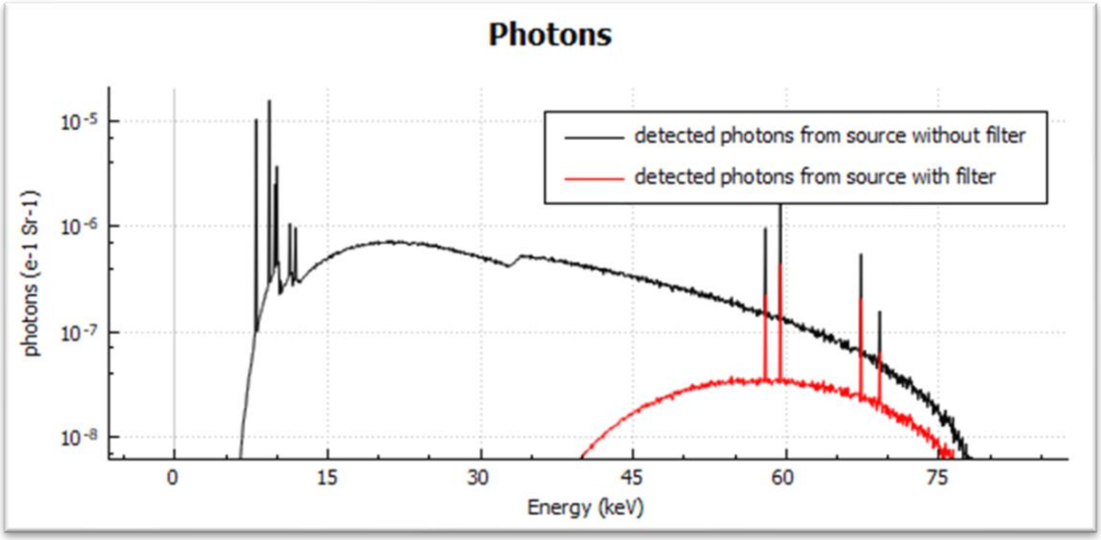

Figure 1.11: Example of X-ray spectrum.

The red one is filtered out and the black one is not filtered out.

1.3 CT workflow

As already mentioned in section 1.1, medical CT and industrial CT differ: in the first apparatus the patient is stationary while the source and the detector rotate around, whereas in the second one source and detector are fixed, while the sample rotates around its own axis. Despite this substantial difference, the CT workflow does not change and consists of two main steps: the acquisition and data reconstruction (Kalender, 2011).

During acquisition step, a set of 2D radiographic projections are collected at various angles, from 0° to 360°. Depending on the sample characteristics (e.g., size, composition, density) and on the information to be obtained, different parameters (e.g., voltage, current, resolution, projection number) can be chosen (Hsieh, 2009).

The intermediate step between projection acquisition and final reconstruction is the creation of sinograms (Figure 1.12): they are images produced by placing in sequence, one below the other, the lines of pixels acquired along the same X-ray path in all object projections acquired at different rotation angles. Each sinogram contains all the information necessary to reconstruct a single slice. Sinogram representation is not generally visible to users (Re, 2013).

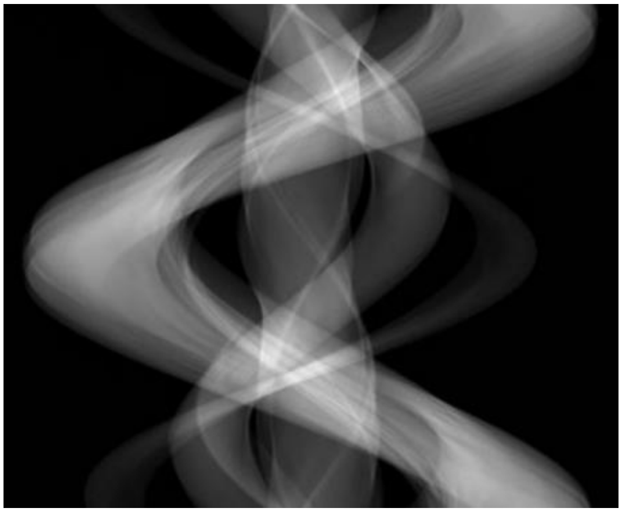

Figure 1.12: example of sinogram.
From Re (2013).

Then, to reconstruct the 3D slices, several approaches are possible. A simplified example is illustrated in Figure 1.13: the object consists of four small blocks; each block has a homogeneous attenuation coefficient μ_1, μ_2, μ_3 and μ_4. The line integrals are measured horizontally, vertically, and diagonally, thus obtaining five different measurements; the number of the independent equations then equals the number of unknowns and allows a unique solution. Generalizing, the object can be divided into *n*-by-*n* small elements and, completing enough independent measurements (n^2), the attenuation coefficient distribution of this object can be uniquely solved (Hsieh, 2009).

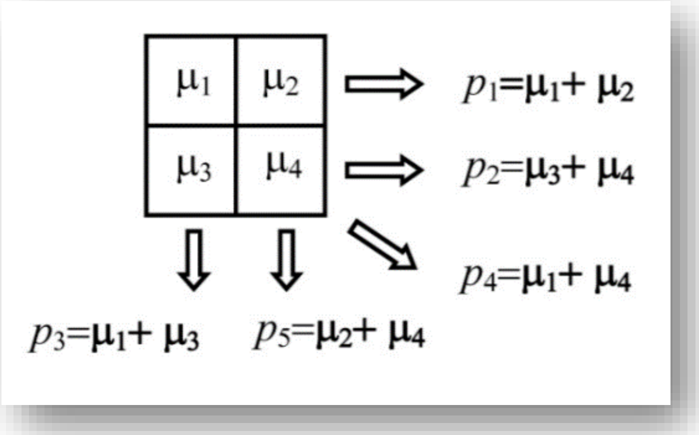

Figure 1.13: Example of an object and its projection.
From Hsieh (2009).

However, in a CT apparatus many equations need to be simultaneously solved and, dividing the object into smaller and smaller elements (corresponding to higher and higher spatial resolution), the solution becomes more difficult. Moreover, in order to have enough independent equations, more than n^2 measurements need to be made (Hsieh, 2009).

The simplest algorithm to obtain CT slices is the simple backprojection: each X-ray transmission path is divided into equidistant elements and each one contributes equally to the total attenuation along the X-ray path, determining the final attenuation coefficient; combining these values, a composite image of attenuation coefficients is obtained (Bushberg, 2012).

Successively, this algorithm was enhanced through the so-called filtered backprojection, which improves image quality by mathematical operations. The blurring caused by the super-position of data from multiple views is removed (*convolution* filter) and the spatial resolution is restored (*deconvolution* filter) and currently it is one of the most widely used reconstruction methods because it is fast and not numerically intensive (Hendee, 2002).

Fourier-based reconstruction is another approach based on homonymous theorem: X-ray attenuation at each angular orientation is separated into frequency components of various amplitudes (Hendee, 2002). Finally, iterative reconstruction is the most recent and advanced algorithm: synthesized forward projections are generated and then the CT acquisition is simulated, comparing the data with the measured one; this iteration loop proceeds until their difference is small (Bushberg, 2012). The reconstructed images have a better quality, but the method is time consuming and numerically intensive, requiring the use of cluster GPU systems (Di Schiavi Trotta *et al.*, 2022a).

1.4 Dual-Energy CT (DECT): state of the art

X-ray attenuation (μ), is the result of the interaction between several different factors, as outlined in 1.2.6 section. Accordingly, materials of different composition may have similar attenuation values, hence impeding a straightforward discrimination from CT imaging techniques. To address this, Dual-Energy CT methods have been introduced: the scientific basis of the method relies on separating the information achievable from Photoelectric effect (related to sample chemical composition) and Compton scattering (related to sample density) using the incident X-ray beam at two different energies, low and high (Bushberg, 2012). As Figure 1.9 illustrates, the predominance of Photoelectric absorption rather than Compton scattering depends simultaneously on the sample composition and the energy involved.

If it is easy and unambiguous to characterize single element compounds by their specific atomic number Z, it is more complex for mixtures: the *effective atomic number* (Z_{eff}) being related to the chemical composition of the samples. There are many definitions of Z_{eff} in the literature and it is possible to classify them in the ones based on calculations involving the atomic number Z_i of the ith atom of the mixture and in the ones assembling the methods based on mass attenuation coefficients database (Bonnin *et al.*, 2014). In this research project, only the first category has been considered for the simplicity of application. Density is also a key property for dual-energy techniques; however, it is preferable to consider *electron density* (ρ_e) because mass density (ρ) does not directly govern how X-rays are attenuated. Electron density represents the number of electrons per unit of volume and it can be measured in $e^{-} \cdot cm^{-3}$; mass and electron density are strictly related and usually are directly proportional (Azevedo *et al.*, 2016).

Alvarez and Macovski (1976) were the first to elaborate the dual-energy theory. They performed a correction on the sinogram to separate Compton scattering from photoelectric absorption, and thus to separate areas having different atomic number or density. This method belongs to the group of pre-reconstruction methods because it acts on sinograms and not on slices (post-reconstruction methods), thus the information provided by polychromatic beam is reduced to an energy level average, losing the energy-dependent details.

During the same year Rutherford *et al.* (1976) proposed a second dual-energy method which is a post-reconstruction. Effective atomic number and electron density are calculated from two CT images obtained at two different X-ray beam energies. However, this type of approach is affected by a loss of accuracy due to of beam hardening artifacts.

Several and different post-reconstruction methods were elaborated afterwards, for example papers by Jackson and Hawkes (1981), Torikoshi (2003), Tsunoo *et al.* (2004) and Bazalova *et al.* (2008).

1.4.1 Non-medical application of Dual-Energy CT

Beyond the medical field Vinegar and Wellington (1987) pioneered a post-reconstruction method applied to petroleum geology research. It is based on material decomposition theory: the μ value (Equation 1.7) of each voxel in a CT slice can be expressed as a linear combination of the attenuation coefficient of each basis materials in that voxel.

$$\mu_E = \mu_{1\,E} \cdot f_1 + \mu_{2\,E} \cdot f_2 \tag{1.7}$$

Where f_1 and f_2 are the volume fractions of materials 1 and 2. The μ values at two energies E_1 and E_2 are calculated as follows (Equations 1.8 and 1.9):

$$\mu_{E_1} = \mu_{1,E_1} \cdot f_1 + \mu_{2,E_1} \cdot f_2 \tag{1.8}$$

$$\mu_{E_2} = \mu_{1,E_2} \cdot f_1 + \mu_{2,E_2} \cdot f_2 \tag{1.9}$$

One of the most successful post-reconstruction methods in the field of geology is from Coenen and Maas (1994). Their technique starts from the definition of mass attenuation coefficient, already given by Vinegar and Wellington (1987), as a function of the element's material properties and the X-ray energy E (Equation 1.10):

$$\frac{\mu(E)}{\rho} = a(E)Z_{eff}^{m} + b(E) \tag{1.10}$$

where ρ is the density and Z_{eff} for the effective atomic number. The coefficients a and b depend only on the energy and m is here Equation fixed at 3.1.

By measuring μ of an unknown material at two different energies, the authors set up a system of equations (Equations 1.11 and 1.12) as follows:

$$\rho = \frac{a_l \mu_h + a_h \mu_l}{a_l b_h - a_h b_l} \tag{1.11}$$

$$Z_{eff} = \sqrt[3.1]{\frac{b_h \mu_l - b_l \mu_h}{a_l \mu_h - a_h \mu_l}} \tag{1.12}$$

Where subscript h indicates high energy and l subscript low energy, respectively. The values of the coefficients a and b are determined by linear regression, using the CT data of reference materials with known chemical composition (i.e., effective atomic number) and density.

They successfully tested the method on a helicopter rotor blade composed of a glass-fibre core surrounded by a carbon-fibre layer embedded in a Shell Epikote epoxy resin matrix, determining the glass content by dual-energy CT analysis.

Afterwards, several geologists started from Coenen and Maas (1994) dual-energy methodology to develop their own research. Van Geet *et al.* (2000) applied this analytical technique to quantify density and effective atomic number distribution in reservoir rocks. Rizescu *et al.* (2001) improved data processing introducing the k parameter, which is the ratio of μ at low and high energy; moreover, they eliminated the beam hardening problem using ^{192}Ir as CT X-ray source. Remeysen and Swennen (2008) distinguished mineral phases and porosity in carbonate reservoir, and then validated the results in thin section, the classical method to study these kinds of samples. Alves *et al.* (2015) implemented the method developing a code for image processing and mineralogical segmentation.

Meanwhile, the technique of materials' decomposition of Vinegar and Wellington (1987) was further developed by Walls and Armbruster (2012) and Miao *et al.* (2019) to respectively evaluate shale reservoirs and estimate fluid saturation and porosity in core flooding test.

Paziresh *et al.* (2016) have applied to the geological field the method previously developed by Alvarez and Macovski (1976) for the medical field. Assuming the knowledge of the incident spectrum, they achieved the analysis both in CT projections to avoid beam hardening artifacts and slices with a beam-hardening correction. They tested the method on several rock samples, in particular carbonates and sandstones.

Eventually, one of the most recent dual-energy methodologies for non-medical applications was implemented at the Centre for X-ray Tomography of Ghent University (UGCT) in the framework of the development of a realistic projection simulator, *Arion* (Dhaene, 2017). The a priori knowledge of X-ray spectra is required to calculate the linear attenuation coefficient μ in each reconstructed voxel.

These methods are efficient but the need to calculate the incident spectrum makes them not easily accessible to everyone and often the calculation is intensive, thus different alternative approaches have been developed.

1.4.2 Stoichiometric calibration

Stoichiometric calibration was firstly developed in the medical field by Schneider *et al.* (1996) for single energy CT, aiming to improve the treatment precision through a good correlation between CT results and investigated samples.

To characterize materials, it is necessary to scan a phantom having known properties (effective atomic number Z_{eff} and electron density ρ_e) to retrieve the so-called reduced Hounsfield Unit u for each element of the phantom. u is stated as:

$$u = \frac{HU+1000}{1000} \tag{1.13}$$

where *HU* stands for Hounsfield units, and it is defined as follows:

$$HU = 1000\,(\frac{\mu}{\mu_{water}} - 1) \tag{1.14}$$

The linear attenuation coefficient of water is conventionally defined as 1. Combining these equations with the definition of μ from Jackson and Hawkes (1981), the following relationship is obtained:

$$u \equiv \frac{\mu}{\mu_{water}} = \rho_e(K_{ph}Z_{eff}^{3.62} + K_{coh}Z_{eff}^{1.86} + K_{KN}) \tag{1.15}$$

K_{ph}, K_{coh} and K_{KN} are coefficients related respectively to photoelectric, coherent and Klein-Nishina cross section and can be determined from a linear regression fit. Once these coefficients are calibrated, unknown materials can be investigated using the same scanning protocol.

Several adaptations for dual-energy CT have been proposed based on the method of Schneider *et al.* (1996) like the work of Bazalova *et al.* (2008) and Landry *et al.* (2013), which allowed to precisely calculate the samples' effective atomic number.

In the framework of this thesis (see the first article, Chapter 2), the most significative stoichiometric calibration method for dual-energy CT was developed by Bourque *et al.* (2014) and it is summarized as follows.

A phantom of known composition and density, having properties similar to the investigated materials (in their case, human tissues), needs be chosen. Then, the values of effective atomic number and electron density are calculated; the ideal evaluation of Z_{eff} requires the knowledge of all CT spectra involved: Bourque *et al.* (2014) defined Z_{eff} as the material's parametric electronic cross section averaged over the incident spectrum, using a method related to mass attenuation coefficients database (section 1.4).

The phantom is scanned with a given pair energy to obtain the pairs of Hounsfield unit (HU), which are then converted into pairs of reduced HU values with Equation 1.13.

The calibration is achieved following the equation:

$$Z_{eff} = \sum_{k=1}^{K} c_k \,\Gamma^{k-1} \tag{1.16}$$

Where K is a parameter establishing the level of accuracy of the relationship and Γ is the ratio of u at low and high energy. c_k is the coefficient to find with the least-square method.

Then, a calibration related to electron density needs to be completed following the equation:

$$\rho_e \equiv \frac{1}{2}\left[\rho_{e,L} + \rho_{e,H}\right] \tag{1.17}$$

with

$$\rho_{e,L/H} \equiv \frac{u_{L/H}}{\sum_{m=1}^{M} b_{\frac{L}{H},m} Z_{eff}^{m-1}} \tag{1.18}$$

Where the subscript L/H represents low or high energy. Here, the coefficients $b_{L,m}$ and $b_{H,m}$ are the coefficient to find with the least-square method.

1.5 Lab CT Scan

This PhD project arises from the *Laboratoire multidisciplinaire de tomodensitométrie pour les ressources naturelles et genie civil* (Lab CT scan), where the quest to improve analytical techniques in several fields, especially the Geosciences, has always been active and avant-garde.

The lab is located at *Institut national de la recherche scientifique, Centre Eau Terre Environment*, Québec City, Canada, and it is the only facility of its kind and size in the country: it is currently equipped with a SIEMENS medical CT and a TESCAN micro-CT.

The lab was established in the 2000s, but scientific projects involving CT instruments date back to the 1990s. Boespflug *et al.* (1994) and Boespflug *et al.* (1995) scanned geological samples at the hospital of Rimouski (CA), but analytical conditions were not ideal. Nevertheless, the first quantitative approach was experimented. The authors first tried to correlate the HU values with materials having known density (Figure 1.14); although the plot can approximately be a linear trend, the property relationship appears more complex. Indeed, only light minerals like quartz or graphite are close to the regression line, probably because of the predominance of Compton scattering caused by the interaction between photons and samples. Then, the CT scan was used to establish the stratigraphy of marine sedimentary sequences. Sedimentary transition zones were described in relation to HU values and grain size variations, entailing preliminary but promising outcomes.

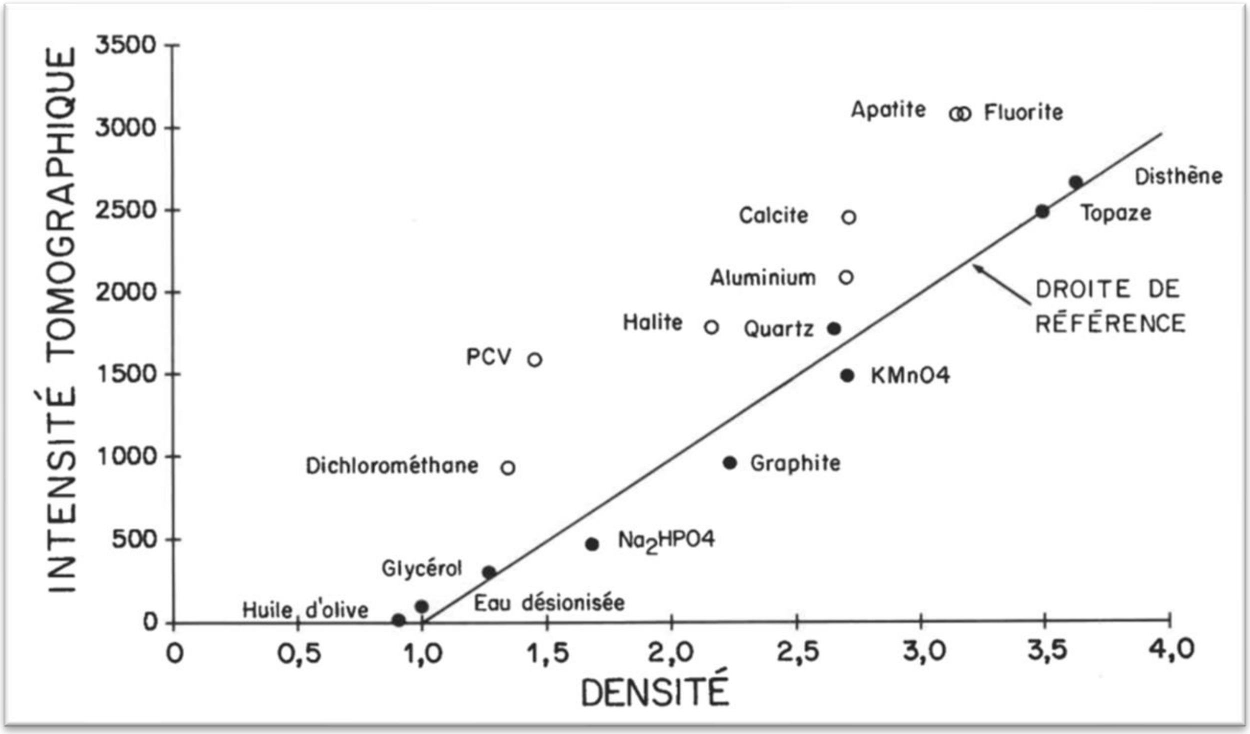

Figure 1.14: Density-dependent tomographic intensity measurements.
From Boespflug *et al.* (1994).

Once a medical CT was installed and fully operational in the lab in 2000, several studies were carried out to quantify geological materials in a non-destructive way. For instance, Duchesne *et al.* (2009) developed a method to convert CT-scan topograms (i.e., longitudinal 2D X-ray images acquired with CT) intensity scale to Hounsfield Unit (obtainable only for tomograms). Topograms can reveal important information about stratigraphy, sedimentology and composition of the cores, thus their research work allowed to retrieve both quantitative and qualitative information. They rearranged the terms of the Beer's law (Equation 1.2) to evaluate the linear attenuation coefficient μ of topograms, and then retrieved HU values by Equation 1.14.

Moreover, trying to improve the correlation between tomographic intensity and the only sample density, they subtracted the Photoelectric absorption contribution from *HU* values and modified *HU* calculation as follows:

$$HU_{photoelectric} = \left[\left(\frac{1+KZ_{eff}^{n}}{1+KZ_{eff}^{water}}\right)\rho_{absolute} - 1\right] \cdot 1000 \tag{1.19}$$

K is a coefficient defined by

$$K = \frac{b}{aE^{3.2}} \tag{1.20}$$

Where *b* is a constant value of $9.8 \cdot 10^{-24}$ keV$^{3.2}$, *a* is the Klein-Nishina coefficient and *E* is the energy in keV.

Larmagnat *et al.* (2019) conducted another significant research project, to quantify pore space and to characterize its distribution within reference rock samples representing different lithologies and porosities. They used the medical CT scanner and an in-house developed core-flooding setup to analyse simultaneously dry and saturated cores to determine their porosity. Then, the authors compared the data obtained from conventional gas porosimetry and showed a good correlation between the techniques.

In conclusion, the laboratory has been conducting several and promising studies of geological samples. They all showed some limitations, including when the characterization of samples was needed. In this case, the reason is that a single energy CT scan may have overlapping gray levels, as mentioned in section 1.4. Therefore, the objectives of this project is to test the dual-energy approach to substantially improve the geological material characterization for future applications in the laboratory.

The current medical CT instrument in the laboratory is a third generation Siemens Somatom Definition AS+128. It is mounted on specially designed rails, that allow the scanner to move around the sample. It is also equipped with the latest generation of Siemens Stellar detectors. It could scan large (up to 70 cm in diameter) and heavy (up to 450 kg) samples with a resolution of 0.1 · 0.1 · 0.6 mm and perform 3D measurements observing changes within samples or in physical models (including channels for studying hydro-sedimentary and porous flow) in real time.

The TESCAN micro-CT scanner (CoreTOM) is a more recent acquisition, and it has been working since summer 2021. Precise details (about 1 µm) can be revealed in small samples, while also being able to scan long cores (about 1 m). Moreover, kinetic scans to monitor inner changes can be obtained.

1.6 Research hypothesis and objectives

In the light of the considerations discussed above, developing a measurement protocol appropriate for geological research and able to retrieve both qualitative and quantitative information, in 3D and in a non-destructive way is relevant. While multispectral imaging meets the need, many scientific questions remain. Indeed, as mentioned in section 1.4, several dual-energy approaches investigating rocks, which are high-density samples, are not easily applicable because of the need of incident spectrum calculation (difficult to obtain and requiring specific physics knowledge from technical staff). In contrast, to simplify the analyses, stoichiometric methods have been developed, but they were never tested on geological materials, since these are much more complex than human tissues (lighter and less variable than rocks and sediments). However, despite these doubts about the applicability of stoichiometric approaches, it was decided to test some of them, and the following objectives were proposed:

1) Evaluating the best stoichiometric calibration method for dual-energy CT to easily identify materials, which are generally studied at Lab CT scan. The most suitable mathematical model and appropriate calibration samples need first to be defined.

2) Testing the model and its applicability on materials typically scanned at Lab CT scan. Varved cores from Arctic lakes were chosen to test the potential of this methodology in paleoclimate research.

3) Testing the model on the new micro-CT scanner, evaluating the quality of the outcomes in comparison with the medical CT.

1.7 Article presentation

The first article (chapter 2): a stoichiometric calibration for dual-energy method, originally developed for medical purposes has been applied for the first time to common minerals to identify them. First, a set of 18 standard samples, covering a range of chemical composition and density encountered in geological specimens was selected to carry out the calibration. Then, a validation was performed analyzing 23 common minerals. Eventually, the property values obtained by the algorithm was compared to an *ad hoc* developed *Python* library developed for 69 common minerals to identify the one with the closest properties. The most important and common minerals were successfully recognized, paving the way for easy access to geological information.

The second article (chapter 3): to satisfy the objective n. 2 of section 1.6, a varved core from South Sawtooth Lake in the Arctic was scanned with the medical CT at two energy and the stoichiometric calibration method of the previous article has been applied. The output was compared against elemental geochemistry obtained using a micro-XRF. Three individual facies were successfully distinguished based on their properties' value range. The limitation of Dual-Energy CT (DECT) applied to sediments was discussed, but also its potential to quantitatively study real geological materials has been demonstrated.

The third article (chapter 4): the third objective outlined in section 1.6 is to apply the methodology using different scanners, i.e., the new CoreTOM micro-CT. Thanks to a grant obtained from Excite Network (www.excite-network.eu), it was possible to make the comparison with an additional instrument, i.e., HECTOR (UGCT, Belgium). Similarities and differences of these three instruments for sample characterization were investigated, and the best parameters were defined. It is not possible to define a unique measurement protocol for every analysis, but different energies, scanners, filters, resolutions or calibration materials need to be chosen depending on the case. Indeed, while the characterization of the samples with HECTOR has performed excellently, long cores cannot be scanned, and the use of medical CT remains necessary.

1.8 References

Alenezi M *et al.* (2018) Klein–Nishina electronic cross-section, Compton cross sections, and buildup factor of wax for radiation shielding and protection. *Journal of Radiological Protection* 38(1):372.

Alvarez RE, Macovski A (1976) Energy-selective reconstructions in X-ray computerized tomography. *Physics in Medicine & Biology* 21(5):733-744.

Alves H *et al.* (2014a) Comparison of pore space features by thin sections and X-ray microtomography. *Applied Radiation and Isotopes* 94:182-190.

Alves H *et al.* (2015) Mineralogy evaluation and segmentation using dual-energy microtomography. *X-Ray Spectrometry* 44(3):99-104.

Arnold J *et al.* (1983) Computed tomographic analysis of meteorite inclusions. *Science* 219(4583):383-384.

Azevedo SG *et al.* (2016) System-Independent Characterization of Materials Using Dual-Energy Computed Tomography. *IEEE TRANSACTIONS ON NUCLEAR SCIENCE* 63(1):341-350.

Baker DR *et al.* (2012) An introduction to the application of X-ray microtomography to the three-dimensional study of igneous rocks. *Lithos* 148:262-276.

Barron A (2023) Applications of Microct Imaging to Archaeobotanical Research. *Journal of Archaeological Method and Theory* 10.1007/s10816-023-09610-z.

Bazalova M *et al.* (2008) Tissue segmentation in Monte Carlo treatment planning: a simulation study using dual-energy CT images. *Radiotherapy and Oncology* 86(1):93-98.

Bendle JM, Palmer AP, Carr SJ (2015) A comparison of micro-CT and thin section analysis of Lateglacial glaciolacustrine varves from Glen Roy, Scotland. *Quaternary Science Reviews* 114:61-77.

Boespflug X, Long BFN, Occhietti S (1995) Cat-Scan in Marine Stratigraphy - a Quantitative Approach. *Marine Geology* 122(4):281-301.

Boespflug X *et al.* (1994) Tomodensitométrie axiale: relation entre l'intensité tomographique et la densité de la matière. *Canadian Journal of Earth Sciences* 31(2):426-434.

Bonnin A *et al.* (2014) Concept of effective atomic number and effective mass density in dual-energy X-ray computed tomography. *Nuclear Instruments and Methods in Physics Research Section B: Beam Interactions with Materials and Atoms* 318:223-231.

Bourque AE, Carrier JF, Bouchard H (2014) A stoichiometric calibration method for dual energy computed tomography. *Physics in Medicine & Biology* 59(8):2059-2088.

Brabant L *et al.* (2012) A novel beam hardening correction method requiring no prior knowledge, incorporated in an iterative reconstruction algorithm. *NDT & E International* 51:68-73.

Brunelle CB *et al.* (2016) Combining CT scan and particle imaging techniques: applications in geosciences. *article de conférence, 4 th International conference on image formation in X-ray computed tomography, Bamberg, Allemagne.*

Bushberg JT, Seibert, J.A., Leidholdt, E.M., Boone, J.M. (2012) *The essential physics of medical imaging.* LWW, Third edition

Cnudde V, Boone MN (2013) High-resolution X-ray computed tomography in geosciences: A review of the current technology and applications. *Earth-Science Reviews* 123:1-17.

Coenen J, Maas J (1994) Material classification by dual-energy computerized X-ray tomography. *International Symposium on Computerized Tomography for Industrial Applications.* p 8-10.

Coolidge WD (1913) A Powerful Röntgen Ray Tube with a Pure Electron Discharge. *Physical Review* 2(6):409-430.

Cormack AM (1963) Representation of a Function by Its Line Integrals, with Some Radiological Applications. *Journal of Applied Physics* 34(9):2722-2727.

Dernaika M (2013) Improved Rock Characterization by Dual Energy CT Scanning: Applications in Various Worldwide Formations.).

Di Schiavi Trotta L *et al.* (2022a) Beam-hardening corrections through a polychromatic projection model integrated to an iterative reconstruction algorithm. *NDT & E International* 126.

Duchesne MJ *et al.* (2009) A rapid method for converting medical Computed Tomography scanner topogram attenuation scale to Hounsfield Unit scale and to obtain relative density values. *Engineering Geology* 103(3-4):100-105.

Elliott JC, Dover S (1982) X-ray microtomography. *Journal of microscopy* 126(2):211-213.

Fortin D *et al.* (2013) Destructive and non-destructive density determination: method comparison and evaluation from the Laguna Potrok Aike sedimentary record. *Quaternary Science Reviews* 71:147-153.

Fourie S (1974) THE CRANIAL MORPHOLOGY OF THRINAXODON LIORTHINUS SEELEY. *Annals of the South African Museum* 65:337-400.

Gaillot P, Duchesne MJ, Blum P (2020) Automatic Data Reduction and Quantification of X-Ray Computed Tomography Images of Sedimentary Cores: Method and Illustration. *Open Journal of Geology* 10(08):874-899.

Hainsworth J, Aylmore L (1983) The use of computer assisted tomography to determine spatial distribution of soil water content. *Soil Research* 21(4):435-443.

Hall-Edwards J (1901) The X Rays in the Diagnosis of Fractures. *British Medical Journal* :1645-1646.

Helliwell JR *et al.* (2013) Applications of X-ray computed tomography for examining biophysical interactions and structural development in soil systems: a review. *European Journal of Soil Science* 64(3):279-297.

Hendee WR, Ritenour, E.R. (2002) *Mediacal Imaging Physics.* A JOHN WILEY & SONS, INC., PUBLICATION, USA, fourth

Hounsfield G (1972) A method of and apparatus for examination of a body by radiation such as X-ray or gamma radiation, The Patent Office, London, England. *British Patent Number GB1283915*.

Hsieh J (2009) *Computed Tomography: principles, design, artifacts and recent advances.* 2009004797, second

Jackson DF, Hawkes DJ (1981) X-ray attenuation coefficients of elements and mixtures. *Physics Reports* 70(3):169-233.

Jussiani EI, Appoloni CR (2015) Effective atomic number and density determination of rocks by X-ray microtomography. *Micron* 70:1-6.

Kalender W (2011) *Computed tomography : fundamentals, system technology, image quality, applications.* Wiley-VCH, Weinheim, 3rd rev.

Kalender WA (2006) X-ray computed tomography. *Physics in Medicine & Biology* 51(13):R29-43.

Ketcham RA, Carlson WD (2001) Acquisition, optimization and interpretation of X-ray computed tomographic imagery: applications to the geosciences. *Computers & Geosciences* 27(4):381-400.

Landry G *et al.* (2013) Deriving effective atomic numbers from DECT based on a parameterization of the ratio of high and low linear attenuation coefficients. *Physics in Medicine & Biology* 58(19):6851-6866.

Larmagnat S *et al.* (2019) Continuous porosity characterization: Metric-scale intervals in heterogeneous sedimentary rocks using medical CT-scanner. *Marine and Petroleum Geology* 109:361-380.

Lisson K *et al.* (2023) *An integrated methodology of micro-CT and thin-section analysis for paleoflow reconstructions in lacustrine event deposits.* Copernicus Meetings, p

Luke AM *et al.* (2013) Comparison of spiral computed tomography and cone-beam computed tomography. *Journal of Indian Academy of Oral Medicine and Radiology* 25(3):173-177.

Miao X *et al.* (2019) Improved Vinegar & Wellington calibration for estimation of fluid saturation and porosity from CT images for a core flooding test under geologic carbon storage conditions. *Micron* 124:102703.

Mizutani R, Suzuki Y (2012) X-ray microtomography in biology. *Micron* 43(2-3):104-115.

Pauwels E (2017) *Optimal use of the polychromaticity in X-ray microtomography for dual energy methods and contrast agent imaging*. (Ghent University).

Paziresh M *et al.* (2016) Tomography of atomic number and density of materials using dual-energy imaging and the Alvarez and Macovski attenuation model. *Journal of Applied Physics* 119(21).

Petrovic AM, Siebert JE, Rieke PE (1982) Soil bulk density analysis in three dimensions by computed tomographic scanning. *Soil Science Society of America Journal* 46(3):445-450.

Pierret A *et al.* (2002) 3D reconstruction and quantification of macropores using X-ray computed tomography and image analysis. *Geoderma* 106(3-4):247-271.

Radon J (1917) Uber die Bestimmung von Funktionen durch ihre Integralwerte langs gewissez Mannigfaltigheiten, Ber. *Verh. Sachs. Akad. Wiss. Leipzig, Math Phys Klass* 69.

Re A (2013) X-ray radiography and tomography of large artworks. *XCIX congresso Società Italiana di Fisica.* SIF, p 1-1.

Re A *et al.* (2015) X-ray tomography of a soil block: a useful tool for the restoration of archaeological finds. *Heritage Science* 3(1).

Remeysen K, Swennen R (2006) Beam hardening artifact reduction in microfocus computed tomography for improved quantitative coal characterization. *International Journal of Coal Geology* 67(1-2):101-111.

Remeysen K, Swennen R (2008) Application of microfocus computed tomography in carbonate reservoir characterization: Possibilities and limitations. *Marine and Petroleum Geology* 25(6):486-499.

Rizescu C, Beşliu C, Jipa A (2001) Determination of local density and effective atomic number by the dual-energy computerized tomography method with the ^{192}Ir radioisotope. *Nuclear Instruments and Methods in Physics Research Section A: Accelerators, Spectrometers, Detectors and Associated Equipment* 465(2-3):584-599.

Rontgen WC (1896) On a New Kind of Rays. *Science* 3(59):227-231.

Rutherford RA, Pullan BR, Isherwood I (1976) Measurement of effective atomic number and electron density using an EMI scanner. *Neuroradiology* 11(1):15-21.

Schlüter S. SA, Brown K., Wildenschild D. (2014) Image processing of multiphase images obtained via X-ray microtomography: A review. *WATER RESOURCES RESEARCH* 50:3615-3639.

Schneider U, Pedroni E, Lomax A (1996) The calibration of CT Hounsfield units for radiotherapy treatment planning. *Physics in Medicine & Biology* 41(1):111-124.

Schröer L *et al.* (2018) Linking microbial activity and the pore structure of a natural rock with X-ray Computed Tomography. *2018 Symposium of the Belgian Society for Microbiology: Microbes in the spotlight.* p 84-84.

Sedigh Rahimabadi P, Khodaei M, Koswattage KR (2020) Review on applications of synchrotron-based X-ray techniques in materials characterization. *X-Ray Spectrometry* 49(3):348-373.

Torikoshi M, Tsunoo T., Sasaki M., Endo M., Noda Y., Ohno Y., Kohno T., Hyodo K., Uesugi K., Yagi N. (2003) Electron density measurement with dual-energy x-ray CT using synchrotron radiation. *Physics in Medicine & Biology* 48:673–685.

Tsunoo T *et al.* (2004) Measurement of electron density and effective atomic number using dual-energy x-ray CT. in *IEEE Symposium Conference Record Nuclear Science 2004.*), p 3764-3768.

Van Geet M, Swennen R, David P (2001a) Quantitative coal characterisation by means of microfocus X-ray computer tomography, colour image analysis and back-scattered scanning electron microscopy. *International Journal of Coal Geology* 46(1):11-25.

Van Geet M, Swennen R, Wevers M (2000) Quantitative analysis of reservoir rocks by microfocus X-ray computerised tomography. *Sedimentary Geology* 132(1-2):25-36.

Vinegar HJ, Wellington SL (1987) Tomographic imaging of three-phase flow experiments. *Review of Scientific Instruments* 58(1):96-107.

Walls J, Armbruster M (2012) Shale Reservoir Evaluation Improved by Dual Energy X-Ray CT Imaging. *Journal of Petroleum Technology* 64(11):28-32.

Yun TS *et al.* (2013) Evaluation of rock anisotropy using 3D X-ray computed tomography. *Engineering Geology* 163:11-19.

Zhao Y *et al.* (2018) Pore structure characterization of coal by synchrotron radiation nano-CT. *Fuel* 215:102-110.

2 IDENTIFICATION OF COMMON MINERALS USING STOICHIOMETRIC CALIBRATION METHOD FOR DUAL-ENERGY CT

Identification des minéraux communs par la méthode de calibration stœchiométrique pour la tomodensitométrie à double énergie.

Authors:

M. Martini[1], P. Francus[1,3], L. Di Schiavi Trotta[2], P. Després[2].

[1]Centre Eau Terre Environnement, Institut national de la recherche scientifique, Québec, Canada

[2]Department of Physics, Physical Engineering and Optics, Université Laval, Québec, Canada

[3]GEOTOP – Research Centre on the Dynamics of the Earth System, Montréal, Québec, H2X 3Y7, Canada

Corresponding author: Margherita Martini (margherita.martini@ete.inrs.ca)

This article was published in *Geochemistry, Geophysics, Geosystem*, 22, e2021GC009885, 2021, AGU

Received: 3 MAY 2021 - Accepted: 19 AUG 2021

https://doi. org/10.1029/2021GC009885

Authors contribution:

Margherita Martini: Conceptualization, Methodology, Software, Data analysis, Original draft preparation, Writing, Review & Editing. Pierre Francus: Conceptualization, Methodology, Project administration, Funding acquisition, Supervision, Writing, Review & Editing. Leonardo Di Schiavi Trotta: Software, Writing, Review & Editing. Philippe Després: Conceptualization, Methodology, Funding acquisition, Supervision, Writing, Review & Editing.

2.1 Résumé

La tomographie médicale à rayons X peut être utilisée pour caractériser rapidement et de manière non destructive la structure et les variations de densité des échantillons géologiques. Des approches multispectrales permettent d'obtenir davantage d'informations sur la nature des échantillons (densité électronique et composition élémentaire). Cet article explore l'une d'entre elles, une méthode de calibration stœchiométrique pour l'imagerie à double énergie, afin d'identifier les minéraux les plus courants. Un ensemble de 18 matériaux de calibration a été sélectionné pour couvrir une gamme de variabilité du numéro atomique effectif (Z_{eff}) et de la densité électronique (ρ_e) rencontrés dans les échantillons géologiques.

La validation de cette calibration a été réalisée en analysant 23 minéraux courants en cartographiant leurs Z_{eff} et ρ_e respectifs afin d'identifier celui dont les propriétés sont les plus proches. Cette étude montre que la méthode stœchiométrique identifie correctement les minéraux les plus importants et les plus courants (quartz, calcite, dolomite) qui ne peuvent généralement pas être distingués à l'aide d'une méthode d'imagerie à énergie unique, bien que les 23 minéraux étudiés n'aient pas tous été correctement déterminés. Nous montrons que cette méthode élaborée précédemment à des fins médicales est également efficace dans le domaine des sciences de la terre.

2.2 Abstract

Medical X-ray computed tomography (CT) can be used to rapidly and non-destructively characterize structure and density variations of geological specimens. More information about the nature of samples (electron density and elemental composition) can be retrieved using multi-spectral approaches. This paper explores one of them, a stoichiometric calibration method for dual-energy imaging, to identify the most common minerals. A set of 18 calibrating materials was selected to cover a range of variability in effective atomic number (Z_{eff}) and electron density (ρ_e) encountered in geological specimens.

The validation of this calibration was performed analyzing 23 common minerals by mapping their respective Z_{eff} and ρ_e in order to identify the one with the closest properties. This study shows that the stoichiometric method correctly identifies the most important and common minerals (quartz, calcite, dolomite) that are usually not distinguishable using a single energy imaging method,

although all the 23 studied minerals were not correctly determined. We show that this method previously elaborated for medical purposes is also efficient in earth science.

2.3 Plain Language Summary

Medical CT-scanners measure the attenuation of X-rays that go through a sample allowing the non-destructive 3D internal structure visualization of a wide range of samples. The attenuation depends on the interaction between incident beam and sample local density and chemical composition. By scanning specimens using two different energies, it is possible to track the attenuation changes (grey level) according to the X-ray spectra, and to use this difference to identify the samples. This paper tests the applicability of one method developed by medical physicists for biological tissues on 23 common minerals. While all minerals are not correctly identified, this method recognizes the most important and common ones in geology (quartz, calcite, dolomite).

2.4 Introduction

X-ray computed tomography (CT) is a non-destructive technique allowing the visualization of sample internal structure. A medical CT scanner consists in an X-ray source and a detector, which face each other and rotate around the sample. Bi-dimensional radiographic projections are acquired at various angles from 0° to 360° and then processed by a mathematical algorithm (i.e., image reconstruction) in order to obtain a 3D visualization of the object. Different types of image reconstructions exist, including the widely used filtered back projection that requires little computational resources but produces less qualitatively accurate images, and iterative reconstruction, based on time consuming and numerically intensive algorithm but providing better images quality (Bushberg, 2012).

The images are displayed in a gray scale related to the X-ray attenuation by the sample materials (Rizescu *et al.*, 2001).

Initially, this technology was developed for medical imaging, but its potential for other domains was rapidly understood (Mees *et al.*, 2003).

This paper explores a specific CT methodology, called dual-energy CT scanning (DECT), elaborated for the first time in the seventies by Alvarez and Macovski (1976). The technique consists in imaging objects with two different X-ray spectra and in combining the results to achieve various objectives, including one allowing the discrimination and identification of materials based on their density and elemental composition. From a physical perspective, DECT exploits the energy dependence of photoelectric absorption and Compton scattering components of total attenuation (Duchesne *et al.*, 2009). The method of Alvarez and Macovski (1976) acts on the 2D radiographic projections and is therefore called a pre-reconstruction one.

During the same year, Rutherford *et al.* (1976) published another DECT methodology which, on the contrary, is post-reconstruction, meaning the correction is performed on the reconstructed data. This method is more sensitive to beam hardening artifacts, caused by the presence of highly attenuating materials in the sample (Remeysen & Swennen, 2006). Several variations of the post-reconstruction approach have been developed afterwards, in order to improve sample characterization (e.g., Jackson and Hawkes (1981), Vinegar and Wellington (1987), Torikoshi (2003); Tsunoo *et al.* (2004), Bazalova *et al.* (2008)).

One of the first DECT post-reconstruction applications in geology field was made by Van Geet *et al.* (2000), who adapted the mathematical formulas previously elaborated by Coenen (1994) in order to quantify the electron density (ρ_e) and the effective atomic number (Z_{eff}) of reservoir rocks, properties originally analyzed only by destructive techniques (Alves *et al.*, 2015). Then, geologists continued to improve this post-reconstruction dual-energy method *ad hoc* for earth sciences (Duliu *et al.*, 2003; Rizescu *et al.*, 2001), sometimes building home-made CT scanner (Iovea, 2006) and better distinguishing similar minerals and rocks (Iovea *et al.*, 2009; Remeysen & Swennen, 2008).

Later, Paziresh *et al.* (2016) applied the method of Alvarez and Macovski (1976) on geological samples adopting a protocol used for medical purposes. DECT techniques typically require the knowledge of the incident X-ray beam spectrum, a feature that is not always easy to calculate or to measure (Remeysen & Swennen, 2006). Therefore, DECT methods that not require spectral information were developed and applied mostly to the field of medical imaging (e.g., Landry *et al.* (2013) and Bourque *et al.* (2014)). While several authors explored the use of DECT on geological samples (e.g., Siddiqui (2004), Alves *et al.* (2015), Jussiani (2015), Victor (2017)), they were mainly using micro-CT instruments for which the incident spectrum was easily available, focussing on artificial dense objects (metal bars) (Haghighi *et al.*, 2011), or requiring intensive computation (Victor, 2017). This paper is the first to explore the use of polynomial DECT protocol to identify natural mineral samples because it has two main advantages: it can easily be applied on medical CT images for which the spectral information of the incident X-ray is not easy to obtain or to measure, and it is computationally light.

2.5 Materials and Methods

2.5.1 CT- scan instrument

The instrument used in this paper is a Siemens Somatom Definition AS+128 located at the *Institut national de la recherche scientifique, Centre Eau Terre Environment*, Québec City, Canada. In this configuration the gantry moves along the examination table where the samples are placed (Figure 2.1) (Brunelle, 2016).

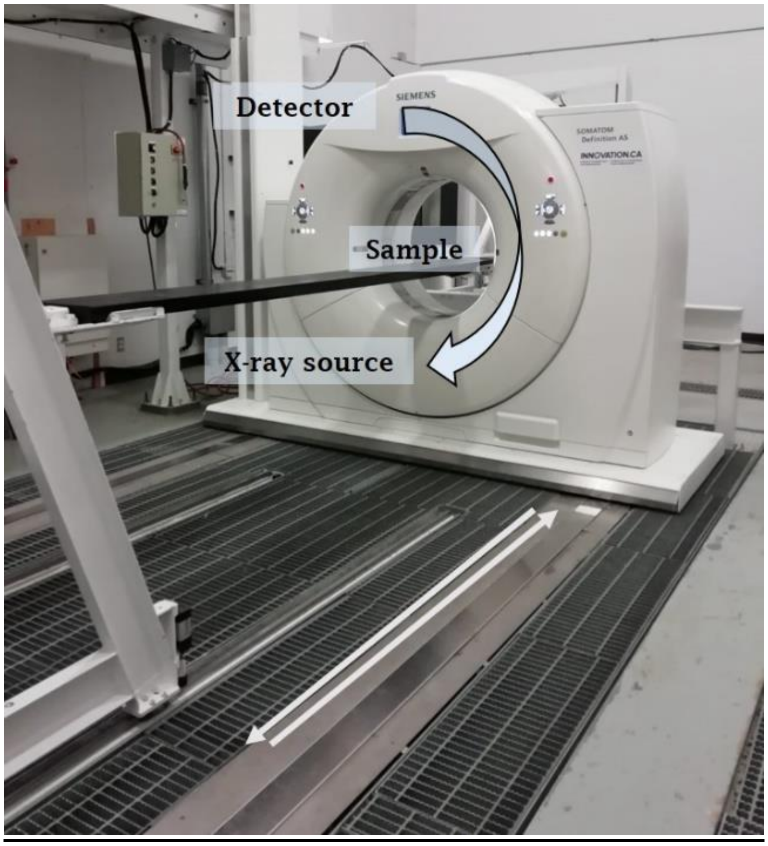

Figure 2.1: Siemens Somatom Definition AS+128.

The instrument is located at *the Institut national de la recherche scientifique, Centre Eau Terre Environnement*, Québec City, Canada. X-ray source and detector face each other in the gantry and rotate around the sample. The scanner moves on rails (white arrows).

The X-ray tube can be operated at potentials between 70 keV and 140 keV and the 64-row detector is from the Stellar$^{\mathrm{Infinity}}$ generation. Images were acquired in spiral mode with a pitch factor of 0.55, at 70 and 140 keV, 495 mA current and a beam collimation of 12 mm. Here, the reconstruction was performed with the ADMIRE suite, belonging to the category of statistical iterative reconstruction methods (Gordic *et al.*, 2014). Reconstructed images are 512 x 512 pixels, covering a field of view of 50 mm x 50 mm wide (voxels of 97 µm along the axis). Pixel values depend on the object attenuation coefficient according to Beer's law (Cnudde & Boone, 2013), and expressed in Hounsfield units (*HU*), a relative scale tied to the attenuation of materials (conventionally water has *HU*=0 and air *HU*=-1000), varying from -1024 to +3071 *HU* (normal scale), providing 4096 levels of grey (Brunelle, 2016). The CT-scale can be extended by scaling down the *HU* value by a factor of 10, expanding the possible values between -10240 and 30710 *HU*, a feature useful for very dense samples (Coolens & Childs, 2003). The reconstruction filter used was the D45s specifically designed by Siemens for dual-energy measurements and providing a balance between the preservation of spatial resolution and noise reduction.

2.5.2 Stoichiometric method

The stoichiometric method developed by Bourque et al. (Bourque *et al.*, 2014) is a dual-energy CT protocol aiming at identifying the nature of biological tissues for medical purposes. It was based on the work of Schneider *et al.* (1996), a calibration elaborated for single energy CT, and Bourque et al. applied it to DECT, in order to facilitate the determination of effective atomic number (Z_{eff}) and electron density (ρ_e).

The theoretical effective atomic number Z_{eff} of samples is calculated with the following equation:

$$Z_{eff} = \sqrt[\beta]{\sum_i^N f_i Z_i^\beta} \tag{2.1}$$

where f_i is the fractional mass of element Z_i. As the literature reports, the exponent β can vary between 2.94 and 3.8 (Bonnin *et al.*, 2014; Spiers, 1946) and it is a function of photon energy, sample materials and system specifics (Alves *et al.*, 2015; Azevedo *et al.*, 2016; Landry *et al.*, 2013).

Then, the theoretical electron density ρ_e, expressed in number of electrons per unit volume (electron·cm^{-3}), is calculated as:

$$\rho_e = \sum_{i=1}^{N} \frac{Z_i}{A_i} \rho \tag{2.2}$$

where A_i is the atomic mass of the element Z_i and ρ is the material mass density (g·cm^{-3}) (Azevedo *et al.*, 2016; Manohara *et al.*, 2008).

The materials linear attenuation coefficient is calculated converting back CT measurements (*HU* values) as (Boespflug *et al.*, 1995; Watanabe, 1999):

$$\mu = \frac{\mu_{sample}}{\mu_{water}} = \left(\frac{HU}{1000}\right) + 1 \tag{2.3}$$

Two different calibration procedures are necessary: the first one relates to the effective atomic number and the second one to the electron density.

First, the two linear attenuation values, measured at low and high energy (Equation 2.3), and the calculated Z_{eff} (Equation 2.1) of the basis set of samples are plotted to estimate the best relationship. In our case a second-order polynomial (Equation 2.4) data-driven empirical model was used to set the *a*, *b* and *c* coefficients of the Z_{eff} calibration.

$$Z_{eff} = a + b \cdot \left(\frac{\mu_{low}}{\mu_{high}}\right) + c \cdot \left(\frac{\mu_{low}}{\mu_{high}}\right)^2 \tag{2.4}$$

It is then possible to achieve the ρ_e calibration (finding another set of coefficients) plotting the ratio between measured μ and ρ_e (Equation 2.2), normalized by water electron density ($\rho_{e\ water}$ = $3.34 \cdot 10^{23}$) and Z_{eff} determined in Equation 2.4:

$$\frac{\mu_{low\ or\ high}}{\rho_e / \rho_{e\ water}} = d + e \cdot Z_{eff} + f \cdot Z_{eff}^2 \tag{2.5}$$

Again, the data-driven empirical model is a second-order polynomial. The μ value can equally be those obtained low or high energy; it is also possible to use both equations to calculate ρ_e and average the outcomes.

2.6 Results

2.6.1 Calibration

The calibration procedure consists in scanning a set of materials with a known chemical composition (their Z_{eff} and ρ_e are calculated using the Equations 2.1 and 2.2) in order to determine the unknown coefficients of Equations 2.4 and 2.5. A set of 18 calibration materials covering the range of Z_{eff} and ρ_e encountered in geological specimens (Figure 2.2) was selected: common geological minerals (halite, crystalline quartz, pyrite, fluorite, albite) completed by Sodium Iodide (NaI) solutions at different concentrations, an aluminum and a titanium bar.

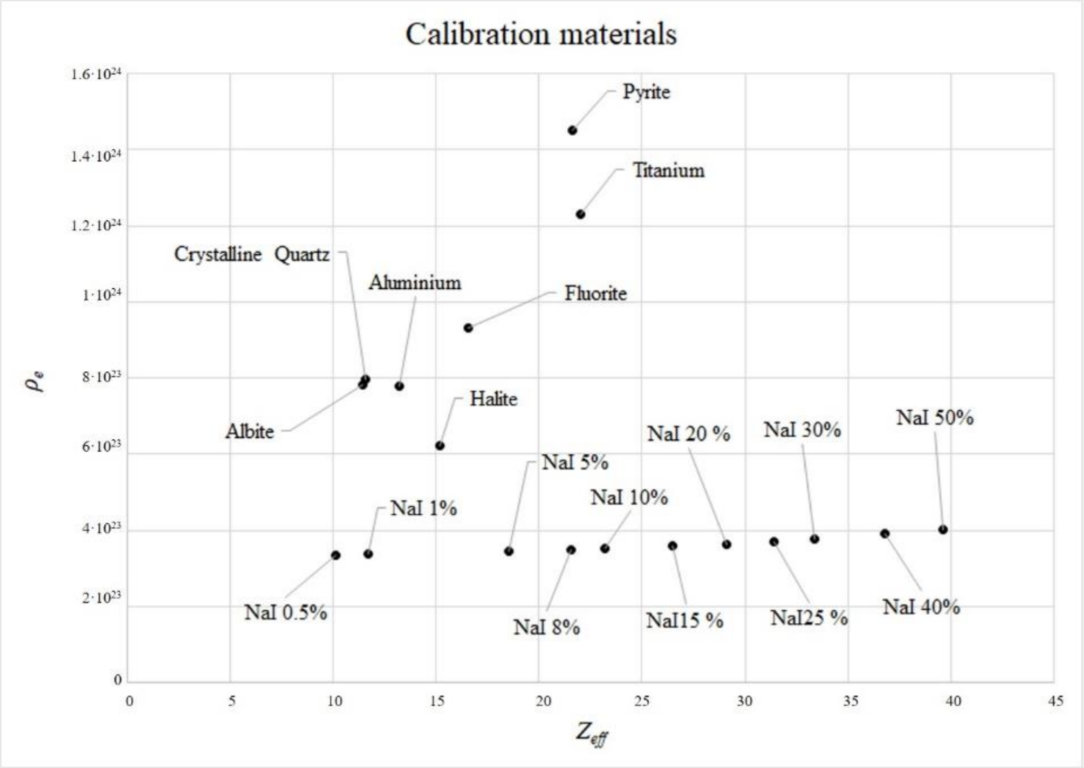

Figure 2.2: Calibration samples.

Electronic density and effective atomic number theoretical value distribution of calibration samples.

The first ones are natural samples, so they do not have a precise chemical composition and always contain impurities, but their presence is important for the subsequent validation, being of the same nature as investigated samples (Stamm, 1974). Figure 2.3 shows an example of a scanned sample (specifically crystalline quartz) in the three dimensions. Details about these calibration materials are available in Table 7.1, Annexe I or in *Borealis* repository.

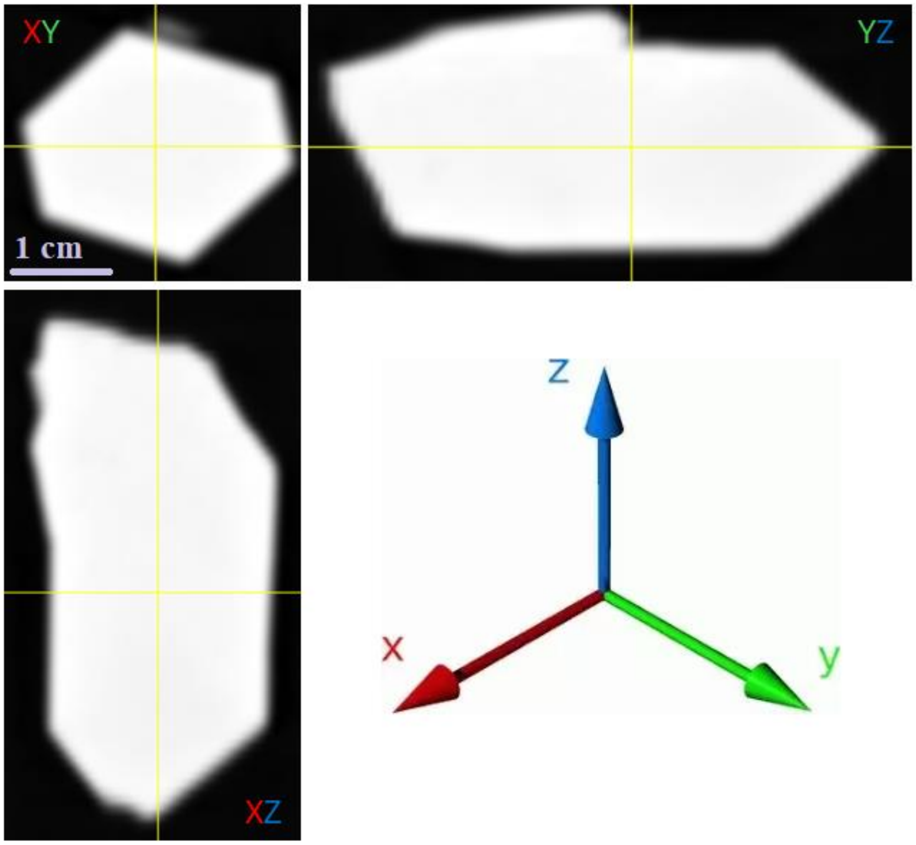

Figure 2.3: Example of scanned mineral.
Crystalline quartz is illustrated in the three different planes of space, X, Y and Z.

As anticipated, the best possible β exponent (Equation 2.1) varies between 2.94 and 3.8 (Bonnin *et al.*, 2014) depending on the material, the instrument and the energy considered. Our choice is based on the behaviour of determination coefficient (R^2) as function of β in the fitting of Equation 2.4; Figure 2.4 shows the best value in the possible range is 2.94.

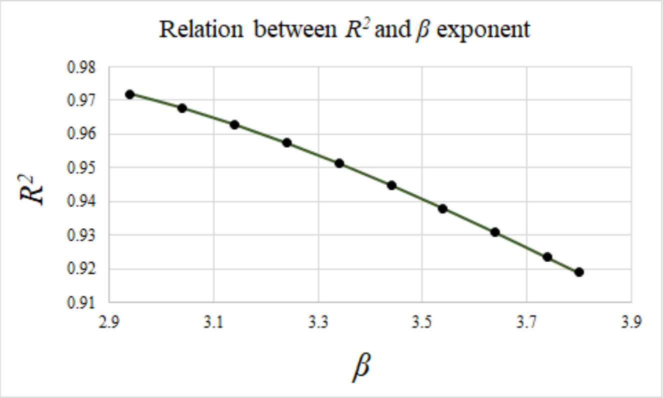

Figure 2.4: *β* choice.

R^2 values against possible *β* of Equation 2.1.

The effective atomic number calibration, following Equation 2.4 to find *a*, *b* and *c* coefficients, is performed by plotting the Z_{eff} and μ_{low}/μ_{high} values of basis samples (Figure 2.5); this fit presents $R^2 = 0.97$.

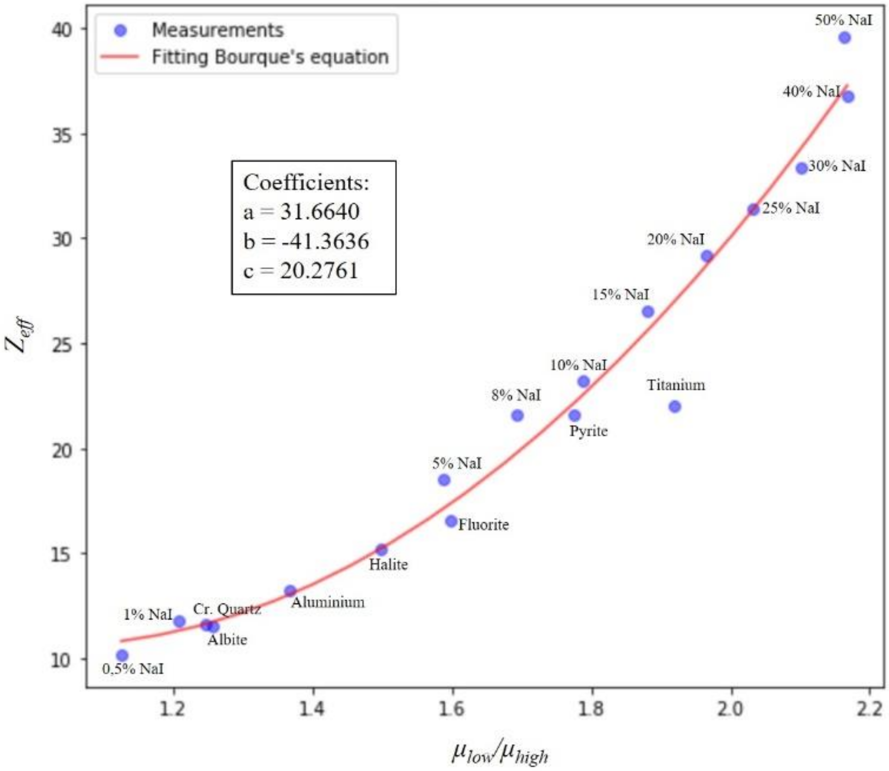

Figure 2.5: Z_{eff} calibration curve and coefficients.

These coefficients are related to Equation 2.4 and calibration curve with μ_{low}/μ_{high} as function of Z_{eff}.

Then, the electron density calibration, related to Equation 2.5 aiming to obtain *d*, *e* and *f* coefficients, is shown in Figure 2.6. As already mentioned, we can freely choose to use μ_{low} or μ_{high} in this model. We opted for μ_{low} obtained at 70 keV because the correlation was stronger (R^2= 0.98) compared to the one obtained at 140 keV (R^2= 0.96).

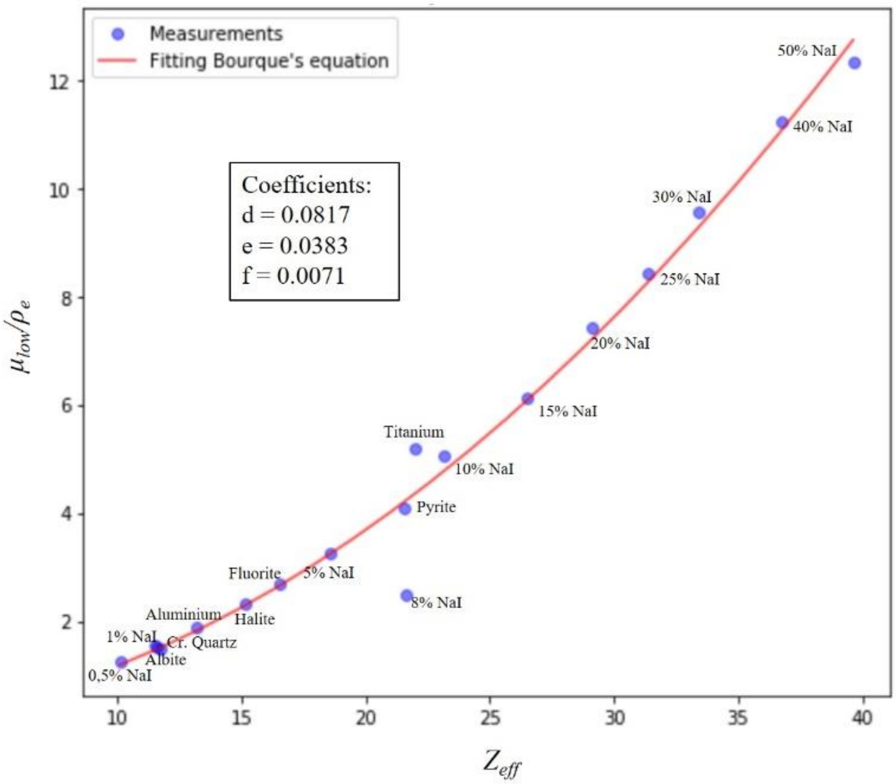

Figure 2.6: ρ_e calibration curve and coefficients.

These coefficients are related to Equation 2.5 and calibration curve with Z_{eff} as function of $\mu_{low}/(\rho_e/\rho_{e\ water})$.

2.6.2 Validation

A set of 23 relatively common minerals were used for the validation of the stoichiometric method (Table 2.1, column 1). Samples were about the same size as the ones of the calibration set (≃ 3 cm x 3 cm) and selected to ensure they cover a wide range of effective atomic number and electronic density. Their theoretical values of Z_{eff} and ρ_e have been calculated using Equations 2.1 and 2.2 (Table 2.1, columns 3 and 4) starting from their theoretical chemical composition (Table 2.1, column 2).

Using the same acquisition conditions of the calibration step (Equation 2.4) the Z_{eff} model and the measured linear attenuation coefficients μ Equation 2.3) at low and high energy (details are available in Table 7.2, Annexe I or in *Borealis* repository), we calculate the minerals Z_{eff} values (Table 2.1, column 5). Then, the relative difference between these measured values of Z_{eff} and the theoretical ones is shown in column 6 (Table 2.1).

Successively and always using the same acquisition conditions, Equation 2.5, the ρ_e model and the measured linear attenuation coefficients μ acquired at low energy, we calculate the minerals ρ_e (Table 2.1, column 7). Again, the relative difference between these measured values of ρ_e and the theoretical ones is shown in column 8 (Table 2.1).

(1)	(2)	(3)	(4)	(5)	(6)	(7)	(8)
Mineral	**Chemical composition**	**Theoretical Z_{eff}**	**Theoretical ρ_e ($e^{-}\cdot cm^{-3}$)**	**Measured Z_{eff}**	**% difference between theoretical and measured Z_{eff} values**	**Measured ρ_e**	**% difference between theoretical and measured ρ_e values**
Albite	$NaAlSi_3O_8$	11.472	$7.82\cdot10^{23}$	11.743	2.4 %	$7.81\cdot10^{23}$	0.1 %
Almandine	$Fe_3^{2+}Al_2Si_3O_{12}$	18.655	$1.23\cdot10^{24}$	20.514	9.9 %	$9.44\cdot10^{23}$	2.2 %
Andesine	$(Ca,Na)(Al,Si)_4O_8$	13.249	$7.97\cdot10^{23}$	12.599	3.1 %	$8.32\cdot10^{23}$	4.3 %
Ankerite	$Ca(Fe^{2+},Mg,Mn)(CO_3)_2$	16.989	$9.05\cdot10^{23}$	15.094	11.2 %	$7.29\cdot10^{23}$	19.4 %
Anorthite	$CaAl_2Si_2O_8$	13.206	$8.21\cdot10^{23}$	12.778	3.2 %	$8.27\cdot10^{23}$	0.6 %
Augite	$(Ca,Mg,Fe^{2+},Fe^{3+},Ti,Al)_2(Si,Al)_2O_6$	14.849	$1.01\cdot10^{24}$	15.589	4.9 %	$9.58\cdot10^{23}$	5.6 %
Biotite	$K(Mg,Fe^{2+})_3$	14.046	$9.26\cdot10^{23}$	13.741	2.2 %	$7.7\cdot10^{23}$	16.1 %
Bytownite	$(Ca,Na)[Al(Al,Si)Si_2O_8]$	12.961	$8.09\cdot10^{23}$	11.953	7.8 %	$8.13\cdot10^{23}$	0.4 %
Calcite	$CaCO_3$	15.079	$8.15\cdot10^{23}$	15.398	2.1 %	$7.96\cdot10^{23}$	2.3 %

Chalcopyrite	$CuFeS_2$	24.568	$1.20\cdot10^{24}$	22.741	7.4 %	$9.55\cdot10^{23}$	20.4 %
Diopside	$CaMgSi_2O_6$	13.729	$1.02\cdot10^{24}$	13.971	1.1 %	$9.59\cdot10^{23}$	6.1 %
Dolomite	$CaMg(CO_3)_2$	13.057	$8.53\cdot10^{23}$	13.101	0.3 %	$8.46\cdot10^{23}$	0.9 %
Gypsum	$CaSO_4\cdot2H_2O$	14.109	$7.11\cdot10^{23}$	14.246	0.9 %	$7.13\cdot10^{23}$	0.2 %
Hematite	Fe_2O_3	22.962	$1.52\cdot10^{24}$	17.882	22.1 %	$1.73\cdot10^{24}$	13.9 %
Ilmenite	$FeTiO_3$	21.327	$1.37\cdot10^{24}$	18.331	14.1 %	$1.40\cdot10^{24}$	2.4 %
Labradorite	$(Ca,Na)(Si,Al)_4O_8$	16.608	$8.06\cdot10^{23}$	12.558	0.4 %	$8.26\cdot10^{23}$	2.5 %
Magnetite	Fe_3O_4	23.231	$1.47\cdot10^{24}$	20.773	10.6 %	$8.57\cdot10^{23}$	41.9 %
Microcline	$KAlSi_3O_8$	13.018	$7.64\cdot10^{23}$	12.558	3.5 %	$7.95\cdot10^{23}$	3.9 %
Muscovite	$KAl_2(Si_3Al)O_{10}(OH,F)_2$	12.403	$8.46\cdot10^{23}$	12.999	4.8 %	$8.06\cdot10^{23}$	4.7 %
Olivine	$(Mg,Fe)_2SiO_4$	15.215	$9.80\cdot10^{23}$	12.701	16.5 %	$9.60\cdot10^{23}$	2.1 %
Phlogopite	$KMg_3(Si_3Al)O_{10}(F,OH)_2$	12.278	$8.46\cdot10^{23}$	14.769	20.3 %	$5.43\cdot10^{23}$	35.7 %
Quartz	SiO_2	11.561	$7.97\cdot10^{23}$	11.632	0.6 %	$8.11\cdot10^{23}$	1.7 %
Talc	$Mg_3Si_4O_{10}(OH)_2$	11.154	$8.30\cdot10^{23}$	11.587	3.9 %	$8.52\cdot10^{23}$	2.7 %

Table 2.1: Validation minerals.

Validation minerals are indicated with their theoretical chemical composition and theoretical Z_{eff} and ρ_e calculated using Equation 2.1 and 2.2. Then, Z_{eff} and ρ_e calculated using stoichiometric method and their relative difference (in %) with the theoretical values.

2.6.3 Mineral identification

The next step is to develop a tool to identify unknown minerals using Z_{eff} and ρ_e values measured by the dual-energy stoichiometric method. An *ad hoc* library of 69 common minerals (chosen from the database http://webmineral.com/, accessed Oct. 2020) was built using Python 3.7 as programming language (*CommonMinerals_database.py* in annexe I or in *Borealis* repository) mapping them to their respective Z_{eff} and ρ_e (theoretically properties calculated by Equations 2.1 and 3.2).

Z_{eff} and ρ_e values differ by two orders of magnitude, thus they are normalized using the feature scaling method (Equation 2.6) (Youn & Jeong, 2009):

$$x' = \frac{x - \min(x)}{\max(x) - \min(x)} \tag{2.6}$$

Where x is the original value and x' is the normalized value. Then, another Python routine (*Minerals_Identification.py*, Annexe I or in *Borealis* repository) searches this library to find the minerals with the shortest Euclidean distance to these theoretical properties and provides a list of minerals with increasing Euclidean distance.

Table 2.2 shows the three closest minerals found using the searching program for each validation set of samples from Table 2.1.

Mineral Specimen	**1st**	**2nd**	**3rd**	
Albite	**Albite**	Anorthoclase	Oligoclase	
Almandine	Fluorite	Ankerite	Epidote	Almandine is the 51th
Andesine	Alunite	Lepidolite	Illite	Andesine is the 12th
Ankerite	Gypsum	Orthoclase	Microcline	Ankerite is the 31th
Anorthite	Aluminum	Lepidolite	**Anorthite**	
Augite	Apatite	Olivine	Fluorite	Augite is 5th
Biotite	Aluminum	Microcline	Orthoclase	Biotite is the 33th
Bytownite	Labradorite	Andesine	Quartz	Bytownite is the 5th
Calcite	**Calcite**	Glauconite	Bassanite	

Chalcopyrite	Epidote	Ankerite	Fluorite	Chalcopyrite is the 32th
Diopside	Olivine	Biotite	Apatite	Diopside is 8th
Dolomite	**Dolomite**	Muscovite	Phlogopite	
Gypsum	**Gypsum**	Orthoclase	Cristobalite	
Hematite	Maghemite	Arsenopyrite	**Hematite**	
Ilmenite	**Ilmenite**	Chromite	Pyrite	
Labradorite	Alunite	Lepidolite	Illite	Labradorite is the 6th
Magnetite	Ankerite	Glauconite	Fluorite	Magnetite is the 65th
Microcline	Andesine	Aluminum	Labradorite	Microcline is 10th
Muscovite	Bytownite	Labradorite	Anorthite	Muscovite is the 15th
Olivine	Enstatite	Andalusite	Biotite	Olivine is the 4th
Phlogopite	Carnallite	Halite	Natron	Phlogopite is the 29th
Quartz	**Quartz**	Andesine	Beryl	
Talc	Phlogopite	Muscovite	Illite	Talc is 4th

Table 2.2: Mineral ranking.

The three closest identified minerals obtained using the searching script applied on the validation set of minerals. The last column shows the rank of the sought mineral when it was not identified in the three closest minerals.

2.7 Discussion

The calibration step yielded very high R^2 correlation coefficients (0.97 for Z_{eff} model and 0.98 for ρ_e model), in spite of two outliers. Titanium bar in Figure 2.5 and 8% NaI in Figure 2.6 do not perfectly fit: considering similar samples perform very well (another pure metal bar and other solutes), it is difficult to explain why these two outliers appear. However, despite their presence, the calibration is adequately performed.

The stoichiometric method validation estimated the effective atomic number Z_{eff} with less than 10% difference compared to theoretical value: out of a total of 23 minerals, 17 have less than 5% difference and, conversely, the largest deviations are for magnetite, ankerite, ilmenite, olivine, phlogopite and hematite in ascending order (Table 2.1).

Bourque *et al.* (2014) obtained a smaller error, but in this study 10% is acceptable considering the samples we investigated, denser and more complex than human tissues; moreover, the final goal is the mineral identification among those of a chosen database, which is influenced by several factors and not only by the percentage error.

Figure 2.7 shows the iterative reweighted least squares trendline (red line) of minerals theoretical versus measured Z_{eff} perfectly matches with the least squares trendline (black line) and the theoretical trendline (dashed line, slope = 1); comparing the slopes, we observe our measurements underestimates the values.

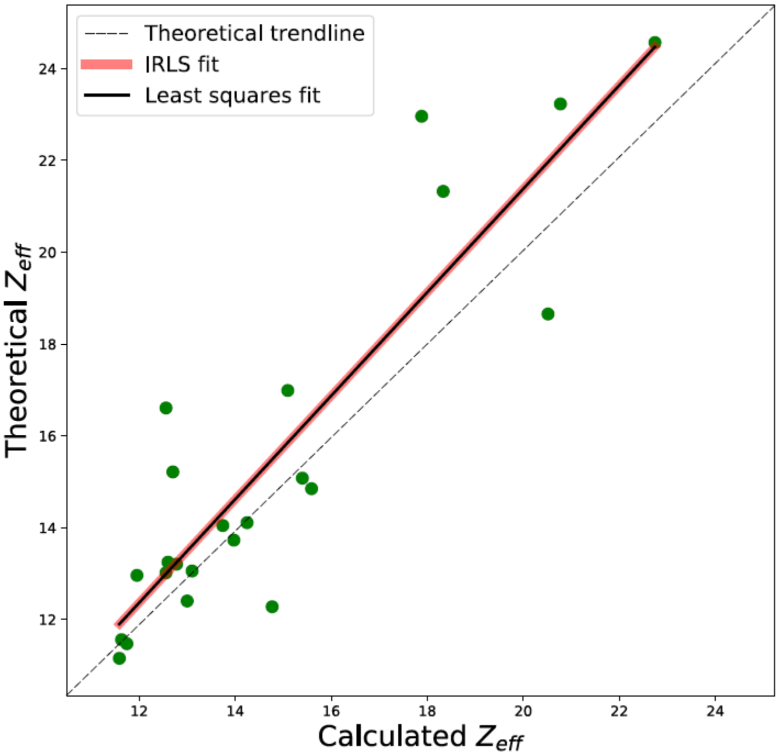

Figure 2.7: IRLS vs least squares fit of Z_{eff}.

Cross plot of theoretical versus measured Z_{eff} of minerals, using stoichiometric method.

The results for electron density ρ_e characterization are similar: 16 minerals have a difference between the measured and the theoretical values of less than 10%, of which 14 of them less than 5%, and the largest difference occurs for hematite, biotite, ankerite, chalcopyrite, almandine, phlogopite and magnetite in ascending order (Table 2.1).

Figure 2.8 shows that iterative reweighted least squares trendline (red line) of minerals theoretical versus measured ρ_e involves a clear improvement of the fit compared to the least square method (black line), perfectly matching with the theoretical dashed line (slope = 1); nevertheless most outliers present underestimated values.

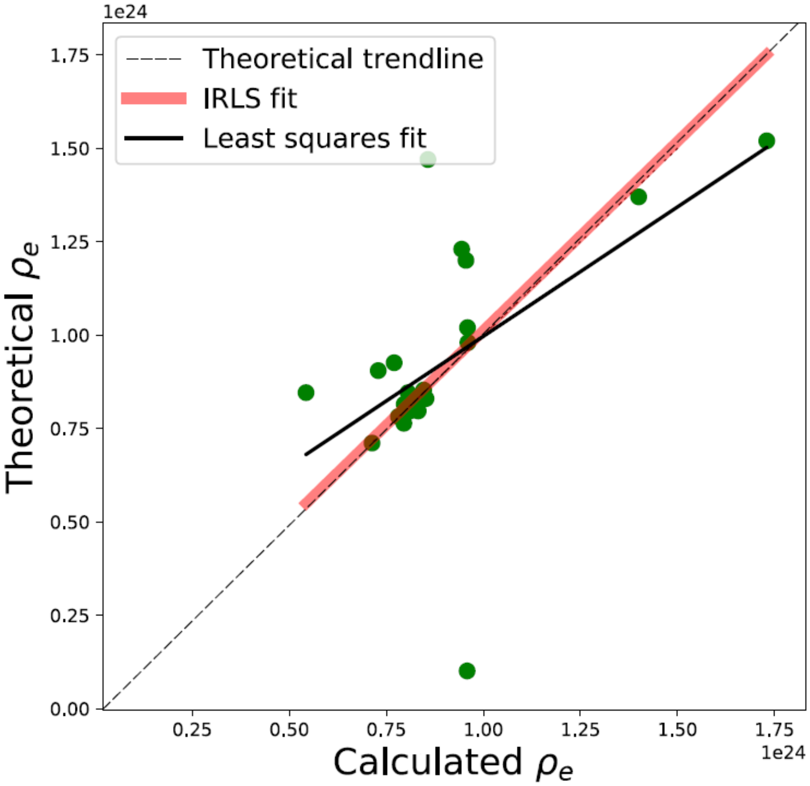

Figure 2.8: IRLS vs least squares fit of ρ_e.

Cross plot of theoretical versus measured ρ_e of minerals, using stoichiometric method.

The identification routine allowed to correctly pinpoint 7 minerals, including very common ones, i.e., albite, quartz and calcite (Table 2.2). An interesting example is hematite: its identification is well performed, although its properties values present a high percentage error. Considering Z_{eff} and ρ_e distribution of the 69-mineral library (Figure 2.9), we observe the majority is situated in a cluster of the graph having small Z_{eff} and ρ_e instead, common minerals with high Z_{eff} and ρ_e are less frequent. Thus, we successfully identified hematite even though its validation performance is weak because the Euclidean distance to its closest neighbour is larger than others (Figure 2.9).

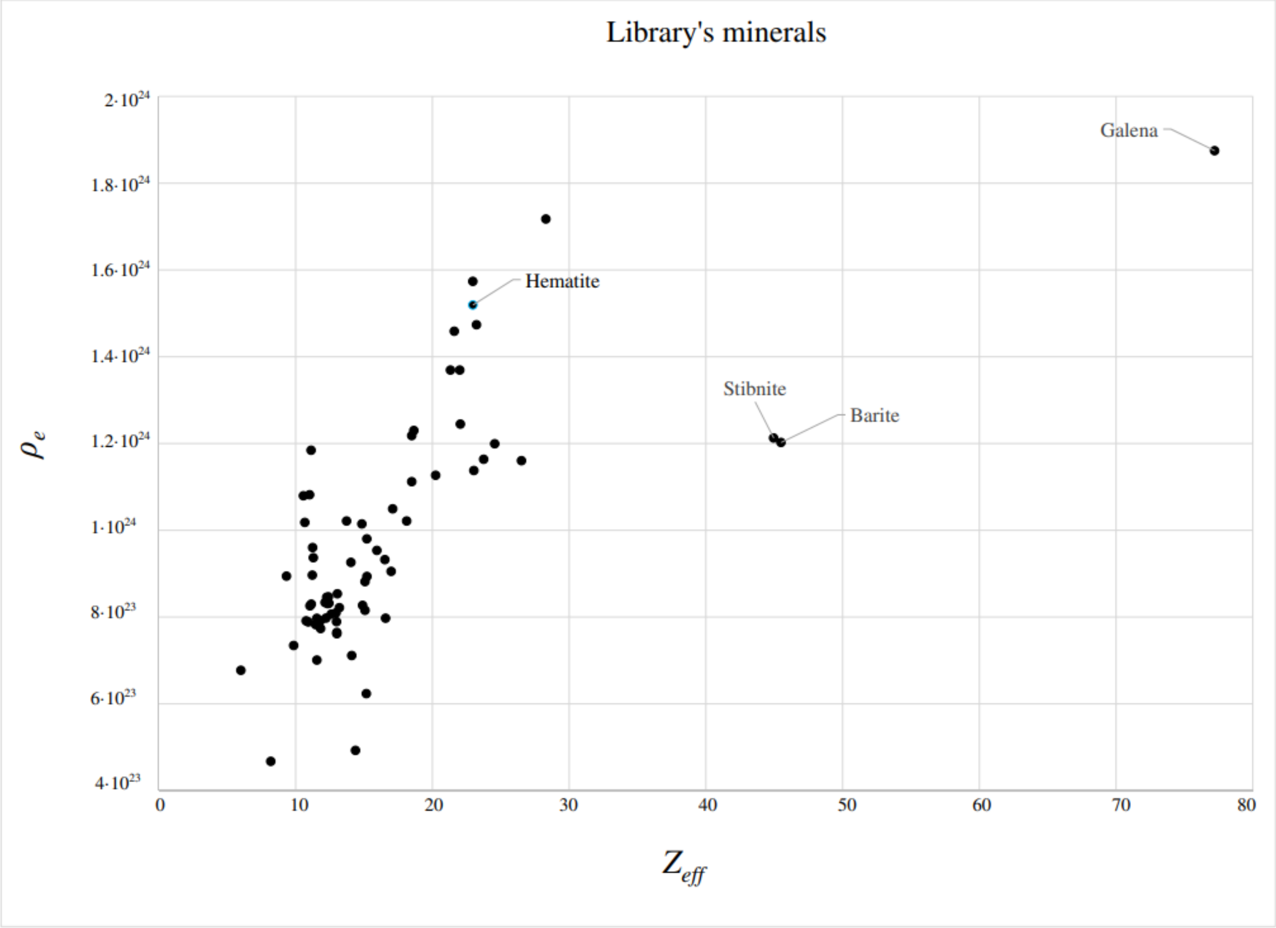

Figure 2.9: Library's minerals.

Cross plot of Z_{eff} versus ρ_e of minerals chosen to develop the Python dictionary.

Several reasons could explain why some mineral samples have a wide difference between theoretical and measured values. First, because natural minerals contain impurities that are unknown in this experiment, it is likely the Z_{eff} and ρ_e calculated using Equations 2.1 and 2.2 and theoretical mineral compositions are not reflecting the actual composition of the minerals used for both the calibration and the validation.

The second reason, similar to the first one, is that some minerals can easily interchange cations within their lattice, yet their precise elemental composition is rather impossible to obtain without specific analysis. Nine validation minerals fall under this case, explaining the poor identification obtained for phyllosilicates, such phlogopite, muscovite and biotite, and others such as ankerite (Table 2.1). However, chalcopyrite, hematite, ilmenite and magnetite, in spite of their chemical formula not allowing for lattice cation substitutions, also have large differences with theoretical results for Z_{eff}, ρ_e or both properties: these minerals are the densest ones and, among the validation samples, it is remarkable that their values are mainly underestimated, according to iterative least squares trend. The performance of the stoichiometric protocol, previously developed for medical physics and human tissues, could be weaker for dense samples. It is possible that the exposure time with our medical CT is too low for having an accurate measurement of μ. Figure 2.10 shows the cross plot of minerals μ at low and high energy and the relative error bars having 95% confidence level: it is calculated following (Hazra, 2017):

$$x \pm Z \frac{s}{\sqrt{n}} \tag{2.7}$$

Where x is our measurement, Z is the value for determining confidence interval (here $Z = 1.96$), s is the standard deviation and n is the number of observations.

In order to avoid the overlapping, only some samples are illustrated but all of them present the same characteristic: horizontal error bar, related to low energy, is larger than the vertical one. This is true for minerals having large or small confidence intervals, so, probably, the need for improving the signal-to-noise ratio is stronger for lower voltage acquisitions (Gordic *et al.*, 2014).

The third possible reason is this stoichiometric method is not so well suited for dense samples; indeed, Bourque et al. used 140 keV as high energy, but the materials they aimed to characterize have smaller values of Z_{eff} and ρ_e than those investigated here. However, this explanation does not hold a close examination of our results because some dense minerals such as hematite and ilmenite (Z_{eff} = 22.96 and 21.3 respectively) are correctly identified (Table 2.2). Our probable explanation is the answer resides in a combination of the above-mentioned factors: some samples have an underestimation for Z_{eff} and an overestimation for ρ_e and inversely, bringing the minerals in a value range favourable to their identification. Indeed, having a small relative difference between theoretical and measured values is not always sufficient to correctly identify the objects using the shortest Euclidean distance.

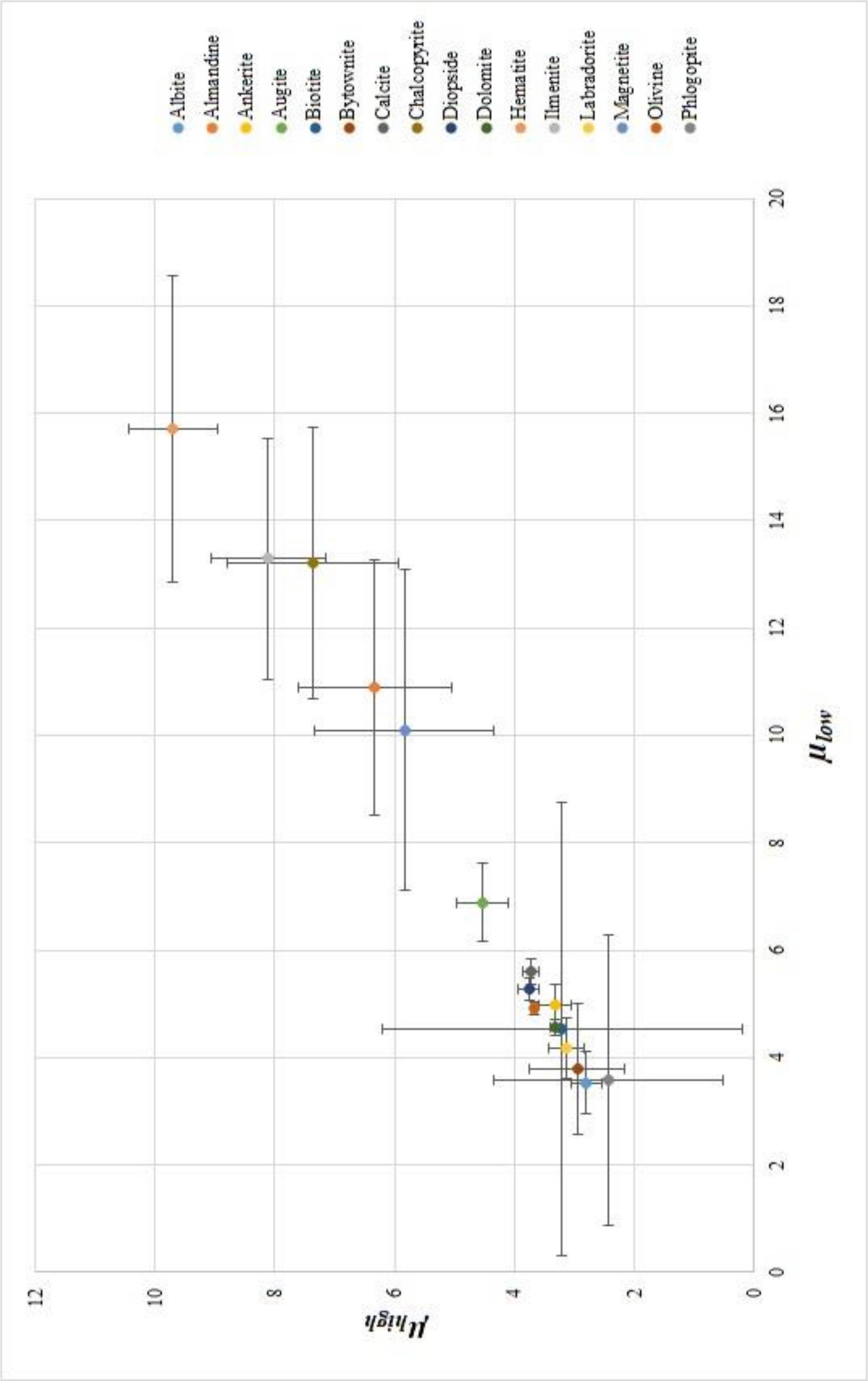

Figure 2.10: Validation minerals and error bars.

Cross plot of minerals *μ* at low and high energy and the relative error bars having 95% confidence level.

A possible improvement of this stoichiometric method could reside in increasing the exposure time or to acquire repeated scans in order to improve the signal-to-noise ratio (e.g., Larmagnat *et al.*, 2019), especially when very dense minerals, reducing the number of photons reaching the detectors, are present.

While the list of existing minerals totals more than 4000, our *ad hoc* library was limited to the 69 most common ones; however, in most cases, some basic knowledge of natural samples such a rock would considerably shorten the list of potential minerals, hence improving the rate of correct classification. If the list of dense potential minerals remains limited to one or two, the method will likely be able to provide a correct identification.

Therefore, despite some drawbacks, stoichiometric method is a suitable option for the characterization of important and common minerals for geological field (quartz, calcite, dolomite) that are not distinguishable using single energy imaging method having very similar density values. Because CT-scanning rock and sediment cores is fast and non-destructive, this method is laying the foundation for an easy access to mineralogical information on geological samples.

2.8 Conclusion

Stoichiometric calibration is a methodology previously elaborated for medical purposes aiming to characterize the human tissues while removing the need for the knowledge of the incident X-ray energy spectra.

This work tested for the first time this technique on geological specimens, materials of greater density than the formerly studied biological samples. Two different calibrations were performed to characterize the effective atomic number and the electron density using 6 natural minerals, 2 metal bars and 11 saline solutions at different concentrations. Then, the calibration was validated with a set of 23 natural mineral samples selected to ensure they cover a wide range property values. Finally, an *ad hoc* routine searches the minerals closest to the calculated Z_{eff} and ρ_e values and provides a list of decreasing possibilities.

We showed this stoichiometric dual-energy CT method is easy to implement and well suited to identify the most common minerals.

2.9 Data availability statement

All the data about calibration materials, measured linear attenuation coefficients μ of minerals and the Python scripts used for their identification are available in the Chapter 7 (Annexe I) and at the *Borealis* repository:

https://dataverse.scholarsportal.info/privateurl.xhtml?token=825cef86-ac16-46ad-9e9f-c3c0604f438b

2.10 Acknowledgements

This research was funded by *Fonds de recherche du Québec – Nature et technologies*. We would like to thank the colleagues Mathieu Des Roches, Philippe Letellier et Louis-Frederic Daigle of the *Institut national de la recherche scientifique* for their support and advice during the analysis carried out in this project.

2.11 References

Alvarez RE, Macovski A (1976) Energy-selective reconstructions in X-ray computerized tomography. *Physics in Medicine & Biology* 21(5):733-744.

Alves H *et al.* (2015) Mineralogy evaluation and segmentation using dual-energy microtomography. *X-Ray Spectrometry* 44(3):99-104.

Azevedo SG *et al.* (2016) System-Independent Characterization of Materials Using Dual-Energy Computed Tomography. *IEEE TRANSACTIONS ON NUCLEAR SCIENCE* 63(1):341-350.

Bazalova M *et al.* (2008) Tissue segmentation in Monte Carlo treatment planning: a simulation study using dual-energy CT images. *Radiotherapy and Oncology* 86(1):93-98.

Boespflug X, Long BFN, Occhietti S (1995) Cat-Scan in Marine Stratigraphy - a Quantitative Approach. *Marine Geology* 122(4):281-301.

Bonnin A *et al.* (2014) Concept of effective atomic number and effective mass density in dual-energy X-ray computed tomography. *Nuclear Instruments and Methods in Physics Research Section B: Beam Interactions with Materials and Atoms* 318:223-231.

Bourque AE, Carrier JF, Bouchard H (2014) A stoichiometric calibration method for dual energy computed tomography. *Physics in Medicine & Biology* 59(8):2059-2088.

Brunelle CB, Des Roches M., Daigle L-F., Francus P., Long B., Després P. (2016) Combining CT scan and particle imaging techniques: applications in geosciences. in *The 4th International Conference on Image Formation in X-Ray Computed Tomography*Bamberg, Germany), p 225-228.

Bushberg JT, Seibert, J.A., Leidholdt, E.M., Boone, J.M. (2012) *The essential physics of medical imaging.* LWW, Third edition

Cnudde V, Boone MN (2013) High-resolution X-ray computed tomography in geosciences: A review of the current technology and applications. *Earth-Science Reviews* 123:1-17.

Coenen JCG, Maas J. (1994) Material classification by dual-energy computerized x-ray tomography. in *International symposium on computerized tomography for industrial applications*), p 120–127.

Coolens C, Childs PJ (2003) Calibration of CT Hounsfield units for radiotherapy treatment planning of patients with metallic hip prostheses: the use of the extended CT-scale. *Phys Med Biol* 48(11):1591-1603.

Duchesne MJ *et al.* (2009) A rapid method for converting medical Computed Tomography scanner topogram attenuation scale to Hounsfield Unit scale and to obtain relative density values. *Engineering Geology* 103(3-4):100-105.

Duliu OG, Rizescu CT, Ricman C (2003) Dual energy gamma-ray axial computer tomography investigation of some metamorphic and sedimentary rocks. *Neues Jahrbuch fòr Geologie und Paläontolgie* 228(3):343-362.

Gordic S *et al.* (2014) Advanced modelled iterative reconstruction for abdominal CT: qualitative and quantitative evaluation. *Clinical Radiology* 69(12):e497-504.

Haghighi RR *et al.* (2011) X-ray attenuation coefficient of mixtures: inputs for dual-energy CT. *Medical physics* 38(10):5270-5279.

Hazra A (2017) Using the confidence interval confidently. *Journal of thoracic disease* 9(10):4125-4130.

Iovea M, Neagu M., Duliu O.G., Oaie G., Ricman C., Mateiasi G. (2006) Dual-Energy Computer Tomography and Digital Radiography Investigation of Organic and Inorganic Materials. in *ECNDT*).

Iovea M *et al.* (2009) Dual-energy X-ray computer axial tomography and digital radiography investigation of cores and other objects of geological interest. *Engineering Geology* 103(3-4):119-126.

Jackson DF, Hawkes DJ (1981) X-ray attenuation coefficients of elements and mixtures. *Physics Reports* 70(3):169-233.

Jussiani EI, Appoloni, C. R. (2015) Effective atomic number and density determination of rocks by X-ray microtomography. *Micron* 70:1-6.

Landry G *et al.* (2013) Deriving effective atomic numbers from DECT based on a parameterization of the ratio of high and low linear attenuation coefficients. *Physics in Medicine & Biology* 58(19):6851-6866.

Larmagnat S *et al.* (2019) Continuous porosity characterization: Metric-scale intervals in heterogeneous sedimentary rocks using medical CT-scanner. *Marine and Petroleum Geology* 109:361-380.

Manohara SR *et al.* (2008) On the effective atomic number and electron density: A comprehensive set of formulas for all types of materials and energies above 1keV. *Nuclear Instruments and Methods in Physics Research Section B: Beam Interactions with Materials and Atoms* 266(18):3906-3912.

Mees F *et al.* (2003) Applications of X-ray computed tomography in the geosciences. *Geological Society, London, Special Publications* 215(1):1-6.

Paziresh M *et al.* (2016) Tomography of atomic number and density of materials using dual-energy imaging and the Alvarez and Macovski attenuation model. *Journal of Applied Physics* 119(21).

Remeysen K, Swennen R (2006) Beam hardening artifact reduction in microfocus computed tomography for improved quantitative coal characterization. *International Journal of Coal Geology* 67(1-2):101-111.

Remeysen K, Swennen R (2008) Application of microfocus computed tomography in carbonate reservoir characterization: Possibilities and limitations. *Marine and Petroleum Geology* 25(6):486-499.

Rizescu C, Beşliu C, Jipa A (2001) Determination of local density and effective atomic number by the dual-energy computerized tomography method with the ^{192}Ir radioisotope. *Nuclear Instruments and Methods in Physics Research Section A: Accelerators, Spectrometers, Detectors and Associated Equipment* 465(2-3):584-599.

Rutherford RA, Pullan BR, Isherwood I (1976) Measurement of effective atomic number and electron density using an EMI scanner. *Neuroradiology* 11(1):15-21.

Schneider U, Pedroni E, Lomax A (1996) The calibration of CT Hounsfield units for radiotherapy treatment planning. *Physics in Medicine & Biology* 41(1):111-124.

Siddiqui S, Khamees, A. A. (2004) Dual-Energy CT-Scanning Applications in Rock Characterization. in *SPE Annual Technical Conference and Exhibition*Houston, Texas).

Spiers FW (1946) Effective atomic number and energy absorption in tissues. *The British journal of radiology* 19(218):52-63.

Stamm D (1974) Calibration and quality control materials. *Clinical Chemistry and Laboratory Medicine* 12(4):137-145.

Torikoshi M, Tsunoo T., Sasaki M., Endo M., Noda Y., Ohno Y., Kohno T., Hyodo K., Uesugi K., Yagi N. (2003) Electron density measurement with dual-energy x-ray CT using synchrotron radiation. *Physics in Medicine & Biology* 48:673–685.

Tsunoo T *et al.* (2004) Measurement of electron density and effective atomic number using dual-energy x-ray CT. in *IEEE Symposium Conference Record Nuclear Science 2004.*), p 3764-3768.

Van Geet M, Swennen R, Wevers M (2000) Quantitative analysis of reservoir rocks by microfocus X-ray computerised tomography. *Sedimentary Geology* 132(1-2):25-36.

Victor RA, Prodanovic, M., Torres-Veredin, C. (2017) Monte Carlo Approach for Estimating Density and Atomic Number From Dual-Energy Computed Tomography Images of Carbonate Rocks. *Journal of Geophysical Research: Solid Earth* 122:9804-9824.

Vinegar HJ, Wellington SL (1987) Tomographic imaging of three-phase flow experiments. *Review of Scientific Instruments* 58(1):96-107.

Watanabe Y (1999) Derivation of linear attenuation coefficients from CT numbers for low-energy photons. *Physics in Medicine & Biology* 44(9):2201-2211.

Youn E, Jeong MK (2009) Class dependent feature scaling method using naive Bayes classifier for text datamining. *Pattern Recognition Letters* 30(5):477-485.

3 EXPLORING THE APPLICATION OF DUAL-ENERGY CT TO DISCRIMINATE SEDIMENT FACIES IN A VARVED SEQUENCE

Exploration de l'application de la tomodensitométrie à double énergie pour discriminer les faciès sédimentaires dans une séquence varvée.

Authors:

M. Martini[1], P. Francus[1,3], L. Di Schiavi Trotta[2], Philippe Letellier[1], Mathieu Des Roches[1], P. Després[2].

[1]Centre Eau Terre Environnement, Institut national de la recherche scientifique, Québec, Canada

[2]Department of Physics, Physical Engineering and Optics, Université Laval, Québec, Canada

[3]GEOTOP – Research Centre on the Dynamics of the Earth System, Montréal, Québec, H2X 3Y7, Canada

Corresponding author: Margherita Martini (margherita.martini@inrs.ca)

This article was published in *The Depositional Record*, 2024; 10: 231–244, IAS

Received: 8 September 2023 - Accepted: 8 January 2024

https://doi.org/10.1002/dep2.271

Authors contribution:

Margherita Martini: Conceptualization, Methodology, Software, Data analysis, Original draft preparation, Writing, Review & Editing. Pierre Francus: Conceptualization, Methodology, Project administration, Funding acquisition, Supervision, Writing, Review & Editing. Leonardo Di Schiavi Trotta: Software, Writing, Review & Editing. Philippe Letellier: Software, Writing, Review & Editing. Mathieu Des Roches: Software, Writing, Review & Editing. Philippe Després: Conceptualization, Methodology, Funding acquisition, Supervision, Writing, Review & Editing

3.1 Résumé

La tomodensitométrie à rayons X en bi-énergie (DECT) permet d'obtenir des images d'objets en utilisant deux faisceaux de rayons X d'énergie différente pour distinguer les différents composants d'un échantillon en fonction de leur densité (densité électronique, ρ_e) et de leur composition élémentaire (numéro atomique effectif, Z_{eff}). L'étalonnage stœchiométrique pour le DECT a déjà été utilisé avec succès pour identifier des minéraux simples et homogènes de manière facile et non destructive. Ici, elle est utilisée pour la première fois pour explorer le potentiel d'un échantillon plus complexe et hétérogène : une carotte de sédiments varvés du lac South Sawtooth dans l'Arctique canadien, composée de trois faciès distincts. Les trois faciès peuvent être distingués avec succès à l'aide du DECT grâce à leurs différentes gammes de valeurs ρ_e et Z_{eff}. Une autre technique de balayage fournissant la composition élémentaire des sédiments a été mise en œuvre : l'analyse µXRF du scanner de carottes a été réalisée à la même résolution que les mesures par tomodensitométrie. Cependant, la corrélation entre les deux techniques de balayage est moins concluante, probablement parce que les analyses n'ont pas été effectuées exactement au même endroit de la carotte. Enfin, l'article aborde les limites de l'utilisation du DECT sur les sédiments, principalement la complexité supplémentaire due aux variations de la taille des grains et de la porosité, mais démontre également son potentiel pour étudier quantitativement les carottes de sédiments d'une manière non destructive.

3.2 Abstract

Dual-energy X-ray Computed Tomography (DECT) images objects using two X-rays incident beams of different energy to distinguish the different components within a sample based on their density (electron density, ρ_e) and elemental composition (effective atomic number, Z_{eff}). The stoichiometric calibration for DECT has already been successfully used to identify single and homogeneous minerals easily and non-destructively. Here it is used for the first time to explore the potential on a more complex and heterogeneous sample: a varved sediment core from South Sawtooth Lake in the Canadian Arctic, consisting of three distinct facies. The three facies can be successfully distinguished from each other using DECT thanks to their different range of their ρ_e and Z_{eff} values. Another scanning technique providing elemental composition of sediments was implemented: µXRF core scanner analysis was accomplished at the same resolution of CT-measurements. However, the correlation between the two scanning techniques is less conclusive,

likely because analyses were not performed at the exact same location of the core. Finally, the paper discusses the limitations using DECT on sediments, mainly the added complexity due to variations in grain size and porosity, but also demonstrates its potential to quantitatively study sediment cores in a non-destructive way.

3.3 Introduction

X-ray computed tomography was developed in the seventies by Godfrey Hounsfield and Allan MacLeod Cormack as a medical imaging technique to obtain images of the human body's interior. In a medical CT scanner, the X-ray source faces the detector and they rotate together around the patient and acquire bi-dimensional radiographic projections at various angles from 0° to 360°. These are processed by a mathematical algorithm (i.e., image reconstruction) to obtain a set of slices permitting a 3D reconstruction (Bushberg, 2012).

Although this technology originated for medical purposes, its potential was soon recognized and applied in several fields like archeology (Re et al., 2015), biology (Mizutani & Suzuki, 2012), wood technology (Onoe et al., 1983), palaeontology (Conroy & Vannier, 1987), marine science (Boespflug et al., 1995) and the geosciences as well (Baker et al., 2012; Coles et al., 1991; Griggs et al., 2015; Vinegar & Wellington, 1987).

A few years after its invention, Alvarez & Macovski (1976) elaborated the technique of Dual-Energy CT (DECT), which in this case consists of imaging a patient using both low and high X-ray energy spectra. This combination allows the discrimination and identification of objects based on their chemical composition and density, which ultimately is related to the differential contribution of photoelectric absorption and Compton scattering as a function of energy (Duchesne et al., 2009). Several groups have implemented DECT methods in the medical field to improve material characterization, e.g., Rutherford et al. (1976), Jackson and Hawkes (1981), Torikoshi (2003), Tsunoo et al. (2004), Bazalova et al. (2008).

Van Geet et al. (2000) applied DECT for the first time in the field of geology, adapting the mathematical formula previously developed by Coenen (1994): they quantified the chemical composition of reservoir rocks, hereafter expressed as effective atomic number (Z_{eff}), and electron density (ρ_e), the latter being, in general, directly proportional to the more common mass density. Then, several geologists conducted experiments to improve this technique for Earth science needs (Alves et al., 2015; Duliu et al., 2003; Iovea, 2006; Paziresh et al., 2016; Remeysen & Swennen, 2008).

These DECT techniques require an understanding of the properties of the incident X-ray beam spectra, which generally is difficult to calculate (Remeysen & Swennen, 2006). However, in the 2000s, medical physicists developed a DECT methods that did not require spectral information, facilitating the analysis (Bourque et al., 2014; Landry et al., 2013). Martini et al. (2021) applied for the first time one of these methods, specifically the stoichiometric calibration method, in the field of geology to identify common minerals.

This paper aims to test the method developed by Martini et al. (2021) on an unconsolidated, fine-grained sediment core from an Arctic varved lake (South Sawtooth Lake), and therefore significantly more compositionally, geochemically and granulometrically complex than the samples analyzed by Martini et al. (2021). The sedimentary record from South Sawtooth Lake allowed to perform a long annually reword paleoclimatic reconstruction for approximately the past three millennia (Lapointe et al., 2020). The succession consists of clastic varves interrupted by rapidly deposited layers (RDL) caused by occasional summer rain events (Lapointe et al., 2019). The goal of the present work is to test the capacity of the stoichiometric calibration method for DECT to discern clastic varves from RDL in a non-destructive way. Its potential in other sedimentary settings is discussed as well.

3.4 Materials and Methods

3.4.1 Core from South Sawtooth Lake

South Sawtooth Lake is located on the Fosheim Peninsula in the Eastern Canadian High-Arctic and contains a varved sequence that has previously been studied by other researchers (Francus et al., 2008; Lapointe et al., 2020; Lapointe et al., 2019; Lewis et al., 2005).

Sediments from the distal part of the basin are particularly interesting because they contain a robust 2900 years long paleoclimatic record (Lapointe et al., 2019). At this site, two main facies are reported. The first is clastic varves as defined by Zolitschka et al. (2015): this facies is from the product of the deposition related to snowmelt in the watershed and consists of medium to fine silt grading upward into a clay cap. Beds are typically less than a mm thick but can be up a few centimetres (Francus et al., 2008). The second facies occurs as interbeds of grain-supported sand-rich-laminae (RDL) that ranged from 0.1 and 13 mm thick. From their stratigraphic position, between the base of silt graded beds and their caps, it was established that they were deposited by resulting from debris flows from the slope surrounding the distal basin and triggered by rare summer rain events (Francus et al., 2008). Their chemical composition differs from the clastic varves, being richer in carbonate, which resembles the lithology in the surrounding slopes and is different from that in the reminder of the watershed. The 2 m long core investigated here (SS12-12-3-2P) was collected in 2012 using an Uwitech piston corer and analyses were performed on the intact archive half of the core.

3.4.2 Medical CT scanner

The medical CT scanner used in this work is a Siemens Somatom Definition AS+128 (Siemens healthcare GmbH, Erlangen, Germany), (Figure 3.1), located at the *Institut national de la recherche scientifique (INRS), Centre Eau Terre Environnement (ETE)*, Québec City Canada.

Figure 3.1 Siemens Somatom Definition AS+128.

It is located at *INRS-ETE*, Québec City Canada. An example of the sediment core being scanned is located in the gantry centre.

The instrument and the acquisition parameters are the same as those used by Martini *et al.* (2021) and are summarized in the following Table 3.1.

X-ray voltages	70 and 140 kV
Pitch factor	0.55
Current	495 mA
Beam collimation	12 mm
Detector	Stellar$^{\text{Infinity}}$ generation
Images acquisition mode	Spiral mode
Reconstruction method	ADMIRE
Reconstructed images	512 x 512 pixels
Voxel size	0.1 x 0.1 x 0.6 mm
Gray level scale	Extended scale, or 2^{16} gray levels
Reconstruction filter	D45s

Table 3.1: CT acquisition parameters.

3.4.3 Characterization method

The stoichiometric calibration protocol used here is briefly outlined below, but details can be found in the original publication (Martini et al., 2021). The method consists in accomplishing two successive calibrations: the first one characterizes the effective atomic number Z_{eff} and the second one the electron density ρ_e. First, the effective atomic number Z_{eff} and electron density ρ_e of a set of standard samples with known composition are calculated (Azevedo et al., 2016; Bonnin et al., 2014):

$$Z_{eff} = \sqrt[\beta]{\sum_i^N f_i Z_i^\beta} \tag{3.1}$$

$$\rho_e = \sum_{i=1}^N \frac{Z_i}{A_i} \rho \tag{3.2}$$

In Equation 3.1, fi is the fractional mass of element Z in the compound. The exponent β is a function of photon energy, sample materials, instrument and analytical settings specific (Alves et al., 2015; Azevedo et al., 2016; Landry et al., 2013) and can vary between 2.94 and 3.8 (Bonnin et al., 2014; Spiers, 1946). In Equation 3.2, A_i is the atomic mass of the element Z_i and ρ is the material mass density (g·cm^{-3}) (Azevedo et al., 2016; Manohara et al., 2008).

Second, the standard samples are scanned, according to acquisition condition described in Table 3.1, at 70 kV and 140 kV and the two material normalized linear attenuation coefficients (μ_{low} and μ_{high}) are calculated from *HU* values following Equation 3.3 (Boespflug *et al.*, 1995; Watanabe, 1999):

$$\mu = \frac{\mu_{sample}}{\mu_{water}} = \left(\frac{HU}{1000}\right) + 1 \tag{3.3}$$

Third, the Z_{eff} calibration procedure described in Martini *et al.* (2021) was performed, plotting the linear attenuation coefficients (Equation 3.3) ratio and the calculated Z_{eff} (Equation 3.1), obtaining a second-order polynomial data-driven empirical model.

$$Z_{eff} = a + b \cdot \left(\frac{\mu_{low}}{\mu_{high}}\right) + c \cdot (\frac{\mu_{low}}{\mu_{high}})^2 \tag{3.4}$$

Finally, ρ_e calibration is achieved plotting the ratio between measured μ (Equation 3.3) and standard samples ρ_e (Equation 2), normalized by water electron density ($\rho_{e\ water}$ = 3.34 E+23 e$^-$ ·cm^{-3}) and Z_{eff} determined in Equation 3.4:

$$\frac{\mu_{low\ or\ high}}{\rho_e/\rho_{e\ water}} = d + e \cdot Z_{eff} + f \cdot Z_{eff}^2 \tag{3.5}$$

Again, the data-driven empirical model is a second-order polynomial. Here, the μ value used in Equation 3.5 can equally be those obtained at low or high energy; it is also possible to use both equations to calculate ρ_e and average the outcomes.

The calibration materials, and consequently the two sets of coefficients, are the same as the ones of Martini *et al.* (2021) (Figure 3.2).

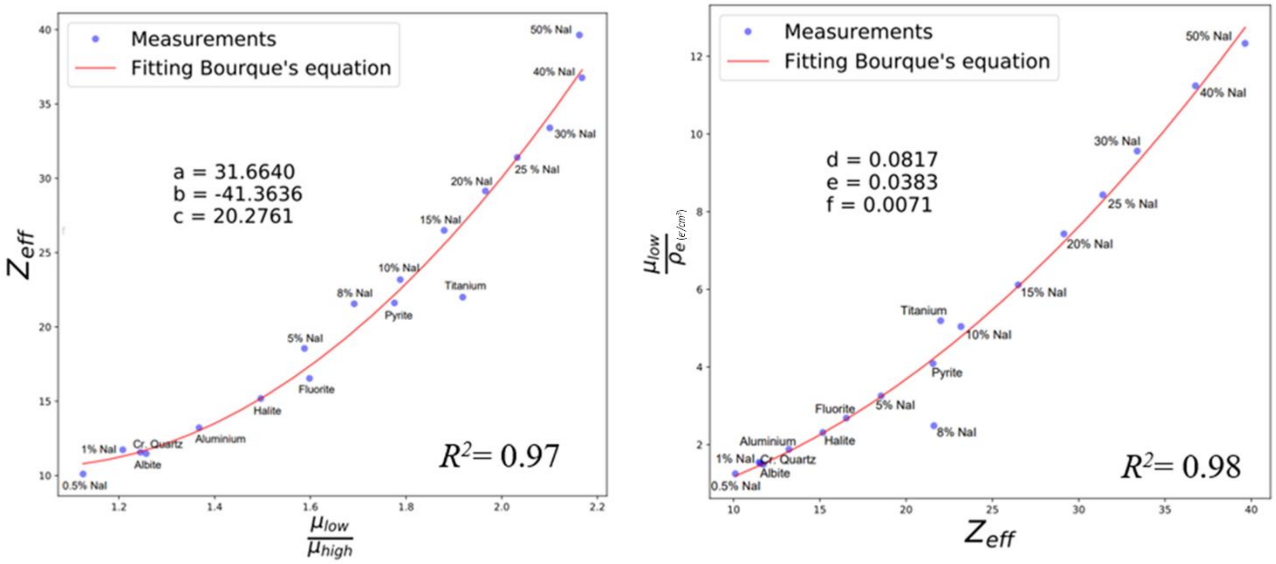

Figure 3.2: Calibration curves and their coefficients.

These two graphs are related to Equation 3.4 on the left and to Equation 3.5 on the right with the respective calibration curves (from Martini *et al*. 2021).

These equations are used to calculate both Z_{eff} and ρ_e for each voxel of each CT-slices (see below).

3.4.4 Selection of the region of interest

A single CT scan slice orientated perfectly perpendicular to the length of the sediment core and positioned in the centre of the core can include several layers, note that laminae along the margins of the core are commonly deformed during coring (Gallmetzer *et al.*, 2016).

Figure 3.3A shows the comparison between a high-resolution picture of the half-core surface and a CT coronal view (i.e. orthogonal to the core length) that was built stacking together the orthogonal slices from a volume within the half core using the software *SedCT* (Reilly *et al.*, 2017). Figure 3.3B shows a screenshot of a *SedCT* interface, where the core orthogonal axial slice is masked in white, and the red line shows the depth at which the CT coronal view was assembled.

The visible layers in the core picture and the CT image do not perfectly match because the core surface is irregular and has been manually smoothed to obtain a “clean surface”, erasing the desiccation cracks visible only in CT images that are assembled from an area located a few millimetres deeper than the core surface.

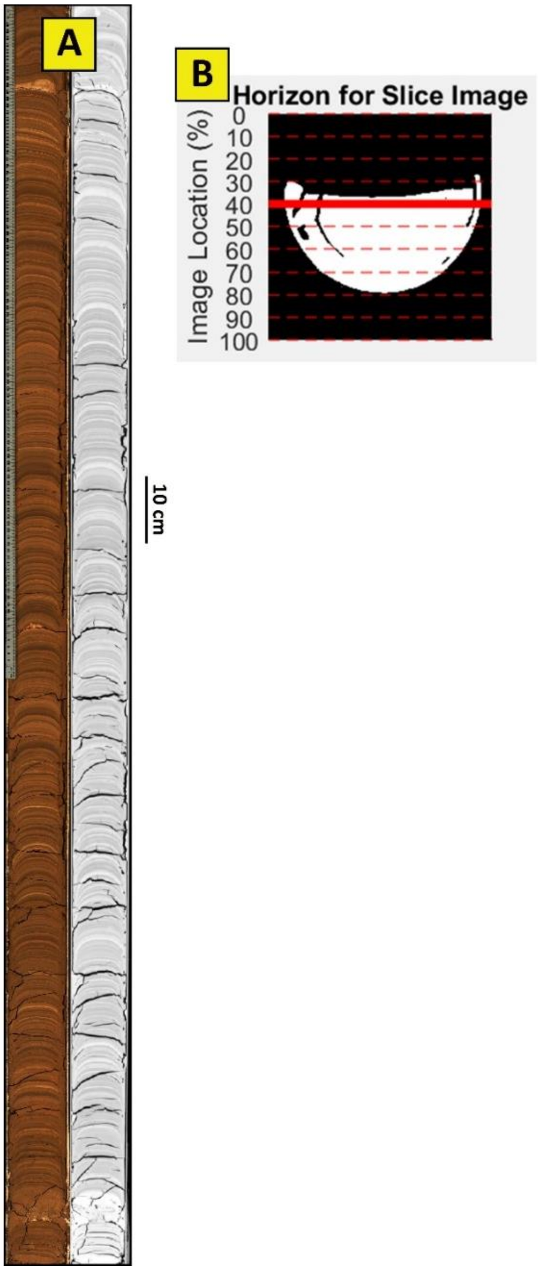

Figure 3.3: South Sawtooth core and axial slice mask.

A) high resolution picture of the half South Sawtooth core surface vs a CT coronal view; B) white mask of an axial slice of the core: the red line indicates the depth at which the CT coronal view was assembled with *SedCT*.

Hence, to mathematically subsample a single varve among the several layers present in only one perpendicular-to-bedding slice, a region of interest (ROI), where Z_{eff} and ρ_e are measured, needs to be defined along the core (Figure 3.4). Regions of interest are about 2 x 2 mm (i.e., 10 x 10 pixels) and were selected using *ImageJ* software in a central zone as close as possible to the half core surface to better compare DECT result with the geochemical measurements made at the surface of the core as described in section 3.4.5.

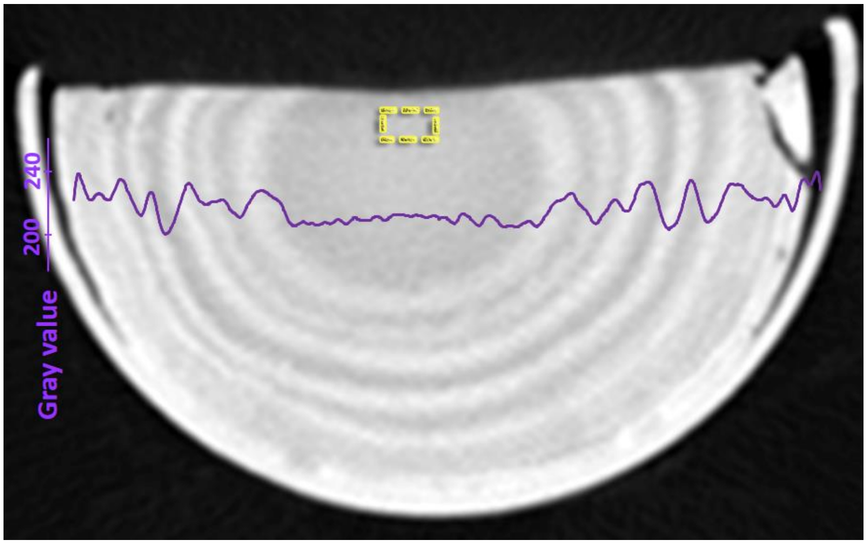

Figure 3.4: Core slice and ROI selection.

ROI selection in a CT scan slice of South Sawtooth core where the deformation caused by coring process is visible and several varves are present. The ROI selection and the gray value calculation were performed using *ImageJ* software.

Z_{eff} and ρ_e were calculated for each pixel of each CT scan ROI slice and then were averaged to obtain one value per slice. Subsequently, these averages will be used to report measurements.

3.4.5 µ-XRF

The ITRAX core scanner (Figure 3.5) located at *INRS-ETE*, Québec City, Canada, was used to measure the elemental variations along the core surface using the parameters outlined in Table 3.2. Chemical analysis, performed before the tomographic acquisition, were acquired at a similar resolution to the CT scans to facilitate their comparison with DECT inferred properties. Prior to measurements the surface of the core was gently scraped to provide the needed smooth surface for the detector (Cuven *et al.*, 2015).

Figure 3.5: ITRAX core scanner.

This instrument is located at *INRS-ETE*, Québec City Canada.

The acquisition parameters used here are summarized in the following Table 3.2.

Tube	Molybdenum
Resolution	600 µm
Exposure time	12 s
Voltage	40 kV
Current	10 mA
Count per second (CPS)	≈ 40000

Table 3.2: µ-XRF acquisition parameters.

Each energy dispersive spectrum was re-evaluated using Cox Analytical RediCore™ software (Löwemark *et al.*, 2019) and then elemental data were normalized by incoherent and coherent ratio (inc/coh), respectively related to Compton and Rayleigh scattering. This normalization allows to account for the matrix, mainly water content and density variations within the sediment (Kylander *et al.*, 2011).

3.4.6 Statistical analysis

The *R commander* package of the software *R* (Fox, 2016) was used to compute the Pearson correlation coefficients (*R*) and the respective pairwise *p*-values between the Itrax and DECT measurements. Then, the *Matplotlib* Python library was used to compute and plot box-and-whisker diagrams of the DECT measurements on the different sedimentological facies.

3.5 Results

Figure 3.6A shows the gray value, Z_{eff} and ρ_e profiles overlayed on the CT coronal view of the core. An enlightenment of a smaller section illustrates the variations at the varve scale: the profiles are interrupted where there is a fracture (i.e., no value) and their trends generally follow the varve boundaries. In those CT images, lighter grey values indicate higher X-rays attenuation due to the heavier/denser material, whereas Z_{eff} and ρ_e profiles have higher values in these intervals. The Itrax core scanner detected several chemical elements. Figure 3.6B shows the Ca profile that is of interest because of the rich carbonate content of the RDLs. The enlarged section shows that the Ca trend well follows the varve boundaries. This is even more clear in the case of the thicker RDL layers: the signal increases in the carbonate-rich layer, it decreases where there is the fracture, and it increases again in the lowest part of the RDL.

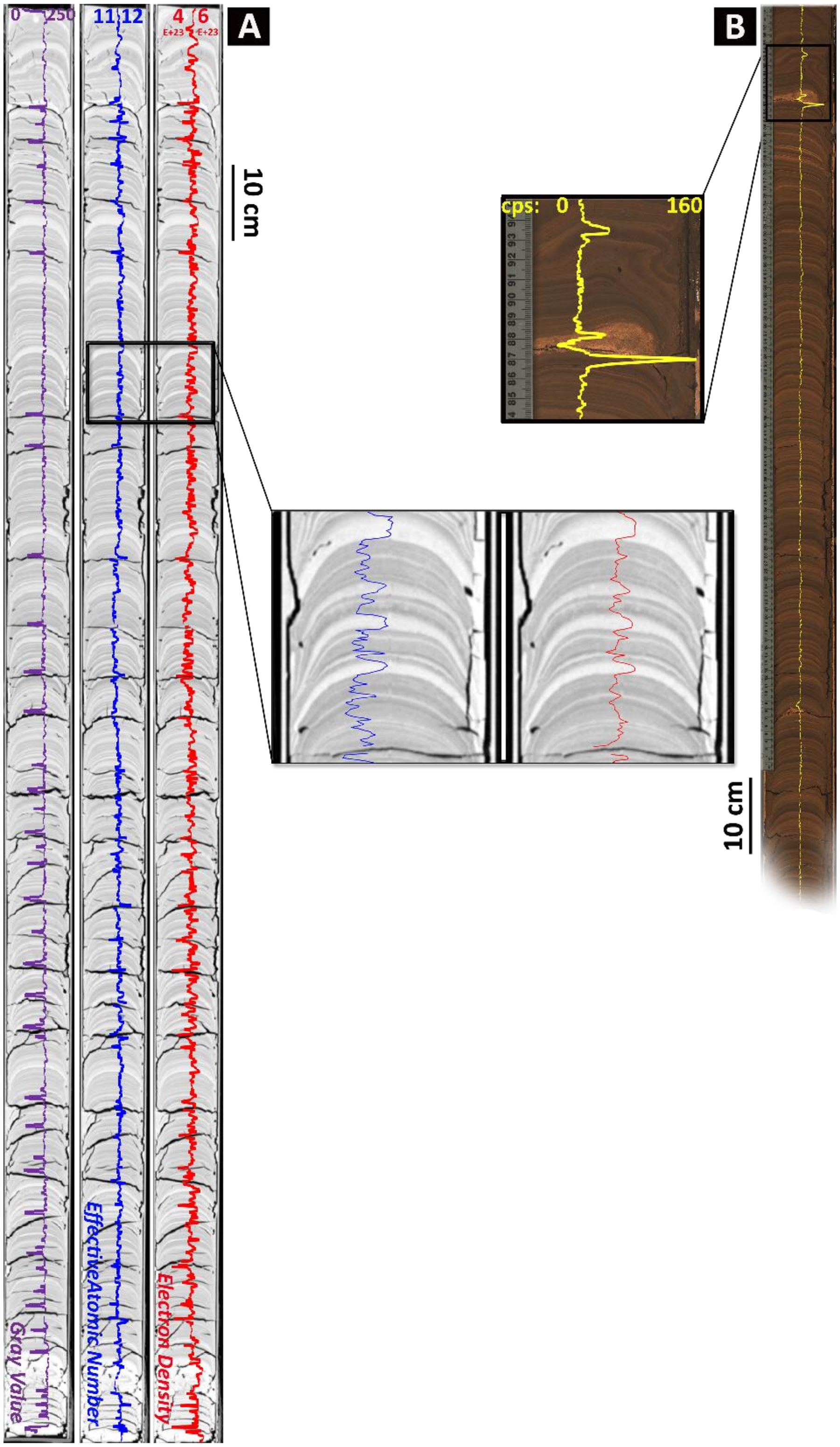

Figure 3.6: CT and Itrax profiles of South Sawtooth core.

A) Gray value (purple), Z_{eff} (blue) and ρ_e (red) profiles overlapped on the CT coronal view. B) Ca profile normalized by inc/coh (yellow curve) detected by Itrax.

The Pearson correlation coefficients R between Itrax and DECT inferred Z_{eff} and ρ_e along the entire core profiles and the respective pairwise p-values ranges are presented in Table 3.3.

	Ca	**Cr**	**Cu**	**Fe**	**Inc/Coh**	**K**	**Mn**	**Ni**	**Pb**	**Rb**	**Si**	**Sr**	**Ti**	**Zn**	**Zr**
ρ_e	0.33 ***	0.13 ***	0.05 **	0.23 ***	-0.33 ***	-0.11 ***	0.24 ***	0.17 ***	0.07 ***	-0.07 **	0.24 ***	0.17	0.35 ***	0.23 ***	0.16 ***
Z_{eff}	0.25 ***	0.1 ***	0.08 ***	0.31 ***	-0.22 ***	-0.01	0.19 ***	-0.04 *	0.06 **	0.03	0.08 ***	0.11 ***	0.28 ***	0.21 *	0.03

Table 3.3: Pearson correlation coefficients *R*.

Pearson correlation coefficients *R* between Itrax and DECT along the entire core profiles. Pairwise *p*-values are represented by stars: (*) <0.05; (**) < 0.01; (***) < 0.001; otherwise the *p*-value is >0.01.

Because the desiccation cracks made aligning the two datasets difficult, only easily recognizable layers in both techniques (as exemplified in the Figure 3.7) were qualitatively selected as archetypal samples of one of the three facies to perform the comparison between µ-XRF and DECT. Twenty-three clastic varves and fifteen RDLs were chosen, and clastic varves were split in two categories, based on their granulometry: fine-grained and coarse-grained.

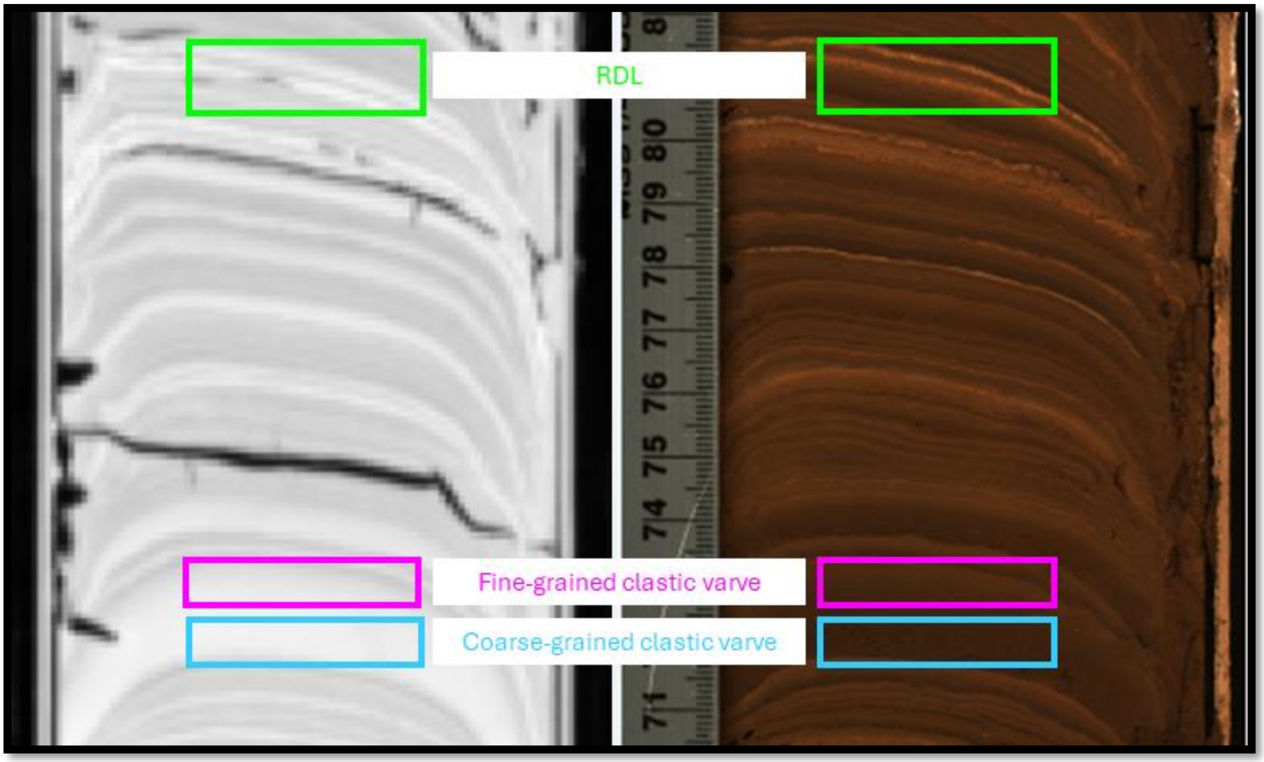

Figure 3.7: Example of archetypal layers.

They have been qualitatively selected as archetypal samples and are easily recognizable in both techniques.

Figure 3.8 shows an example of the layers that were used for this analysis in the upper part of the core: the white vertical line represents the point where the ROI was chosen and its intersection with the coloured horizontal lines (coarse-grained clastic varves in light blue, fine-grained clastic varves in fuchsia and RDL in green) is the exact layer that was used for this analysis.

The Pearson correlation coefficients and the respective pairwise *p*-values ranges performed on these 38 clearly identified layers are presented in Table 3.4.

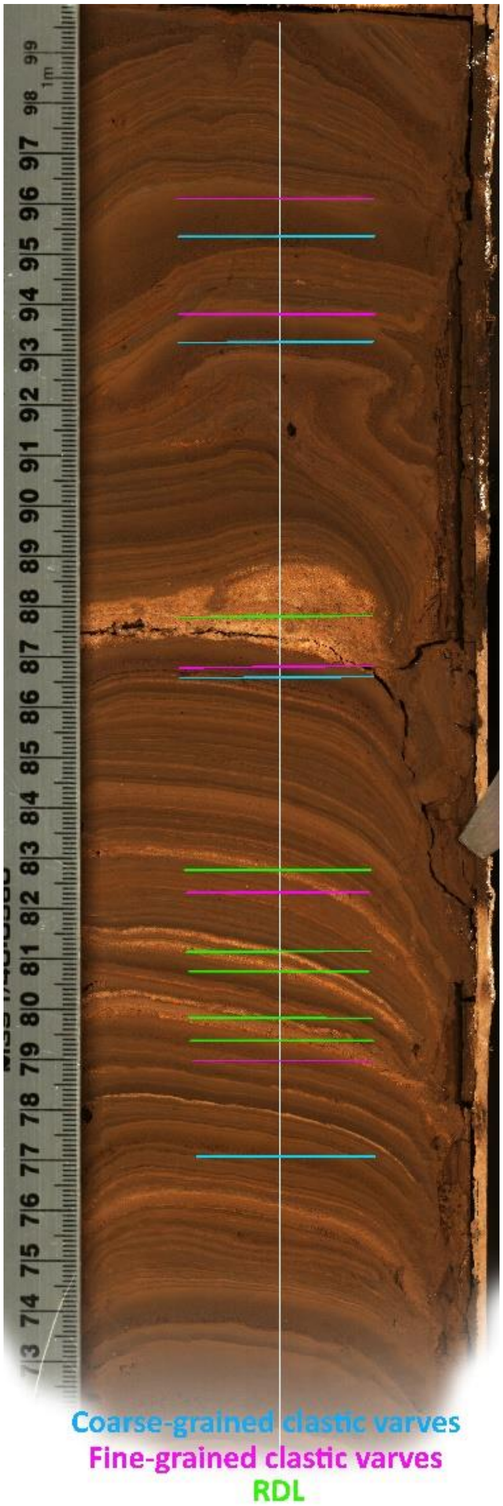

Figure 3.8: Example of the archetypal layers identification.

These layers have been chosen to be individually analyzed. The vertical white line represents the point where the ROI was chosen in archetypal coarse-grained clastic varves in light blue, fine-grained clastic varves in fuchsia and RDL in green. DECT and µXRF measurments taken into account in Table 3.4 have been performed where the white line of ROI crosses the coloured lines of layers.

	Coarse-grained clastic varves		**Fine-grained clastic varves**		**RDL**	
	ρ_e	Z_{eff}	ρ_e	Z_{eff}	ρ_e	Z_{eff}
Ca	0.43 ***	0.19 *	0.04	-0.23 *	0.19	0.48 ***
Cr	0.16	0.09	0.008	-0.01	-0.08	0.26
Cu	-0.0001	-0.04	-0.23 *	-0.005	0.11	0.16
Fe	0.37 ***	0.45 ***	0.26 *	0.14	-0.28 *	0.21
Inc/Coh	-0.27 **	-0.15	-0.29 **	0.19 *	-0.31 *	-0.06
K	0.09	0.19 *	-0.44 ***	0.16	0.19	-0.007
Mn	0.37 ***	0.17	0.14	-0.19	0.08	0.48 ***
Ni	0.19 *	0.12	0.19 **	-0.28 *	0.11	-0.26
Pb	0.0647	0.07	0.09	0.16	-0.11	0.13
Rb	-0.03	0.15	-0.16	0.13	-0.02	0.21
Si	0.36 ***	0.24 *	0.29 **	-0.24 *	0.21	-0.31 ***
Sr	0.009	-0.16 *	0.38 ***	-0.24 *	-0.24	-0.06 ***
Ti	0.36 ***	0.14 *	0.46 ***	-0.14 **	-0.27 *	0.19 ***
Zn	0.16	0.03	0.007	0.003	0.21	0.37 **
Zr	0.44 ***	0.11	-0.01	-0.31 **	0.47 *	0.29 *

Table 3.4: Correlation matrices between Itrax and DECT results.

These correlation matrices between Itrax and DECT results on selected sedimentological layers as examplified in Figure 3.8. Pairwise *p*-values are represented by stars: (*) <0.05; (**) < 0.01; (***) < 0.001; otherwise, the *p*-value is >0.01.

Then, Z_{eff} and ρ_e of each ROI voxel were represented in a box-and-whisker diagram to verify that the three facies, i.e. coarse-grained clastic varves, fine-grained clastic varves and RDL, can be identified based on their DECT properties (Figure 3.9).

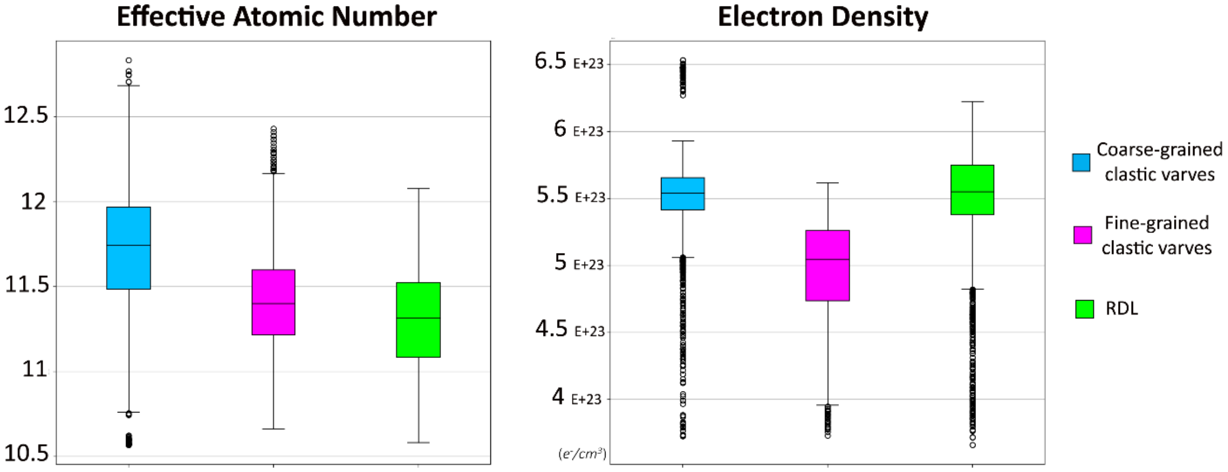

Figure 3.9: Z_{eff} and ρ_e box-and-whisker diagrams.

Coarse-grained clastic varves are represented in light blue, fine-grained clastic varves in fuchsia, and RDL in green. ρ_e is expressed in $e^{-}\cdot cm^{-3}$.

Figure 3.10 shows the image of a thin section and the Z_{eff} (blue) and ρ_e (red) profiles; the lower part is characterized by a thick RDL (green) where Z_{eff} is low, and ρ_e is high. This RDL is overlaid by a succession of fine-grained clastic varves (fuchsia), having slightly higher Z_{eff} values, while the ρ_e profile drops to the lowest values. Finally, the coarse-grained clastic varve (light blue) at the top is characterized by highest Z_{eff} values and increasing ρ_e values.

Figure 3.9 and Figure 3.10 show that the combination Z_{eff} and ρ_e values measured using DECT are different for the three main facies.

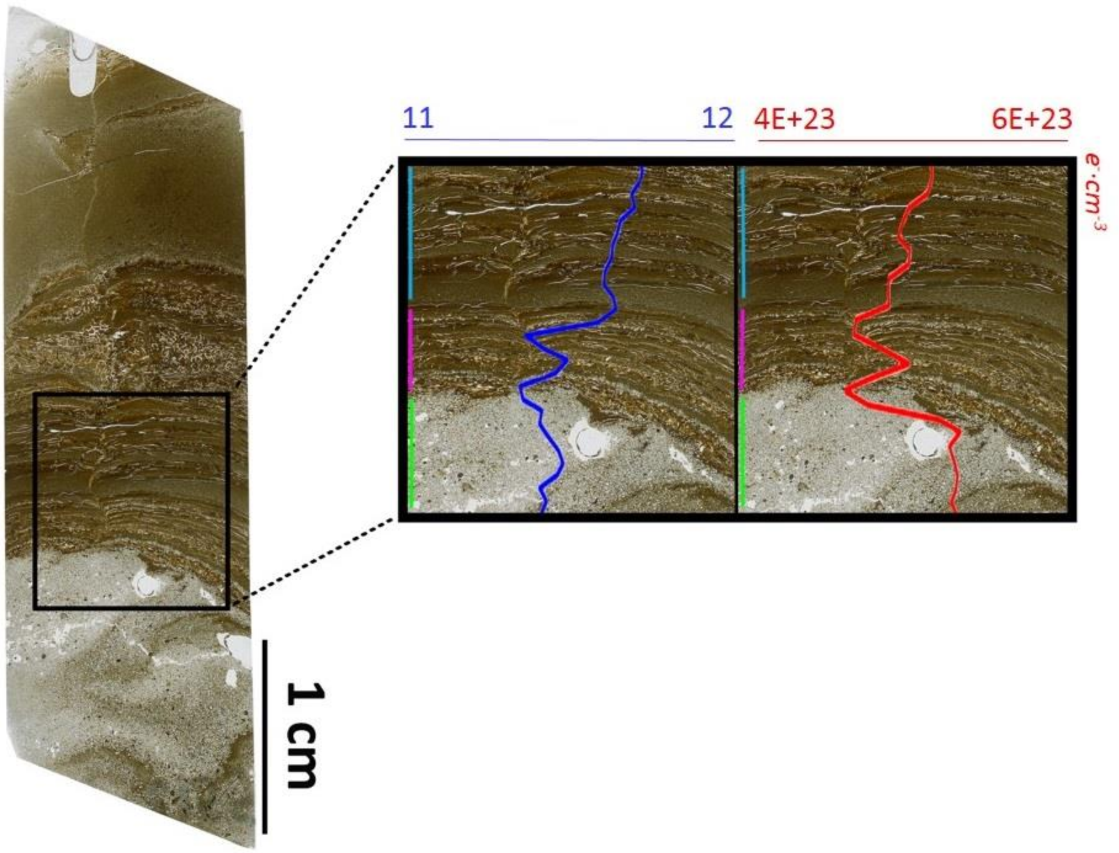

Figure 3.10: Thin section of South Sawtooth core.

It has been sampled in the upper part of the core where the *Z_{eff}* (blue) and *ρ_e* (red) expressed in *$e^{-}\cdot cm^{-3}$* profiles are overlapped. Vertical bars on the left shows the limits of the different facies (green, RDL; fuchsia, fine-grained varves; light blue, coarse-grained varves).

3.6 Discussion

3.6.1 DECT and chemical elements

DECT differentiated the three main facies based on their Z_{eff} and ρ_e but could not identify their chemical composition. Indeed, the Pearson correlation coefficients calculated along the entire core (Table 3.3) are relatively weak except for Ca, Ti and Inc/Coh versus ρ_e and Fe versus Z_{eff} that are above 0.3 and are highly significant with *p*-values <.0001.

The negative correlation between ρ_e and the ratio Inc/coh of the Itrax is meaningful because the latter is an indicator of the density of the sediment matrix (Croudace *et al.*, 2019). This observation in coherent with the study of Fortin *et al.*, (2013) that have reported a high correlaiton (i.e., 0.64) between the density measured by gamma ray attenuation and XRF coh/incoh in a long sediment core. Thus, the negative correlation between ρ_e and the Inc/coh ratio found in the present study is consistent. The relatively high correlation values of Ca, Ti and Fe with ρ_e and/or Z_{eff} can be explained by the fact that these elements are abundant (Lapointe *et al.*, 2019) in the South Sawtooth Lake sediments and are well detected by the Itrax.

The relatively weak correlations can be explained by several factors: first, it is impossible to perfectly align the two profiles because of the desiccation cracks and the slight changes due to the scraping of the surface in preparation for the Itrax analyses. Several attempts to realign the two datasets using the *QAS* software (Kotov & Pälike, 2019) were unsuccessful and hampered by the high frequency change in sediment elemental composition because of the varved nature of the sediment. Second, the Itrax measures the geochemistry at the surface of the core, whereas CT scanning is a 3D technique, so there will always be a mismatch between the analysed spots, which in turn make comparison difficult. Moreover CT scan images can be affected by beam hardening, an artefact that affects the attenuation profile, creating high- and low- attenuation artifacts in the image; it is caused by preferential attenuation of low energy photons biasing the reconstructed images quality mainly at the phase interfaces (Di Schiavi Trotta *et al.*, 2022b). In our case, beam hardening was relatively mild. Third, the core is very long, and the more than forty-five thousand data points reduce the calculated *R*, even if the *p*-values are significance. Indeed, the correlation is inversely related to the amount of data (i.e. the highest possible correlation is between two points, defining a linear relationship) and this effect is illustrated by the higher *R* values obtained with a reduced set of points in Table 3.4 (Benesty *et al.*, 2009). To improve the comparison between DECT and Itrax analyses and to reduce misalignment between the two datasets in the future, it is suggested to make CT-scans on unopened fresh cores that have been carefully oriented with marks to be able to cut the cores in two halves along a known plane for the subsequent XRF analysis. The latter should be performed immediately thereafter to avoid any shrinkage or motion of the sediment within the core liner. Moreover, CT scanning again the opened core halves would be useful for verification purposes.

As illustrated in Figure 3.9, the three different sedimentological facies can be discriminated by a combination of the two properties measured and calculated using DECT.

Coarse-grained clastic varves have the highest mean Z_{eff} of the three facies probably because they are enriched in elements with high atomic number. They also have a high average ρ_e value that is generally proportional to mass density, a characteristic that is consistent with high HU values observed on single energy CT images of this facies. Ti and Si ($R = 0.36$) are often linked with clastic input (Balascio & Bradley, 2012; Kylander *et al.*, 2011; McWethy *et al.*, 2010) in Arctic settings devoid of diatoms. Moreover, as reported by Lapointe *et al.* (2020), Ti is a proxy for summer temperature at South Sawtooth Lake and its good correlation with CT properties may be an opportunity to use DECT for paleoclimate reconstructions. Calcium and Fe also have a strong correlation with ρ_e in coarse-grained clastic varves (R = 0.43 and 0.37 respectively); these elements are reported to covary with Si and Ti (Lapointe *et al.* (2020), and hence are also related to detrital input. While Zr is present in trace amount in the sediments, and therefore is not responsible for the high mean Z_{eff} and ρ_e values to higher values, it is interesting to note that it has a good correlation (R=0.44) with ρ_e in the coarse-grained clastic varves facies (Table 3.4), but this correlation does not occur in fine-grained clastic varves. Manganese is more difficult to interpret because if its redox sensitivity (Lapointe *et al.*, 2019).

Fine-grained clastic varves have the lowest ρ_e (Figure 3.9), which is consistent with the low attenuation values (low HU values) in the CT scans. Titanium is better correlated to Z_{eff} in the this fine-grained facies compared to coarse-grained clastic varves, which is consistent with observations made with Itrax and scanning electron microscope (Lapointe *et al.*, 2019) that shows the highest Ti content in medium silts layers. Potassium is negatively correlated to ρ_e, which is surprising because this element is linked to the clay cap of these clastic varves (Cuven *et al.*, 2010; Lapointe *et al.*, 2019).

Figure 3.9 shows RDLs have Z_{eff} values similar to fine-grained clastic varves and ρ_e values similar to coarse-grained clastic varves. Again, high density values are also registered by the CT in these layers. More intriguing is the low Z_{eff} value in RDLs because these layers are rich in carbonate and theoretical Z_{eff} of calcite (15.07) is higher than quartz (11.56). The presence of carbonates is confirmed by the good correlation between Ca and Z_{eff} (R = 0.48). A possible explanation for the low average Z_{eff} values of the RDL resides in the heterogeneity of this sedimentary layer: the carbonate presence could increase the Z_{eff} value, but this facies is characterized by large intergranular spaces that are either empty, or filled in with grains composed of lighter elements (Francus *et al.*, 2008).

The lowest ρ_e encountered in fine-grained clastic varves could be counterintuitive and against the fact that a volume filled with smaller grains entails fewer intergranular spaces, and therefore should be denser. However, the thin0-section view shows a lot of cracks in the fine-grained clastic varves (Figure 3.11) likely lowering the ρ_e density value. Figure 3.11 shows the boundary between RDL and fine-grained clastic varves at the scanning electron microscopy (SEM). Note that these cracks are likely due to the making of thin-sections, but the average density of the whole area should be similar to the one of the original pristine facies.

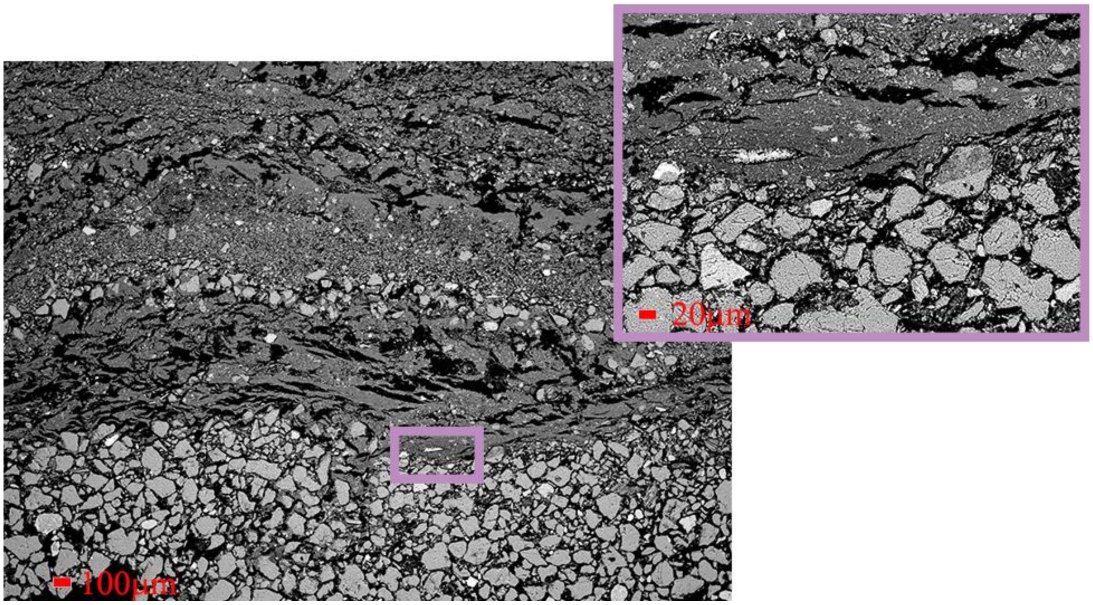

Figure 3.11: SEM image of layer boundary.

Boundary between RDL and fine-grained clastic varves acquired by scanning electron microscopy (SEM). The intergranular space of RDL is not empty but filled with finer sediments.

3.6.2 Facies identification

The possibility to distinguish the three facies only based on DECT was tested using only the voxel values between first and third quartiles of the boxplot in Figure 3.9 (Table 3.5).

Facies	Z_{eff}	ρ_e ($e^{-} \cdot cm^{-3}$)
Coarse-grained clastic varves	11.49 - 11.99	5.42E+23 - 5.65E+23
Fine-grained clastic varves	11.22 - 11.61	4.74E+23 - 5.26E+23
RDL	11.08 - 11.53	5.38E+23 - 5.75E+23

Table 3.5: DECT properties and quartiles.

Classification of the three different facies based on the first and third quartile values (Figure 3.9) of Z_{eff} and ρ_e.

The result of this classification is outlined in Figure 3.12 on a section of a sediment core. Each point corresponds to a voxel on which this calculation has been performed Figure 3.12; about 6% of the voxels are identified as coarse-grained clastic varves, about 62% as fine-grained clastic varves and about 16% as RDL. Moreover about 14% is empty and these gaps represent the whiskers and the outliers visible in the boxplots of Figure 3.9

.

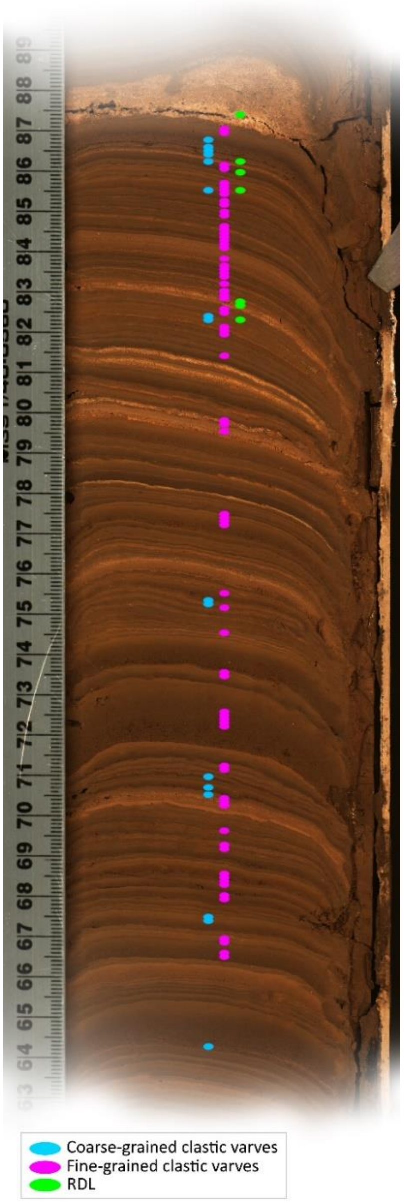

Figure 3.12: DECT properties and quartiles.

Coarse-grained clastic varves (light blue), fine-grained clastic varves (fuchsia) and RDL (green) identified from the statistical property values of first and third quartiles from box-and-whisker diagram, and overlain on a section of core.

This facies classification based on DECT method can be accomplished in 3D as well. First, the grey values of the slices were segmented according to the values in Table 3.5 and then the slices were stacked (Figure 3.13). Again, the inner empty parts (in black) are the whiskers and the outliers visible in the boxplots of Figure 3.9.

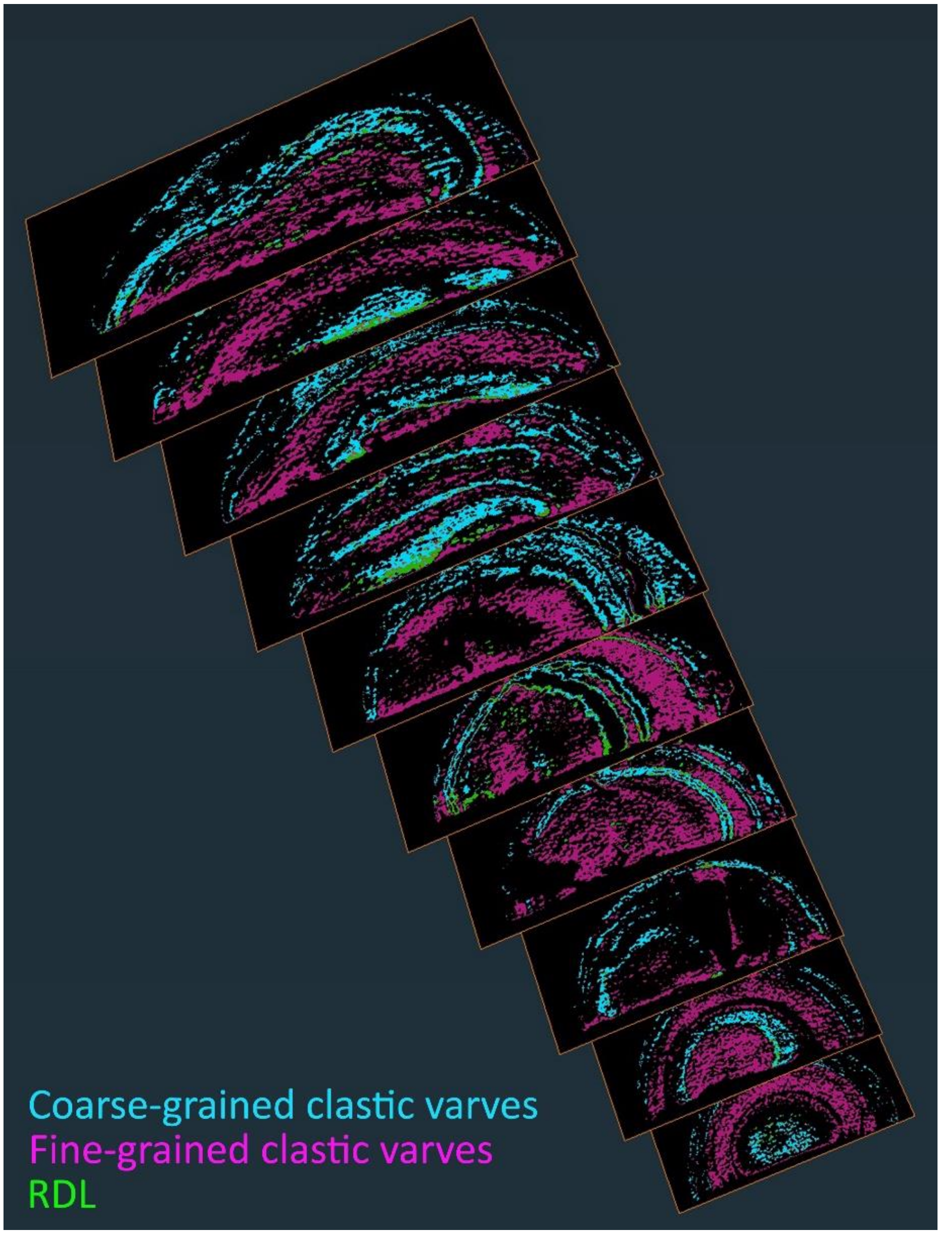

Figure 3.13: DECT properties and quartiles in 3D.

Stack of slices for the 3D volume reconstruction where the three different facies are identified according to DECT values reported in Table 3.5. Coarse-grained clastic varves are in light blue, fine-grained clastic varves in fuchsia and RDL in green.

Stacking all the slices is also possible to build up the entire volume of the segmented facies; Figure 3.14 shows the 3D reconstruction of a core section (on the right) where the different sedimentological layers are well visible and reflect the reality of the high-resolution picture (on the left side).

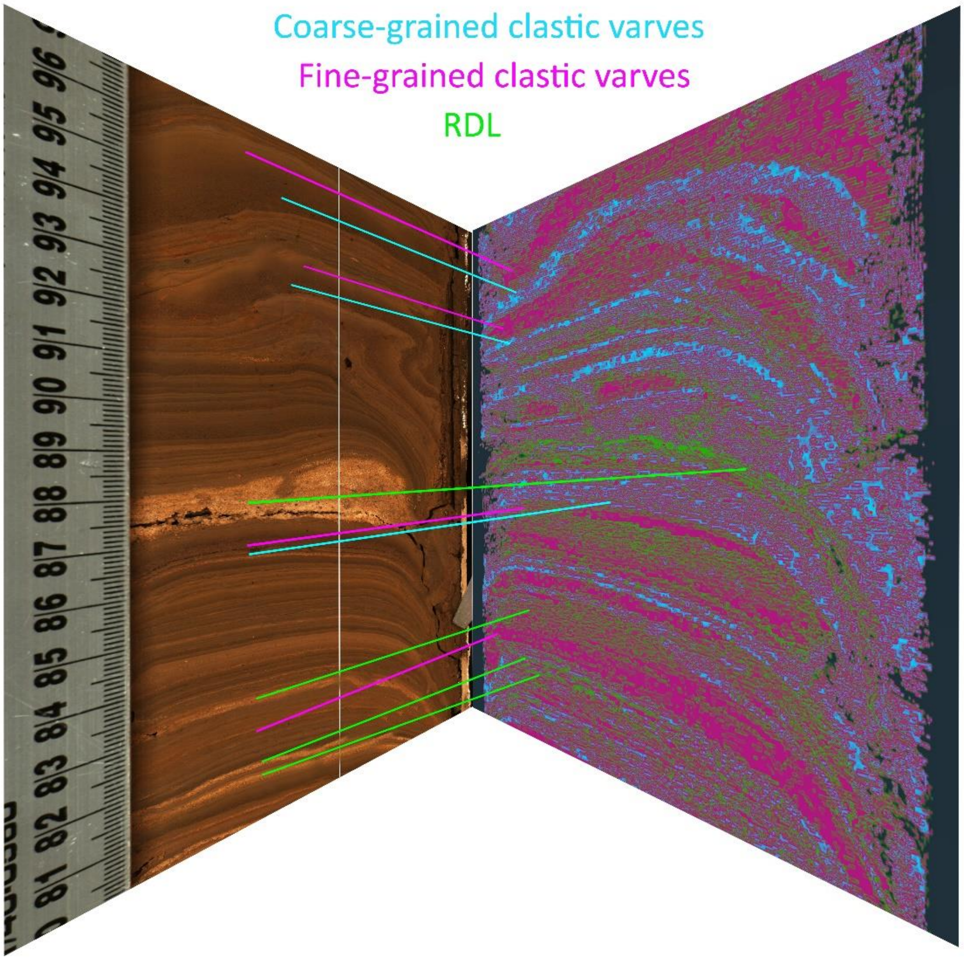

Figure 3.14: DECT validation: high resolution picture.

High resolution picture where the three facies are highlighted on the left and segmented facies in 3D on the right. Again, the facies are identified according to DECT values reported in Table 3.5 and coarse-grained clastic varves are in light blue, fine- grained clastic varves in fuchsia and RDL in green.

To further validate our approach the grain-size measured by Lapointe *et al.* (2019) on single layers using image analysis of SEM images was compared with the facies classification by DECT. Figure

3.15 shows that the coarsest grains, i.e. the 99th percentile and the median, are found in the layers identified as RDL, while the finest grain-size are found in the layers identified as fine clastic varves.

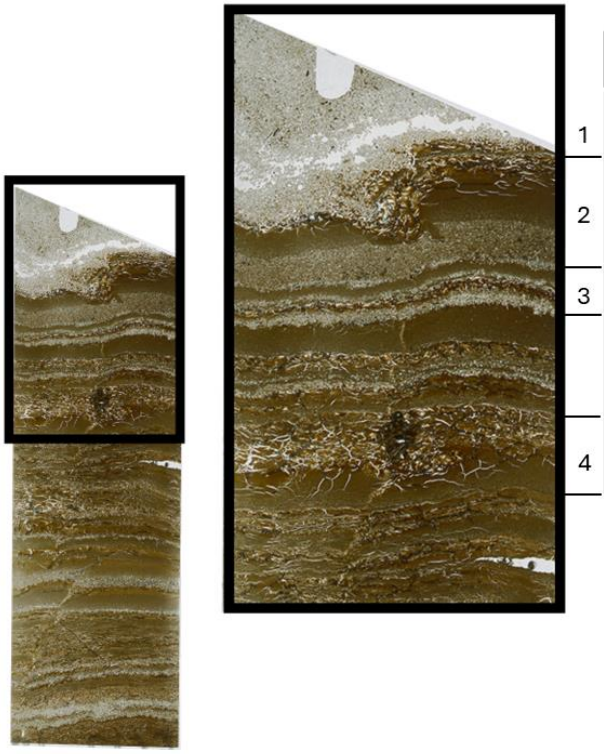

	Varve Thickness	Granulometry (median)	Percentile 99	DECT
1	28.69 mm	≈ 11.7 µm	≈139.24 µm	RDL
2	4.44 mm	≈ 5.5 µm ≈7.9 µm ≈ 6.9 µm	≈ 21.97 µm ≈ 43.32 µm ≈ 42.61 µm	Fine Coarse Coarse
3	2.49 mm	≈ 7.7 µm	≈ 71.73 µm	Coarse
	-	-	-	-
4	3.33 mm	≈ 5.4 µm	≈ 16.32 µm	Fine

Figure 3.15: DECT validation: granulometry.

DECT facies classification compared to granulometry analyses from Lapoine *et al.* (2019). It was not possible to make this comparison on the layers thinner than 1 mm, because each individual CT slices is 600 µm thick, precluding a good alignment between the two datasets.

Recognizing the three facies might be of interest for paleoclimatic reconstructions, but its application to other fields of Earth Science is not excluded. In this example, RDLs are interpreted as summer rain events, rich in Ca. As reported in Lapointe *et al.* (2019) an increasing grain size and Ca over the last few hundred years would be due to an increase in summer rainfall, an interpretation consistent with progressive climate warming. However, using the Ca profile acquired by the Itrax alone does not uniquely identify an RDL since Ca enrichment is also associated with coarse grained varves. RDL characterisation is relevant for paleoclimatic studies at this site, and this task seems to be possible with DECT.

This DECT approach to identify sediment facies remains in its infancy because several questions remain. For instance, in our example, there are opposing effect between grain size and the presence of minerals with heavier elements on the values of Z_{eff} and ρ_e. Applying the DECT technique to artificial samples with known granulometry, porosity and mineralogy should help disentangle the complexity in natural samples.

3.7 Conclusion

Dual-energy CT stoichiometric calibration is here applied for the first time on a sample as complex as a varved sediment core. This sedimentary sequence contains three main facies, i.e. fine-grained clastic varves, coarse-grained clastic varves and grain-supported sand-rich-laminae rapidly deposited layers. DECT was able to differentiate the three main facies based on their unique combination of Z_{eff} and ρ_e. Significant correlations were found between these two properties and some elements measured by µ-XRF at the same resolution, but it was not possible to infer the exact chemical composition of the facies.

Stoichiometric calibration DECT has the advantage to be quick, non-destructive and to perform the analysis in 3D.

In this test sample, the identification of RDL has interesting prospects as this facies was not unambiguously identified by other scanning techniques such as single energy CT scans and µ-XRF, and has an interesting paleohydrological signature that could be useful in future paleoclimatic studies.

Although this method is still in its infancy and more tests are required to better explore the combined effects of porosity, permeability and grain-size variations on the outcomes of DECT, this paper paves the way for a new approach in sedimentological studies.

3.8 Acknowledgements

This research was funded by *Fonds de recherche du Québec–Nature et technologies*, *Natural Sciences and Engineering Research Council of Canada*, *Canada Research Chairs Program* and *Fonation canadienne pour l’innovation*. We would like to thank Arnaud De Coninck, Léo Chassiot and Tiziano Michelessi for their support and advice during data analysis and production of figures.

3.9 Data Availability Statement

The Python codes allowing to perform the DECT profiles of Z_{eff} and ρ_e (Figure 3.6) and the 3D volume reconstruction where the three different facies are identified (Figure 3.12) are available in the Chapter 8, Annexe II, and at the *Borealis* repository: https://doi.org/10.5683/SP3/RRS4DO

3.10 References

Akbari A. GS (2015) Micro-CT scanning of soil aggregate: the importance of image thresholding. in *2nd International Conference on Tomography of Materials and Structures*Québec, QB, Canada), p 622-626.

Alenezi M *et al.* (2018) Klein–Nishina electronic cross-section, Compton cross sections, and buildup factor of wax for radiation shielding and protection. *Journal of Radiological Protection* 38(1):372.

Alvarez RE, Macovski A (1976) Energy-selective reconstructions in X-ray computerized tomography. *Physics in Medicine & Biology* 21(5):733-744.

Alves H *et al.* (2014a) Comparison of pore space features by thin sections and X-ray microtomography. *Applied Radiation and Isotopes* 94:182-190.

Alves H *et al.* (2015) Mineralogy evaluation and segmentation using dual-energy microtomography. *X-Ray Spectrometry* 44(3):99-104.

Alves H, Lima I, Lopes RT (2014b) Methodology for attainment of density and effective atomic number through dual energy technique using microtomographic images. *Applied Radiation and Isotopes* 89:6-12.

Arnold J *et al.* (1983) Computed tomographic analysis of meteorite inclusions. *Science* 219(4583):383-384.

Azevedo SG *et al.* (2016) System-Independent Characterization of Materials Using Dual-Energy Computed Tomography. *IEEE TRANSACTIONS ON NUCLEAR SCIENCE* 63(1):341-350.

Baker DR *et al.* (2012) An introduction to the application of X-ray microtomography to the three-dimensional study of igneous rocks. *Lithos* 148:262-276.

Balascio NL, Bradley RS (2012) Evaluating Holocene climate change in northern Norway using sediment records from two contrasting lake systems. *Journal of Paleolimnology* 48(1):259-273.

Barron A (2023) Applications of Microct Imaging to Archaeobotanical Research. *Journal of Archaeological Method and Theory* 10.1007/s10816-023-09610-z.

Bazalova M *et al.* (2008) Tissue segmentation in Monte Carlo treatment planning: a simulation study using dual-energy CT images. *Radiotherapy and Oncology* 86(1):93-98.

Bendle JM, Palmer AP, Carr SJ (2015) A comparison of micro-CT and thin section analysis of Lateglacial glaciolacustrine varves from Glen Roy, Scotland. *Quaternary Science Reviews* 114:61-77.

Benesty J *et al.* (2009) Pearson Correlation Coefficient. *Noise Reduction in Speech Processing*, Processing STIS (Édit.) Vol 2. p 1-4.

Boespflug X, Long BFN, Occhietti S (1995) Cat-Scan in Marine Stratigraphy - a Quantitative Approach. *Marine Geology* 122(4):281-301.

Boespflug X *et al.* (1994) Tomodensitométrie axiale: relation entre l'intensité tomographique et la densité de la matière. *Canadian Journal of Earth Sciences* 31(2):426-434.

Bonnin A *et al.* (2014) Concept of effective atomic number and effective mass density in dual-energy X-ray computed tomography. *Nuclear Instruments and Methods in Physics Research Section B: Beam Interactions with Materials and Atoms* 318:223-231.

Bourgault P (2017) *De la boîte noire à la science: reconstruction tomographique contrôlée.* INRS, p

Bourque AE, Carrier JF, Bouchard H (2014) A stoichiometric calibration method for dual energy computed tomography. *Physics in Medicine & Biology* 59(8):2059-2088.

Brabant L *et al.* (2012) A novel beam hardening correction method requiring no prior knowledge, incorporated in an iterative reconstruction algorithm. *NDT & E International* 51:68-73.

Brunelle CB *et al.* (2016) Combining CT scan and particle imaging techniques: applications in geosciences. *article de conférence, 4 th International conference on image formation in X-ray computed tomography, Bamberg, Allemagne.*

Brunelle CB, Des Roches M., Daigle L-F., Francus P., Long B., Després P. (2016) Combining CT scan and particle imaging techniques: applications in geosciences. in *The 4th International Conference on Image Formation in X-Ray Computed Tomography*Bamberg, Germany), p 225-228.

Bushberg JT, Seibert, J.A., Leidholdt, E.M., Boone, J.M. (2012) *The essential physics of medical imaging.* LWW, Third edition

Butler BM, Hillier S (2021) powdR: An R package for quantitative mineralogy using full pattern summation of X-ray powder diffraction data. *Computers & Geosciences* 147.

Cnudde V, Boone MN (2013) High-resolution X-ray computed tomography in geosciences: A review of the current technology and applications. *Earth-Science Reviews* 123:1-17.

Cnudde V *et al.* (2006) Recent progress in X-ray CT as a geosciences tool. *Applied Geochemistry* 21(5):826-832.

Coenen J, Maas J (1994) Material classification by dual-energy computerized X-ray tomography. *International Symposium on Computerized Tomography for Industrial Applications.* p 8-10.

Coenen JCG, Maas J. (1994) Material classification by dual-energy computerized x-ray tomography. in *International symposium on computerized tomography for industrial applications*), p 120–127.

Coolens C, Childs PJ (2003) Calibration of CT Hounsfield units for radiotherapy treatment planning of patients with metallic hip prostheses: the use of the extended CT-scale. *Phys Med Biol* 48(11):1591-1603.

Coolidge WD (1913) A Powerful Röntgen Ray Tube with a Pure Electron Discharge. *Physical Review* 2(6):409-430.

Cormack AM (1963) Representation of a Function by Its Line Integrals, with Some Radiological Applications. *Journal of Applied Physics* 34(9):2722-2727.

Croudace IW *et al.* (2019) Current perspectives on the capabilities of high resolution XRF core scanners. *Quaternary International* 514:5-15.

Cuven S *et al.* (2015) Optimization of Itrax Core Scanner Protocols for the Micro X-Ray Fluorescence Analysis of Finely Laminated Sediment: A Case Study of Lacustrine Varved Sediment from the High Arctic. *Micro-XRF Studies of Sediment Cores,* (Developments in Paleoenvironmental Research, Research DIP (Édit.) Springer, Vol 14. p 279-303.

Cuven S, Francus P, Lamoureux SF (2010) Estimation of grain size variability with micro X-ray fluorescence in laminated lacustrine sediments, Cape Bounty, Canadian High Arctic. *Journal of Paleolimnology* 44(3):803-817.

Dernaika M (2013) Improved Rock Characterization by Dual Energy CT Scanning: Applications in Various Worldwide Formations.).

Di Schiavi Trotta L *et al.* (2022a) Beam-hardening corrections through a polychromatic projection model integrated to an iterative reconstruction algorithm. *NDT & E International* 126.

Di Schiavi Trotta L *et al.* (2022b) Beam-hardening corrections through a polychromatic projection model integrated to an iterative reconstruction algorithm. *NDT & E International* 126:102594.

Duchesne MJ *et al.* (2009) A rapid method for converting medical Computed Tomography scanner topogram attenuation scale to Hounsfield Unit scale and to obtain relative density values. *Engineering Geology* 103(3-4):100-105.

Duliu OG, Rizescu CT, Ricman C (2003) Dual energy gamma-ray axial computer tomography investigation of some metamorphic and sedimentary rocks. *Neues Jahrbuch fòr Geologie und Paläontolgie* 228(3):343-362.

Eberl DD (2003) User Guide to RockJock - A Program for Determining Quantitative Mineralogy from X-Ray Diffraction Data. 10.3133/ofr200378.

Elliott JC, Dover S (1982) X-ray microtomography. *Journal of microscopy* 126(2):211-213.

Fortin D *et al.* (2013) Destructive and non-destructive density determination: method comparison and evaluation from the Laguna Potrok Aike sedimentary record. *Quaternary Science Reviews* 71:147-153.

Fourie S (1974) THE CRANIAL MORPHOLOGY OF THRINAXODON LIORTHINUS SEELEY. *Annals of the South African Museum* 65:337-400.

Fox J (2016) *Using the R Commander.* Chapman and Hall/CRC Press. https://socialsciences.mcmaster.ca/jfox/Books/RCommander/

Francus P *et al.* (2008) Limnological and sedimentary processes at Sawtooth Lake, Canadian High Arctic, and their influence on varve formation. *Journal of Paleolimnology* 40(3):963-985.

Gagnon-Poiré A *et al.* (2021) Reconstructing past hydrology of eastern Canadian boreal catchments using clastic varved sediments and hydro-climatic modelling: 160 years of fluvial inflows. *Climate of the Past* 17(2):653-673.

Gaillot P, Duchesne MJ, Blum P (2020) Automatic Data Reduction and Quantification of X-Ray Computed Tomography Images of Sedimentary Cores: Method and Illustration. *Open Journal of Geology* 10(08):874-899.

Gallmetzer I *et al.* (2016) An innovative piston corer for large-volume sediment samples. *Limnology and Oceanography Methods* 14(11):698-717.

Gordic S *et al.* (2014) Advanced modelled iterative reconstruction for abdominal CT: qualitative and quantitative evaluation. *Clinical Radiology* 69(12):e497-504.

Haghighi RR *et al.* (2011) X-ray attenuation coefficient of mixtures: inputs for dual-energy CT. *Medical physics* 38(10):5270-5279.

Hainsworth J, Aylmore L (1983) The use of computer assisted tomography to determine spatial distribution of soil water content. *Soil Research* 21(4):435-443.

Hall-Edwards J (1901) The X Rays in the Diagnosis of Fractures. *British Medical Journal* :1645-1646.

Hazra A (2017) Using the confidence interval confidently. *Journal of thoracic disease* 9(10):4125-4130.

Helliwell JR *et al.* (2013) Applications of X-ray computed tomography for examining biophysical interactions and structural development in soil systems: a review. *European Journal of Soil Science* 64(3):279-297.

Hendee WR, Ritenour, E.R. (2002) *Mediacal Imaging Physics.* A JOHN WILEY & SONS, INC., PUBLICATION, USA, fourth

Hounsfield G (1972) A method of and apparatus for examination of a body by radiation such as X-ray or gamma radiation, The Patent Office, London, England. *British Patent Number GB1283915*.

Hsieh J (2009) *Computed Tomography: principles, design, artifacts and recent advances.* 2009004797, second

Iovea M, Neagu M., Duliu O.G., Oaie G., Ricman C., Mateiasi G. (2006) Dual-Energy Computer Tomography and Digital Radiography Investigation of Organic and Inorganic Materials. in *ECNDT*).

Iovea M *et al.* (2009) Dual-energy X-ray computer axial tomography and digital radiography investigation of cores and other objects of geological interest. *Engineering Geology* 103(3-4):119-126.

Jackson DF, Hawkes DJ (1981) X-ray attenuation coefficients of elements and mixtures. *Physics Reports* 70(3):169-233.

Jussiani EI, Appoloni CR (2015) Effective atomic number and density determination of rocks by X-ray microtomography. *Micron* 70:1-6.

Jussiani EI, Appoloni, C. R. (2015) Effective atomic number and density determination of rocks by X-ray microtomography. *Micron* 70:1-6.

Kalender W (2011) *Computed tomography : fundamentals, system technology, image quality, applications.* Wiley-VCH, Weinheim, 3rd rev.

Kalender WA (2006) X-ray computed tomography. *Physics in Medicine & Biology* 51(13):R29-43.

Keller AA (1997) High resolution cat imaging of fractures in consolidated materials. *International Journal of Rock Mechanics and Mining Sciences* 34(3-4):155.e151-155.e116.

Ketcham RA, Carlson WD (2001) Acquisition, optimization and interpretation of X-ray computed tomographic imagery: applications to the geosciences. *Computers & Geosciences* 27(4):381-400.

Kotov S, Pälike H (2019) QAnalySeries – a cross-platform time series tuning and analysis tool.).

Kylander ME *et al.* (2011) High-resolution X-ray fluorescence core scanning analysis of Les Echets (France) sedimentary sequence: new insights from chemical proxies. *Journal of Quaternary Science* 26(1):109-117.

Landry G *et al.* (2013) Deriving effective atomic numbers from DECT based on a parameterization of the ratio of high and low linear attenuation coefficients. *Physics in Medicine & Biology* 58(19):6851-6866.

Lapointe F *et al.* (2020) Annually resolved Atlantic sea surface temperature variability over the past 2,900 y. *Proceedings of the National Academy of Sciences* 117(44):27171-27178.

Lapointe F *et al.* (2019) Chronology and sedimentology of a new 2.9 ka annually laminated record from South Sawtooth Lake, Ellesmere Island in this NOAA depository: https://www.ncdc.noaa.gov/paleo/study/33214. *Quaternary Science Reviews* 222.

Larmagnat S *et al.* (2019) Continuous porosity characterization: Metric-scale intervals in heterogeneous sedimentary rocks using medical CT-scanner. *Marine and Petroleum Geology* 109:361-380.

Lisson K *et al.* (2023) *An integrated methodology of micro-CT and thin-section analysis for paleoflow reconstructions in lacustrine event deposits.* Copernicus Meetings, p

Löwemark L *et al.* (2019) Practical guidelines and recent advances in the Itrax XRF core-scanning procedure. *Quaternary International* 514:16-29.

Luke AM *et al.* (2013) Comparison of spiral computed tomography and cone-beam computed tomography. *Journal of Indian Academy of Oral Medicine and Radiology* 25(3):173-177.

Manohara SR *et al.* (2008) On the effective atomic number and electron density: A comprehensive set of formulas for all types of materials and energies above 1keV. *Nuclear Instruments and Methods in Physics Research Section B: Beam Interactions with Materials and Atoms* 266(18):3906-3912.

Martini M *et al.* (2021) Identification of Common Minerals Using Stoichiometric Calibration Method for Dual-Energy CT. *Geochemistry Geophysics Geosystems* 22(11):1-14.

McWethy DB *et al.* (2010) Rapid landscape transformation in South Island, New Zealand, following initial Polynesian settlement. *Proceedings of the National Academy of Sciences* 107(50):21343-21348.

Mees F *et al.* (2003) Applications of X-ray computed tomography in the geosciences. *Geological Society, London, Special Publications* 215(1):1-6.

Miao X *et al.* (2019) Improved Vinegar & Wellington calibration for estimation of fluid saturation and porosity from CT images for a core flooding test under geologic carbon storage conditions. *Micron* 124:102703.

Mizutani R, Suzuki Y (2012) X-ray microtomography in biology. *Micron* 43(2-3):104-115.

Ni X *et al.* (2017) Quantitative 3D spatial characterization and flow simulation of coal macropores based on μCT technology. *Fuel* 200:199-207.

Onoe M *et al.* (1983) Computed tomography for measuring annual rings of a live tree. *Proceedings of the IEEE* 71(7):907-908.

Pauwels E (2017) *Optimal use of the polychromaticity in X-ray microtomography for dual energy methods and contrast agent imaging*. (Ghent University).

Paziresh M *et al.* (2016) Tomography of atomic number and density of materials using dual-energy imaging and the Alvarez and Macovski attenuation model. *Journal of Applied Physics* 119(21).

Petrovic AM, Siebert JE, Rieke PE (1982) Soil bulk density analysis in three dimensions by computed tomographic scanning. *Soil Science Society of America Journal* 46(3):445-450.

Pierret A *et al.* (2002) 3D reconstruction and quantification of macropores using X-ray computed tomography and image analysis. *Geoderma* 106(3-4):247-271.

Radon J (1917) Uber die Bestimmung von Funktionen durch ihre Integralwerte langs gewissez Mannigfaltigheiten, Ber. *Verh. Sachs. Akad. Wiss. Leipzig, Math Phys Klass* 69.

Re A (2013) X-ray radiography and tomography of large artworks. *XCIX congresso Società Italiana di Fisica.* SIF, p 1-1.

Re A *et al.* (2015) X-ray tomography of a soil block: a useful tool for the restoration of archaeological finds. *Heritage Science* 3(1).

Reilly BT, Stoner JS, Wiest J (2017) SedCT: MATLAB ™ tools for standardized and quantitative processing of sediment core computed tomography (CT) data collected using a medical CT scanner. *Geochemistry, Geophysics, Geosystems* 18(8):3231-3240.

Remeysen K, Swennen R (2006) Beam hardening artifact reduction in microfocus computed tomography for improved quantitative coal characterization. *International Journal of Coal Geology* 67(1-2):101-111.

Remeysen K, Swennen R (2008) Application of microfocus computed tomography in carbonate reservoir characterization: Possibilities and limitations. *Marine and Petroleum Geology* 25(6):486-499.

Rizescu C, Beşliu C, Jipa A (2001) Determination of local density and effective atomic number by the dual-energy computerized tomography method with the ^{192}Ir radioisotope. *Nuclear Instruments and Methods in Physics Research Section A: Accelerators, Spectrometers, Detectors and Associated Equipment* 465(2-3):584-599.

Rontgen WC (1896) On a New Kind of Rays. *Science* 3(59):227-231.

Rutherford RA, Pullan BR, Isherwood I (1976) Measurement of effective atomic number and electron density using an EMI scanner. *Neuroradiology* 11(1):15-21.

Schlüter S. SA, Brown K., Wildenschild D. (2014) Image processing of multiphase images obtained via X-ray microtomography: A review. *WATER RESOURCES RESEARCH* 50:3615-3639.

Schneider U, Pedroni E, Lomax A (1996) The calibration of CT Hounsfield units for radiotherapy treatment planning. *Physics in Medicine & Biology* 41(1):111-124.

Schröer L *et al.* (2018) Linking microbial activity and the pore structure of a natural rock with X-ray Computed Tomography. *2018 Symposium of the Belgian Society for Microbiology: Microbes in the spotlight.* p 84-84.

Sedigh Rahimabadi P, Khodaei M, Koswattage KR (2020) Review on applications of synchrotron-based X-ray techniques in materials characterization. *X-Ray Spectrometry* 49(3):348-373.

Sénéchal P *et al.* (2023) Characterization of oil shales: discriminating power of spectral over conventional X-ray radiography. in *EXCITE workshop*Granada).

Siddiqui S, Khamees, A. A. (2004) Dual-Energy CT-Scanning Applications in Rock Characterization. in *SPE Annual Technical Conference and Exhibition*Houston, Texas).

Sittner J *et al.* (2020) Spectral X-ray computed micro tomography: 3-dimensional chemical imaging. *X-Ray Spectrometry* 50(2):92-105.

Spiers FW (1946) Effective atomic number and energy absorption in tissues. *The British journal of radiology* 19(218):52-63.

Stamm D (1974) Calibration and quality control materials. *Clinical Chemistry and Laboratory Medicine* 12(4):137-145.

Torikoshi M, Tsunoo T., Sasaki M., Endo M., Noda Y., Ohno Y., Kohno T., Hyodo K., Uesugi K., Yagi N. (2003) Electron density measurement with dual-energy x-ray CT using synchrotron radiation. *Physics in Medicine & Biology* 48:673–685.

Tsunoo T *et al.* (2004) Measurement of electron density and effective atomic number using dual-energy x-ray CT. in *IEEE Symposium Conference Record Nuclear Science 2004.*), p 3764-3768.

Van Daele M *et al.* (2014) Multidirectional, synchronously-triggered seismo-turbidites and debrites revealed by X-ray computed tomography (CT). *Sedimentology* 61(4):861-880.

Van Geet M, Swennen R, David P (2001a) Quantitative coal characterisation by means of microfocus X-ray computer tomography, colour image analysis and back-scattered scanning electron microscopy. *International Journal of Coal Geology* 46(1):11-25.

Van Geet M, Swennen R, Wevers M (2000) Quantitative analysis of reservoir rocks by microfocus X-ray computerised tomography. *Sedimentary Geology* 132(1-2):25-36.

Van Geet M, Swennen R, Wevers M (2001b) Towards 3-D petrography: application of microfocus computer tomography in geological science. *Computers & Geosciences* 27(9):1091-1099.

Victor RA, Prodanovic, M., Torres-Veredin, C. (2017) Monte Carlo Approach for Estimating Density and Atomic Number From Dual-Energy Computed Tomography Images of Carbonate Rocks. *Journal of Geophysical Research: Solid Earth* 122:9804-9824.

Vinegar HJ, Wellington SL (1987) Tomographic imaging of three-phase flow experiments. *Review of Scientific Instruments* 58(1):96-107.

Vlassenbroeck J *et al.* (2006) Octopus 8: A High Performance Tomographic Reconstruction Package for X-ray Tube and Synchrotron micro-CT. *Advances in X-ray Tomography for Geomaterials,* https://doi.org/10.1002/9780470612187.ch13. p 167-173.

Walls J, Armbruster M (2012) Shale Reservoir Evaluation Improved by Dual Energy X-Ray CT Imaging. *Journal of Petroleum Technology* 64(11):28-32.

Watanabe Y (1999) Derivation of linear attenuation coefficients from CT numbers for low-energy photons. *Physics in Medicine & Biology* 44(9):2201-2211.

Youn E, Jeong MK (2009) Class dependent feature scaling method using naive Bayes classifier for text datamining. *Pattern Recognition Letters* 30(5):477-485.

Yun TS *et al.* (2013) Evaluation of rock anisotropy using 3D X-ray computed tomography. *Engineering Geology* 163:11-19.

Zhao Y *et al.* (2018) Pore structure characterization of coal by synchrotron radiation nano-CT. *Fuel* 215:102-110.

4 GUIDELINES FOR THE CHARACTERIZATION OF GEOLOGICAL SAMPLE WITH DUAL-ENERGY CT: COMPARISON OF THREE DIFFERENT SCANNERS

Lignes directrices pour la caractérisation des échantillons géologiques par tomodensitométrie à double énergie : comparaison de trois scanners différents

Authors :

Martini M.[1], Francus P.[1,3], Schröer L.[4], Buyse F.[4], Kibleur P.[4], Cnudde V.[4], Di Schiavi Trotta L.[2], Després P.[2]

[1]Centre Eau Terre Environnement, Institut national de la recherche scientifique, Québec, Canada

[2]Department of Physics, Physical Engineering and Optics, Université Laval, Québec, Canada

[3]GEOTOP – Research Centre on the Dynamics of the Earth System, Montréal, Québec, H2X 3Y7, Canada

[4]Centre for X-Ray Tomography (UGCT), Ghent University, Ghent, Belgium

Ready to be submitted in *Geostandards and Geoanalytical Research*, IAG

Authors contribution:

Margherita Martini: Conceptualization, Methodology, Software, Data analysis, Original draft preparation, Writing, Review & Editing. Pierre Francus: Conceptualization, Methodology, Project administration, Funding acquisition, Supervision, Writing, Review & Editing. Laurenz Schröer: Data acquisition, Writing, Review & Editing. Florian Buyse: Data acquisition, Writing, Review & Editing. Pierre Kibleur: Conceptualization, Writing, Review & Editing. Veerle Cnudde: Financial support. Leonardo Di Schiavi Trotta: Software, Writing, Review & Editing. Philippe Després: Conceptualization, Methodology, Funding acquisition, Supervision, Writing, Review & Editing.

4.1 Résumé

La méthode d'étalonnage stœchiométrique pour la tomographie informatisée à double énergie (DECT) est une technique multispectrale déjà utilisée en géologie pour caractériser les matériaux sur la base de leur numéro atomique effectif (Z_{eff}) et de leur densité électronique (ρ_e) sans connaissance préalable du faisceau de rayons X incident.

Dans cet article, la composition chimique et minéralogique de trois échantillons de roches a été déterminée, ainsi que leur densité et leur homogénéité. Ces échantillons ont également été scannés à l'aide de trois instruments différents (un scanner médical, un micro-CT personnalisé et un micro-CT commercial) et caractérisés à l'aide d'une méthode calibrée stœchiométriquement.

Plusieurs paramètres d'acquisition ont été testés afin d'identifier les paramètres les plus appropriés. Certains paramètres tels que les énergies incidentes, la résolution et les matériaux d'étalonnage se sont avérés avoir un impact significatif sur la précision de la caractérisation.

La détermination d'un protocole de mesure général applicable aux échantillons géologiques s'est révélée difficile car plusieurs facteurs, dont la nature de l'échantillon, les objectifs de l'étude et les limites instrumentales, influencent la méthode. Néanmoins, la comparaison des résultats obtenus par les trois scanners met en évidence les paramètres clés à prendre en compte pour effectuer une caractérisation utile d'un échantillon de roche avec la DECT.

4.2 Abstract

The stoichiometric calibration method for dual-energy computed tomography (DECT) is a multispectral technique, already used in the geosciences to characterize materials based on their effective atomic number (Z_{eff}) and their electron density (ρ_e) without previous knowledge of the incident X-ray beam. In this research paper, the chemical and mineralogical composition of three rock samples was determined, as well as their density and homogeneity. These samples were then scanned with three different instruments: a medical CT, a custom-built micro-CT, and a commercial micro-CT, and characterized with the stoichiometrically calibrated method. Several acquisition settings were tested to identify the most suitable parameters for sample characterization. Some parameters such as the incident energies, the resolution and the calibration materials proved to have a significant impact on the accuracy of the characterization.

The definition of a general measurement protocol for geological samples was found to be difficult because of several complicating factors, including the nature of the sample, objectives of the study, and instrumental limitations that influence DECT characterization. Nonetheless, comparison of the results obtained by the three scanners brings out the key parameters to be considered to perform a useful rock sample characterization with DECT.

4.3 Introduction

X-ray Computed Tomography (CT) is an imaging technique used to visualize the inner structure of a sample in a non-destructive way. Even though it was originally developed for medical purposes, its potential in other field became rapidly clear (Kalender, 2011). The first non-medical application dates back to 1974, when Fourie (Fourie, 1974) studied the cranial morphology of an ancient tetrapod. Then, other research fields like archeology (Re *et al.*, 2015), biology (Mizutani & Suzuki, 2012), marine science (Boespflug *et al.*, 1995) and geology (Cnudde & Boone, 2013; Cnudde *et al.*, 2006) also utilized and benefitted from CT scans.

CT geological applications cover many topics, from the investigation of meteorites (Arnold *et al.*, 1983), the analysis of sedimentary facies succession (Van Daele *et al.*, 2014), to the study of the paleoclimate through varved lakes (Gagnon-Poiré *et al.*, 2021). CT scans have also improved the assessment of rock porosity, useful for petroleum research and fluid flow experiments for examining fractures in natural building stones (Keller, 1997; Vinegar & Wellington, 1987). Depending on the purpose of the research, the type of instrument may change, especially with respect to the required resolution and sample size; yet, nano-CT, micro-CT (or µ-CT) or medical CT could be used (Akbari A., 2015; Boespflug *et al.*, 1995; Ni *et al.*, 2017; Zhao *et al.*, 2018).

For particularly difficult sample characterizations, standard CT acquisition procedures have been developed further. “Dual-energy CT” (DECT) consists in imaging an object using two different X-ray energy spectra (low and high) and facilitates the characterization using two physical properties: the effective atomic number (Z_{eff}, related to chemical composition) and the electron density (ρ_e, generally proportional to the more common mass density). Here too, the DECT method was first developed for medical purposes, but geological applications quickly arose. Van Geet *et al.* (2000), adapting the mathematical formula of Coenen (1994), quantified, for the first time the above-mentioned properties of reservoir rocks. Since then, many authors have used and improved DECT techniques to study geological materials (Alves *et al.*, 2015; Duliu *et al.*, 2003; Iovea *et al.*, 2009; Paziresh *et al.*, 2016; Remeysen & Swennen, 2008). One of the most recent

DECT applications to Earth science is the work of Martini *et al.* (2021) and Martini *et al.* (2024).They applied a stoichiometric calibration method that previously had been developed to differentiate human tissues (Bourque *et al.*, 2014) on minerals and varved core respectively. Unlike the other DECT techniques, the stoichiometric calibration method has the significant advantage of not requiring the knowledge of the incident X-ray spectrum.

The present work aims to test the DECT methodology of Martini *et al.* (2021) on three different scanners (a medical CT, a custom built micro-CT, and a commercial micro-CT) to determine the best-suited acquisition device and the best acquisition settings to characterize three rock samples of known composition. The paper discusses the best possible analytical procedure in the light of the similarities and differences arising from the wide range of settings tested (i.e., sets of calibration materials, multiple energies, different level of resolution) and used with the three instruments.

4.4 Materials and Method

4.4.1 Samples: mineralogical and chemical analysis

The three different rock samples analyzed in this study are chalk from Dover, England (left), hematitic-oolite from Clinton, NY, USA (centre) and chert from Joplin, Missouri, USA (right) (Figure 4.1). About 20 mg were taken from each sample where the arrows point (Figure 4.1) for destructive mineralogical and chemical analyses.

Figure 4.1: Tested rocks samples.

Chalk (left), hematitic oolite (centre) and chert (right). The arrows point where the samples were extracted for destructive analyses.

The samples' mineralogical and elemental composition was obtained by X-ray diffraction (XRD), inductively coupled plasma atomic emission spectroscopy (ICP-AES) and carbon-hydrogen-nitrogen (CHN) analyses.

For XRD analyses, samples were first powdered and doped with corundum as per internal standard. Then the analyses were carried out using a PANalytical X'Pert Powder (Malvern PANalytical, Almelo, The Netherlands and Malvern, UK) at 45 kV and 40 mA at the *Université du Québec à Rimouski*. The XRD diffractograms were converted to weight percentage by *powdR* (Butler & Hillier, 2021) and *RockJock* (Eberl, 2003) software, quantifying the main mineralogical components. The weight percentage of the total minerals calculated was normalized to 100%.

For the ICP-AES analyses, samples were frozen, freeze-dried, powdered and an alkaline fusion with HNO_3, $HClO_4$ and HF was performed. They were analyzed by an Agilent 5110 Dual View (Agilent Technologies, Mulgrave, Australia) at the *Institut National de la Recherche Scientifique*, Québec City. LKSD-2, LKSD-4, Buffalo and IAEA soil 7 were used as standard. Raw data are expressed in ppb and then converted into oxide percentages.

Third, CHN analysis was performed using an elemental analyzer Flash 2000 (Thermo Scientific, Waltham, USA) at the *Institut National de la Recherche Scientifique*, Québec City, obtaining the percentage of the three elements in relation to the analysed samples mass (mg). To obtain 100%, the percentage of oxygen was calculated by subtracting the percentage of these elements from the total.

4.4.2 CT- scanners

The analysis was conducted with three X-ray CT devices. The first one is a medical CT scanner Somatom Definition AS+128 (Siemens healthcare GmbH, Erlangen, Germany) located at the *Institut national de la recherche scientifique, Centre Eau Terre Environnement*, Canada. The X-ray tube can be operated between 70 kV and 140 kV at current ranging between 20 mA and 800 mA, producing a fan beam. The instrument is equipped with an aluminum bowtie filter, aimed at reducing the dose for patients and reducing cupping artifacts (Bushberg, 2012); this filter also allows the bandwidth of incident X-rays to be made smaller (Di Schiavi Trotta *et al.*, 2022). The curved 64-row detector is from the Stellar$^{\text{Infinity}}$ generation. The ADMIRE suite (statistical iterative reconstruction method) was used to reconstruct 512 x 512 pixels wide images. Voxels are anisotropic and the best resolution is 0.1 x 0.1 x 0.6 mm (Gordic *et al.*, 2014).

The second device is the HECTOR micro-CT system, located at Ghent University Centre for X-ray Tomography (UGCT), in Belgium. It was developed and built by UGCT. The X-ray tube can be operated up to 240 kV but was used at a maximum of 220 kV during the experiments, producing a cone beam. The X-ray tube can deliver up to 280 W of X-ray flux, with focal spot size of 4 µm. A metal plate (e.g., Cu, Al or Sn) can be placed in front of the source to filter the beam. The 43 x 43 cm^2 flat-panel detector consists of a Cesium Iodide scintillator and generate 2880 x 2880 pixels images. The image reconstructions are based on a filtered backprojection algorithm and are performed with the in-house-developed *Octopus Reconstruction (XRE)* (Vlassenbroeck *et al.*, 2006). Voxels are isotropic and the maximum resolution is approximately 3 µm.

A simulation software (*Arion*) developed at UGCT is also available to model sample attenuation for specific acquisition parameters of the HECTOR scanner. The HECTOR spectrum has been modeled and *Arion* provides very accurate image simulations (Dhaene *et al.*, 2015). The knowledge of the spectrum typically yields better results in dual-energy CT endeavours (Bourque *et al.*, 2014), an hypothesis that was tested during this project. Because *Arion* incorporates the HECTOR incident spectrum only, simulations are limited to this device.

Finally, a CoreTOM micro-CT system (TESCAN XRE, Brno – Kohoutovice, Czech Republic), located at the *Institut national de la recherche scientifique, Centre Eau Terre Environment,* Canada, was used as the third micro-CT device. It was developed and designed for multiscale imaging; the X-ray tube operates between 30 kV and 230 kV, with a maximum power of 300 W, producing again a cone beam. Again, a metal plate (e.g., Cu, Al, or Sn) can be placed in front of the source to filter the beam. The detector is 42.8 x 42.8 cm^2 flat panel (2856 x 2856 pixels), consisting of amorphous Si and Gadolinium Oxysulfide scintillator. The TESCAN image reconstruction software *Panthera,* also based on the filtered backprojection algorithm, is used. Voxels are isotropic and the maximum resolution is approximately 3 µm (Godinho *et al.*, 2021; Van den Bulcke *et al.*, 2019). The CoreTOM is an upgraded and commercially available version of HECTOR, and they hence have quite similar capabilities. It is therefore interesting to see if similar measurements are produced in a DECT study.

4.4.3 DECT: Characterization by stoichiometric method

The DECT method used here is identical to that described in Martini *et al.* (2021) and can be summarised as follows.

a) The effective atomic number Z_{eff} and electron density ρ_e (number of electrons per unit volume, *moles-e⁻/cm³*) of a set of calibration materials having known composition were calculated using the equations:

$$Z_{\mathrm{eff\_Calc}} = \sqrt[\beta]{\sum_{i}^{N} f_i Z_i^{\beta}} \tag{4.1}$$

$$\rho_{\mathrm{e\_Calc}} = \sum_{i=1}^{N} \frac{Z_i}{A_i} \rho \tag{4.2}$$

In Equation 4.1, f_i is the fractional mass of element Z_i. The exponent β is a function of photon energy, sample materials, instrument, and analytical specific settings (Alves *et al.*, 2015; Azevedo *et al.*, 2016; Landry *et al.*, 2013) and can vary between 2.94 and 3.8 (Bonnin *et al.*, 2014; Spiers, 1946). In Equation 2, A_i is the atomic mass of the element Z_i and ρ is the material mass density (g/cm^3), calculated using a pycnometer (Azevedo *et al.*, 2016; Manohara *et al.*, 2008). In this paper, Z_{eff} and ρ_e obtained by Equations 4.1 and 4.2 are defined as "calculated" (Z_{eff_Calc} and ρ_{e_Calc}).

b) The calibration samples were scanned and their attenuation coefficients, at low and high energy (μ_{low} and μ_{high}), were calculated from the attenuation gray values in the reconstructed images. The attenuation μ obtained from medical CT scanners is determined as follows, given that Hounsfield units (*HU*) are produced as output (Boespflug *et al.*, 1995; Watanabe, 1999):

$$\mu = \frac{\mu_{\mathrm{sample}}}{\mu_{\mathrm{water}}} = \left(\frac{\text{gray level expressed in HU units}}{1000}\right) + 1 \tag{4.3}$$

For micro-CT the gray levels are not expressed in *HU,* instead they are determined by the slope and offset of the gray values histograms that are usually different for each sample, because they are based on the range of values chosen by the operator during reconstruction. Using the metadata of each image stack, the attenuation coefficient is calculated as follows:

$$\mu = (\text{gray level}*\text{slope}) + \text{offset} \tag{4.4}$$

The gray level histograms of natural rocks or minerals (Figure 4.2) are seldom normal because they often contain some degree of heterogeneity and thus their gray level histograms display some skewness. Therefore, to better capture this statistical particularity, both the mean and mode of gray values were tested as statistical descriptors of small but representative slices extracted in regions of interest (ROI).

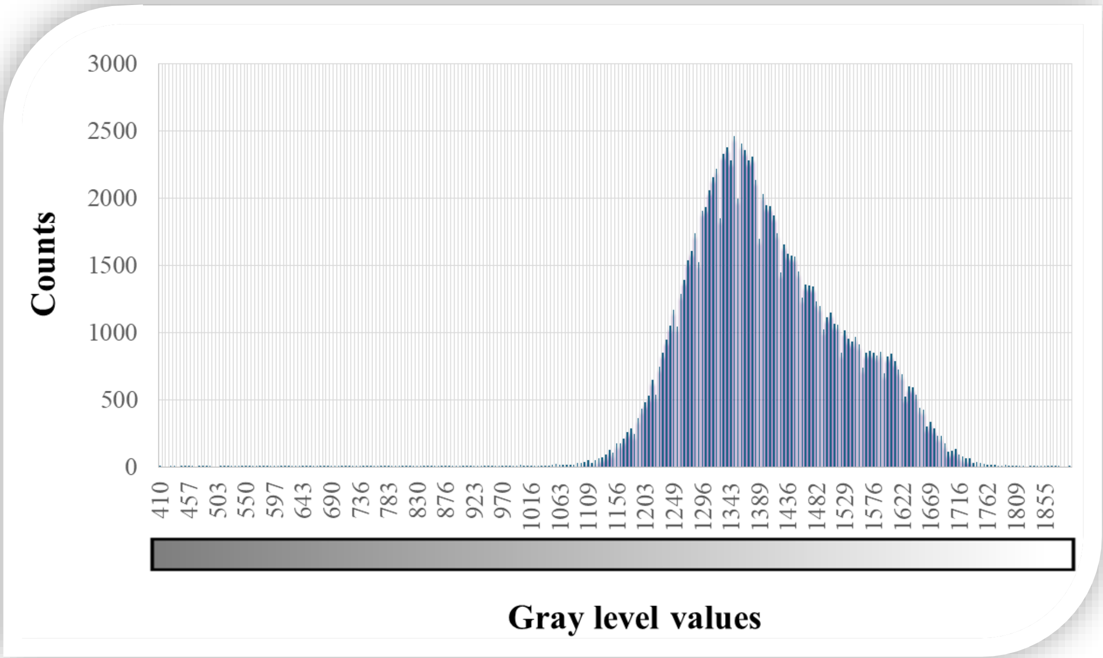

Figure 4.2: Gray level histogram.
It is an example of the gray level histogram of a geological sample.

c) The ratio of μ calculated from the calibration samples' scans obtained at low and high energy (Equations 4.3 or 4.4) are plotted against their calculated Z_{eff} (Equation 4.1), and a second-order polynomial empirical model is fitted to this data to obtain the Z_{eff} calibration equation.

$$\mathrm{Z_{eff}} = \mathrm{a} + \mathrm{b} \cdot \left(\frac{\mu_{\mathrm{low}}}{\mu_{\mathrm{high}}}\right) + \mathrm{c} \cdot \left(\frac{\mu_{\mathrm{low}}}{\mu_{\mathrm{high}}}\right)^2 \tag{4.5}$$

d) The ratio between measured μ (Equations 4.3 or 4.4) and calculated ρ_e (Equation 4.2) of calibration samples, normalized by the electron density of water ($\rho_{e\ water}$ = 3.34 E+23 e^-

/cm^3) and Z_{eff} determined in Equation 4.5 are plotted in a second step, again to obtain a second-order polynomial empirical model that can be used as a ρ_e calibration equation.

$$\frac{\mu_{\mathrm{low\ or\ high}}}{\rho_e/\rho_{\mathrm{e\ water}}} = \mathrm{d} + \mathrm{e} \cdot \mathrm{Z_{eff}} + \mathrm{f} \cdot \mathrm{Z_{eff}^2} \tag{4.6}$$

In this Equation (4.6), the μ value used can equally be those obtained at low or high energy.

Once the two sets of calibration coefficients are found, Z_{eff} and ρ_e obtained by Equations 4.5 and 4.6 are going to be defined as “measured” in this paper (Z_{eff_Meas} and ρ_{e_Meas}).

All μ values were measured in a central zone of each rock sample to ensure a meaningful comparison with their mineralogical and chemical analyses.

4.4.4 Data acquisition

As in Martini *et al.* (2021), calibration materials were scanned to determine the coefficients *a* to *e* of Equations 4.5 and 4.6 and this procedure has been repeated for each instrument. Here, different sets of calibration materials (stochastically chosen and pinpointed in Table 4.1) were tested using the three above-mentioned scanners; their calculated Z_{eff_Calc} and ρ_{e_Calc} values presented in Table 9.1, Annexe III. The blue set (*b*-) is the same used by Martini *et al.* (2021).

b-	Same set of calibration materials of medical CT: NaI solutions at 50%, 40%, 30%, 25%, 20%, 15%, 10%, 8%, 5%, 1%, 0.5%, Al and Ti bar, Halite, Crystalline Quartz, Pyrite, Fluorite and Albite
r-	Only solid materials: Al, Ti and Zn bar, Crystalline Quartz, Albite, Fluorite, Halite, Hematite, Microcline and Pyrite
y-	Al, Ti and Zn bar, Albite, Crystalline Quartz, Fluorite, Halite, Microcline, Pyrite, NaI solutions at 20%, 15%, 5% and 1%
c-	Al, Ti and Zn bar, Albite, Crystalline Quartz, Fluorite, Halite, Hematite, Microcline, NaI solutions at 20%, 15%, 5% and 1%
m-	Al, Ti and Zn bar, Albite, Crystalline Quartz, Fluorite, Halite, Microcline, NaI solutions at 20%, 15% and 1%. This set of samples will be tested using Hector scanner as well.

g-	Al, Ti and Zn bar, Albite, Crystalline Quartz, Fluorite, Halite, Microcline, NaI solutions at 20%, 15%, 5% and 1%

Table 4.1: Set of calibration samples.

These are the different materials used for the calibrations during the tests.

The rock samples were first scanned with the medical-CT: the instrument, the acquisition parameters, the calibration materials (*b*-set) and the resulting coefficients *a* to *e* from Equations 4.5 and 4.6 are the same as those in Martini *et al.* (2021). However, some additional calculations were made: μ has been evaluated using not only the mode but also the mean of gray level histogram, and ρ_{e_Meas} has been measured using not only $\mu_{70\ kV}$ but also $\mu_{140\ kV}$. The scan time is about 5 seconds for both energies.

Before scanning the samples at UGCT with HECTOR, the in-house-developed software *Arion* (specifically, the setup optimizer module) (Dhaene *et al.*, 2015), simulating the detector spectral sensitivity and the related linear attenuation coefficient of samples, was used to test scanner settings, and find the ones that would allow best to characterize the samples. Considering the size and density of investigated samples, some parameters were fixed: power at 25 W, resolution at 25 µm (isotropic voxel size), 1 mm Cu plate filter. The simulations of the μ of the three rock samples as measured by HECTOR used the following tube voltage: 90, 110, 120, 130, 140, 160, 170 and 220 kV. These linear attenuation coefficients were then used to obtained simulated Z_{eff_Meas} and ρ_{e_Meas}.

The samples were then scanned at HECTOR using the best settings found in simulations, which are 110 and 220 keV, 25 W, 1 mm Cu filter and resolution at 25 µm. The acquisition duration for each sample ranged from 15 to 20 minutes for high energies and 1 hour for low energies.

In the third part of the project, the samples were scanned with the CoreTOM device. Two different acquisition conditions were chosen: one aiming to emulate HECTOR, thus using the same settings, and another that covered a wider energy range. For the second setting, a 1.5 mm Cu plate was placed in front of the X-ray source to filter out the lower energy components. Then, all the samples were acquired at 90, 160 and 230 kV offering three energy ratios (90/160, 90/230, 160/230). CoreTOM was operated at a power of 50 W, and the reconstructed voxel size was set to 50 µm. Here, all the calibration sets listed in Table 4.1 were tested to find the best sample combinations. The acquisition duration was comparable to the one previously reported for HECTOR.

4.5 Results

4.5.1 XRD, ICP-AES and CHN

The mineralogy of the three rock samples is shown in Table 4.2.

Identified Minerals: XRD	**Chalk**	**Hematitic-oolite**	**Chert**
Quartz	13.1%	14.7%	100.0%
K feldspar	0.5%	0.4%	-
Calcite	85.9%	-	-
Fe-Dolomite	-	30.3%	-
Diopside	-	0.7%	-
Fosterite	-	1.3%	-
Pyrite	-	0.2%	-
Hematite	-	35.0%	-
Fluorapatite	-	3.1%	-
Kaolinite	-	1.5%	-
Chlorite	-	13%	-
Illite	0.5%	-	-
Total	*100%*	*100%*	*100%*

Table 4.2: XRD results.

Mineralogical composition of the three rock samples measured by XRD.

The elemental composition of the rock specimens determined by both ICP-AES and CHN is presented in the following Table 4.3.

Detected elements: ICP-AES and CHN	**% in Chalk**	**% in Hematitic-oolite**	**% in Chert**
Al	0.82%	2.01%	*
Ca	30.23%	7.65%	0.1%
Fe	0.81%	30.99%	0.3%
K	0.38%	*	*
Mg	0.3%	3.18%	*
Mn	*	0.27%	-
Na	*	*	0.02%
P	0.18%	0.41%	-
Si	7.67%	7.57%	45.81%
S	*	0.39%	*
Ti	0.11%	*	-
As, Ba, Cd, Co, Cr, Cu, La, Mo, Ni, Pb, Sc, Sr, V, Y, Zn, Zr	*	*	*
C	9.45%	4.4%	0%
H	-	-	-
O	49.78%	42.83%	53.61%
Total	*100%*	*100%*	*100%*

Table 4.3: ICP-AES and CHN results.

Percentage of elements detected by ICP-AES and CHN analysis in chalk, hematitic-oolite and chert. * indicate concentration lower than 0.1%.

Once the elemental composition of each sample has been obtained, it was possible to precisely calculate Z_{eff_Calc} using the Equation 4.1 and ρ_{e_Calc} using Equation 4.2 (Table 4.4).

Rock	Z_{eff_Calc}	ρ_{e_Calc}
Chalk	14.67	4.35E+23
Hematitic-oolite	18.81	7.70E+23
Chert	11.75	7.00E+23

Table 4.4: Calculated properties of the three rock samples.

Calculated Z_{eff_Calc} and ρ_{e_Calc} values of chalk, hematitic-oolite and chert. The electron density ρ_e values are in units of *moles-e⁻/cm³*.

4.5.2 Medical-CT experiments

Calibration curves for the medical CT scanner are illustrated in Figure 4.3. As described in section 4.4.4, Martini *et al.* (2021) have already obtained two calibration curves, identified as D (Z_{eff} model using the mode of gray level histogram in μ calculation) and E (ρ_e model using $\mu_{70\ kV}$ and the mode of gray level histogram in μ calculation) in Figure 4.3. F represents the ρ_e model using $\mu_{140\ kV}$ obtained by the gray level mode. Using the mean of gray level histogram, A represents the Z_{eff} model, B the ρ_e model using $\mu_{70\ kV}$ and C is the ρ_e model using $\mu_{140\ kV}$. The correlation coefficient R^2 for the calibration curves are quite similar, comprised between 0.96 and 0.98.

The μ values at low and high energy of the three samples were determined using Equation 4.3. Their measured Z_{eff_Meas} and ρ_{e_Meas} were obtained using Equations 4.5 and 4.6 and calculated for both mean and mode of gray level histogram. Table 4.5 presents the difference between the calculated Z_{eff_Calc} and ρ_{e_Calc} (Table 4.4) and the measured ones with dual-energy medical CT.

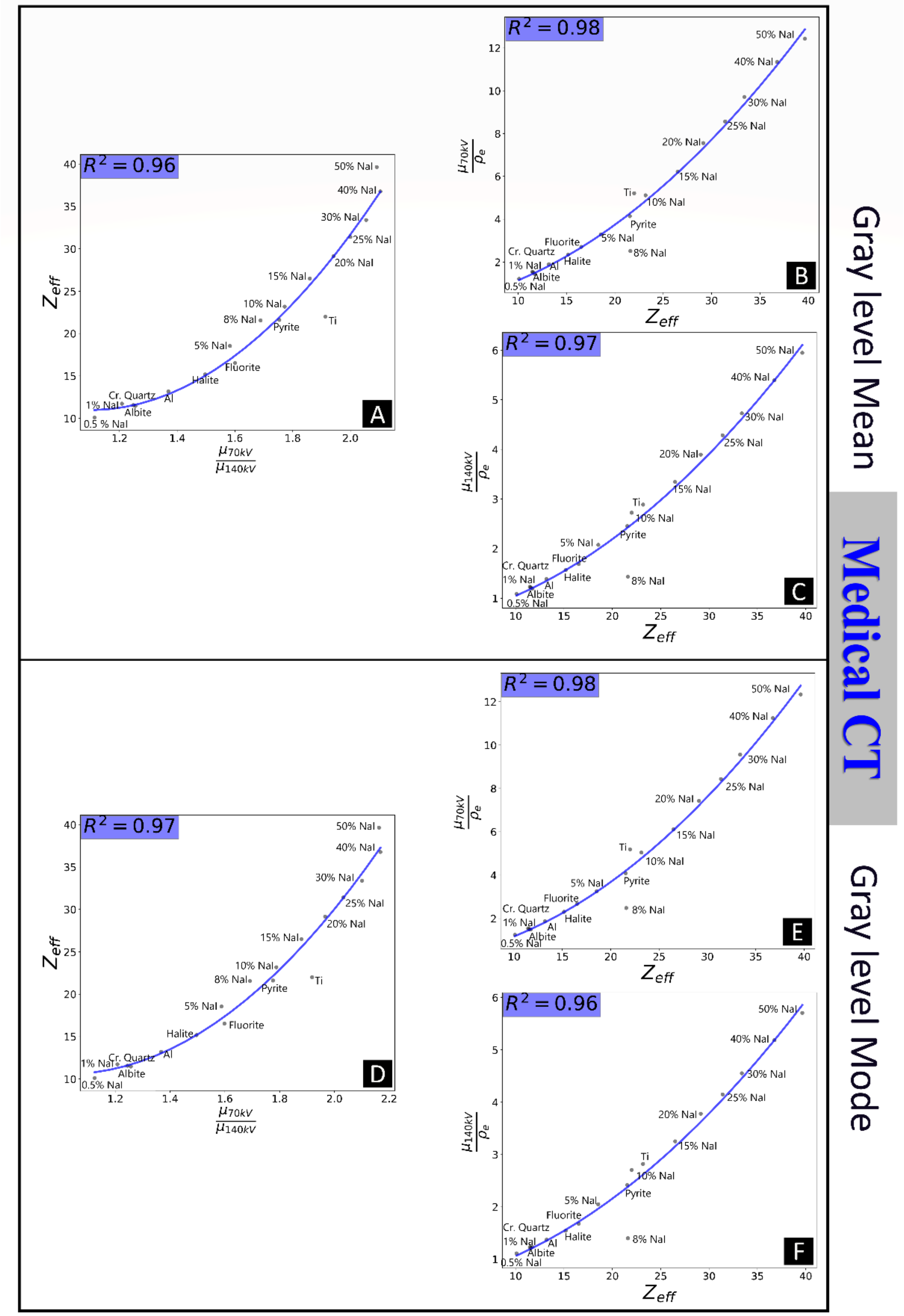

Figure 4.3: Medical CT calibration curves.

Calibration curves determined with the medical CT scanner and *b*-set of the calibration samples. Using the mean of gray level histogram, there is A) Z_{eff} model; B) ρ_e model using $\mu_{70\,kV}$; C) ρ_e model using $\mu_{70\,kV}$. Using the mode of gray level histogram, there is D) Z_{eff} model; E) ρ_e model using $\mu_{70\,kV}$; F) ρ_e model using $\mu_{70\,kV}$. D and E are identical to calibration curves of Martini *et al.* (2021).

	Medical CT			
	Chalk	**Hematitic-oolite**	**Chert**	
Z_{eff_Calc}	14.67	18.81	11.75	
ρ_{e_Calc}	4.35E+23	7.70E+23	7.00E+23	
Z_{eff_Meas}	14.63	20.67	11.59	**Gray level Mode**
% difference	*0.26%*	*9.94%*	*1.33%*	
ρ_{e_Meas} **using** $\mu_{70\ kV}$	5.29E+23	7.97E+23	7.71E+23	
% difference	*21.38%*	*3.49%*	*10.12%*	
ρ_{e_Meas} **using** $\mu_{140\ kV}$	5.15E+23	7.96E+23	7.60E+23	
% difference	*18.28%*	*3.31%*	*8.59%*	
Z_{eff_Meas}	14.66	16.46	11.47	**Gray level Mean**
% difference	*0.04%*	*12.46%*	*2.38%*	
ρ_{e_Meas} **using** $\mu_{70\ kV}$	4.78E+23	8.98E+23	7.62E+23	
% difference	*9.93%*	*16.67%*	*8.81%*	
ρ_{e_Meas} **using** $\mu_{140\ kV}$	4.64E+23	8.84E+23	7.46E+23	
% difference	*6.75%*	*14.75%*	*6.61%*	

Table 4.5: Medical CT, characterization results.

Z_{eff_Meas} and ρ_{e_Meas} of the three rock samples measured using DECT and the medical CT scanner, using both mean and mode of gray level histograms. The percentage difference is with the calculated properties Z_{eff_Calc} and ρ_{e_Calc} of Table 4.4. The electron density ρ_e values are in units of *moles-e$^-$/cm^3*.

4.5.3 Arion and HECTOR experiments

Twenty-eight acquisition settings (different low energies and different sets of calibration materials) were tested with *Arion*: the calibration curves were plotted using linear attenuation coefficients obtained from the software.

Simulated calibration curves obtained with *m*-set of standard materials and 110 kV as low energy are illustrated in Figure 4.4. The correlation coefficients R^2 are above 0.96 in all cases.

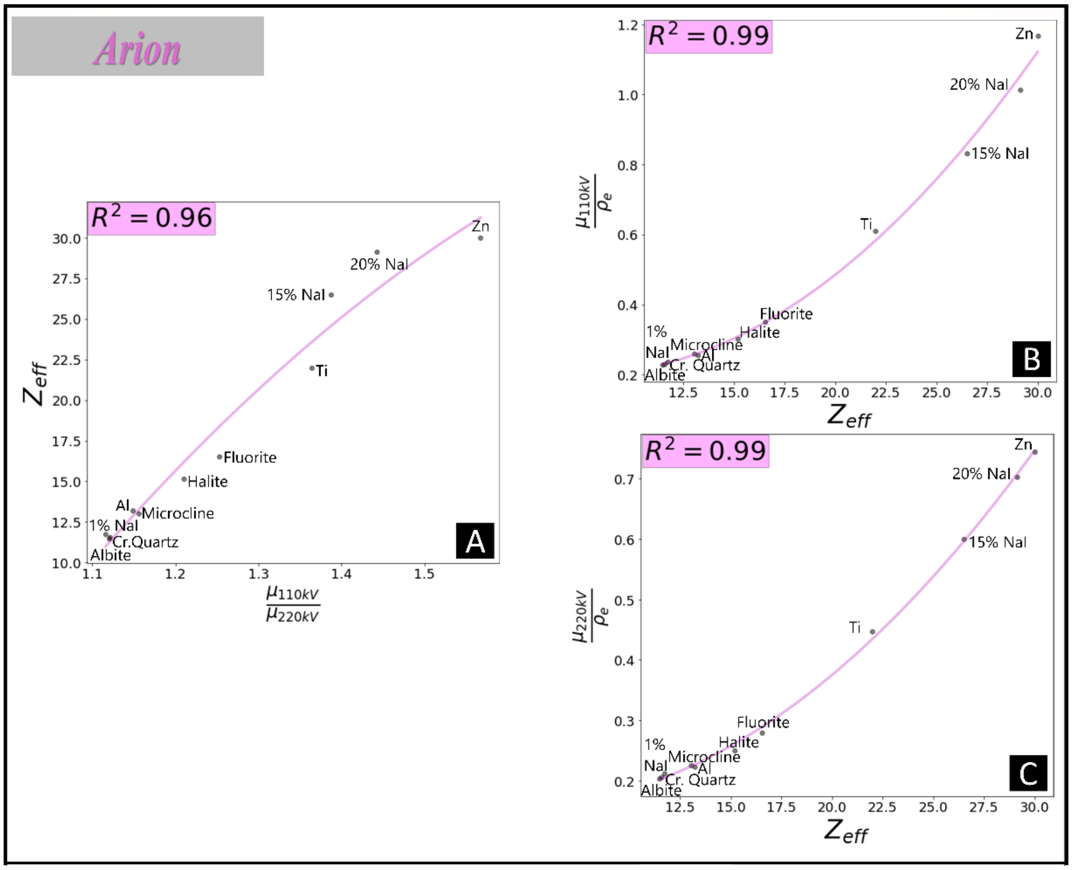

Figure 4.4: *Arion* calibration curves.

A) Z_{eff} calibration using simulated $\mu_{110\ kV}/\mu_{220\ kV}$; B) ρ_e calibration using simulated $\mu_{110\ kV}$; C) ρ_e calibration using simulated $\mu_{220\ kV}$. Note that a mean and a mode cannot be extracted for the μ values simulated by *Arion Optimizer*.

$Z_{eff\_Meas\_Sim}$ and $\rho_{e\_Meas\_Sim}$ values (from *Arion* simulations) were then determined using Equations 4.5 and 4.6 and the percentage difference with the calculated properties (Z_{eff_Calc} and ρ_{e_Calc}, Table 4.4) are shown in Table 4.6.

	Arion		
	Chalk	**Hematitic-oolite**	**Chert**
Z_{eff_Calc}	14.67	18.81	11.75
ρ_{e_Calc}	4.35E+23	7.70E+23	7.00E+23
$Z_{eff\_Meas\_Sim}$	16.72	23.33	11.71
% difference	*13.96%*	*24.05%*	*0.33%*
$\rho_{e\_Meas\_Sim}$ **using** $\mu_{110\ kV}$	5.12E+23	5.87E+23	5.93E+23
% difference	*17.69%*	*23.79%*	*15.34%*
$\rho_{e\_Meas\_Sim}$ **using** $\mu_{220\ kV}$	5.04E+23	5.88E+23	5.93E+23
% difference	*15.93%*	*23.69%*	*15.32%*

Table 4.6: *Arion*, characterization results.

Rocks' properties using the μ simulated values with *Arion Optimizer* ($Z_{eff\_Meas\_Sim}$ and $\rho_{e\_Meas\_Sim}$) and the percentage difference with calculated properties (Z_{eff_Calc} and ρ_{e_Calc} of Table 4.4). The electron density ρ_e values are in units of $moles\text{-}e^-/cm^3$.

The results obtained using the *m*-set and the ratio $\mu_{110\ kV}$ / $\mu_{220\ kV}$ are the closest to calculated values for all three rocks. Some examples of the other outcomes are presented in Table 9.2., Annexe III.

Once the best acquisition parameters were determined by the *Arion* (module *Optimizer*) results, all the samples were scanned by HECTOR at 110 kV and 220 kV. Six calibration curves (Figure 4.5) were obtained using the *m*- set of calibration materials (Table 4.1).

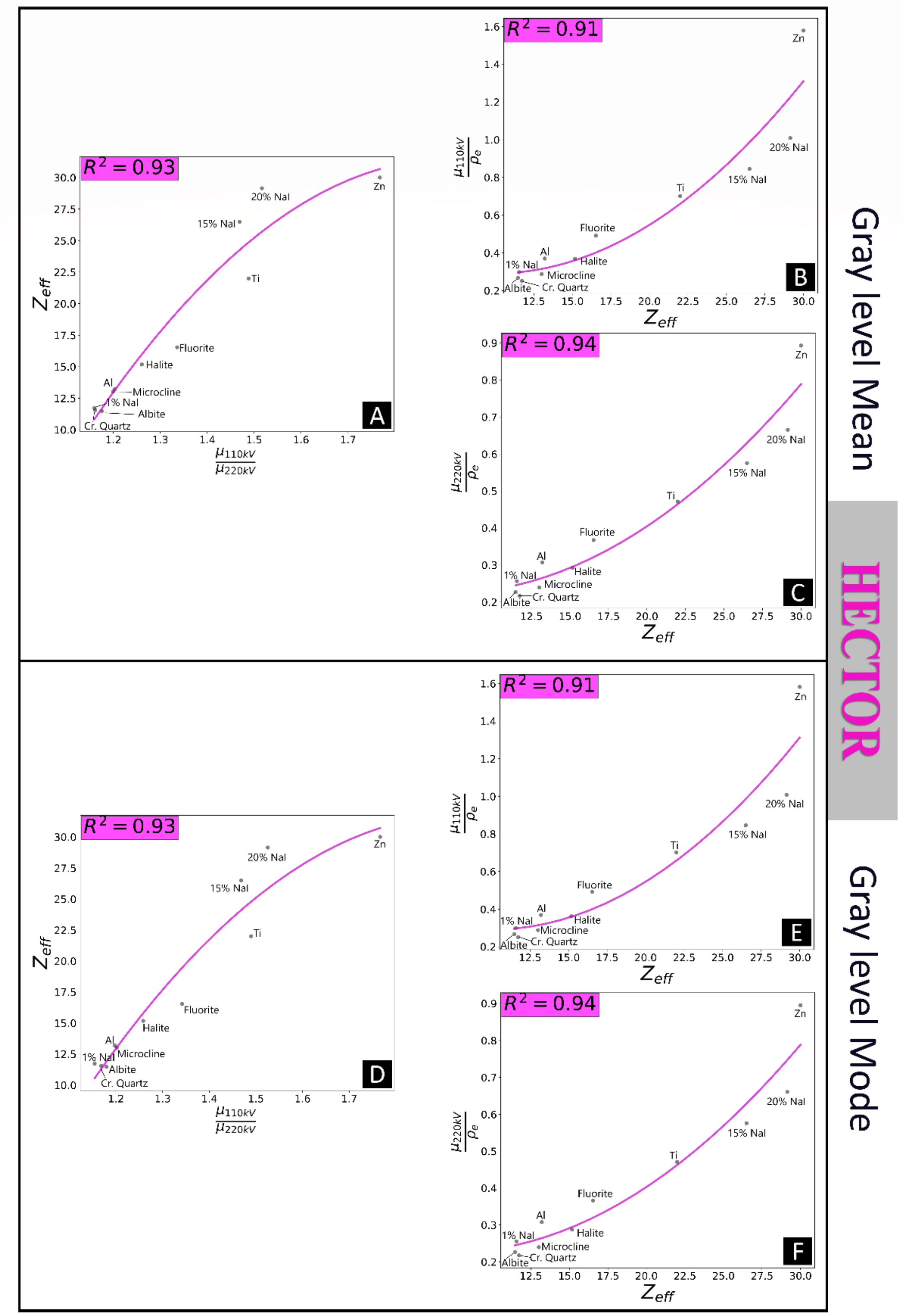

Figure 4.5: HECTOR calibration curves.

Calibration curves determined with HECTOR scanner and *m*-set of calibration samples. Using the mean of gray level histogram, there is A) Z_{eff} model; B) ρ_e model using $\mu_{110\,kV}$; C) ρ_e model using $\mu_{220\,kV}$. Using the mode of gray level histogram, there is D) Z_{eff} model; E) ρ_e model using $\mu_{110\,kV}$; F) ρ_e model using $\mu_{220\,kV}$.

The rock samples μ values at both energies were obtained using Equation 4.4., and their Z_{eff_Meas} and ρ_{e_Meas} values were retrieved using Equations 4.5 and 4.6. For each evaluation both mean and mode of gray level histogram were used. Table 4.7 presents the difference between the calculated Z_{eff_Calc} and ρ_{e_Calc} (Table 4.4) and the measured ones with dual-energy HECTOR scanner.

	HECTOR			
	Chalk	**Hematitic-oolite**	**Chert**	
Z_{eff_Calc}	14.67	18.81	11.75	
ρ_{e_Calc}	4.35E+23	7.70E+23	7.00E+23	
Z_{eff_Meas}	15.18	18.79	11.71	**Gray level Mode**
% difference	*3.52%*	*0.05%*	*0.27%*	
ρ_{e_Meas} **using** $\mu_{110\ kV}$	4.57E+23	7.71E+23	6.58E+23	
% difference	*4.91%*	*0.05%*	*5.91%*	
ρ_{e_Meas} **using** $\mu_{220\ kV}$	4.52E+23	7.72E+23	6.80E+23	
% difference	*3.78%*	*0.25%*	*2.84%*	
Z_{eff_Meas}	15.25	18.91	11.72	**Gray level Mean**
% difference	*3.96%*	*0.53%*	*0.23%*	
ρ_{e_Meas} **using** $\mu_{110\ kV}$	4.72E+23	7.96E+23	6.77E+23	
% difference	*8.45%*	*3.37%*	*3.21%*	
ρ_{e_Meas} **using** $\mu_{220\ kV}$	4.42E+23	7.49E+23	6.71E+23	
% difference	*1.41%*	*2.74%*	*4.04%*	

Table 4.7: HECTOR, characterization results.

Z_{eff_Meas} and ρ_{e_Meas} measured using DECT and the HECTOR scanner and using both mean and mode of gray level histograms. The percentage difference is with Z_{eff_Calc} and ρ_{e_Calc} of Table 4.4. The electron density ρ_e values are in units of $moles\text{-}e^{-}/cm^{3}$.

4.5.4 CoreTOM experiments

The same acquisition conditions of HECTOR and the same set of calibration materials (*m*-set) were used with the CoreTOM scanner, to reproduce similar results. Figure 4.6 shows the calibration curves obtained using the mean of gray level histogram to calculate μ (A is Z_{eff} model, B ρ_e model using $\mu_{110\ kV}$ and C ρ_e model using $\mu_{220\ kV}$) and the mode (D is Z_{eff} model, E ρ_e model using $\mu_{110\ kV}$ and F ρ_e model using $\mu_{220\ kV}$).

Again, μ values at both energies were calculated using Equation 4.4., and their Z_{eff_Meas} and ρ_{e_Meas} values were measured using Equations 4.5 and 4.6, and both mean and mode of gray level histogram were used. Table 4.8 presents the outcomes and the difference between the calculated Z_{eff_Calc} and ρ_{e_Calc} and the measured ones with dual-energy CoreTOM scanner at the same conditions of the previous measurements with HECTOR scanner.

Then, different calibrations aiming to investigate a wider range of energies and calibration sets were performed: Figure 4.7 shows the curves for Z_{eff} and ρ_e models obtained using the *g*-set of calibration materials (Table 4.1). As described in section 2.4, different energies couples are used. The calibration curves for the other sets of Table 4.1 are available in Figures 9.1 and 9.2, Annexe III. The correlation coefficients R^2 are between 0.85 and 0.96, lower values than the ones previously obtained and, again, they are quite similar when the mean and the mode are compared. F and N, ρ_e models obtained with $\mu_{230\ kV}$ (both mean and mode of gray levels), have highest R^2. Z_{eff} calibration curves change their shape according to the energy used, while ρ_e calibration curves do not.

Using the μ values calculated with Equation 4.4, Z_{eff_Meas} and ρ_{e_Meas} values were obtained using Equations 4.5 and 4.6. Table 4.9 presents Z_{eff_Meas} and ρ_{e_Meas} obtained with CoreTOM scanner, *g*-set of calibration materials and three different energy couples, as well as the difference between the calculated Z_{eff_Calc} and ρ_{e_Calc}. All the results are available in Table 9.3 and 9.4, Annexe III.

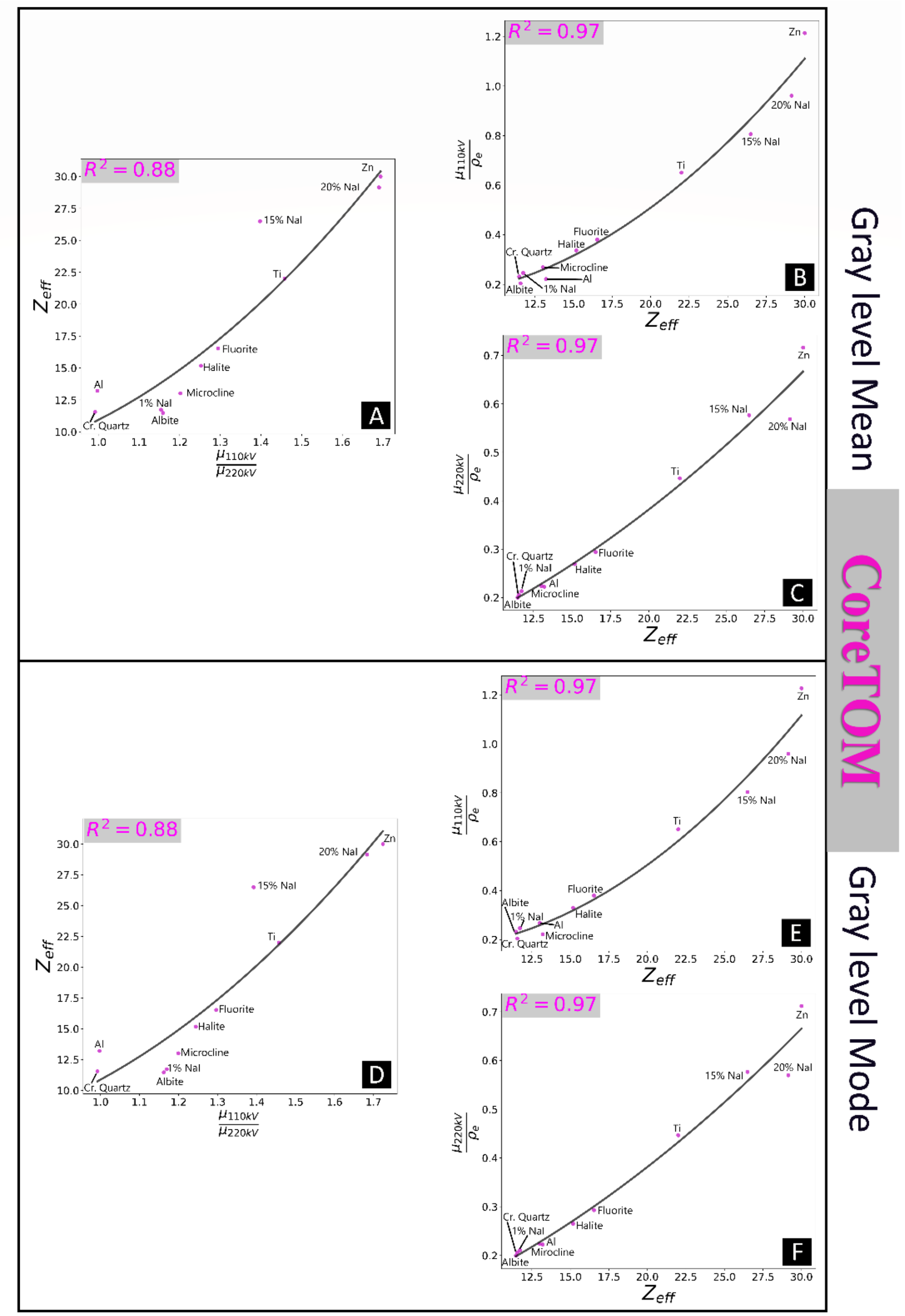

Figure 4.6: CoreTOM calibration curves.

Calibration curves for the CoreTOM scanner using the same acquisition conditions and set of calibration materials (*m*-set) of HECTOR. A) Z_{eff} model; B) ρ_e model using $\mu_{110\,kV}$; C) ρ_e model using $\mu_{220\,kV}$ using the mean of gray level histograms. D) Z_{eff} model; E) ρ_e model using $\mu_{110\,kV}$; F) ρ_e model using $\mu_{220\,kV}$ using the mode of gray level histograms.

	CoreTOM			
	Chalk	**Hematitic-oolite**	**Chert**	
Z_{eff_Calc}	14.67	18.81	11.75	
ρ_{e_Calc}	4.35E+23	7.70E+23	7.00E+23	
Z_{eff_Meas}	15.41	16.07	13.81	**Gray level Mode**
% difference	*4.98%*	*14.49%*	*17.55%*	
ρ_{e_Meas} **using** $\mu_{110\ kV}$	5.52E+23	1.05E+24	6.79E+23	
% difference	*3.81%*	*36.71%*	*2.92%*	
ρ_{e_Meas} **using** $\mu_{220\ kV}$	4.21E+23	9.71E+23	6.53E+23	
% difference	*3.42%*	*26.03%*	*6.62%*	
Z_{eff_Meas}	15.41	20.33	13.78	**Gray level Mean**
% difference	*5.06%*	*8.17%*	*17.36%*	
ρ_{e_Meas} **using** $\mu_{110\ kV}$	4.63E+23	9.45E+23	6.83E+23	
% difference	*6.35%*	*22.68%*	*2.31%*	
ρ_{e_Meas} **using** $\mu_{220\ kV}$	4.32E+23	8.61E+23	6.57E+23	
% difference	*0.74%*	*11.81%*	*5.98%*	

Table 4.8: CoreTOM, characterization results.

Z_{eff_Meas} **and** ρ_{e_Meas} **measured using CoreTOM scanner and the same DECT protocol previously used for HECTOR scanner and using both the mean and mode of gray level histograms. The percentage difference is with** Z_{eff_Calc} **and** ρ_{e_Calc} **of Table 4.4. The electron density** ρ_e **values are in units of** $moles\text{-}e^-/cm^3$**.**

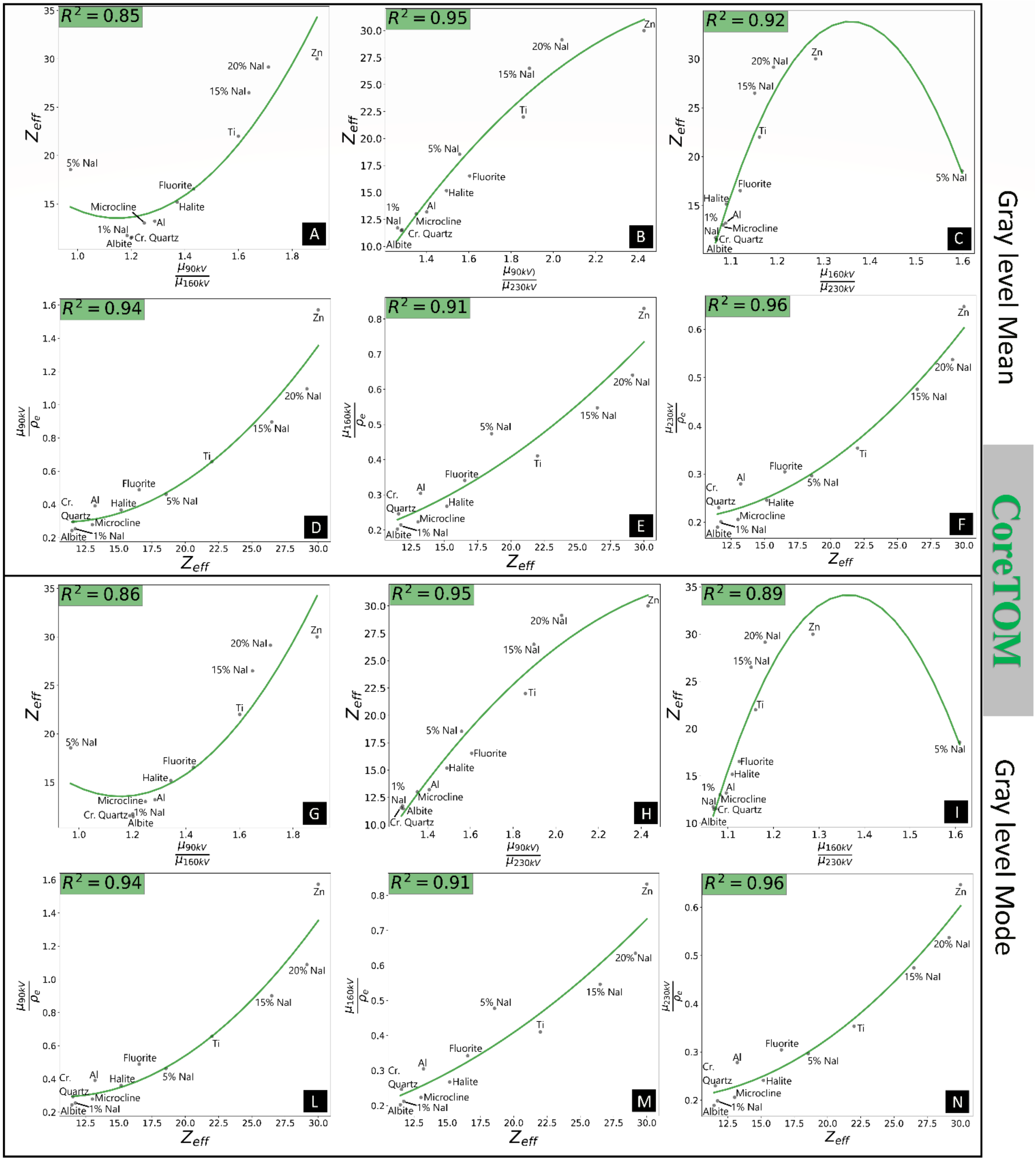

Figure 4.7: CoreTOM calibration curves.

Z_{eff} calibration curves obtained using mean gray level histogram and $\mu_{90\,kV}/\mu_{160\,kV}$ (A), $\mu_{90\,kV}/\mu_{230\,kV}$ (B), and $\mu_{160\,kV}/\mu_{230\,kV}$ (C); using mode gray level histogram and $\mu_{90\,kV}/\mu_{160\,kV}$ (G), $\mu_{90\,kV}/\mu_{230\,kV}$ (H), and $\mu_{160\,kV}/\mu_{230\,kV}$ (I); ρ_e model obtained using mean gray level histogram and $\mu_{90\,kV}$ (D), $\mu_{160\,kV}$ (E), and $\mu_{230\,kV}$ (F); using mode gray level histogram and $\mu_{90\,kV}$ (L), $\mu_{160\,kV}$ (M), and $\mu_{230\,kV}$ (N).

		CoreTOM			
		Chalk	**Hematitic-oolite**	**Chert**	
	Z_{eff_Calc}	14.67	18.81	11.75	
	ρ_{e_Calc}	4.35E+23	7.70E+23	7.00E+23	
$\mu_{90\ kV}/\mu_{160\ kV}$	Z_{eff_Meas}	14.71	19.06	13.75	**Gray level Mode**
	% difference	*0.27%*	*1.39%*	*17.07%*	
	ρ_{e_Meas} **using** $\mu_{90\ kV}$	5.01E+23	9.26E+23	6.48E+23	
	% difference	*15.06%*	*20.15%*	*7.36%*	
	ρ_{e_Meas} **using** $\mu_{160\ k}$	3.77E+23	6.03E+23	5.27E+23	
	% difference	*13.47%*	*21.71%*	*24.62%*	
$\mu_{90\ kV}/\mu_{230\ kV}$	Z_{eff_Meas}	15.45	21.66	11.86	
	% difference	*5.32%*	*15.21%*	*0.98%*	
	ρ_{e_Meas} **using** $\mu_{90\ kV}$	5.50E+23	9.78E+23	8.61E+23	
	% difference	*26.23%*	*26.93%*	*23.07%*	
	ρ_{e_Meas} **using** $\mu_{230\ kV}$	3.78E+23	5.62E+23	6.54E+23	
	% difference	*13.31%*	*27.02%*	*6.48%*	
$\mu_{160\ kV}/\mu_{230\ kV}$	Z_{eff_Meas}	14.86	19.95	11.24	
	% difference	*1.31%*	*6.08%*	*4.31%*	
	ρ_{e_Meas} **using** $\mu_{160\ kV}$	4.55E+23	7.67E+23	7.10E+23	
	% difference	4.58%	0.41%	1.44%	
	ρ_{e_Meas} **using** $\mu_{230\ kV}$	4.99E+23	8.69E+23	7.60E+23	
	% difference	14.51%	12.84%	8.61%	
$\mu_{90\ kV}/\mu_{160\ kV}$	Z_{eff_Meas}	14.62	22.42	13.76	**Gray level Mean**
	% difference	*0.31%*	*19.24%*	*17.12%*	
	ρ_{e_Meas} **using** $\mu_{90\ kV}$	4.75E+23	7.62E+23	6.13E+23	
	% difference	*9.11%*	*1.15%*	*12.45%*	
	ρ_{e_Meas} **using** $\mu_{160\ kV}$	3.60E+23	4.66E+23	4.98E+23	
	% difference	*17.39%*	*39.57%*	*28.78%*	

$\mu_{90\ kV}/\mu_{230\ kV}$	Z_{eff_Meas}	15.39	24.74	11.96	
	% difference	*4.92%*	*31.59%*	*1.82%*	
	ρ_{e_Meas} **using** $\mu_{90\ kV}$	5.66E+23	1.03E+24	8.70E+23	
	% difference	*30.08%*	*33.16%*	*24.28%*	
	ρ_{e_Meas} **using** $\mu_{230\ kV}$	3.90E+23	5.36E+23	6.61E+23	
	% difference	*10.41%*	*30.38%*	*5.54%*	
$\mu_{160\ kV}/\mu_{230\ kV}$	Z_{eff_Meas}	15.94	24.32	11.74	
	% difference	*8.61%*	*29.36%*	*0.02%*	
	ρ_{e_Meas} **using** $\mu_{160\ kV}$	4.33E+23	6.52E+23	6.98E+23	
	% difference	*0.46%*	*15.39%*	*0.26%*	
	ρ_{e_Meas} **using** $\mu_{230\ kV}$	4.76E+23	7.62E+23	7.47E+23	
	% difference	*9.41%*	*1.06%*	*6.75%*	

Table 4.9: CoreTOM, characterization results.

Z_{eff_Meas} and ρ_{e_Meas} measured using DECT with three different energy couples, both mean and mode of gray level histograms and the CoreTOM scanner. The percentage difference is with Z_{eff_Calc} and ρ_{e_Calc} of Table 4.4. The electron density ρ_e values are in units of $moles\text{-}e^-/cm^3$.

4.6 Discussion

XRD analysis (Table 4.2) showed that the chalk and hematitic-oolite samples are mineralogically heterogeneous, whereas the chert is pure. µ-CT slices of these rocks (Figure 4.8) illustrate that chalk (left) and chert (right) have a homogeneous dense texture, but hematitic-oolite (centre) is very heterogeneous. Note that for hematitic-oolite only an oolitic section was selected.

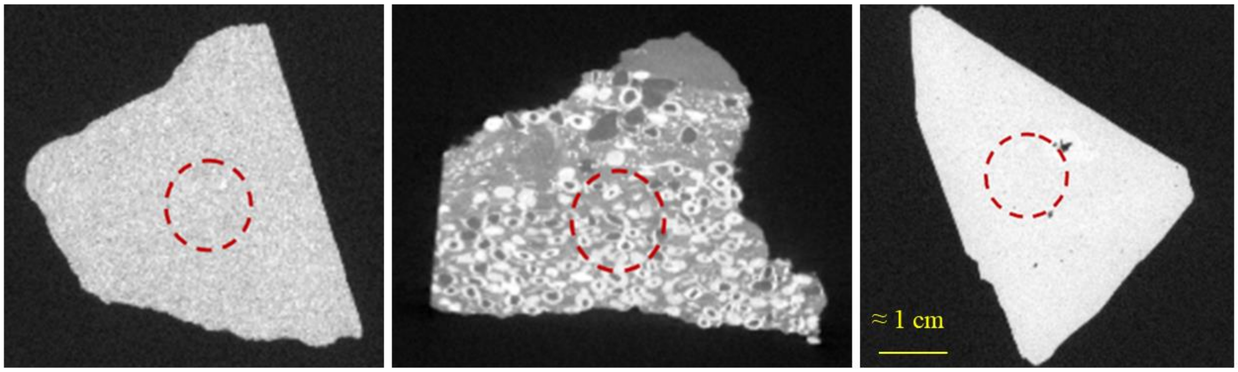

Figure 4.8: Rock sample slices.

Slices of chalk (left), hematitic-oolite (centre) and chert (right) acquired with the Hector scanner at 220 kV; the dotted circle indicates where analyses were performed.

4.6.1 Medical CT

The calibration curves reported in Figure 4.3 yielded high R^2 correlation coefficients. There is no significant difference between the curves obtained with the mean or the mode of gray level values. One outlier is present in each curve, but, as reported previously by Martini *et al.* (2021), it is difficult to explain why they appear because they are values for NaI solution samples that otherwise perform very well. Despite their presence the calibration is efficient. Indeed, Martini *et al.* (2021) identified several pure common minerals using this DECT protocol and this medical scanner, including pure calcite, hematite, and quartz, comparable with the rocks characterized in this work. They obtained a difference for both properties (Z_{eff} and ρ_e) of about 2% for a calcite mineral and about 1% for a quartz mineral, slightly lower than values reported here for rock samples (Table 4.5, gray level mode). However, their pure hematite was characterized by a difference of 22% for Z_{eff} and 14% for ρ_e, which is larger than the value obtained for the hematitic-oolite (about 10% for Z_{eff} and 4% for ρ_e Table 4.5, gray level mode). To understand these differences, some factors should be considered. Martini *et al.* (2021) compared their measured

Z_{eff} and ρ_e with theoretical properties of commercially purchased mineral “standards” with no control on the possibility for minerals to contain impurities. The samples here are natural rocks and not standards, so porosity and heterogeneity have an influence on X-rays attenuation. For example, theoretical electron density of hematite was estimated to be about 1.5E+24 *moles-e*$^{-}$*/cm*^{3} in Martini *et al.* (2021), whereas it is only 7.7E+23 *moles-e*$^{-}$*/cm*^{3} (Table 4.4) for hematitic-oolite: a lower density entails a better signal-to-noise ratio (especially at 70 kV) and in turn a better material discrimination (Hendee, 2002).

In this experiment, the choice between mean and mode for μ calculation was tested. For the medical CT scanner, the determined μ are not significantly different. However, among the results presented in Table 4.5, one is noteworthy: the percent difference between measured and calculated properties of hematitic-oolite is always smaller when the mode of gray level histogram is used. Table 4.2 and 4.3 show that the rock is heterogeneous, and Figure 4.9 that its gray level is not normally distributed. Therefore, using the mode seems better to characterize such heterogenous samples.

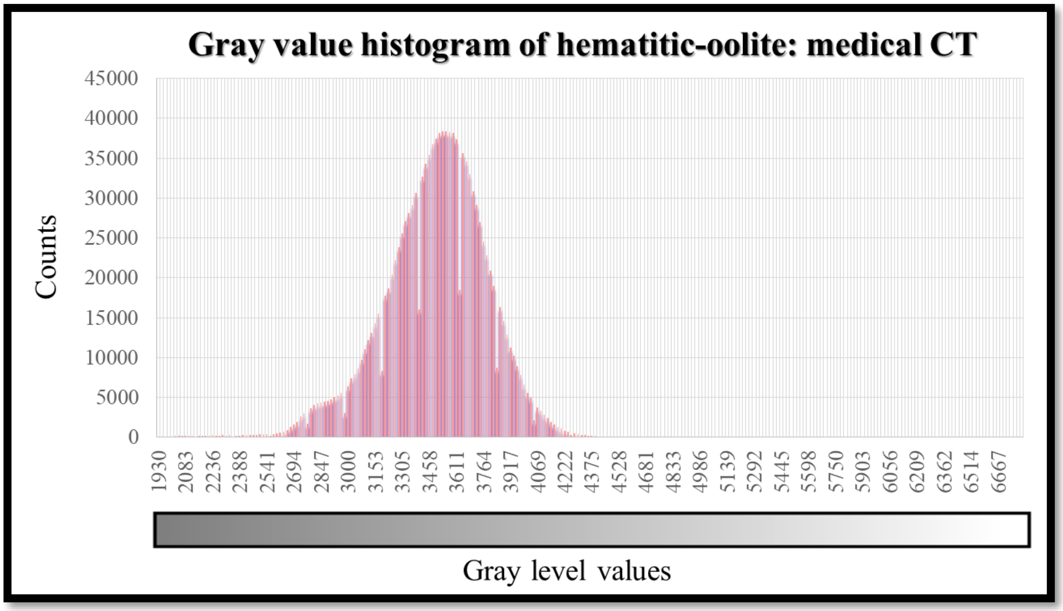

Figure 4.9: Gray level histogram of hematitic-oolite, medical CT.

This gray level histogram of hematitic-oolite is from medical CT slices, acquired at 140 kV.

Another important consideration about the outcomes obtained by Martini *et al.* (2021) is that they opted for μ_{low} in the ρ_e model because the correlation was stronger. Indeed, Figure 4.3 shows R^2

= 0.98 in ρ_e model using $\mu_{70\ kV}$ and $R^2 = 0.96$ in ρ_e model using $\mu_{140\ kV}$. However, as described in Table 4.5, this is not always true: hematitic-oolite presents an electron density that is closer to calculated value using $\mu_{140\ kV}$, probably because of the higher X-ray penetration.

4.6.2 *Arion* and HECTOR

The calibration curves obtained using the μ values from Setup *Optimizer* (Figure 4.4) yielded the highest R^2 correlation coefficients, although the Z_{eff} calibration curves do not perfectly fit all the data points. This mismatch between curves and data points is more pronounced in the calibration obtained with HECTOR (Figure 4.5), and in this case R^2 correlation coefficients are lower. Both *Arion* and HECTOR Z_{eff} calibration curves (Figure 4.4A and Figures 4.5A and 4.5D) showed a concave shape, lighter for the former and more pronounced for the latter.

The rock characterization obtained with μ values from Setup *Optimizer* have a maximum percent difference between simulated and calculated properties of 25% (specifically, for hematitic-oolite sample), which is comparable with the one obtained with medical CT scanner. However, the characterization with HECTOR entails a percentage difference between measured and calculated properties smaller than the modeled ones (Table 4.7), i.e., generally less than 5%. The explanation probably lies in the irregular sample shape. Setup *Optimizer* considers mainly homogeneous cylindrical shape; thus, the simulation result may not be perfectly representative of the samples analysed here.

Although the general difference between the values obtained by the mean and the mode of gray levels is not significant, again the choice of the mode rather than mean in hematitic-oolite characterization improves the results. The gray level histogram from a HECTOR slice is bimodal: the difference between Figures 4.9 and 4.10 is due to the instrumental resolution, 600 μm for medical CT and 25 μm for HECTOR, which, in the case of HECTOR, better reveals the presence of two dominant components.

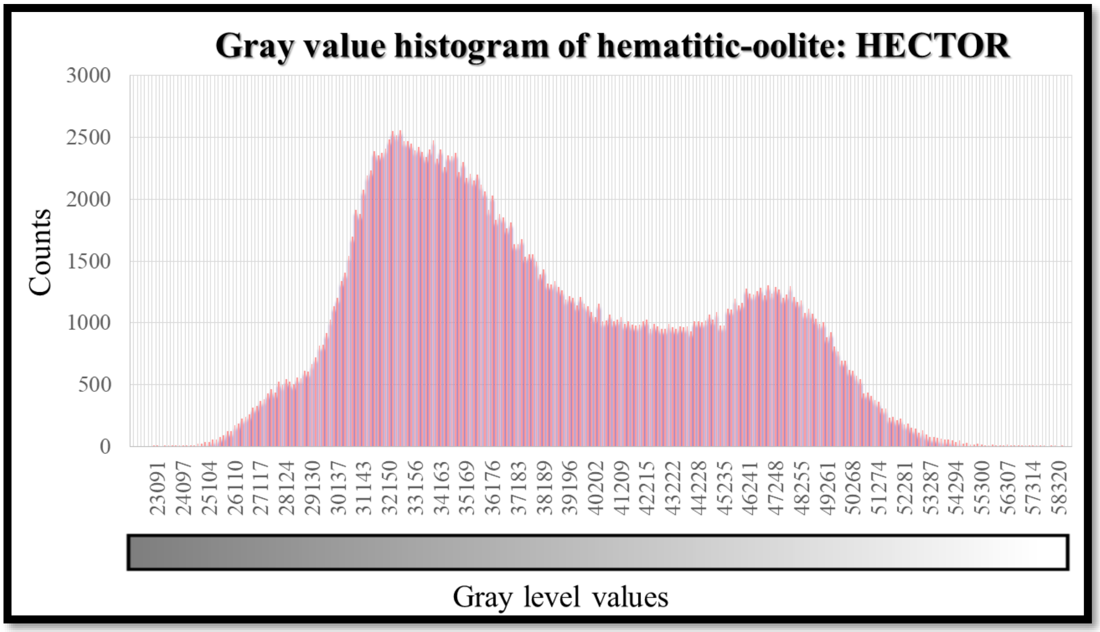

Figure 4.10: Gray level histogram of hematitic-oolite, HECTOR.

This gray level histogram of hematitic-oolite is from HECTOR slice, acquired at 110 kV.

Table 4.7 shows that the percentage difference with Z_{eff_Calc} and ρ_{e_Calc} is the smallest, entailing the best results among these three scanners. However, using gray level mode and μ calculated at high energy, 220 kV, is the best choice to determine ρ_e.

4.6.3 CoreTOM

The calibration curves obtained with the CoreTOM scanner using the same acquisition conditions than HECTOR and the same set of calibration materials (*m*-set) (Figure 4.6) yielded high R^2 correlation coefficients (between 0.88 and 0.97). An outlier (15% NaI) and a mismatch between data points and curves are visible in both Z_{eff} models (Figure 4.6A and D). The outlier is difficult to explain because other solutes perform well; moreover, this 15% NaI sample, despite not perfectly fitting the curve is not an outlier in the HECTOR calibration. Here, Z_{eff} curve, unlike the one obtained at HECTOR, has a convex shape. This rock characterisation (Table 4.8) does not perform as well as those accomplished using HECTOR scanner (Table 4.7), even though the acquisition settings is the same.

The calibration curves aiming to cover a wide range of energies (Figure 4.7) have lower R^2 correlation coefficients than the ones obtained using the same acquisition condition of HECTOR

(Figure 4.6); the deviations between the data points and the best fitting curves are larger for the CoreTOM, but there are no pronounced outliers. As in the case of the medical CT scanner, using the mean rather than the mode of the histogram gray values does not provide an overwhelmingly lower percentage difference.

The $\mu_{90\ kV}/\mu_{160\ kV}$ settings of the CoreTOM are the ones being the closest to the medical CT scanner (i.e., 70/140 kV), it is interesting to note that the difference between calculated and measured properties is more pronounced when using the CoreTOM (an average difference of about 7% for medical CT *vs* an average difference of about 12% for both Z_{eff} and ρ_e with CoreTOM). This is probably due to the sue of two different kinds of filters of the incident X-ray beam; indeed, the bowtie filter of medical CT makes the X-ray bandwidth narrower than metal plates typically used in micro-CT (Primak *et al.*, 2010).

Although the results presented in Table 4.9 show high variability, it is observed that $\mu_{160\ kV}/\mu_{230\ kV}$ allows to lower the percentage difference with calculated values and this happens whenever the curve of the Z_{eff} model has a concave shape. In summary, the parameters that best characterize the three rocks using the CoreTOM scanner are: $\mu_{160\ kV}/\mu_{230\ kV}$ for Z_{eff} characterization, $\mu_{160\ kV}$ for ρ_e characterization, mode of gray level histogram, with the *g*-set of calibration materials (Table 4.1).

4.6.4 Curve shape in Z_{eff} calibration model

The most important interaction between photons and materials in dual-energy CT techniques are photoelectric absorption and Compton scattering. The former dominates at lower energies and depends on target chemical composition (Z_{eff}), the latter is predominant at higher energies and is related to sample density (ρ_e). It is not possible determining a threshold energy between these two phenomena because target composition and X-ray spectrum, which is related to the tube of CT scanner, are involved as well (Johnson, 2012). As reported by Saldaña *et al.* (2012), the predominance of these two phenomena is inversely proportional: photoelectric absorption decreases with increasing energy and, conversely, the Compton scattering increases with increasing energy (Figure 4.11).

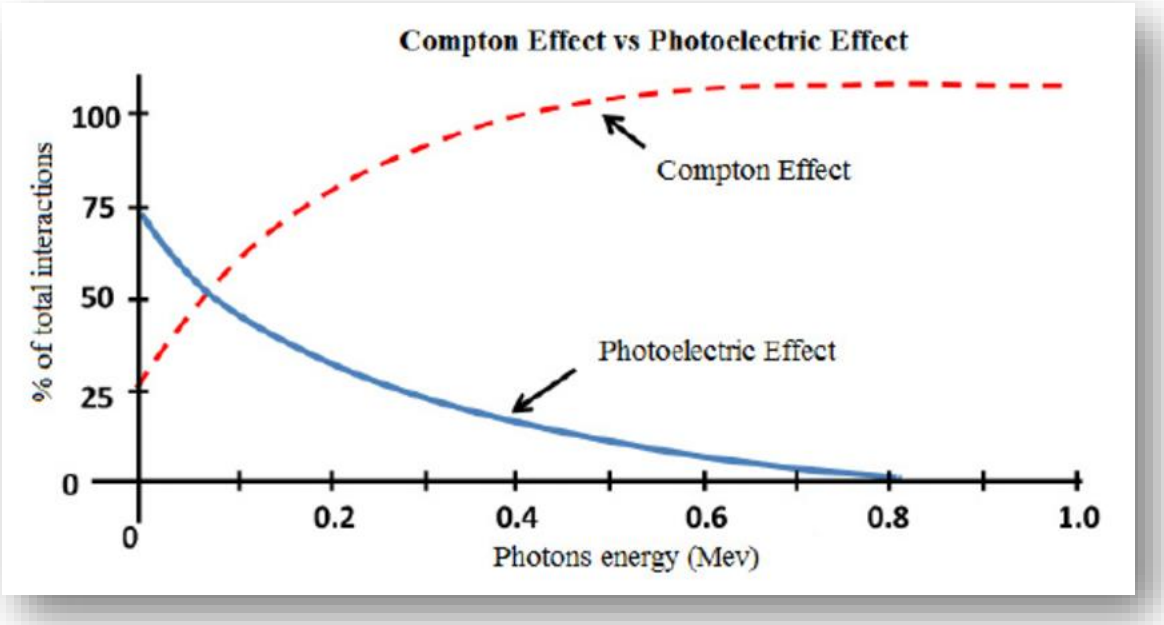

Figure 4.11: Rate of photoelectric absorption and Compton effect in relation to the incident beam energy. From Saldaña *et al.* (2012).

Most geological materials have a high X-ray attenuation, so the energy used must be high enough to penetrate the material but not too high so as not to lose the influence of photoelectric absorption. Observing the graph in Figure 4.11, the best energy should be as close as possible to the phenomena intersection to maximize the influence of photoelectric absorption and have a good material penetration. However, this intersection point is not universal but depends on the material target as well as the incident energy, and it can be summarised in the attenuation coefficient. Figure 4.12 (Pots, 2022) shows an example of the attenuation coefficient and the interaction predominance according to different energies.

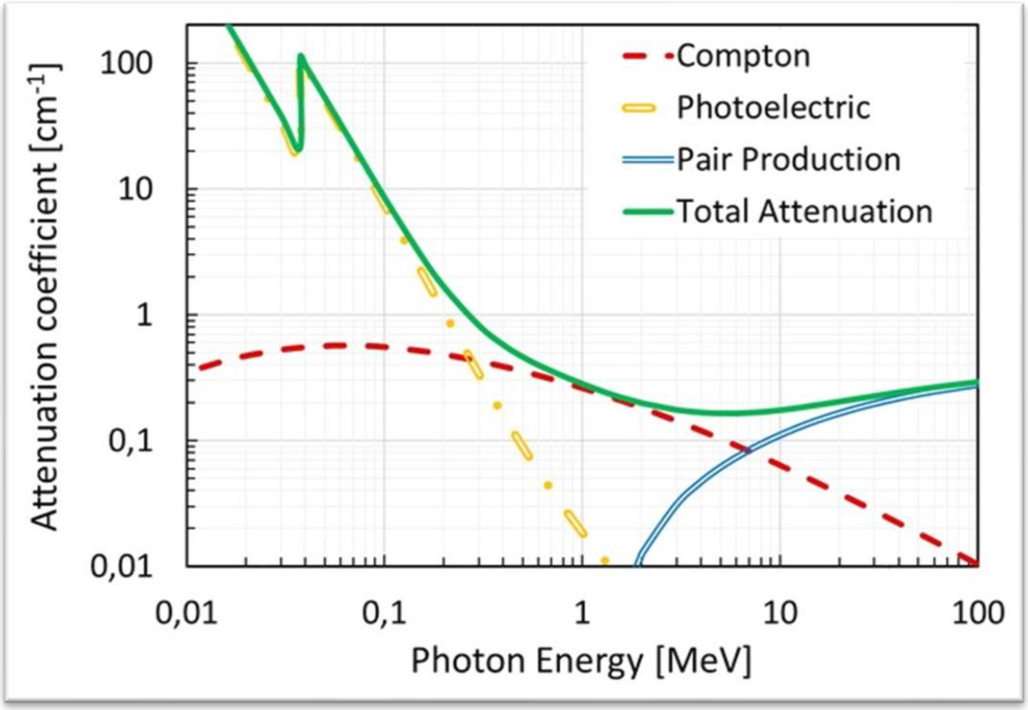

Figure 4.12: Attenuation coefficient of BaF$_2$.

Attenuation coefficient of BaF$_2$ for different photon energies (green) and contributions of photoelectric effect (yellow), Compton scattering (red) and pair production (blue). 4.89 g/cm^3 as BaF$_2$ density have been used (Pots, 2022).

Observing the Z_{eff} model in Figure 4.7, the curve shape changes with increasing energy and it occurs in each calibration (Figures 9.1 and 9.2 in Annexe III show the curves achieved using every set of calibration materials). The plot obtained by $\mu_{90\ kV}/\mu_{160\ kV}$ (Figure 4.7A) has a convex fit, like the one obtained by medical CT scanner (Figure 4.3), where the energies involved are comparable (70 kV and 140 kV). Increasing the high energy of the μ ratio ($\mu_{90\ kV}/\mu_{230\ kV}$) (Figure 4.7B) straightens the curve and increasing both energies further ($\mu_{160\ kV}/\mu_{230\ kV}$), makes the curve concave (Figure 4.7C). 5% NaI solution could be interpreted as an outlier in Figure 4.7A and C; however, it does not exhibit the same behavior in other calibration curves, and other solutes present in the calibrations sets perform well. If these outliers were removed, the curve would remain concave (although less pronounced). Thus, their presence seems not to affect the curve shape of the calibration models Here, the energies involved are comparable with those used in HECTOR (110 kV and 220 kV), where Z_{eff} model presents a concave shape as well (Figure 4.5).

Observing the results, the best rock characterisation occurs at higher energies and when the shape of Z_{eff} curve becomes concave. This could be interpreted as an approach of material attenuation to the intersection between photoelectric absorption and Compton scattering, where the influence of the former is maximised compared to the use of lower energy. Figure 4.11 shows that photoelectric absorption and Compton scattering have an opposite trend with increasing energy, and this is in line with the calibration obtained at higher energy, where Z_{eff} model is concave and ρ_e model is convex.

Finding the best energy couple for each material based on the specific attenuation can be mathematically done if spectrum information is available. However, not all geology laboratories have the necessary knowledge and trained personnel to calculate the best settings. Thus, the guideline to look at the curve shape would improve and fasten the material characterisation.

4.6.5 Scanner comparison

The three CT scanners characterized three different rocks with different levels of accuracy. The least effective scanner was the medical CT, which led to measured Z_{eff_Meas} and ρ_{e_Meas} having up to 10% difference on average compared to calculated values. This is not surprising because the medical CT and the image reconstruction algorithms are optimized to scan human bodies, as quickly as possible and with the lowest possible doses. They are not designed for geological materials, but the fast scan large samples is an advantage, especially when it comes to study long geological sequences from cores. The CoreTOM performs better (the lowest percentage difference with the measured values is about 5%) using higher energy. HECTOR was the scanner that had the best results (less than 5% difference on average compared to calculated values).

Another important difference among the three experiments is the resolution, related to a different scanning time (section 4.4.4). Figure 4.13 shows the difference of the images captured with the hematitic-oolite, the most heterogeneous specimen. On the left, the sample has been scanned with the medical CT at 140 kV and anisotropic voxels of 0.1 x 0.1 x 0.6 mm: its heterogeneity is barely visible. In the centre, the scan was obtained with CoreTOM at 160 kV and isotropic voxels 50 µm: the resolution markedly improves, and the rock heterogeneity is well visible, although it is slightly noisy. On the right, the hematitic-oolite has been scanned with HECTOR at 110 kV and isotropic voxels 25 µm: details, sharpness and contrast are excellent and in terms of imaging this is the best outcome.

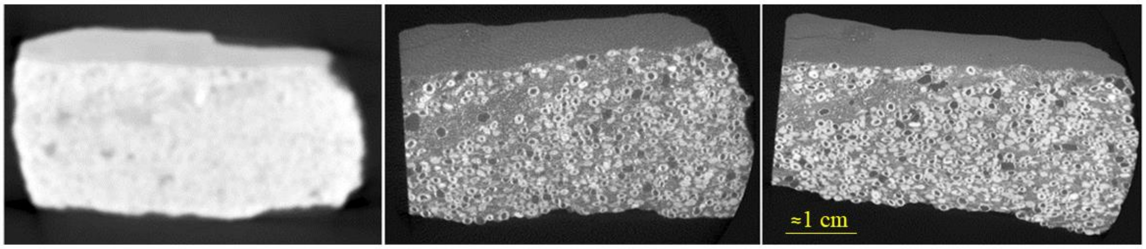

Figure 4.13: Hematitic-oolite acquired with the three scanners.

Slices of hematitic-oolite scanned with medical CT and 600 μm resolution (left), CoreTOM and 50 μm resolution (center), HECTOR and 25 μm resolution (right).

If the sample and its details are not well detected, some misinterpretation can occur, as the Figures 4.9 and 4.10 demonstrate, where the gray level histogram turns out to be bimodal with improving resolutions.

Different sets of calibration materials (Table 4.1) were tested in this paper. Their choice played a fundamental role for the final characterization according to the instrument. *b*-set turned out to be the best one for medical CT scanner, *g*-set for CoreTOM scanner and *m*-set for HECTOR scanner. Thus, it is not possible to define a universal set of calibration materials. The comparison between the calibration obtained with HECTOR (Figure 4.5) and CoreTOM (Figure 4.6) using identical settings confirms this observation: the attenuation of the samples, the correlation coefficients and the shape of the calibration curves change. The most marked differences appear in Z_{eff}-models where the distribution of the samples for the same energy ratio varies so much that they modify the shape of the curve, which is concave for HECTOR and convex for CoreTOM. In general, the smallest difference with calculated Z_{eff_Calc} and ρ_{e_Calc} were obtained when the Z_{ef} calibration curve had a concave shape, probably because the photoelectric absorption effect is maximized in relation to calibration samples and spectrum of the specific tube used.

4.7 Conclusion

Three geological rocks (chalk, hematitic-oolite and chert) with contrasting density, chemistry and mineralogy have been analyzed to precisely calculate their effective atomic number and electron density.

They were then characterized by the dual-energy CT stoichiometric method using three different instruments: a medical CT, a custom-built micro-CT, and a commercial micro-CT.

Five different energy couples, six sets of calibration materials, two statistical descriptors of gray level histogram to calculate μ and different resolutions were tested to study changes in the characterization of the samples.

Each scanner has its own best setting that was evaluated using the lowest percentage difference between the measured and the calculated Z_{eff} and ρ_e:

- about 10% difference using the medical CT scanner;
- less than 5% difference using HECTOR;
- about 5% difference using the commercial micro-CT.

Three rocks have also been characterized with different levels of accuracy. Yet, defining a general DECT protocol proved to be unfeasible because several factors must be considered: each scanner has its own instrumental properties which influence the measurements, and, depending on the sample and the expected outcome, one instrument is more suitable than the other.

However, the following guidelines are proposed:

- the selection of best statistical descriptor of the gray levels histogram should consider the heterogeneity of rock sample to calculate μ;
- the best characterizations are obtained when the Z_{eff} calibration curve has a concave shape;
- the knowledge of the incident spectrum facilitates the selection of the best acquisition settings for a specific instrument, as showed by the results obtained with HECTOR. Yet, it does not turn out to be essential, as demonstrated by the results of the CoreTOM;
- there are no universal best acquisition settings because they depend on the scanner characteristics, mainly the incident spectrum and on the type of samples being analyzed.

4.8 Acknowledgements

This research was funded by *Fonds de recherche du Québec–Nature et technologies*, *Natural Sciences and Engineering Research Council of Canada*, *Canada Research Chairs Program* and *Canada Foundation for Innovation.*

The *Excite Network* funded by the European Union's Horizon 2020 research and innovation programme under grant agreement No 10100561 and the *UGent* Core facility, UGCT

(BOF.COR.2022.0009). The authors thank Prof. Matthieu Boone (Ghent University), Dr. Jan Dewanckele (TESCAN) and Philippe Letellier (INRS) for their support and advice.

4.9 References

Akbari A. GS (2015) Micro-CT scanning of soil aggregate: the importance of image thresholding. in *2nd International Conference on Tomography of Materials and Structures*Québec, QB, Canada), p 622-626.

Alves H *et al.* (2015) Mineralogy evaluation and segmentation using dual-energy microtomography. *X-Ray Spectrometry* 44(3):99-104.

Arnold J *et al.* (1983) Computed tomographic analysis of meteorite inclusions. *Science* 219(4583):383-384.

Boespflug X, Long BFN, Occhietti S (1995) Cat-Scan in Marine Stratigraphy - a Quantitative Approach. *Marine Geology* 122(4):281-301.

Bourque AE, Carrier JF, Bouchard H (2014) A stoichiometric calibration method for dual energy computed tomography. *Physics in Medicine & Biology* 59(8):2059-2088.

Bushberg JT, Seibert, J.A., Leidholdt, E.M., Boone, J.M. (2012) *The essential physics of medical imaging.* LWW, Third edition

Butler BM, Hillier S (2021) powdR: An R package for quantitative mineralogy using full pattern summation of X-ray powder diffraction data. *Computers & Geosciences* 147.

Cnudde V, Boone MN (2013) High-resolution X-ray computed tomography in geosciences: A review of the current technology and applications. *Earth-Science Reviews* 123:1-17.

Cnudde V *et al.* (2006) Recent progress in X-ray CT as a geosciences tool. *Applied Geochemistry* 21(5):826-832.

Coenen JCG, Maas J. (1994) Material classification by dual-energy computerized x-ray tomography. in *International symposium on computerized tomography for industrial applications*), p 120–127.

Di Schiavi Trotta L *et al.* (2022) Beam-hardening corrections through a polychromatic projection model integrated to an iterative reconstruction algorithm. *NDT & E International* 126.

Duliu OG, Rizescu CT, Ricman C (2003) Dual energy gamma-ray axial computer tomography investigation of some metamorphic and sedimentary rocks. *Neues Jahrbuch fòr Geologie und Paläontolgie* 228(3):343-362.

Eberl DD (2003) User Guide to RockJock - A Program for Determining Quantitative Mineralogy from X-Ray Diffraction Data. 10.3133/ofr200378.

Fourie S (1974) THE CRANIAL MORPHOLOGY OF THRINAXODON LIORTHINUS SEELEY. *Annals of the South African Museum* 65:337-400.

Gagnon-Poiré A *et al.* (2021) Reconstructing past hydrology of eastern Canadian boreal catchments using clastic varved sediments and hydro-climatic modelling: 160 years of fluvial inflows. *Climate of the Past* 17(2):653-673.

Gordic S *et al.* (2014) Advanced modelled iterative reconstruction for abdominal CT: qualitative and quantitative evaluation. *Clinical Radiology* 69(12):e497-504.

Hendee WR, Ritenour, E.R. (2002) *Mediacal Imaging Physics.* A JOHN WILEY & SONS, INC., PUBLICATION, USA, fourth

Iovea M *et al.* (2009) Dual-energy X-ray computer axial tomography and digital radiography investigation of cores and other objects of geological interest. *Engineering Geology* 103(3-4):119-126.

Johnson TR (2012) Dual-energy CT: general principles. *AJR Am J Roentgenol* 199(5 Suppl):S3-8.

Kalender W (2011) *Computed tomography : fundamentals, system technology, image quality, applications.* Wiley-VCH, Weinheim, 3rd rev.

Keller AA (1997) High resolution cat imaging of fractures in consolidated materials. *International Journal of Rock Mechanics and Mining Sciences* 34(3-4):155.e151-155.e116.

Martini M *et al.* (2024) Exploring the application of dual-energy CT to discriminate sediment facies in a varved sequence. *The Depositional Record* 10(1):231-244.

Martini M *et al.* (2021) Identification of Common Minerals Using Stoichiometric Calibration Method for Dual-Energy CT. *Geochemistry Geophysics Geosystems* 22(11):1-14.

Mizutani R, Suzuki Y (2012) X-ray microtomography in biology. *Micron* 43(2-3):104-115.

Ni X *et al.* (2017) Quantitative 3D spatial characterization and flow simulation of coal macropores based on μCT technology. *Fuel* 200:199-207.

Paziresh M *et al.* (2016) Tomography of atomic number and density of materials using dual-energy imaging and the Alvarez and Macovski attenuation model. *Journal of Applied Physics* 119(21).

Pots RH (2022) *Investigation of new technologies to improve light collection from scintillating crystals for fast timing*. (Dissertation, RWTH Aachen University, 2022).

Primak AN *et al.* (2010) Dual-source dual-energy CT with additional tin filtration: Dose and image quality evaluation in phantoms and in vivo. *AJR Am J Roentgenol* 195(5):1164-1174.

Re A *et al.* (2015) X-ray tomography of a soil block: a useful tool for the restoration of archaeological finds. *Heritage Science* 3(1).

Remeysen K, Swennen R (2008) Application of microfocus computed tomography in carbonate reservoir characterization: Possibilities and limitations. *Marine and Petroleum Geology* 25(6):486-499.

Saldaña G *et al.* (2012) High Density Devices Applied to a Gamma-Camera Implementation. (Advanced Image Acquisition, Processing Techniques and Applications I. InTech2012).

Van Daele M *et al.* (2014) Multidirectional, synchronously-triggered seismo-turbidites and debrites revealed by X-ray computed tomography (CT). *Sedimentology* 61(4):861-880.

Van Geet M, Swennen R, Wevers M (2000) Quantitative analysis of reservoir rocks by microfocus X-ray computerised tomography. *Sedimentary Geology* 132(1-2):25-36.

Vinegar HJ, Wellington SL (1987) Tomographic imaging of three-phase flow experiments. *Review of Scientific Instruments* 58(1):96-107.

Vlassenbroeck J *et al.* (2006) Octopus 8: A High Performance Tomographic Reconstruction Package for X-ray Tube and Synchrotron micro-CT. *Advances in X-ray Tomography for Geomaterials,* https://doi.org/10.1002/9780470612187.ch13. p 167-173.

Zhao Y *et al.* (2018) Pore structure characterization of coal by synchrotron radiation nano-CT. *Fuel* 215:102-110.

5 GENERAL DISCUSSION

Multispectral approaches for X-ray tomography date back to the seventies, and while in one respect the technique may seem old, its potential has not yet been fully exploited, especially in the geosciences. Indeed, although several papers have been published (section 1.4.4), this method has yet to become routinely employed in Earth Science laboratories equipped with CT scanners. A probable explanation lies in the fact that geological materials are very diverse: minerals, rocks and sediments have a very different structure in terms of density, heterogeneity, cohesion, or chemical composition. Yet, finding a common analytical procedure fitting the needs of each research topic is not easy. Moreover, many conventional DECT techniques (spectral method) depend on knowledge of the CT scanner photon incident spectra to guarantee an accurate effective atomic number determination, which could be difficult to obtain (Chapter 1: Z_{eff} is related to photoelectric absorption, related in turn to incident X-ray beam). Spectrum calculation requires operators with specialized physics and engineering skills that are not common, especially in geology laboratories. Although the creation of an interdisciplinary team is encouraged to cover many aspects of science, this is not always possible, and it becomes necessary to look for a viable alternative. Thus, finding a method able to easily give qualitative and quantitative information from X-ray CT data, exploring the eventual limitations and making the operators aware, is crucial.

5.1 Preliminary tests

Testing stoichiometric calibration methods was chosen for this project because no a priori knowledge of the incident X-ray spectrum is needed, which simplifies the calculations and eases its implementation. Moreover, the methodology does not require intensive computation capabilities and can be implemented using a laptop.

Although the stoichiometric calibration method of Bourque *et al.* (2014) was selected for the development of this work (see section 1.4.2), it was neither the only one available nor the first to be tested in the framework of this project.

The parametrization of energy ratios to derive the effective atomic numbers (but not the electron density) from DECT, developed by Landry *et al.* (2013), initially seemed to be the most appropriate technique; indeed, the authors were able to accurately retrieve the Z_{eff} of human tissues without the knowledge of the X-ray beam using the following mathematical formula:

$$\frac{\mu_{\mathrm{low\ E}}}{\mu_{\mathrm{high\ E}}} \approx \frac{A_{\mathrm{low\ E}} + B_{\mathrm{low\ E}} Z_{\mathrm{eff}}^{n-1} + C_{\mathrm{low\ E}} Z_{\mathrm{eff}}^{m-1}}{A_{\mathrm{high\ E}} + B_{\mathrm{high\ E}} Z_{\mathrm{eff}}^{n-1} + C_{\mathrm{high\ E}} Z_{\mathrm{eff}}^{m-1}} \tag{5.1}$$

A, B and C correspond, respectively, to the contribution of Compton scattering, Rayleigh scattering (negligible) and photoelectric absorption; the exponent *n* and *m* are related to the latter two physical interactions and typically take the values of 2.86 and 4.62 (Landry *et al.*, 2013). The results they obtained are particularly consistent because their accuracy was superior to the conventional spectral methods. Thus, since the calculation of Z_{eff} could be tricky (Bonnin *et al.*, 2014; Landry *et al.*, 2013), it was decided at the beginning of this work, to calculate the effective atomic number with the mathematical equation (Equation 5.1) developed by Landry *et al.* (2013) and the electron density with the expression (Equation 1.18) developed by Bourque *et al.* (2014), even this technique allows to calculate Z_{eff} as well (section 1.4.2).The anticipated advantage to mix the two approaches is to use the best estimation of Z_{eff} by Landry *et al.* (2013) to limit the propagation of the error in ρ_e calculation.

To validate this workflow, some preliminary tests were conducted on previously scanned images at the INRS. Indeed, the database of the lab contains multi kV CT-scan images because DECT was previously explored by Bourgault (2017), but no specific conclusion was obtained. Thus, Z_{eff} values for 45 minerals, differing in chemical composition and density, were calculated using Landry *et al.* (2013) equation (Equation 5.1). Then, ρ_e was calculated using the Bourque *et al.* (2014) equation (Equation 1.18). However, the results were not satisfactory.

Thus, both Bourque *et al.* (2014) equations were tested (Equation 1.16 to calculate Z_{eff} and Equation 1.18 to calculate ρ_e) and the obtained values turned out to be consistently more accurate. Although the Landry technique has yielded excellent results in the medical field, it was ineffective in characterizing samples with a heavier chemical composition than that of human tissues. The method of Bourque *et al.* (2014) and polynomial regression, therefore, proved to be more suitable for geological samples.

5.2 Methodology definition

After opting to use the methodology developed previously by Bourque *et al.* (2014) for the calculation of Z_{eff} and ρ_e, the first tests were carried out with a medical-CT using specimens already owned by the laboratory (i.e., all the investigated minerals), while others were purposely purchased (i.e., Titanium and Zinc bar) and in-house fabricated (i.e., all the NaI solutions).

The first part of this study (Chapter 2) tackled only on common and compositionally simple geological minerals. After obtaining Z_{eff} and ρ_e using this DECT methodology, a *Python* routine was developed to verify its accuracy; it consists of a dictionary having information on 69 minerals, mapped to their theoretical Z_{eff} and ρ_e: among more than 4000 existing minerals, only the most common ones were selected because increasing number of minerals would have resulted in finding specimens unlikely to be present in common rocks, and therefore would have decreased the efficiency of the method. Nevertheless, if a rare mineral needs to be identified in the frame of a study, or if the mineralogy of a rock is known and the goal of the DECT characterization is to look at the distribution of the minerals within the rock, the list of potential minerals can be customized in the library. that mineral can be added to the library.

The main goal of this study is not finding an alternative to identify minerals but pave the way for a successful implementation of DECT in Earth Science laboratories. Several dual-energy methodologies applied to Earth science were listed in the first chapter of this thesis, but as already explained, they are more computationally complex and often limited to the study of very few samples (Paziresh *et al.*, 2016), i.e. those methods are not well suited to most minerals that are found in the geological realm. Moreover, many of these studies seem to be designed for very specific goals, aiming to identify only specific minerals, being the focus of only one research field (Remeysen & Swennen, 2008), others do not share the codes (Alves *et al.*, 2015). Most previous works were not usable by other geoscientists. As a result, dual-energy techniques have never become routine analyses except in some companies, where the methodology remains proprietary and inaccessible to the public. This article, already published in the journal "*Geochemistry, Geophysics, Geosystems*", precisely explained each step of the work and made available to everyone the in-house developed *Python* routines to allow any laboratory with any kind of access (even in the hospital, like Boespflug *et al.* (1995) used to do before the Lab CT Scan establishment) to a medical CT scanner to be able to perform their first non-destructive 3D identification of geological material.

However, some limitation must be considered. Mineral samples here investigated have been compared with their theoretical properties, and not with their actual ones. Thus, even the results are quite accurate and satisfying, they remain theoretical and possible impurities (due to the very nature of the samples) were not considered. Moreover, the calibration is strongly dependent to the device. Some mineral samples owned by the laboratory that were previously multi kV scanned have not been used in this experiment because the detector has been changed in between and same measurements could not be guaranteed. Yet, if there are no instrumental changes, the calibration can be reused, otherwise it will have to be redone, entailing additional time, budget, and available staff.

Despite these considerations, these mineral analyses gave promising outcomes, demonstrating that this stoichiometric calibration method can successfully characterize even samples with higher Z_{eff} and ρ_e values than in human tissue, for which medical scanners were firstly developed.

5.3 Application of the method to a real case study

A more complex geological sample was investigated. A varved sequence from South Sawtooth Lake in the Canadian Arctic was scanned at low and high energy to characterize three sedimentary facies (Chapter 3). This core has already been the subject of numerous scientific papers (Francus *et al.*, 2008; Lapointe *et al.*, 2020; Lapointe *et al.*, 2019) because it contains an interesting and rare annually resolved 2.9 ka paleoclimate record.

Analyzing this core with DECT was not trivial because several additional challenges needed to be faced. For instance, its granulometry is highly heterogeneous, involving different porosities, which influence the calculation of Z_{eff} and ρ_e. Moreover, the diverse shape of the grains can also affect the analysis due to varying interaction between the grains and the incident photons, e.g., angular grains could be more susceptible to beam hardening than rounded grains. Eventually, the variability of these properties within single sedimentary facies prevents to define a specific value for Z_{eff} and ρ_e for each layer. This causes a main problem: not having a specific reference makes impossible to accurately define an analytical margin of error. Moreover, the dependence on CT resolution plays an important role. It is possible to distinguish among macro-, meso- and micro-scale of variability, meaning details on the order of cm, mm and µm, respectively. Macro variations are clearly visible with a medical-CT scanner and do not create problems in the study. The meso-differences are more difficult to distinguish, but thanks to the dual-energy technique they can be well detected over a very long sedimentary sequence like the one from South Sawtooth Lake. However, micro differences cannot be discerned with this tool. Indeed, a voxel (0.1 x 0.1 x 0.6 mm) may contain multiple materials, which should have different gray levels, but, due to insufficient resolution results in an unrealistic averaging of gray levels. It is very important to take these factors into consideration when dealing with DECT analysis.

Despite these drawbacks, a strategy was developed to retrieve information that is geologically meaningful, as described in the paper. The first step was the selection of a ROI to obtain an investigation zone small enough to have only one relatively homogeneous sedimentary layer per slice. Then, three different facies (coarse-grained clastic varves, fine-grained clastic varves and rapidly deposited layers) were picked according to the existing literature presented in this section.

The core was studied with the DECT technique and multiple layers of the three different facies were grouped to carry out a statistical analysis (see Chapter 3). Even if several outliers are present, the box-and-whisker diagrams of Z_{eff} and ρ_e show the three sedimentary layers can be characterized based on their properties (Figure 5.8), having different ranges of values. Unfortunately, the comparison with micro-XRF core scanner, normally used for elemental composition, did not lead to expected results (see Chapter 3). Nevertheless, Itrax scanner was the best choice as it allowed analysis at the same resolution as CT scanner (i.e., 600 μm).

While these measurements were conducted on a well-known and already extensively studied core, the efficiency of our DECT technique on sediment cores may look underperforming in comparison with some commercial products available. Indeed, despite this “simplification”, the foundation for a new approach to the characterization of sedimentary records, which can be accessible to everyone, was laid. As it has already been anticipated, some companies offer dual-energy analysis on rock cores, obtaining apparently reliable results. However, their detailed method remains proprietary and often they applied DECT on samples easier to interpret, i.e., consolidated rock cores with no porosity variations and very sharp mineralogical and lithological contrasts. The core from South Sawtooth Lake is more complex being unconsolidated, containing mineralogical variations, consisting of very thin and inclined varves, and having multiple fractures. Here the *Python* routines that allowed the study to be carried out were presented, each step explained in detail so any geological laboratory can easily repeat the measurements. Further developments outlined in section 5.5 below will contribute to bridge the gap with these commercial products.

This study demonstrated this technique is suitable to identify rapidly deposited layers (e.g., volcanic eruption, earthquakes, or avalanches), which often have a coarser grain seize. However, some events are tenuous in the sedimentary sequence such as crypto-tephra. These layers are too thin to be identified with a medical CT scanner, but using a micro-CT is a avenue to be investigated.

5.4 Application of the technique on different CT scanners

The idea to pursue a comparison of different CT-scanners arose from the laboratory's recent acquisition of CoreTOM micro-CT and from some preliminary tests on minerals showing totally different results compared to the ones previously obtained with the medical-CT scanner. Indeed, devising a measurement protocol means not only finding something that works in a particular case, but making it usable for multiple cases while ensuring its repeatability. Thus, providing guidelines for DECT analyses is essential to escort future users from different geological laboratories to obtain the best possible results.

The study highlighted key factors that must be considered before starting DECT analyses. First of all, it has been shown how X-ray spectra are different from each other, even if the instruments are similar (Tescan built the CoreTOM using HECTOR as a prototype). This specific interaction between the incident beam and the analyzed materials also affects the calibration and the choice of standard samples to carry it out. Indeed, as the comparison between HECTOR and CoreTOM showed, using the same acquisition conditions does not guarantee that the same results will be obtained because the interaction between a spectrum and a specific material is unique. Moreover, the most appropriate energy pair is not universal but depends on the scanner.

Despite these considerations and although it could be argued that there might be perfect analysis conditions for each instrument, the guidelines to follow in the real world are simpler. Even without knowing the specific spectrum, it is suggested to choose an energy pair powerful enough to allow enough X-rays to penetrate the investigated materials and reach the detector in sufficient quantity to ensure a signal-to-noise ratio that is adequate for a geological characterization. That means always using the maximum possible energy as high energy pair member. The choice of low energy is trickier because it must be high enough to penetrate the material but not too high so as not to lose the influence of photoelectric absorption (Chapter 4). Indeed, as the outcomes for the CoreTOM showed, 90 kV did not perform as well as 160 kV as a low-energy pair member, although at first, it might seem better to choose energies far apart to well separate the influence of both photoelectric absorption and Compton scattering.

It is suggested to choose a wide range of standard materials and determine the ones that yield the best results, for example, by conducting a test with a known sample. This test is proposed because, as the results have shown, the correlation coefficient R^2 does not guarantee the best characterization. It is recommended that these standard samples cover a wide range of Z_{eff} and ρ_e values and that they be as similar as possible values to those in the samples being studied. In other words, to characterize geological samples, it is recommended to use geological standard materials.

In addition, to achieve better results, it is important to verify that the shape of Z_{eff} calibration curve is concave and if the investigated materials are inhomogeneous, it is better to use the mode instead of the mean of the histogram of the gray levels to calculate μ to attenuate the artefacts induced by beam hardening.

Although it is not possible to define a standard measurement protocol for all laboratories, since each CT scanner is different, these guidelines allow to help achieving a successful characterization of geological materials using DECT.

5.5 On-going development and future perspective for sediment cores

DECT provide two separate series of numerical values, and they can be presented as two profiles to be superimposed on the sagittal images of the cores, either as two separate images, one related to Z_{eff} and another to ρ_e, or as a scatter plot of the properties. The first two methodologies provide visual aid of the sediment image, but they lose the information related to the pair values. Instead, the third correlates the pair values but lose the information related to the location in the image of the core investigated and in the case of geological sequences.

Thus, to make these measurements more readable, a *Python* routine, which combines the scatter plot and the sagittal property of the image, was developed.

The vertical core image is reconstructed from the orthogonal slices, picking up a central line having a width of one pixel, and in each one of them Z_{eff} and ρ_e are calculated. The combination of these properties refers to a colorimetric scatter plot having the electronic density on the y-axis and the effective atomic number on the x-axis. The outcome is a sagittal image of the core, where the different colours represent a pair of Z_{eff} and ρ_e values allowing the characterization of sedimentary facies based on DECT analysis by stoichiometric method (see, for example, Figure 5.1).

The user can change the calibration coefficients (from *a* to *f*, see Chapter 2) and it is also able to modify the range of values of the properties (in Figure 5.1, $9 < Z_{eff} < 14$ and $2E+23 < \rho_e < 8E+23$) depending on the characteristic of the core investigated. Hence, the user can highlight the range of its choice that can better outline details of interest. Higher out-of-range values appear in white, and the lower ones in black. This *Python* routine automatically runs on both medical- and micro-

CT (these scanners produce different format images). In addition to facilitate the interpretation of the results obtained by DECT, this script can help to recognize facies in a sedimentary sequence or build composite sequences.

Although the work in this thesis has provided an excellent foundation for the transformation of DECT into a routine analysis technique, other developments can be envisioned at the *Laboratoire multidisciplinaire de tomodensitométrie pour les ressources naturelles et le génie civil*.

First, the calculation of X-ray beam impacting on the detectors of both the medical- and micro-CT scanners is suggested. By introducing the spectrum into the calculation of Z_{eff}, a more accurate value can be obtained. Second, it is suggested to carry out future dual-energy scans of sediment cores on unopened cores to reduce beam hardening and facilitate the alignment with other measurements, such as the ones acquired by micro-XRF.

Then, the acquisition of a new instrument, capable of acquiring dual-energy images in a single scan, could be considered. They are common in the medical field, but similar instruments are being developed for industrial purposes as well. They are called “Spectral X-ray micro-CT” and have a great potential in materials identification (Sittner *et al.*, 2020), as some works demonstrated (Sénéchal *et al.*, 2023). This kind of micro-CT is not yet popular, but it shows good prospects for innovative research in Earth sciences and civil engineering (domains that study very dense materials). It will also allow for shorter analysis times because it will not be necessary to perform two consecutive scans, as it was the case in this project. Therefore, CT analyses allow for both qualitative and quantitative (Z_{eff} and ρ_e) information and it would improve the research quality in many areas.

In the framework of this research project, specific algorithms to improve the image quality and to correct the beam hardening artifacts has been developed, like described in the work of Di Schiavi Trotta *et al.* (2022b). Combining these innovative algorithms with the characterization of materials with DECT should pave the way to more robust analyses. While this thesis has focused on the geological aspect, the project may have a broader application, such as the research that is carried out every day at the laboratory which includes archaeology, metallurgy, paleontology, and civil engineering.

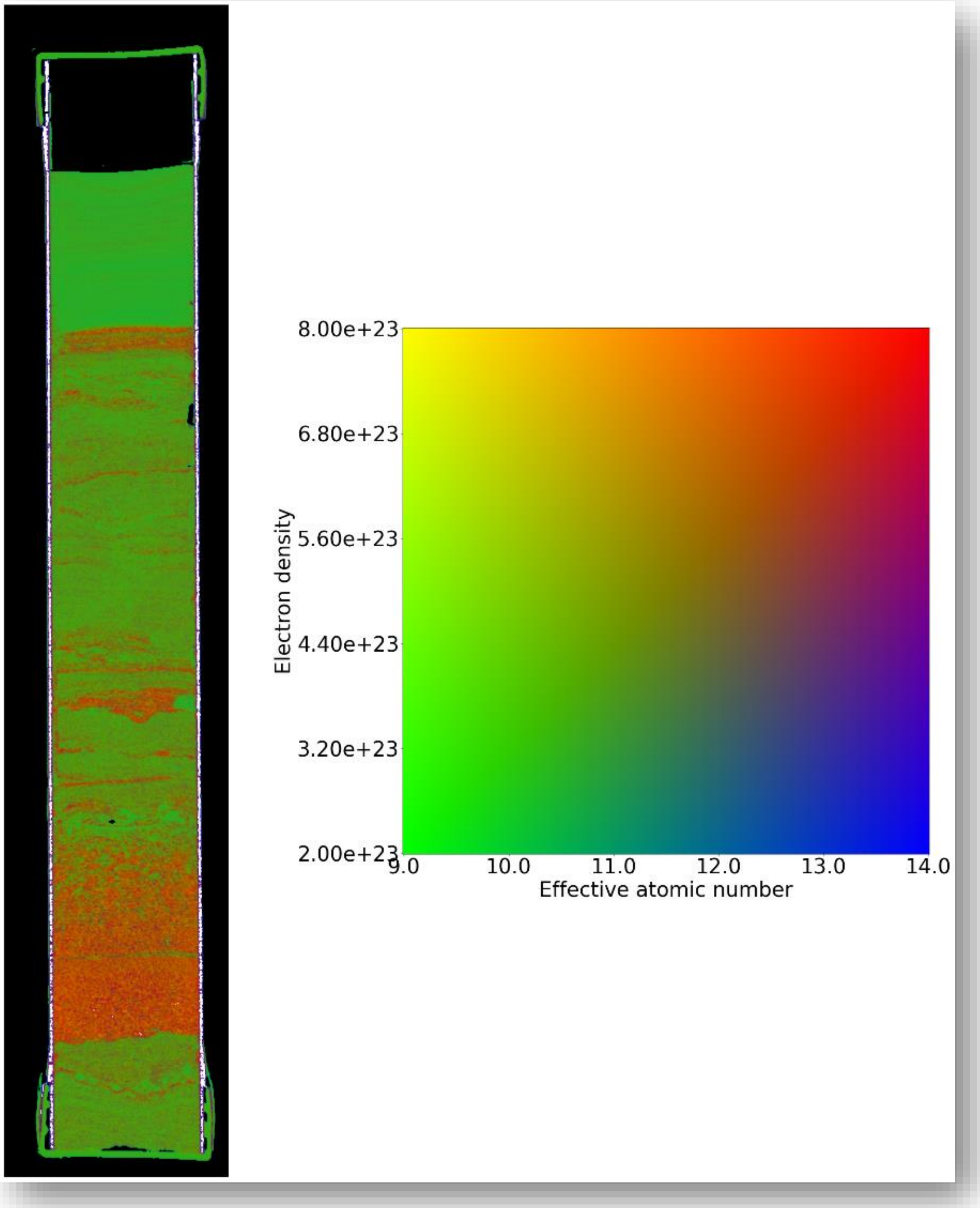

Figure 5.1: Example of the result from the new *Python* routine.

CT sagittal image of core from Manicouagan Lake, Québec, Canada, reconstructed with dual-energy method using the in-house developed algorithm. This core is divided into two zones: orange and green. The former is characterized by high values of Z_{eff} and ρ_e, and the latter by low values. In the bottom the sediment contains a mixture of denser material and alternating several layers. Then, a sudden geologic event, characterized by dense material only having a visibly coarser grain size, happened. In the upper part, the green is visibly deeper and without orange stains.

5.6 References

Alves H *et al.* (2015) Mineralogy evaluation and segmentation using dual-energy microtomography. *X-Ray Spectrometry* 44(3):99-104.

Boespflug X, Long BFN, Occhietti S (1995) Cat-Scan in Marine Stratigraphy - a Quantitative Approach. *Marine Geology* 122(4):281-301.

Bonnin A *et al.* (2014) Concept of effective atomic number and effective mass density in dual-energy X-ray computed tomography. *Nuclear Instruments and Methods in Physics Research Section B: Beam Interactions with Materials and Atoms* 318:223-231.

Bourgault P (2017) *De la boîte noire à la science: reconstruction tomographique contrôlée.* INRS, p

Bourque AE, Carrier JF, Bouchard H (2014) A stoichiometric calibration method for dual energy computed tomography. *Physics in Medicine & Biology* 59(8):2059-2088.

Di Schiavi Trotta L *et al.* (2022b) Beam-hardening corrections through a polychromatic projection model integrated to an iterative reconstruction algorithm. *NDT & E International* 126:102594.

Francus P *et al.* (2008) Limnological and sedimentary processes at Sawtooth Lake, Canadian High Arctic, and their influence on varve formation. *Journal of Paleolimnology* 40(3):963-985.

Landry G *et al.* (2013) Deriving effective atomic numbers from DECT based on a parameterization of the ratio of high and low linear attenuation coefficients. *Physics in Medicine & Biology* 58(19):6851-6866.

Lapointe F *et al.* (2020) Annually resolved Atlantic sea surface temperature variability over the past 2,900 y. *Proceedings of the National Academy of Sciences* 117(44):27171-27178.

Lapointe F *et al.* (2019) Chronology and sedimentology of a new 2.9 ka annually laminated record from South Sawtooth Lake, Ellesmere Island in this NOAA depository: https://www.ncdc.noaa.gov/paleo/study/33214. *Quaternary Science Reviews* 222.

Paziresh M *et al.* (2016) Tomography of atomic number and density of materials using dual-energy imaging and the Alvarez and Macovski attenuation model. *Journal of Applied Physics* 119(21).

Remeysen K, Swennen R (2008) Application of microfocus computed tomography in carbonate reservoir characterization: Possibilities and limitations. *Marine and Petroleum Geology* 25(6):486-499.

Sénéchal P *et al.* (2023) Characterization of oil shales: discriminating power of spectral over conventional X-ray radiography. in *EXCITE workshop*Granada).

Sittner J *et al.* (2020) Spectral X-ray computed micro tomography: 3-dimensional chemical imaging. *X-Ray Spectrometry* 50(2):92-105.

6 CONCLUSION

This thesis developed a non-destructive measurement protocol based on multispectral CT scanning to be applied on geological analyses. Although dual-energy methods have already been used in the past, they have never become a routine technique and their potential in Earth Science has never been fully explored.

The stoichiometric calibration method (initially developed for the study of human tissues) was chosen because it combines simplicity of application and calculation and showed promising results following some preliminary tests.

First, the method was developed for a medical CT scanner aiming to identify several common minerals. The study demonstrated the suitability of the technique for geologically dense materials.

Second, a real case study was investigated. A varved sediment core with three main sedimentary facies, having distinct granulometry and chemical compositions was analyzed. The stoichiometric calibration method allowed these facies to be differentiated based on a difference in effective atomic number and electron density, and therein laying the foundation for a method applicable in several fields, such as environmental sedimentology, climate reconstruction, paleoseismology, and reservoir characterization.

Third, three impure rock specimens of known composition were characterized using three different scanners: a medical CT, a custom-built micro-CT and a commercial micro-CT. Different setting were then tested, demonstrating that the best acquisition conditions are different for each instrument. It was shown that it is unrealistic to develop a measurement protocol valid for every laboratory. However, some important guidelines are defined to help scientists in their characterization studies.

Finally, this thesis provides all the steps to be followed to complete a full characterization of geological materials, but that can also be applied in other fields. This technique can easily be implemented as a routine analysis.

7 ANNEXE I

7.1 Supplementary Data article 1

***READ ME.txt* aims to explain how the two *.py* files work.**

Here all the necessary steps to properly use the Python Scripts are illustrated:

- Run CommonMinerals_database.py.

- Open Mineral_Identification.py.

- Line 9: you have to select the path in order to identify the folder where you saved the scripts. E.g. 'C:/Users/name/Documents/Python/Martini Article'.

- Run Mineral_Identification.py: a sentence will appear, asking you to enter the value you measured with the stoichiometric method of effective atomic number Zeff using β = 2.94; write it and click enter.

- Another sentence will appear, asking you to enter the value you measured with the stoichiometric method of electron density ρe; write it and click enter.

- A list of minerals with an increasing Euclidean distance respect to the values you previously entered will come out.

***CommonMinerals_database.py* is the Python dictionary, aiming to map 69 common minerals (chosen from those of the database http://webmineral.com/) to their respective Z_{eff} and ρ_e (calculated by Equations 2.1 and 2.2).**

```
COMMON_MINERALS_DATABASE= {
"Albite": {
"Density": 2.62,
"Zeff-2.94": 11.472469048079818,
"Rhoe": 7.822362362208457e+23},
```

"Almandine": {
"Density": 4.2,
"Zeff-2.94": 18.65580128131639,
"Rhoe": 1.2297205743608494e+24},

"Aluminum": {
"Density": 2.72,
"Zeff-2.94": 12.999999999999998,
"Rhoe": 7.89217181371944e+23},

"Alunite": {
"Density": 2.75,
"Zeff-2.94": 12.440680019015005,
"Rhoe": 8.316186725786584e+23},

"Anatase": {
"Density": 3.88,
"Zeff-2.94": 18.496549512270903,
"Rhoe": 1.111740293335479e+24},

"Andalusite": {
"Density": 3.15,
"Zeff-2.94": 11.301372465584183,
"Rhoe": 9.365145980883788e+23},

"Andesine": {
"Density": 2.67,
"Zeff-2.94": 12.227482060552354,
"Rhoe": 7.9732054000141e+23},

"Anhydrite": {
"Density": 2.97,
"Zeff-2.94": 15.220445327229688,
"Rhoe": 8.933645039811451e+23},

"Ankerite": {
"Density": 3.05,
"Zeff-2.94": 16.989965876203932,
"Rhoe": 9.050789472291957e+23},

"Anorthite": {
"Density": 2.75,
"Zeff-2.94": 13.206712870129392,
"Rhoe": 8.214535541898868e+23},

"Anorthoclase": {
"Density": 2.59,
"Zeff-2.94": 11.833528139737307,
"Rhoe": 7.732764442275475e+23},

"Apatite": {
"Density": 3.19,
"Zeff-2.94": 15.944600287530207,
"Rhoe": 9.534213090816498e+23},

"Aragonite": {
"Density": 2.93,
"Zeff-2.94": 15.079105270531949,
"Rhoe": 8.814778263270499e+23},

"Arsenopyrite": {
"Density": 6.19,
"Zeff-2.94": 28.31287230230339,
"Rhoe": 1.716974851597177e+24},

"Augite": {
"Density": 3.4,
"Zeff-2.94": 14.849587650317085,
"Rhoe": 1.0144416284586273e+24},

"Barite": {
"Density": 4.48,
"Zeff-2.94": 45.50668904785854,
"Rhoe": 1.2022119317354036e+24},

"Bassanite": {
"Density": 2.73,
"Zeff-2.94": 14.902703710890085,
"Rhoe": 8.268109088264593e+23},

```
"Beryl": {
"Density": 2.77,
"Zeff-2.94": 11.05942235833542,
"Rhoe": 8.255291503149175e+23},

"Biotite": {
"Density": 3.1,
"Zeff-2.94": 14.046773677034428,
"Rhoe": 9.258643836533364e+23},

"Brucite": {
"Density": 2.37,
"Zeff-2.94": 9.863732255733968,
"Rhoe": 7.342062889122694e+23},

"Bytownite": {
"Density": 2.71,
"Zeff-2.94": 12.960435882124468,
"Rhoe": 8.094421164679726e+23},

"Calcite": {
"Density": 2.71,
"Zeff-2.94": 15.079105270531949,
"Rhoe": 8.152917779338925e+23},

"Carnallite": {
"Density": 1.6,
"Zeff-2.94": 14.384873297437753,
"Rhoe": 4.924130042726895e+23},

"Chalcopyrite": {
"Density": 4.2,
"Zeff-2.94": 24.56896250882139,
"Rhoe": 1.1990357200880123e+24},

"Chromite": {
"Density": 4.8,
"Zeff-2.94": 22.008354300105445,
"Rhoe": 1.3688945412453796e+24},
```

```
"Chrysoberyl": {
"Density": 3.67,
"Zeff-2.94": 10.576415960142025,
"Rhoe": 1.0791868584289274e+24},

"Chrysotile": {
"Density": 2.6,
"Zeff-2.94": 10.771962060200371,
"Rhoe": 7.909995420156529e+23},

"Corundum": {
"Density": 4.01,
"Zeff-2.94": 11.140570346462736,
"Rhoe": 1.1842115612297979e+24},

"Cristobalite": {
"Density": 2.33,
"Zeff-2.94": 11.560477823722744,
"Rhoe": 7.005952578061032e+23},

"Diaspore": {
"Density": 3.38,
"Zeff-2.94": 10.681789452284558,
"Rhoe": 1.0179378129433702e+24},

"Diopside": {
"Density": 3.4,
"Zeff-2.94": 13.729071217690343,
"Rhoe": 1.0211624278161763e+24},

"Dolomite": {
"Density": 2.84,
"Zeff-2.94": 13.057015776464228,
"Rhoe": 8.532855576995039e+23},

"Enstatite": {
"Density": 3.2,
"Zeff-2.94": 11.245948074258495,
"Rhoe": 9.59811909386283e+23},
```

"Epidote": {
"Density": 3.45,
"Zeff-2.94": 18.12325012592457,
"Rhoe": 1.0211699694872161e+24},

"Fluorite": {
"Density": 3.18,
"Zeff-2.94": 16.534892305653504,
"Rhoe": 9.320734568765346e+23},

"Galena": {
"Density": 7.6,
"Zeff-2.94": 77.21864154864417,
"Rhoe": 1.874605443991355e+24},

"Glauconite": {
"Density": 2.68,
"Zeff-2.94": 16.58253894948988,
"Rhoe": 7.970714890613709e+23},

"Glaucophane": {
"Density": 2.99,
"Zeff-2.94": 11.224293649935728,
"Rhoe": 8.962617515483455e+23},

"Goethite": {
"Density": 4.27,
"Zeff-2.94": 22.05402451394516,
"Rhoe": 1.244403004079193e+24},

"Graphite": {
"Density": 2.25,
"Zeff-2.94": 6.0,
"Rhoe": 6.768873934491745e+23},

"Gypsum": {
"Density": 2.31,
"Zeff-2.94": 14.109186794487982,
"Rhoe": 7.110138562283063e+23},

```
"Halite": {
"Density": 2.16,
"Zeff-2.94": 15.176649191711663,
"Rhoe": 6.232064526020011e+23},

"Hematite": {
"Density": 5.3,
"Zeff-2.94": 22.962882975471693,
"Rhoe": 1.5190372179494435e+24},

"Hypersthene": {
"Density": 3.55,
"Zeff-2.94": 17.10308637060637,
"Rhoe": 1.049064026074775e+24},

"Illite": {
"Density": 2.75,
"Zeff-2.94": 12.163368559319558,
"Rhoe": 8.333013359883595e+23},

"Ilmenite": {
"Density": 4.79,
"Zeff-2.94": 21.327622060076482,
"Rhoe": 1.3689929105349204e+24},

"Kaolinite": {
"Density": 2.6,
"Zeff-2.94": 10.931109154249787,
"Rhoe": 7.884444458232063e+23},

"Labradorite": {
"Density": 2.7,
"Zeff-2.94": 12.608880891340997,
"Rhoe": 8.06370120227054e+23},

"Lepidolite": {
"Density": 2.79,
"Zeff-2.94": 12.343416688851939,
"Rhoe": 8.307764506798478e+23},
```

```
"Maghemite": {
"Density": 5.49,
"Zeff-2.94": 22.962882975471693,
"Rhoe": 1.573493269158952e+24},

"Magnesite": {
"Density": 2.98,
"Zeff-2.94": 9.334341979935015,
"Rhoe": 8.939584252776136e+23},

"Magnetite": {
"Density": 5.15,
"Zeff-2.94": 23.231442049098938,
"Rhoe": 1.4734604107077724e+24},

"Malachite": {
"Density": 4.03,
"Zeff-2.94": 23.75592913066598,
"Rhoe": 1.163413497726181e+24},

"Microcline": {
"Density": 2.56,
"Zeff-2.94": 13.018089835859668,
"Rhoe": 7.643776077589823e+23},

"Muscovite": {
"Density": 2.83,
"Zeff-2.94": 12.403685488223708,
"Rhoe": 8.463916659996968e+23},

"Natron": {
"Density": 1.46,
"Zeff-2.94": 8.18749815885618,
"Rhoe": 4.670722907434973e+23},

"Oligoclase": {
"Density": 2.65,
"Zeff-2.94": 11.811749605955505,
"Rhoe": 7.912595574302625e+23},
```

"Olivine": {
"Density": 3.3,
"Zeff-2.94": 15.215313578500988,
"Rhoe": 9.799833719966463e+23},

"Orthoclase": {
"Density": 2.55,
"Zeff-2.94": 13.018089835859668,
"Rhoe": 7.613917577286738e+23},

"Phlogopite": {
"Density": 2.83,
"Zeff-2.94": 12.278340928732225,
"Rhoe": 8.45520800891534e+23},

"Pyrite": {
"Density": 5.01,
"Zeff-2.94": 21.61117061278521,
"Rhoe": 1.458562676967126e+24},

"Pyrrhotite": {
"Density": 3.95,
"Zeff-2.94": 23.0431217917461,
"Rhoe": 1.1374228242278168e+24},

"Quartz": {
"Density": 2.65,
"Zeff-2.94": 11.560477823722744,
"Rhoe": 7.968143490069414e+23},

"Rutile": {
"Density": 4.25,
"Zeff-2.94": 18.496549512270903,
"Rhoe": 1.2177567646071614e+24},

"Siderite": {
"Density": 3.87,
"Zeff-2.94": 20.242908072785397,
"Rhoe": 1.1265233868351479e+24},

"Sphalerite": {
"Density": 4.08,
"Zeff-2.94": 26.519795186799314,
"Rhoe": 1.1601775620015652e+24},

"Spinel": {
"Density": 3.65,
"Zeff-2.94": 11.02849073408292,
"Rhoe": 1.0815372267469047e+24},

"Stibnite": {
"Density": 4.56,
"Zeff-2.94": 44.965119767008325,
"Rhoe": 1.2125375751271634e+24},

"Talc": {
"Density": 2.75,
"Zeff-2.94": 11.154207579655175,
"Rhoe": 8.296348568982661e+23},
}

Minerals_Identification.py **is the Python script searching the previously mentioned dictionary to find and identify the samples with the shortest Euclidean distance of these theoretical properties, normalized using the feature scaling method because of the different orders of magnitude.**

```
import sys
sys.path.insert(1, '')
import CommonMinerals_database
import math
import numpy as np
from sklearn.preprocessing import normalize
from scipy.spatial import distance

min_Zeff = np.min([COMMON_MINERALS_DATABASE[key]["Zeff-2.94"] for key in
COMMON_MINERALS_DATABASE.keys()])
max_Zeff = np.max([COMMON_MINERALS_DATABASE[key]["Zeff-2.94"] for key in
COMMON_MINERALS_DATABASE.keys()])
range_Zeff = max_Zeff - min_Zeff

min_Rhoe = np.min([COMMON_MINERALS_DATABASE[key]["Rhoe"] for key in
COMMON_MINERALS_DATABASE.keys()])
max_Rhoe = np.max([COMMON_MINERALS_DATABASE[key]["Rhoe"] for key in
COMMON_MINERALS_DATABASE.keys()])
range_Rhoe = max_Rhoe - min_Rhoe

new_dict = {key:{"Zeff_norm":(COMMON_MINERALS_DATABASE[key]["Zeff-2.94"] - min_Zeff)/range_Zeff,
                 "Rhoe_norm":(COMMON_MINERALS_DATABASE[key]["Rhoe"]-min_Rhoe)/range_Rhoe}
                   for key in COMMON_MINERALS_DATABASE.keys()}

calculated_Zeff = float(input ("Enter the measured Zeff: "))
calculated_rhoe = float(input ("Enter the measured electron density: "))
calculated_Zeff_norm = ((calculated_Zeff - min_Zeff)/(max_Zeff - min_Zeff))
calculated_rhoe_norm = ((calculated_rhoe - min_Rhoe)/(max_Rhoe - min_Rhoe))

single_mineral = {}
listoflists = []
for k in new_dict.keys():
    single_mineral = new_dict[k]
    Zeff = single_mineral["Zeff_norm"]
```

```
    rhoe =  single_mineral["Rhoe_norm"]
    dst= [str((distance.euclidean([calculated_Zeff_norm,calculated_rhoe_norm],[Zeff,rhoe]))) + "="  + str(k)]
    listoflists.append(dst)
finalresult=sorted(listoflists)

print('\n')
for count, item in enumerate(finalresult):
    print(count+1, item)
```

Material	Effective Atomic Number	Electron Density	μ_{low} 70 keV	μ_{high} 140 keV
NaI 50%	39.64	4.04E+23	14.92	6.9
NaI 40%	36.77	3.92E+23	13.18	6.08
NaI 30%	33.39	3.79E+23	10.86	5.17
NaI 25%	31.39	3.71E+23	9.37	4.61
NaI 20%	29.14	3.63E+23	8.08	4.11
NaI 15%	26.49	3.58E+23	6.56	3.49
NaI 10%	23.17	3.52E+23	5.31	2.97
NaI 8%	21.55	3.49E+23	4.28	2.53
NaI 5%	18.54	3.44E+23	3.35	2.11
NaI 1%	11.73	3.38E+23	1.51	1.25
NaI 0.5%	10.11	3.36E+23	1.26	1.12
Aluminium	13.21	7.81E+23	4.39	3.21
Halite	15.17	6.23E+23	4.31	2.28
Crystalline Quartz	11.56	7.98E+23	3.61	2.9
Pyrite	21.61	1.45E+24	10.85	6.11
Fluorite	16.54	9.32E+23	7.48	4.68
Albite	11.47	$7.82\cdot10^{23}$	3.62	2.88
Titanium	22	1.23E+24	19.07	9.94

Table 7.1: Details about the standard samples.

Effective atomic number (column 2) and electron density (column 3) calculated using the Equations 2.1 and 2.2 of the paper; then, linear attenuation coefficients at low (column 4) and high (column 5) energy are calculated using Equation 2.3.

Mineral	μ_{low} 70 keV	μ_{high} 140 keV
Albite	3.53	2.8
Almandine	10.89	6.33
Andesine	4.21	3.15
Ankerite	4.97	3.33
Anorthite	4.18	3.08
Augite	6.89	4.54
Biotite	4.53	3.2
Bytownite	3.78	2.95
Calcite	5.61	3.72
Chalcopyrite	13.21	7.36
Diopside	5.26	3.76
Dolomite	4.56	3.32
Gypsum	4.41	3.05
Hematite	15.72	9.7
Ilmenite	13.29	8.11
Labradorite	4.16	3.12
Magnetite	10.1	5.84
Microcline	4	3
Muscovite	4.29	3.14
Olivine	4.92	3.66
Phlogopite	3.57	2.42
Quartz	3.61	2.89
Talc	3.77	3.03

Table 7.2: Linear attenuation coefficients of minerals.

These samples have been used for their characterization using Equations 2.4 and 2.5 in the validation part of the test. These μ values are calculated alike the previous standard samples.

8 ANNEXE II

8.1 Supplementary Data article 2

READ ME.txt aims to explain how the two .py files work.

Profiles Zeff and Rhoe.py

- After selecting a ROI in dicom slices, a stack of tiff is created: first of all the script transform this tiff stack into an array.
- Then, it is necessary to enter the path of your computer where the tiff stack folders are saved. Line 78 for images acquired at low energy and line 96 for images acquired at high energy.
- Run the script and both profiles and numerical values will be automatically generated.

Facies discrimination.py

- Enter the path of your computer where dicom slices are saved (line 101 for images acquired at low energy and line 108 for images acquired at high energy).
- Run the script and the final volume will be automatically generated.

Profiles Zeff and Rhoe.py is the Python script aiming to plot Z_{eff} and ρ_e properties calculated using DECT method.

```
import numpy as np
from pathlib import Path
import SimpleITK as sitk
import matplotlib.pyplot as plt
from scipy import stats
from scipy import ndimage
import array as arr
import pandas as pd
import csv

def img2array ( img ):
    return sitk.GetArrayFromImage( img )

def saveimg_from_array ( array , image_filename ):
    sitk.WriteImage( sitk.GetImageFromArray(array), str(image_filename ) )

def tif2array ( tif_path ):

    # Get tif individual images
    files = sorted(Path(tif_path).glob("*.tif"))
    # Transform into list of str
    files = [str(x) for x in files]

    # Prepares reading
    reader = sitk.ImageFileReader()
    reader.SetImageIO("TIFFImageIO")

    # Get number of files (dimension in z)
    dimz = len(files)

    # What if dimz = 1? (much simpler)
    if dimz == 1:
        reader.SetFileName(files)
        image = reader.Execute();
        image_array = img2array(image)
```

```
        return image_array

    # Reads files in loop (start with index 0 to get dimensions)
    reader.SetFileName(files[0])
    image = reader.Execute();
    image_array = img2array(image)

    # Get dimensions
    dim_xy = image_array.shape

    # Initialize array that contains all images
    image_stack = np.zeros( (dimz,) + dim_xy )

    # Populate first index
    image_stack[0] = image_array

    # Iterate over the other images
    for x in enumerate(files[1::]):
        reader.SetFileName(x[1])
        image = reader.Execute()
        image_stack[x[0]+1] = img2array(image)
    return image_stack



if __name__ == '__main__':
    import sys
    try:
        input_dir = sys.argv[1]
        output_image = sys.argv[2]
        saveimg_from_array ( tif2array(input_dir) , output_image  )
    except IndexError:
        print("<tiff_directory> <output_image_filename>")

    # enter the path of images acquired at low energy
    img_tiff_low = tif2array(" ")

    array_mu_low=[]
    for i in img_tiff_low:
        mu_pixel_low = ((i/1000)+1)
        mu_pixel_flat_low = mu_pixel_low.flatten()
```

```
    object_index = mu_pixel_flat_low > 1
    mu_pixel_flat_threshold_low = mu_pixel_flat_low[object_index]
    if (mu_pixel_flat_threshold_low.size / mu_pixel_flat_low.size) < 0.7:
        array_mu_low.append(np.nan)
        continue



    media_low = np.mean(mu_pixel_flat_threshold_low)
    array_mu_low.append(media_low)



# enter the path of images acquired at high energy
img_tiff_high = tif2array(" ")

array_mu_high=[]
for i in img_tiff_high:
    mu_pixel_high = ((i/1000)+1)
    mu_pixel_flat_high = mu_pixel_high.flatten()
    object_index = mu_pixel_flat_high > 1
    mu_pixel_flat_threshold_high = mu_pixel_flat_high[object_index]
    if (mu_pixel_flat_threshold_high.size / mu_pixel_flat_high.size) < 0.7:
        array_mu_high.append(np.nan)
        continue

    media_high = np.mean(mu_pixel_flat_threshold_high)
    array_mu_high.append(media_high)




mu1_over_mu2 = np.divide(array_mu_low, array_mu_high)

a=31.6640
b=-41.3636
c=20.2761



Zeff = (a) + (b * mu1_over_mu2) + (c * (mu1_over_mu2**2))

plt.figure(figsize=(15, 8))
plt.xticks(fontsize=20)
```

```
plt.yticks(fontsize=20)
plt.xlabel("Slices", size=30)
plt.ylabel("$Z_{eff}$", size=30)
display(plt.plot(Zeff, color='blue'))
plt.savefig('Title of Zeff profile image.pdf')


rho_W = 3.3427966648311874E+23

d=0.0817
e=0.0383
f=0.0071

denominator=[]
for i in Zeff:
    y=(d) + (e*i) + f*(i**2)
    denominator.append(y)

rho=(np.divide(array_mu_low, denominator))*rho_W

plt.figure(figsize=(15, 8))
plt.xticks(fontsize=20)
plt.yticks(fontsize=20)
plt.xlabel("Slices", size=30)
plt.ylabel("$Rho_{e}$", size=30)
display(plt.plot(rho, color='red'))
plt.savefig('Title of Rhoe profile image.pdf')

pd.DataFrame([Zeff, rho]).transpose().to_excel('Properties values of each slice.xlsx', header=False, index=False)
```

Profiles Zeff and Rhoe.py **is the Python script aiming to generate figures like 3.12 and 3.13.**

```
import numpy as np
from pathlib import Path
import SimpleITK as sitk
import matplotlib.pyplot as plt
from scipy import stats
from scipy import ndimage
import array as arr
import pandas as pd
import csv
import itertools
from openpyxl import load_workbook
import pydicom
import os
from  skimage import io
import matplotlib.pyplot as plt

def img2array ( img ):
   return sitk.GetArrayFromImage( img )

def saveimg_from_array ( array , image_filename ):
   sitk.WriteImage( sitk.GetImageFromArray(array), str(image_filename ) )

def tif2array ( tif_path ):

   # Get tif individual images
   files = sorted(Path(tif_path).glob("*.tif"))
   # Transform into list of str
   files = [str(x) for x in files]

   # Prepares reading
   reader = sitk.ImageFileReader()
   reader.SetImageIO("TIFFImageIO")

   # Get number of files (dimension in z)
   dimz = len(files)

   # What if dimz = 1? (much simpler)
```

```
    if dimz == 1:
        reader.SetFileName(files)
        image = reader.Execute();
        image_array = img2array(image)
        return image_array

    # Reads files in loop (start with index 0 to get dimensions)
    reader.SetFileName(files[0])
    image = reader.Execute();
    image_array = img2array(image)

    # Get dimensions
    dim_xy = image_array.shape

    # Initialize array that contains all images
    image_stack = np.zeros( (dimz,) + dim_xy )

    # Populate first index
    image_stack[0] = image_array

    # Iterate over the other images
    for x in enumerate(files[1::]):
        reader.SetFileName(x[1])
        image = reader.Execute()
        image_stack[x[0]+1] = img2array(image)
    return image_stack

def dicom2array(folder_path):

    dicom_files = sorted([file for file in os.listdir(folder_path) if file.endswith('.dcm')], key=len)
    slices = []
    for file in dicom_files:
        file_path = os.path.join(folder_path, file)
        ds = pydicom.dcmread(file_path)
        slices.append(ds.pixel_array)

    stack = np.stack(slices, axis=0)
    stack = stack.astype(int)
    stack = stack*10-10240
    stack = stack.astype(int)
```

```
    return stack

if __name__ == '__main__':
    import sys
    try:
        input_dir = sys.argv[1]
        output_image = sys.argv[2]
        saveimg_from_array ( tif2array(input_dir) , output_image  )
    except IndexError:
        print("<tiff_directory> <output_image_filename>")



    # enter the  the path of images acquired at low energy
    img_low = dicom2array(" ")
    mu_pixel_low = ((img_low/1000)+1)
    object_index = mu_pixel_low > 1
    array_mu_low = mu_pixel_low * object_index



    #  the path of images acquired at high energy
    img_high = dicom2array(" ")
    mu_pixel_high = ((img_high/1000)+1)
    array_mu_high = mu_pixel_high

    mu1_over_mu2 = np.divide(array_mu_low, array_mu_high)

    a=31.6640
    b=-41.3636
    c=20.2761
    Zeff = (a) + (b * mu1_over_mu2) + (c * (mu1_over_mu2**2))

    rho_W = 3.3427966648311874E+23
    d=0.0817
    e=0.0383
    f=0.0071

    denominator = (d) + (e*Zeff) + f*(Zeff**2)
    rho= ((np.divide(array_mu_low, denominator)*rho_W)/1e+23)
```

```
binary_Zeff = np.logical_and(Zeff>11.08, Zeff<11.53)
binary_rho = np.logical_and(rho>5.38, rho<5.75)
rdl = np.logical_and(binary_rho, binary_Zeff)

binary_Zeff = np.logical_and(Zeff>11.22, Zeff<11.61)
binary_rho = np.logical_and(rho>4.74, rho<5.26)
fine_grained = np.logical_and(binary_rho, binary_Zeff)

binary_Zeff = np.logical_and(Zeff>11.49, Zeff<11.99)
binary_rho = np.logical_and(rho>5.43, rho<5.65)
coarse_grained = np.logical_and(binary_rho, binary_Zeff)

final_volume = rdl+fine_grained*2+coarse_grained*4

saveimg_from_array ( final_volume.astype('int16') , 'final_volume_test.tif' )
```

9 ANNEXE III

9.1 Supplementary Data article 3

Material	Effective Atomic Number	Electron Density (e^-/cm^3)
NaI 50%	39.64	4.04E+23
NaI 40%	36.77	3.92E+23
NaI 30%	33.39	3.79E+23
NaI 25%	31.39	3.71E+23
NaI 20%	29.14383268	3.64E+23
NaI 15%	26.49532521	3.59E+23
NaI 10%	23.17	3.52E+23
NaI 8%	21.55	3.49E+23
NaI 5%	18.54890461	3.44E+23
NaI 1%	11.73104801	3.38E+23
NaI 0.5%	10.11	3.36E+23
Aluminium bar	13.21	7.81E+23
Halite	15.17664919	6.23E+23
Cr. Quartz	11.56047782	7.97E+23
Pyrite	21.61117061	1.46E+24
Fluorite	16.53489231	9.32E+23
Titanium bar	22.00001037	1.23E+24
Zinc bar	30.00000385	1.94E+24
MicroclineRose	13.01808984	7.64E+23
Hematite	22.96288298	1.52E+24
Albite	11.47246905	7.82E+23

Table 9.1: Calibration samples.

Effective atomic number and electron density of the calibration materials calculated using the Equations 4.1 and 4.2 of the paper.

	Rock	CalculatedZ_{eff}	Calculated ρ_e (e^-/cm^3)	Measured Z_{eff}	*% error*	Measured ρ_e using $\mu_{110\ kVv}$ (e^-/cm^3)	*% error*	Measured ρ_e using $\mu_{220\ kV}$ (e^-/cm^3)	*% error*
y-	Chert	11.75	7.00E+23	11.95	*1.75%*	5.52E+23	*7.12%*	5.53E+23	*6.89%*
	Hematitic-oolite	18.81	7.70E+23	22.65	*20.51%*	6.21E+23	*36.13%*	6.21E+23	*36.14%*
	Chalk	14.67	4.35E+23	16.66	*15.58%*	5.19E+23	*17.04%*	5.17E+23	*17.26%*
c-	Chert	11.75	7.00E+23	11.68152	*0.55%*	5.67E+23	*4.55%*	5.67E+23	*4.57%*
	Hematitic-oolite	18.81	7.70E+23	23.23173	*23.54%*	6.09E+23	*37.39%*	6.24E+23	*35.81%*
	Chalk	14.67	4.35E+23	17.10756	*16.59%*	5.16E+23	*17.51%*	5.24E+23	*16.21%*
g-	Chert	11.75	7.00E+23	11.74168	*0.04%*	5.90E+23	*0.77%*	5.85E+23	*1.61%*
	Hematitic-oolite	18.81	7.70E+23	23.46217	*24.77%*	5.78E+23	*40.58%*	5.67E+23	*41.69%*
	Chalk	14.67	4.35E+23	16.82926	*14.71%*	5.04E+23	*19.39%*	4.88E+23	*21.91%*

Table 9.2: Example of other characterization, *Arion*.

Effective atomic number and electron density measured using linear attenuation coefficients μ from Arion Optimizer and different sets of calibration materials.

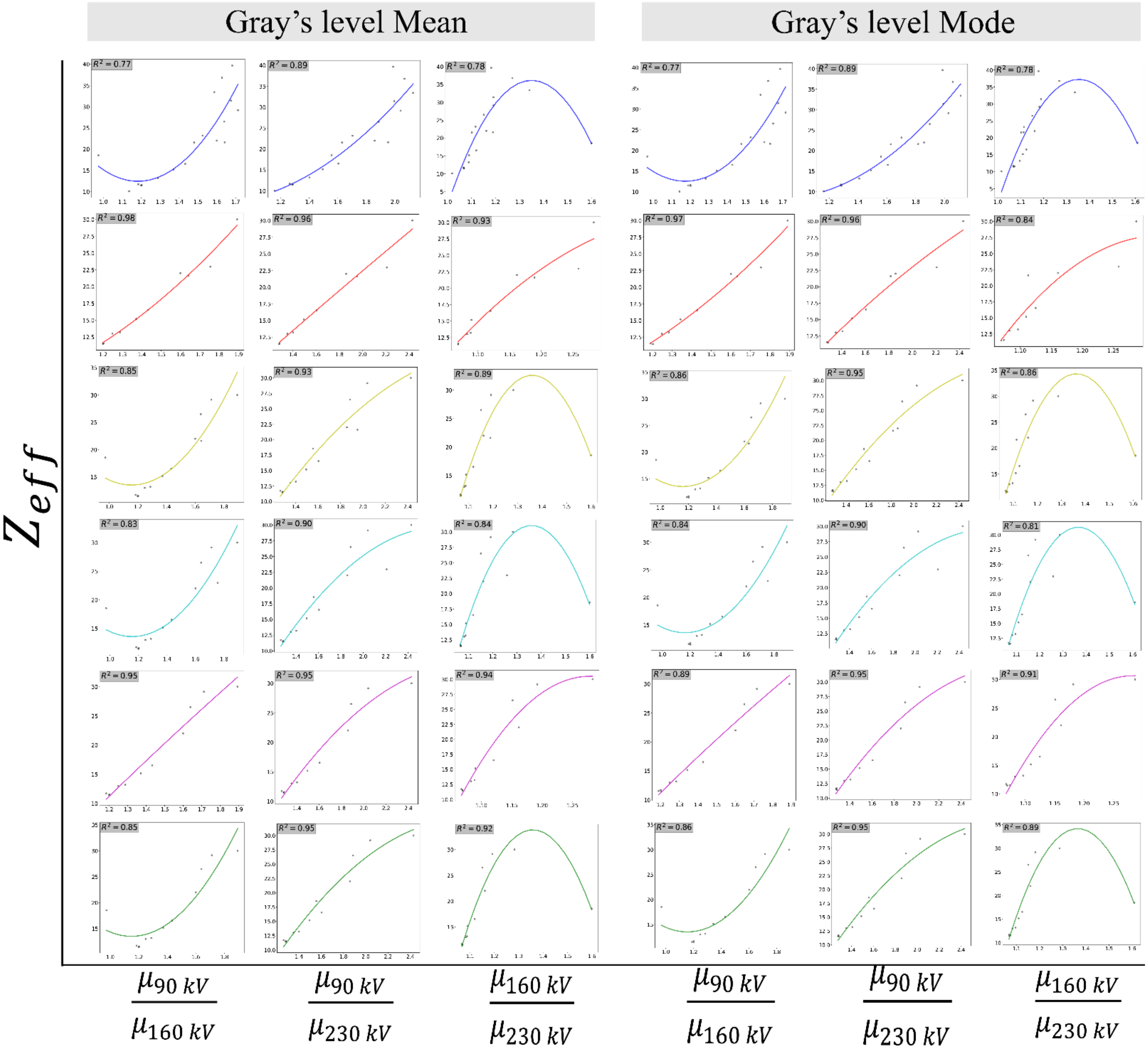

Figure 9.1: Z_{eff} calibration curves, CoreTOM.

These curves re obtained with CoreTOM scanner at different energies and using different sets of calibration materials.

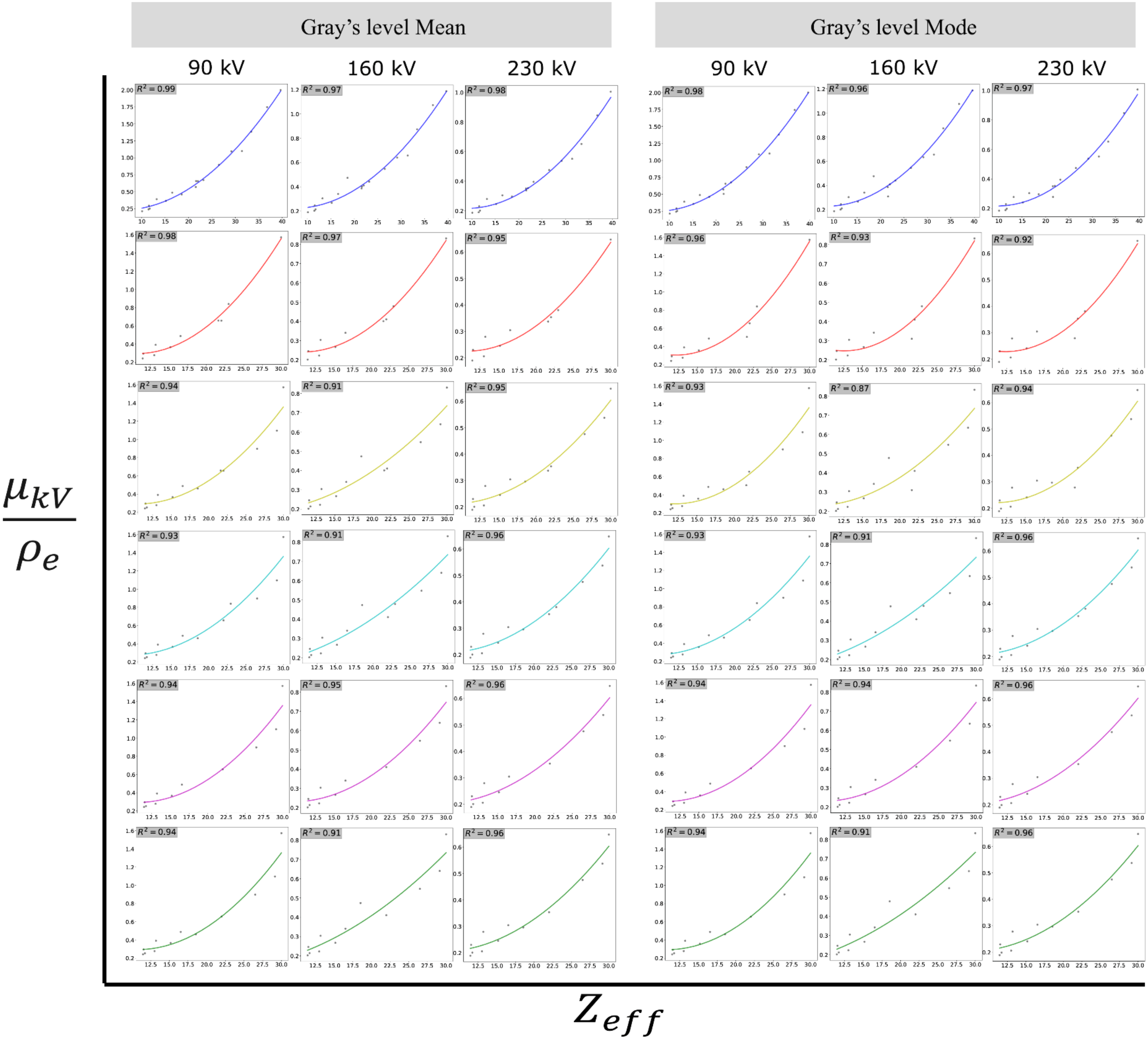

Figure 9.2: ρ_e calibration curves, CoreTOM.

These curves are obtained with CoreTOM scanner at different energies and using different sets of calibration materials.

	Gray's level Mean						Gray's level Mode						
Rock	Z_{eff_Meas} $\mu_{90\ kV}/\mu_{160\ kV}$	% error	Z_{eff_Meas} $\mu_{90\ kV}/\mu_{230\ kV}$	% error	Z_{eff_Meas} $\mu_{160\ kV}/\mu_{230\ kV}$	% error	Z_{eff_Meas} $\mu_{90\ kV}/\mu_{160\ kV}$	% error	Z_{eff_Meas} $\mu_{90\ kV}/\mu_{230\ kV}$	% error	Z_{eff_Meas} $\mu_{160\ kV}/\mu_{230\ kV}$	% error	
Chert	12.61	*7.32%*	12.28	*4.59%*	13.79	*17.42%*	12.81	*9.02%*	12.15	*3.47%*	13.91	*18.34%*	b-
Hematitic-oolite	29.17	*55.13%*	27.61	*46.82%*	26.81	*42.56%*	22.66	*20.54%*	22.24	*18.29%*	23.06	*22.65%*	
Chalk	13.99	*4.63%*	14.91	*1.57%*	18.14	*23.67%*	14.45	*1.47%*	14.81	*0.93%*	17.72	*20.81%*	
Chert	12.24	*4.18%*	12.21	*3.94%*	11.99	*2.09%*	12.36	*5.25%*	12.15	*3.48%*	11.72	*0.24%*	r-
Hematitic-oolite	21.61	*14.88%*	21.16	*12.56%*	20.72	*10.17%*	19.16	*1.88%*	19.14	*1.77%*	18.63	*0.89%*	
Chalk	14.07	*4.08%*	14.27	*2.73%*	14.79	*0.82%*	14.43	*1.66%*	14.56	*0.72%*	14.63	*0.28%*	
Chert	13.72	*16.81%*	12.06	*2.72%*	11.79	*0.43%*	13.72	*16.84%*	11.88	*1.19%*	11.64	*0.91%*	y-
Hematitic-oolite	22.27	*18.44%*	24.02	*27.76%*	23.59	*25.46%*	18.97	*0.91%*	21.39	*13.79%*	20.31	*7.97%*	
Chalk	14.55	*0.81%*	15.18	*3.51%*	15.72	*7.14%*	14.65	*0.09%*	15.34	*4.56%*	15.24	*3.91%*	
Chert	13.77	*17.25%*	12.08	*2.89%*	12.22	*4.01%*	13.76	*17.16%*	11.99	*2.11%*	11.81	*0.54%*	c-
Hematitic-oolite	21.81	*16.01%*	23.95	*27.35%*	22.88	*21.71%*	18.66	*0.72%*	21.18	*12.63%*	19.17	*1.94%*	
Chalk	14.55	*0.81%*	15.35	*4.67%*	15.76	*7.45%*	14.62	*0.33%*	15.41	*5.01%*	14.87	*1.35%*	
Chert	12.13	*3.23%*	11.91	*1.42%*	11.28	*3.94%*	12.16	*3.49%*	11.82	*0.61%*	10.65	*9.34%*	m-
Hematitic-oolite	24.28	*29.14%*	24.63	*30.99%*	25.22	*34.12%*	21.45	*14.09%*	21.54	*14.57%*	20.68	*9.98%*	
Chalk	14.92	*1.73%*	15.31	*4.31%*	16.22	*10.56%*	15.29	*4.23%*	15.36	*4.74%*	14.95	*1.89%*	
Chert	13.76	*17.12%*	11.96	*1.82%*	11.74	*0.02%*	13.75	*17.07%*	11.86	*0.98%*	11.24	*4.31%*	g-
Hematitic-oolite	22.42	*19.24%*	24.74	*31.59%*	24.32	*29.36%*	19.06	*1.39%*	21.66	*15.21%*	19.95	*6.08%*	
Chalk	14.62	*0.31%*	15.39	*4.92%*	15.94	*8.61%*	14.71	*0.27%*	15.45	*5.32%*	14.86	*1.31%*	

Table 9.3: Example of other Z_{eff} characterizations, CoreTOM.

Results of the rocks' Z_{eff_Meas} measured using DECT method with three different energy couples and the CoreTOM scanner; the percentage difference with calculated properties (Z_{eff_Calc} of Table 4.4) is indicated for each measurement. Both mean and mode of gray level histogram were used.

	Gray's level Mode												
	from Z_{eff_Meas} using $\mu_{90\ kV}/\mu_{160\ kV}$				**from Z_{eff_Meas} using $\mu_{90\ kV}/\mu_{230\ kV}$**				**from Z_{eff_Meas} using $\mu_{160\ kV}/\mu_{230\ kV}$**				
Rock	**ρ_{e_Meas} using $\mu_{90\ kV}$**	***% error***	**ρ_{e_Meas} using $\mu_{160\ kV}$**	***% error***	**ρ_{e_Meas} using $\mu_{90\ kV}$**	***% error***	**ρ_{e_Meas} using $\mu_{230\ kV}$**	***% error***	**ρ_{e_Meas} using $\mu_{160\ kV}$**	***% error***	**ρ_{e_Meas} using $\mu_{230\ kV}$**	***% error***	
Chert	6.81E+23	*2.64%*	5.54E+23	*20.78%*	8.20E+23	*17.25%*	6.23E+23	*10.89%*	6.88E+23	*1.73%*	7.36E+23	*5.21%*	b-
Hematitic-oolite	7.04E+23	*8.68%*	4.58E+23	*40.51%*	1.03E+24	*34.25%*	5.95E+23	*22.81%*	7.38E+23	*4.22%*	8.36E+23	*8.53%*	
Chalk	5.01E+23	*14.92%*	3.76E+23	*13.58%*	6.03E+23	*38.51%*	4.14E+23	*4.88%*	4.41E+23	*1.29%*	4.83E+23	*10.91%*	
Chert	6.57E+23	*6.13%*	5.34E+23	*23.62%*	8.06E+23	*15.24%*	6.13E+23	*12.42%*	6.73E+23	*3.78%*	7.21E+23	*3.01%*	r-
Hematitic-oolite	8.80E+23	*14.25%*	5.73E+23	*25.56%*	1.32E+24	*70.84%*	7.57E+23	*1.77%*	9.12E+23	*18.41%*	1.03E+24	*34.17%*	
Chalk	5.03E+23	*15.56%*	3.78E+23	*13.11%*	6.38E+23	*46.59%*	4.38E+23	*0.66%*	4.85E+23	*11.37%*	5.31E+23	*21.94%*	
Chert	6.32E+23	*9.65%*	5.14E+23	*26.49%*	8.24E+23	*17.75%*	6.26E+23	*10.52%*	6.74E+23	*3.66%*	7.22E+23	*3.15%*	y-
Hematitic-oolite	9.30E+23	*20.75%*	6.06E+23	*21.32%*	1.04E+24	*35.39%*	6.00E+23	*22.15%*	7.66E+23	*0.51%*	7.22E+23	*6.31%*	
Chalk	4.95E+23	*13.69%*	3.72E+23	*14.51%*	5.76E+23	*32.31%*	3.96E+23	*9.14%*	4.53E+23	*3.94%*	4.96E+23	*13.81%*	
Chert	6.15E+23	*12.09%*	5.00E+23	*28.48%*	8.75E+23	*25.01%*	6.65E+23	*5.01%*	7.10E+23	*1.46%*	7.60E+23	*8.63%*	c-
Hematitic-oolite	8.77E+23	*13.82%*	5.71E+23	*25.84%*	1.06E+24	*37.55%*	6.09E+23	*20.91%*	8.42E+23	*9.27%*	9.54E+23	*23.83%*	
Chalk	4.72E+23	*8.28%*	3.55E+23	*18.57%*	5.74E+23	*31.71%*	3.94E+23	*9.54%*	4.71E+23	*8.06%*	5.15E+23	*18.32%*	
Chert	6.78E+23	*3.09%*	5.52E+23	*21.16%*	8.55E+23	*22.25%*	6.50E+23	*7.11%*	7.19E+23	*2.71%5*	7.70E+23	*9.97%*	m-
Hematitic-oolite	7.11E+23	*7.68%*	4.63E+23	*39.85%*	1.09E+24	*41.55%*	6.27E+23	*18.61%*	7.20E+23	*6.59%*	8.15E+23	*5.84%*	
Chalk	4.69E+23	*7.59%*	3.52E+23	*19.09%*	6.09E+23	*39.83%*	4.18E+23	*3.97%*	4.48E+23	*2.81%*	4.90E+23	*12.56%*	
Chert	6.48E+23	*7.36%*	5.27E+23	*24.62%*	8.61E+23	*23.07%*	6.54E+23	*6.48%*	7.10E+23	*1.44%*	7.60E+23	*8.61%*	g-
Hematitic-oolite	9.26E+23	*20.15%*	6.03E+23	*21.71%*	9.78E+23	*26.93%*	5.62E+23	*27.02%*	7.67E+23	*0.41%*	8.69E+23	*12.84%*	
Chalk	5.01E+23	*15.06%*	3.77E+23	*13.47%*	5.50E+23	*26.23%*	3.78E+23	*13.31%*	4.55E+23	*4.58%*	4.99E+23	*14.51%*	

	Gray's level Mean												
	from Z_{eff} calculated using $\mu_{90\ kV}/\mu_{160\ kV}$				**from Z_{eff} calculated using $\mu_{90\ kV}/\mu_{230\ kV}$**				**from *Zeff* calculated using $\mu_{160\ kV}/\mu_{230\ kV}$**				
Rock	**ρ_{e_Meas} using $\mu_{90\ kV}$**	***% error***	**ρ_{e_Meas} using $\mu_{160\ kV}$**	***% error***	**ρ_{e_Meas} using $\mu_{90\ kV}$**	***% error***	**ρ_{e_Meas} using $\mu_{230\ kV}$**	***% error***	**ρ_{e_Meas} using $\mu_{160\ kV}$**	***% error***	**ρ_{e_Meas} using $\mu_{230\ kV}$**	***% error***	
Chert	6.72E+23	*3.93%*	5.47E+23	*21.84%*	8.29E+23	*18.48*	6.30E+23	*9.95%*	6.51E+23	*6.92%*	6.97E+23	*0.36%*	b-
Hematitic-oolite	5.14E+23	*33.22%*	3.14E+23	*59.18%*	9.13E+23	*18.55*	4.77E+23	*38.03%*	5.96E+23	*22.59%*	6.97E+23	*9.48%*	
Chalk	4.99E+23	*14.55%*	3.78E+23	*13.27%*	6.06E+23	*39.09*	4.17E+23	*4.19%*	4.00E+23	*8.21%*	4.39E+23	*0.87%*	
Chert	6.55E+23	*6.43%*	5.33E+23	*23.88%*	8.09E+23	*15.61*	6.15E+23	*12.13%*	6.78E+23	*3.11%*	7.26E+23	*3.71%*	r-
Hematitic-oolite	7.59E+23	*1.46%*	4.64E+23	*39.76%*	1.27E+24	*64.91*	6.64E+23	*13.79%*	8.47E+23	*9.89%*	9.90E+23	*28.51%*	
Chalk	4.86E+23	*11.55%*	3.68E+23	*15.54%*	6.19E+23	*42.11*	4.26E+23	*2.12%*	4.70E+23	*7.86%*	5.16E+23	*18.56%*	
Chert	6.18E+23	*11.66%*	5.03E+23	*28.13%*	8.41E+23	*20.25%*	6.39E+23	*8.61%*	6.83E+23	*2.41%*	7.31E+23	*4.46%*	y-
Hematitic-oolite	7.76E+23	*0.75%*	4.74E+23	*38.41%*	1.05E+24	*36.87%*	5.51E+23	*28.45%*	6.70E+23	*12.96%*	7.84E+23	*1.77%*	
Chalk	4.80E+23	*10.22%*	3.63E+23	*16.55%*	5.72E+23	*31.44%*	3.94E+23	*9.46%*	4.34E+23	*0.25%*	4.77E+23	*9.63%*	
Chert	6.18E+23	*11.67%*	5.03E+23	*28.14%*	8.27E+23	*18.23%*	6.29E+23	*10.14%*	7.00E+23	*0.01%*	7.49E+23	*7.05%*	c-

Hematitic-oolite	8.03E+23	*4.17%*	4.91E+23	*36.31%*	1.01E+24	*30.77%*	5.27E+23	*31.63%*	7.51E+23	*2.51%*	8.78E+23	*13.99%*	🟦
Chalk	4.78E+23	*9.71%*	3.62E+23	*16.94%*	5.42E+23	*24.54%*	3.74E+23	*14.21%*	4.54E+23	*4.14%*	4.99E+23	*14.47%*	
Chert	6.75E+23	*3.58%*	5.49E+23	*21.56%*	8.58E+23	*22.59%*	6.52E+23	*6.82%*	6.99E+23	*0.15%*	7.48E+23	*6.88%*	m-
Hematitic-oolite	6.60E+23	*14.38%*	4.03E+23	*47.66%*	1.08E+24	*40.06%*	5.64E+23	*26.78%*	5.95E+23	*22.79%*	6.96E+23	*9.71%*	
Chalk	4.79E+23	*9.88%*	3.62E+23	*16.81%*	6.17E+23	*41.63%*	4.25E+23	*2.44%*	4.15E+23	*4.69%*	4.56E+23	*4.74%*	
Chert	6.13E+23	*12.45%*	4.98E+23	*28.78%*	8.70E+23	*24.28%*	6.61E+23	*5.54%*	6.98E+23	*0.26%*	7.47E+23	*6.75%*	g-
Hematitic-oolite	7.62E+23	*1.15%*	4.66E+23	*39.57%*	1.03E+24	*33.16%*	5.36E+23	*30.38%*	6.52E+23	*15.39%*	7.62E+23	*1.06%*	
Chalk	4.75E+23	*9.11%*	3.60E+23	*17.39%*	5.66E+23	*30.08%*	3.90E+23	*10.41%*	4.33E+23	*0.46%*	4.76E+23	*9.41%*	

Table 9.4: Example of other ρ_e characterizations, CoreTOM.

Results of the rocks' ρ_{e_Meas} measured using DECT method with three different energy couples and the CoreTOM scanner; the percentage difference with calculated properties (ρ_{e_Calc} of Table 4.4) is indicated for each measurement. Both mean and mode of gray level histogram were used.